The Power Spectrum and Bispectrum of Inflation and Cosmic Defects

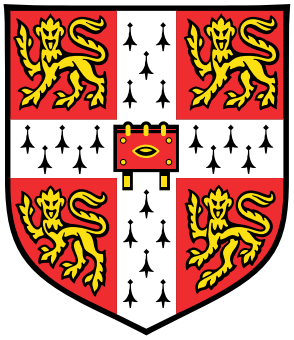

Andrei Lazanu

Department of Applied Mathematics and Theoretical Physics
University of Cambridge

This dissertation is submitted for the degree of
Doctor of Philosophy

Gonville and Caius College June 2016

DECLARATION

This dissertation is my own work and contains nothing which is the outcome of work done in collaboration with others, except as specified in the text and Acknowledgements. Except where specific reference is made to the work of others, the contents of this dissertation are original and have not been submitted in whole or in part for consideration for any other degree or qualification in this, or any other university. Chapter 3 is based on results published in Refs. [1, 2] done in collaboration with Paul Shellard and Martin Landriau. Chapter 4 contains the results presented in Ref. [3] done with Paul Shellard and Carlos Martins. Chapters 5 and 6 contain work done in collaboration with Paul Shellard, Tommaso Giannantonio and Marcel Schmittfull and published in Refs. [4, 5].

Andrei Lazanu
June 2016

ACKNOWLEDGEMENTS

First of all I am grateful to my supervisor, Paul Shellard, for his guidance, support and encouragement throughout my PhD and for sharing some of his expertise in physics and cosmology with me. It has been a great privilege to work with him and his physical insight has proved invaluable over the last few years. Moreover, I am very grateful to him for reading my thesis and for making suggestions for improving it.

I am indebted to Tommaso Giannantonio for his patience, input and support over the last two years and for our collaboration on the large-scale structure of the Universe which is described in the second part of the thesis. I wish to also thank him for reading through the manuscript of my thesis.

I would like to thank my other collaborators, in particular Martin Landriau, Carlos Martins and Marcel Schmittfull for the fruitful work that we have done and which has led to the completion of many interesting projects. I am also grateful to James Fergusson and Levon Pogosian for many enlightening discussions. The numerous computations presented in this thesis were performed on the COSMOS Shared Memory system at DAMTP, and I would like to mention here the COSMOS team: Andrey Kaliazin, Juha Jäykkä, James Briggs and Kacper Kornet for providing invaluable guidance with various computational aspects.

During middle and high schools, my interests in mathematics were encouraged by a number of excellent teachers. In particular, I would like to mention the two projects that I have been involved and that had a significant impact on my future scientific development and career, *MathForum* from the University of Drexel and *NRICH*, part of the *Millennium Mathematics Project* at Cambridge. Special thanks go to Terry Trotter from the *MathForum* who has been a great mentor in Algebra and Toni Beardon from *NRICH* whose guidance has helped me greatly before coming to do my undergraduate studies in Cambridge.

My PhD was supported by a studentship from the Science and Technology Facilities Council (STFC). For the final year I am grateful to have received generous funding from Gonville and Caius College, Cambridge, the Cambridge Philosophical Society, the Centre

for Theoretical Cosmology and the Department of Applied Mathematics and Theoretical Physics.

This thesis is dedicated to my parents for their consistent and enduring love, support and encouragement over the years.

ABSTRACT

Much of the recent progress in cosmology has come from studying the power spectrum of the cosmic microwave background (CMB). The latest results from the Planck satellite confirmed that the inflationary paradigm with the ΛCDM six-parameter model provides a very good description of the observed structures in the Universe. Even so, additional parameters, such as cosmic defects, are still allowed by current observational data. Additionally, many of the inflationary models predict a significant departure from Gaussianity in the distribution of primordial perturbations. Higher order statistics, such as the bispectrum, are required to test and constrain such models. The late-time distribution of matter in the Universe - large-scale structure (LSS) - contains much more information than the CMB that has not yet been used. In this thesis, we look at both problems: the effects of cosmic defects, in particular cosmic strings and domain walls on the CMB power spectrum through numerical simulations, and the dark matter bispectrum of large-scale structure. Topological defects are predicted by most inflationary theories involving symmetry breaking in the early Universe. In this thesis we study the effects of cosmic strings and domain walls on the CMB by determining their power spectrum. We use Nambu-Goto and field theory simulations for cosmic strings and domain walls respectively, and we determine the power spectra they produce with a modified Einstein-Boltzmann solver sourced by unequal time correlators from components of the energy-momentum tensor of the defects. We use these spectra together with CMB likelihoods to obtain constraints on the energy scales of formation of the cosmic defects, finding $G\mu/c^2 < 1.29 \times 10^{-7}$ and $\eta < 0.93$ MeV (at 95% confidence level) for cosmic strings and domain walls respectively, when using the Planck satellite likelihoods. For the matter bispectrum of LSS, we compare different perturbative and phenomenological models with measurements from N-body simulations by using shape and amplitude correlators and we determine on which scales and for which redshifts they are accurate. We propose a phenomenological 'three-shape' model, based on the fundamental shapes we have observed by studying the halo model that are also present in the simulations. When calibrated on the simulations, this model accurately describes the bispectrum on all scales and redshifts considered, providing a prototype bispectrum HALOFIT-like methodology that could be used to describe and test parameter dependencies.

TABLE OF CONTENTS

List of figures **xiii**

List of tables **xxiii**

1 Introduction **1**

1.1 The standard cosmological model 3
1.2 The formation of structures 6
1.2.1 Gauge transformations 8
1.2.2 Synchronous gauge perturbations 9
1.2.3 Growth of structure 11
1.3 The Boltzmann Equation 14
1.4 The Cosmic Microwave Background 19
1.5 Outline of the Thesis 22

2 Cosmic Defects **25**

2.1 Introduction 25
2.2 Domain walls 27
2.3 Cosmic strings 29
2.4 Monopoles 31
2.5 Textures 32

3 Cosmic Strings **35**

3.1 Cosmic string models 35
3.1.1 Abelian-Higgs model 36
3.1.2 Nambu-Goto model 37
3.2 Cosmic string simulations 42
3.3 Unequal-time correlator approach 44
3.4 Evolution of the UETCs and resolution effects 48

3.5 Analytic UETC model . . . 55
3.6 Power spectrum obtained from eigendecomposition of UETCs . . . 58
3.7 String tension constraints . . . 63
3.7.1 Background on methods . . . 63
3.7.2 BICEP2 experiment . . . 66
3.7.3 Results for the *Planck* likelihood . . . 67
3.7.4 Results for the *Planck* & BICEP2 likelihoods . . . 72
3.8 Discussion and conclusions . . . 80

4 Domain Walls **83**
4.1 Domain walls equations of motion . . . 83
4.2 Formalism for calculating the power spectrum . . . 85
4.3 Simulations . . . 87
4.4 Results . . . 89
4.5 CMB constraints on domain walls . . . 92
4.6 Conclusions . . . 94

5 Perturbative and Halo Models for the Large Scale Structure of the Universe **97**
5.1 Introduction . . . 97
5.2 Perturbation theory models of Large Scale Structure . . . 100
5.2.1 Standard Perturbation Theory . . . 101
5.2.2 Effective Field Theory . . . 108
5.2.3 Renormalised Perturbation Theory . . . 111
5.2.4 Resummed Lagrangian perturbation theory . . . 123
5.2.5 Nine-parameter model . . . 125
5.3 Phenomenological halo models . . . 127
5.3.1 Standard halo model . . . 127
5.3.2 Combined halo-PT model . . . 133

6 Comparison between Theoretical LSS Models and *N*-Body Simulations **139**
6.1 Introduction and correlators . . . 139
6.1.1 Shape and amplitude correlators . . . 139
6.1.2 Three canonical shape functions . . . 142
6.1.3 Scale-dependent or ‘sliced’ correlators . . . 146
6.2 Shapes of the theoretical models . . . 146
6.2.1 Shapes of the perturbative bispectrum models . . . 146

6.2.2 Halo model shapes 148
6.3 Polyspectra from simulations 153
6.3.1 *N*-body simulations 153
6.3.2 Power spectrum 154
6.3.3 Modal bispectrum methodology 156
6.3.4 Bispectrum reconstruction from simulations 158
6.4 Towards a three-shape bispectrum benchmark model 159
6.4.1 Simulation bispectrum shapes 161
6.4.2 Two-halo boost model 163
6.4.3 Two-shape time-shift model 164
6.4.4 Three-shape bispectrum model 165
6.4.5 Directions for further improvement 169
6.5 Bispectrum model comparison with simulations 170
6.5.1 Testing alternative perturbative approaches 170
6.5.2 Testing phenomenological halo models 177
6.6 Conclusions 183

7 Conclusions **187**
7.1 Effects of topological defects on CMB 187
7.2 Matter bispectrum of large-scale structure 188

References **191**

LIST OF FIGURES

1.1 Temperature anisotropies in the sky as viewed by the *Planck* satellite with galaxy contributions obscuring the equatorial region (at 143 GHz). The figure is reproduced from Ref. [6]. 2

1.2 Temperature power spectrum as measured by the Planck Collaboration (blue data points) with the maximum likelihood temperature power spectrum (top panel). The bottom panel represents residuals with respect to the red curve. This plot is Fig. 1 of Ref. [7]. 21

2.1 Potential $V(\phi)$ characterising the formation of domain walls. 28

2.2 Static solution of Eq. (2.9) illustrating the formation of domain walls (left) and energy density of this solution (right). 29

2.3 Mexican hat potential $V(\phi)$ characterising the formation of cosmic strings. . 30

3.1 Comparison of AH (left) and Nambu-Goto (right) cosmic string simulations, taken from Ref. [8]. 41

3.2 Evolution of the string network in the simulation covering the matter era (redshift range 945 to 37.2, from left to right). 43

3.3 Energy density component of the string network in real space evaluated at time 384 out of 1536 for the simulation in the radiation era for the six resolutions considered: 128^3, 256^3, 512^3, 768^3, 1024^3 and 1536^3 points. . . 49

3.4 Scalar UETCs obtained from a grid resolution of 1024^3: the figures of the left represent oblique 3D views of the three scalar UETCs ($\langle\Theta_{00}\Theta_{00}\rangle(k\tau,k\tau')$ - top, $\langle\Theta^S\Theta^S\rangle(k\tau,k\tau')$ - middle and $\langle\Theta_{00}\Theta^S\rangle(k\tau,k\tau')$ - bottom), the top right plot represents a contour plot of $\langle\Theta_{00}\Theta_{00}\rangle$ in linear scale and two bottom right plots represent the three scalar equal time correlators in linear and logarithmic scales. 50

3.5 Vector and tensor UETC components obtained from a grid resolution of 1024^3: oblique 3D views of $\langle \Theta^V \Theta^V \rangle (k\tau, k\tau')$ and $\langle \Theta^T \Theta^T \rangle (k\tau, k\tau')$ (left) and the corresponding equal time correlators (right). 51

3.6 Network correlation in the initial conditions from the simulation covering the matter era: left - oblique 3D view, right - front view. 52

3.7 $\langle \Theta_{00} \Theta_{00} \rangle$ UETCs calculated between one snapshot of the simulation and the whole simulation from different starting point, exhibiting scale invariance. In the bottom two rhs plots, the two plotted curves are indistinguishable. Scaling can be observed between the figures despite the correlation time used. 53

3.8 $\langle \Theta_{00} \Theta_{00} \rangle$ equal time correlators at different resolutions. 54

3.9 Evolution of the averaged shape and amplitude correlators. 55

3.10 Comparison between the TT power spectrum for USM , Abelian-Higgs and Nambu-Goto simulated strings. Simulation 1 covers the radiation era, Simulation 2 the matter era, and Simulation 3 matter and cosmological constant eras. The USM and Abelian-Higgs power spectra are the standard results used in the *Planck* cosmic defects paper [9]. All power spectra are normalised to $C_{10}^{\text{strings}} = 1$. 57

3.11 Power spectra of the cosmic strings obtained from the simulations in the radiation era assuming scale invariance. From left to right: scalar, vector, and tensor power spectra; from top to bottom: TT, EE, TE, and BB power spectra ($G\mu = 1.5 \times 10^{-7}$). The numbers in the legend represent the number of eigenvectors used. The colours in the tensor spectra plots represent different numbers of eigenvectors used compared to the scalar and vector spectra. . . 60

3.12 Comparison between the TT power spectra obtained through the best fit method and using eigenvectors ($G\mu = 2.07 \times 10^{-6}$). 61

3.13 Power spectra of the cosmic strings obtained by using each of the three sets of UETCs and assuming scaling for the whole history of the Universe. The red, green, and blue show the power spectra considering the extrapolation of the results obtained in the radiation, matter, and matter + Λ epochs. The contributions from the UETCs from just the time interval where they are valid are plotted in the yellow, cyan, and magenta curves, and their sum is in black. The black curve represents the final overall power spectrum obtained. From left to right: The scalar, vector, and tensor power spectra; from top to bottom the TT, EE, TE, and BB power spectra ($G\mu = 1.5 \times 10^{-7}$). 64

3.14 Comparison between the TT power spectra obtained using the three simulations and the USM, Abelian-Higgs (standard results) and CMBACT version 4. In the left plot, the string tension is $G\mu = 2.07 \times 10^{-6}$, showing that the USM and the Nambu-Goto strings have different amplitudes compared to the Abelian-Higgs ones; in the right plot, amplitudes are normalised to $C_{10}^{\text{strings}} = 1$, emphasising the similar shapes of the power spectra considered. 65

3.15 Marginalised likelihoods in the *Planck* + WP & strings model. 68

3.16 Marginalised likelihoods obtained when adding cosmic strings, N_{eff} and tensor modes (r). 72

3.17 Mean likelihoods of the samples (red dotted lines) and marginalised probabilities (blue solid lines) for parameter f_{10} in the following situations (from left to right and top to bottom): *Planck* & strings; *Planck* & strings & N_{eff}; *Planck* & strings & r; *Planck* & strings & N_{eff} & r, *Planck* & N_{eff} & running & cosmic strings. The green and cyan curves respectively represent the mean likelihoods and marginalised probabilities of the samples after the introduction of HighL & BAO. 73

3.18 Two-dimensional marginalised likelihoods in the f_{10}-N_{eff}, H_0-N_{eff} and n_s-N_{eff} planes in the following cases (top to bottom): N_{eff} only (no strings), N_{eff} and cosmic strings, N_{eff}, running and cosmic strings, N_{eff}, running and cosmic strings, with SPT/ACT and BAOs. 74

3.19 Marginalised likelihoods in the f_{10}-$\Omega_b c^2$ plane (left) and best fit of the BB power spectrum using the *Planck* and BICEP2 likelihoods with cosmic strings at $G\mu = 1.74 \times 10^{-7}$ (right) and ΛCDM. 75

3.20 Marginalised likelihoods in the f_{10}-$\Omega_b c^2$ and f_{10}-r planes for BICEP2 likelihoods with strings and tensor modes (left) and best fit of the BB power spectrum using the *Planck* and BICEP2 likelihoods with cosmic strings at $G\mu = 1.44 \times 10^{-7}$, ΛCDM and r (right). 75

3.21 Mean likelihoods of the samples (red dotted lines) and marginalised probabilities (blue solid lines) for parameter f_{10} in the following situations (from left to right and top to bottom): *Planck* & BICEP & strings; *Planck* & BICEP & strings & r; *Planck* & BICEP & strings & N_{eff} & r, *Planck* & BICEP & N_{eff} & running & r & cosmic strings. The green and cyan curves respectively represent the mean likelihoods and marginalised probabilities of the samples after the introduction of HighL & BAO. 76

3.22 Two-dimensional marginalised likelihoods in the f_{10}-$N_{\rm eff}$, H_0-$N_{\rm eff}$ and n_s-$N_{\rm eff}$ planes in the following cases (top to bottom): $N_{\rm eff}$ only (no strings), $N_{\rm eff}$ and cosmic strings, $N_{\rm eff}$, running and cosmic strings, $N_{\rm eff}$, running and cosmic strings, with SPT/ACT and BAOs. 79

4.1 Three-dimensional plots of the energy density component of the energy-momentum tensor of the domain wall network at five times through the simulation (left to right and top to bottom). 88
4.2 Scaling behaviour of the UETC in the radiation (blue) and matter (green) eras. 89
4.3 Two-dimensional slices through the domain wall network showing the energy density of the walls in the matter era during the scaling regime of the simulation. The four panels represent snapshots taken at roughly equal conformal time steps between the beginning and end of the simulation (from left to right and top to bottom). The colour bars show the magnitude of the energy density of the network in the units of the simulation. 90
4.4 Power spectra of domain walls showing the individual results from the radiation (in blue) and matter (in green) eras as well as total power spectra for scalars, vectors and tensors in the temperature and polarisation (EE, TE and BB) channels. In the case of the TE polarisation we have plotted the negative parts with dashed lines in the same colours as their positive counterparts. In the plots $\sigma/t_0 = 1.5 \times 10^{-7}$. 91
4.5 Comparison between the domain walls power spectra from radiation & matter eras and radiation, matter & Λ eras. In the plots $\sigma/t_0 = 1.5 \times 10^{-7}$. 92
4.6 Comparison between the CMB power spectrum (from Planck) and the power spectrum from domain walls (normalised at the 2σ value of the energy scale) in the two scenarios considered. 93

5.1 Equilateral (*left*), squeezed (*middle*) and flattened bispectra (*right*) from perturbation theories at $z = 0$. We show the theoretical predictions of the tree-level bispectrum, SPT, EFT and the one- and two-loop MPTBREEZE bispectra. For this last model, we observe that the wavenumber at which the theory starts decaying increases significantly when adding the two-loop terms in the case of the equilateral and flattened configurations, closely following the EFT model down to smaller scales, while for the squeezed configuration the improvement is negligible. Bispectra are plotted in units of $(\mathrm{Mpc}/h)^6$ throughout the LSS chapters. 122

6.1 The tetrapyd bispectrum domain consists of a tetrahedral region (blue) defined by the wavevector triangle condition in Eq. (5.41), together with a pyramidal region (green) bounded by the resolution limit $k_{\rm max}$. For the autocorrelator bispectrum this has a sixfold symmetry, so to illustrate the internal structure of the bispectrum (equilateral limit) we will split the tetrapyd across the vertical plane given by the red-dashed lines, removing the front half as shown in Fig. 6.2. 140

6.2 The split 3D tetrapyd region used to illustrate the SN-weighted bispectrum showing only the back half with $k_1 < k_2$. Colour-coded regions show the location of the 'squeezed' (red), 'flattened' (green) and 'equilateral' or 'constant' (blue) shape signals. In the bispectrum ansatz Eq. (6.9) the shape $S(k_1,k_2,k_3)$ is defined on the $K \equiv k_1+k_2+k_3 = $ const. cross-sectional planes, while the scale-dependence $f(K)$ is given along the dashed diagonal $k_1 = k_2 = k_3$. 141

6.3 (a) The SN-weighted 'constant' bispectrum of Eq. (6.11) with a broadly equilateral signal shown together with (b) the 'squeezed' or local model (Eq. 6.12) with high signal at the edges near $k_i \approx 0$ (shown at redshift $z = 0$). Note that the plotted 'constant' bispectrum does not have a constant cross-sectional shape because of the non-uniform signal-to-noise weighting (Eq. 6.2) particularly near the edges; here $S^{\rm const.}$ in Eq. (6.11) is multiplied by $f(K) = K^3$ (the colour scale is normalised). 144

6.4 Flattened shapes: (a) The SN-weighted tree-level bispectrum of Eq. (6.14) compared with (b) the nonlinear tree-level model (Eq. 6.15), both shown at redshift $z = 2$. Note that this flattened shape is dominated by signal on the outer tetrapyd face (front left) where $k_1 + k_2 \approx k_3$ (see Fig. 6.2 for the geometry). The nonlinear tree-level amplitude is substantially higher than the tree-level, but they share an excellent binned shape correlation (Eq. 6.17), which always remains above 99%. 145

6.5 Shapes of the perturbation theory bispectra. For each of the theoretical bispectra considered, we show the shape correlators in k slices $\mathscr{S}^S$ (Eq. 6.16) with respect to the constant, squeezed and tree-level shapes (Eqs. 6.11-6.14). The left panel shows the one-loop SPT shape correlators, the central panel shows the EFT counterterm ($-B_{c_s}$) shapes, and the right panel refers to the MPTBREEZE one-loop shapes. All panels refer to $z = 0$. In the case of SPT (left), the thick lines represent the sum of the positive terms of the one-loop expansion (B_{222} and $B^{(I)}_{321}$), while the thin lines refer to the sum of the negative terms ($B^{(II)}_{321}$ and B_{411}). 147

6.6 Shapes of the halo model bispectrum. We show the correlation of the three components of the halo model with the constant, squeezed and tree-level shapes at redshifts $z = 0$ (upper panels) and $z = 2$ (lower panels). The left panels show that the one-halo term has a constant shape (Eq. 6.11), the central panels demonstrate that the two-halo term is nearly fully correlated with the squeezed shape (Eq. 6.12), and the right panels indicate that the three-halo term has the same shape as the tree-level bispectrum (Eq. 6.14). These results hold independent of scale and redshift. 149

6.7 Equilateral one-halo (top panel) and two-halo (bottom panel) bispectra at $z = \{0,1,2,3\}$ (solid lines, from top to bottom), compared with the corresponding fitting function from Eqs. (6.20, 6.24) (dashed lines). The dotted lines refer to the corrected two-halo fitting function of Eq. (6.25). 150

6.8 The SN-weighted one-halo bispectrum of Eq. (5.177) (upper panel) compared at $z = 0$ with the one-halo constant shape ansatz of Eq. (6.19) with scale-dependence $f_{1h}(K)$ given by Eqs. (6.20, 6.22) (lower panel). This fit is visually hard to distinguish reflecting the high total correlation achieved over all lengthscales (and redshifts). The cross-sectional shape does not appear constant because of the SN-weighting (Eq. 6.1). 151

6.9 The SN-weighted two-halo bispectrum of Eq. (5.178) at $z = 0$, showing the strongly squeezed signal. Like the one-halo bispectrum shown in Fig. 6.8, an excellent fit to this model can be obtained with the separable ansatz of Eq. (6.23) using the standard 'squeezed' shape (Eq. 6.12). 152

6.10 Overview of the matter power spectra predicted by the range of theoretical models we consider, compared with data measured from N-body simulations. The data points are combined from N-body simulations with three different box sizes. The upper and lower rows refer to perturbation theories and halo models respectively. The columns refer to $z = 0$, 1 and 2 from left to right; in each plot, the main upper panel shows the power spectra comparison, while the smaller lower panel shows the residuals with respect to the HALOFIT prediction. 155

6.11 Evolution of the SN-weighted 3D bispectrum from N-body simulations into the nonlinear regime with $k_i \leq 2\,h/\mathrm{Mpc}$ at redshifts (a) $z = 3$, (b) $z = 2$, (c) $z = 1$, and (d) $z = 0$. The bispectrum colour scheme is scaled with the growth factor $D(z)$ and the tetrahedral geometry of the bispectrum domain is illustrated in Fig. 6.2. Note the presence of both a strong flattened and squeezed signal shape at redshifts $z = 2, 3$ (front left face of tetrapyd and lower edge respectively in panels a, b). At lower redshift this is overtaken by a strong uniform or one-halo signal throughout the interior region for $k \gtrsim 1\,h/\mathrm{Mpc}$ (front right face in panel d). The colour scale is fixed at $z = 3$ in (a) to encompass all values up to the maximum. It is then scaled with the growth rate expected for the tree-level signal to aid physical interpretation and reveal non-linear growth rates. This means at small scales in (d) at $z = 0$ the colour scale is saturated, which is useful to highlight features at intermediate scales. 160

6.12 Sliced shape correlations of the measured N-body bispectrum with the three canonical shapes: constant (Eq. 6.11), squeezed (Eq. 6.12) and tree-level (Eq. 6.14) shown at redshifts $z = \{0, 1, 2\}$ (upper to lower panels). The sliced or binned shape correlator on a given $K = k_1 + k_2 + k_3$ slice is defined in Eq. (6.17). 162

6.13 Equilateral configuration of the halo model bispectrum at $z = 0$ (top panel) and $z = 2$ (bottom panel), showing the contributions of the three components of the halo model, contrasted with the measurements from N-body simulations (cyan points). Note the emerging deficit on intermediate scales at $z = 2$. 163

6.14 Best-fit boost coefficient to simulations for the two-halo term compared to $D(z)^{-1.7}$. 164

6.15 The SN-weighted two-halo bispectrum (Eq. 5.178) (left panel) at $z = 2$ compared to the best-fit two-halo squeezed shape ansatz (Eq. 6.23); this allows the 'three-shape' benchmark model to accurately match the simulation data shown in Fig. 6.11. The two-halo model clearly exhibits a large deficit and does not describe squeezed contributions adequately at higher redshift. 167

6.16 Comparison between the measured N-body matter bispectrum and the three-shape model. The left panel shows the binned amplitude $|B|^S(K)$ from the simulations (points and dashed lines) and from the fitted three-shape model (solid lines) at redshifts $z = \{0, 1, 2, 3\}$. The top and bottom right panels show a relative comparison between the simulations and the benchmark model, using the binned shape and amplitude correlators, $\mathscr{S}^S$ and $\mathscr{A}^S$. These results demonstrate that the three-shape model exhibits a high shape correlation on all scales and describes the simulated data well. 168

6.17 Comparison at redshift $z = 2$ of the SN-weighted bispectrum for perturbative models with the simulation data (top left): the perturbative models are respectively tree-level bispectrum (top centre), non-linear tree-level (top right), standard one-loop perturbation theory SPT (bottom left), one-loop effective field theory EFT (bottom centre) and renormalised perturbation theory MPT (bottom right); RLPT is not plotted as it appears very similar to MPT. Note that all perturbation theories have signal concentrated at flattened triangles (front left face), and so are highly correlated with the tree-level bispectrum shape of Eq. (6.14), when using the binned shape correlator (Eq. 6.17). The N-body bispectrum also exhibits a squeezed signal for $k \gtrsim 0.4\,h/\mathrm{Mpc}$. We have chosen $z = 2$ so that the PT models decay at higher k and there is more signal to display, but the general behaviour is similar at lower z. 171

6.18 Comparison of perturbation theory models of the matter bispectrum with N-body simulations, at redshifts 0, 1, 2 (left to right), for the equilateral, squeezed, and flattened configurations (top to bottom). The lower panels show the residuals with respect to the tree-level model. 173

6.19 The amplitude $\mathscr{A}$ (top row) and shape $\mathscr{S}$ (bottom row) correlators at redshifts 0, 1, 2 for the perturbative methods, obtained by comparing with the benchmark model. The shaded areas represent error estimates between the benchmark model and the simulations and are explained in the main body of the text. 176

6.20 Comparison between N-body simulation bispectrum (left panels) with the standard halo bispectrum model Eqs. (5.177-5.179) (centre panels) and the 'three-shape' benchmark model Eq. (6.40) (right panels) shown at two redshifts $z = 0, 2$. The standard halo model is effectively normalised to fit the measured bispectrum at $z = 0$, which is also achieved well by the phenomenological 'three-shape' model (upper panels). However, at higher redshift $z = 2$ the halo model exhibits the wrong growth rates for the flattened three-halo and squeezed two-halo configurations, yielding a substantial deficit (lower panel centre); the measured bispectrum behaviour can be accommodated in the three-shape benchmark model (lower panel right). 178

6.21 Comparison of phenomenological non-linear models of the matter bispectrum with N-body simulations, at redshifts 0, 1, 2 (left to right), for the equilateral, squeezed, and flattened configurations (top to bottom). The lower panels show the substantial residuals with respect to the standard halo model for $z > 0$, demonstrating that the simple three-shape benchmark model provides a good fit to the N-body matter bispectrum for all three limits and redshifts. 180

6.22 The amplitude $\mathscr{A}$ (top row) and shape $\mathscr{S}$ (bottom row) correlators at redshifts 0, 1, 2 for the phenomenological halo models, obtained by comparing with the three-shape benchmark model. The shaded areas represent error estimates between the three-shape benchmark model and the simulations and are explained in Subchapter 6.5.1. 181

LIST OF TABLES

2.1 Classification of topological defects by homotopy group of the manifold and dimensionality. 27

3.1 Shape and amplitude correlators of the UETCs at different simulation resolutions and the UETC at resolution 1280^3 55

3.2 Shape and amplitude correlators for UETCs in the three simulations 57

3.3 Constraints on the fitted cosmological parameters, together with 1σ error bars in a full likelihood analysis (with all relevant nuisance parameters) with and without cosmic strings in the case of *Planck* and WMAP polarisation . 68

3.4 Values of the cosmological parameters when considering only the *Planck* likelihoods with 1σ error bars, obtained by considering a full likelihood analysis (all cases also include the *Planck* nuisance parameters) 70

3.5 Values of the cosmological parameters when considering only the *Planck* and WP likelihoods with 1σ error bars, obtained by considering a full likelihood analysis 71

3.6 Values of the cosmological parameters in the *Planck* + WP + BICEP2 likelihoods case with 1σ error bars, obtained by considering a full likelihood analysis (all cases also include the *Planck* nuisance parameters) obtained when considering tensor modes and cosmic strings 76

3.7 Values of the cosmological parameters in the *Planck* + WP + BICEP2 likelihoods case with 1σ error bars, obtained by considering a full likelihood analysis (all cases also include the *Planck* nuisance parameters) 77

3.8 Values of the cosmological parameters in the *Planck* + WP + BICEP2 likelihoods case with 1σ error bars, obtained by considering a full likelihood analysis 78

4.1 Constraints on the fitted cosmological parameters, together with 1σ error bars in a full likelihood analysis (with all relevant nuisance parameters) with and without domain walls in the case of *Planck* and WMAP polarisation in the two domain walls scenarios considered. 94

5.1 Domain of validity for perturbation theory: wavenumber $k^*_{\rm max}$ where the two perturbative expansions being compared show relative deviations greater than 10% (20%). 123

6.1 Wavenumber $k^*_{\rm max}$ where the total correlator $\mathscr{T}$ (Eq. 6.6) between the perturbative theory and the benchmark model deviates by more than 10% (5%) from unity. In the case of $z = 0$, we only report the 10% results, as the accuracy of the benchmark model is lower. 175

6.2 Wavenumber $k^*_{\rm max}$ where the amplitude deviation for phenomenological halo models is greater than 20% when compared to the three-shape benchmark model matched to simulations. (The small k excess problem of the standard halo model is ignored.) At $z = 0$ all models agree within 20% over the entire range of scales. 182

CHAPTER 1

INTRODUCTION

Although cosmological ideas have always fascinated people, the development of modern cosmology is associated with the general theory of relativity at the beginning of the twentieth century which made possible the creation of the first mathematical model describing the whole observed Universe [10]. The starting point was the *Cosmological principle* stating that the Universe is homogeneous and isotropic on large scales. The formulation of the Big-Bang model began with Georges Lemaître and his "primordial atom" in the 1920s [11] and it was developed more quantitatively in the 1940s with the work of George Gamow and his collaborators [12].

New ideas and building blocks have appeared since then, such as dark energy, dark matter and the hot early Universe. Since the discovery of the Cosmic Microwave Background (CMB) radiation by Penzias and Wilson in 1965 [11], cosmology began to progress more rapidly [13]. This started with a much better theoretical understanding of the phenomena in the very early Universe, which have been confirmed by observations. The key elements for this groundbreaking progress are associated with particle physics, specifically the development of the gauge theories of electromagnetic, weak and strong interactions. These have allowed researchers to investigate the properties of matter at densities 80 orders of magnitude greater than the nuclear density, at times as early as 10^{-10} seconds after the Big Bang. At such early times the three fundamental interactions are expected to be unified, which shows how important cosmology can be to particle physics as well.

The 1980s saw the development of another extraordinary model, the inflationary theory [14]. This theory assumes that the Universe underwent an accelerated (exponential) expansion phase, called inflation, just after its formation and that all elementary particles were formed at the end of this rapid expansion. This inflationary phase is also responsible for the creation of the large scale structure in the Universe (LSS), such as galaxies. Small quantum fluctuations

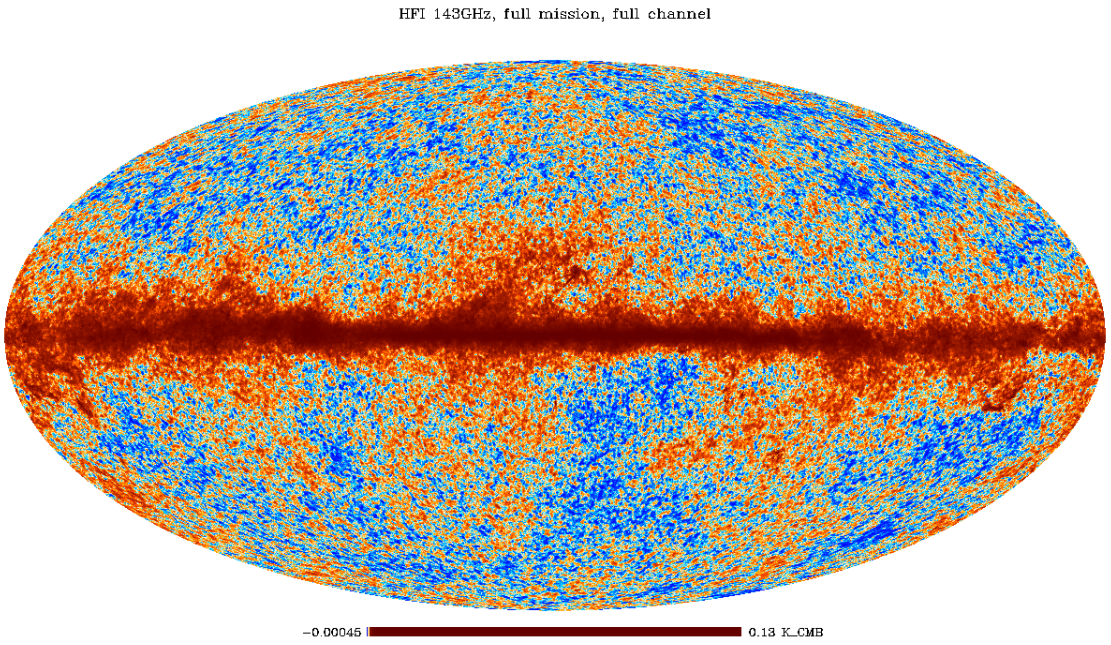

Fig. 1.1 Temperature anisotropies in the sky as viewed by the *Planck* satellite with galaxy contributions obscuring the equatorial region (at 143 GHz). The figure is reproduced from Ref. [6].

created during inflation can get amplified, eventually generating the large-scale structures that are observed today. Moreover, this model also solves many cosmological puzzles, such as the flatness problem, the homogeneity problem and the isotropy problem.

A powerful method for testing this theory is the study of the anisotropy in the CMB. Temperature anisotropies are produced by the quantum fluctuations generated during the inflationary phase, The first confirmation of the model appeared from the results of the *COBE* satellite (launched in November 1989) [15]. More recent probes have greatly increased the precision of these observation: *WMAP* (launched 2001) [16] and *Planck* (launched 2009) [17, 18].

The scientific results of the *Planck* collaboration offer a robust support for the standard, six parameter ΛCDM model of cosmology. These parameters are: the baryon density $\Omega_b h^2$, the cold dark matter density $\Omega_c h^2$, the optical depth to reionisation τ, the acoustic scale θ, the amplitude A_s, and the spectral index of density fluctuations n_s. Improved measurements for the parameters defining this model were recently released [6, 7]. In Fig. 1.1, the 143 GHz CMB map measured by the *Planck* satellite is presented.

In the meantime, the results mentioned in the previous paragraphs have been enhanced by more classical methods. The age of the Universe has been estimated using the spectra of thorium and uranium in the atmospheres of old stars and the Hubble Space Telescope (launched in 1990) has given an accurate estimate of the Hubble constant [19]. Supernovae measurements established that the Universe is accelerating [20, 21], a fact confirmed later by precision CMB results, *i.e.* that the energy density of the Universe is dominated by a cosmological constant or 'dark energy'.

These empirical results have given rise to the so called *Standard Cosmological Model* [22]. The precision of the measurements of its cosmological parameters has been greatly increased in the last couple of years, notably using *Planck* satellite results.

1.1 The standard cosmological model

Consider a space-time metric $g_{\mu\nu}$ with line element expressed as $ds^2 = g_{\mu\nu}dx^\mu dx^\nu$. Throughout this thesis, the following metric convention is used: $(-,+,+,+)$ and we also consider units such that $c = 1$.

Einstein showed that using the Postulates of General relativity the field equations satisfy the following equation:

$$G_{\mu\nu} = 8\pi G T_{\mu\nu} + \Lambda g_{\mu\nu}\,, \tag{1.1}$$

where $G_{\mu\nu}$ is the Einstein tensor describing the geometric properties of spacetime, $T_{\mu\nu}$ is the energy-momentum tensor which describes the properties of matter and Λ is a constant, called the cosmological constant. To express the Einstein tensor in terms of the metric, one must define the Christoffel symbols:

$$\Gamma^\mu_{\nu\rho} = \frac{1}{2}g^{\mu\sigma}\left(\partial_\rho g_{\sigma\nu} + \partial_\nu g_{\sigma\rho} - \partial_\sigma g_{\nu\rho}\right)\,, \tag{1.2}$$

the Ricci tensor $R_{\mu\nu}$ and Ricci scalar R:

$$R_{\mu\nu} = \partial_\rho \Gamma^\rho_{\mu\nu} - \partial_\nu \Gamma^\rho_{\mu\rho} + \Gamma^\sigma_{\sigma\rho}\Gamma^\rho_{\mu\nu} - \Gamma^\rho_{\mu\sigma}\Gamma^\sigma_{\nu\rho}\,, \tag{1.3}$$

$$R = g^{\mu\nu}R_{\mu\nu}\,, \tag{1.4}$$

with partial derivative $\partial_\rho \equiv \frac{\partial}{\partial x^\rho}$. The Einstein tensor has the following expression:

$$G_{\mu\nu} \equiv R_{\mu\nu} - \frac{1}{2}R g_{\mu\nu}\,. \tag{1.5}$$

When considering small particle velocities v satisfying $v \ll c$ and weak fields, equation (1.1) reduces to

$$\nabla^2\phi = 4\pi G\rho \tag{1.6}$$

in the absence of the cosmological constant, where $g_{00} = 1 - 2\phi$, thus recovering the usual Poisson equation of Newtonian mechanics.

The most general spacetime metric of a homogeneous and isotropic expanding universe that is path connected can be expressed as [23]

$$ds^2 = -dt^2 + a(t)^2\left[\frac{dr^2}{1-kr^2} + r^2\left(d\theta^2 + \sin^2\theta d\phi^2\right)\right], \tag{1.7}$$

where k is a constant that can be fixed to the values -1, 0 and 1 by suitable rescaling of the variables (if the universe is open, flat, or closed respectively) and $a(t)$ is the scale factor of the Universe. This is called the Friedmann-Lemaître-Robertson-Walker (FLRW) metric [24, 25].

We are interested however in the matter content of the Universe, rather than the simple vacuum solution. This can be treated as a perfect fluid, which has an energy-momentum tensor of the form

$$T^{\mu}{}_{\nu} = (\rho + p)u^{\mu}u_{\nu} + p\delta^{\mu}_{\nu}, \tag{1.8}$$

where ρ and p represent the density and pressure of the fluid, and u^{μ} is its 4-velocity vector. In the case of an universe consisting of multiple particle species, these quantities are the sum of the counterparts from each species. By using isotropy and homogeneity considerations, it can be shown that the matter energy-momentum tensor has a simple diagonal form,

$$T^{\mu}{}_{\nu} = \begin{pmatrix} -\rho & 0 & 0 & 0 \\ 0 & p & 0 & 0 \\ 0 & 0 & p & 0 \\ 0 & 0 & 0 & p \end{pmatrix}. \tag{1.9}$$

The Christoffel symbols (1.2) can be used to define the covariant derivative:

$$\nabla_{\mu}T^{\nu\rho} = \partial_{\mu}T^{\nu\rho} + \Gamma^{\nu}_{\mu\sigma}T^{\sigma\rho} + \Gamma^{\rho}_{\mu\sigma}T^{\nu\sigma}. \tag{1.10}$$

As the Einstein tensor is covariantly conserved (Bianchi identity),

$$\nabla_{\nu}G^{\mu\nu} = 0 \tag{1.11}$$

and from the Einstein Equation (1.1) we deduce that the energy-momentum tensor is also conserved:

$$\nabla_\nu T^{\mu\nu} = 0\,. \tag{1.12}$$

In order to solve the Einstein Equation we first need to calculate the Einstein tensor in this metric (1.7). By calculating the Christoffel symbols (1.2), we determine the Ricci tensor (1.3) and scalar (1.4) in this coordinate system. Its non-vanishing components are:

$$R_{00} = -3\frac{\ddot{a}}{a}\,, \tag{1.13}$$

$$R_{11} = \frac{a\ddot{a} + 2\dot{a}^2 + 2k}{1 - kr^2}\,, \tag{1.14}$$

$$R_{22} = r^2(a\ddot{a} + 2\dot{a}^2 + 2k)\,, \tag{1.15}$$

$$R_{33} = r^2(a\ddot{a} + 2\dot{a}^2 + 2k)\sin^2\theta\,, \tag{1.16}$$

$$R = \frac{6}{a^2}(a\ddot{a} + \dot{a}^2 + k)\,. \tag{1.17}$$

By considering the $\mu = 0$ component of Eq. (1.12) and substituting the expression for the energy momentum tensor (1.9), the conservation equation for a cosmological fluid is obtained,

$$\dot{\rho} = -3\frac{\dot{a}}{a}(\rho + p)\,. \tag{1.18}$$

By considering the 00 and ij components of Eq. (1.1), we obtain the Friedmann equations [14]:

$$\left(\frac{\dot{a}}{a}\right)^2 + \frac{k}{a^2} = \frac{8\pi G}{3}\rho + \frac{\Lambda}{8\pi G}\,, \tag{1.19}$$

$$\frac{\ddot{a}}{a} = -\frac{4\pi G}{3}(\rho + 3p) + \frac{\Lambda}{8\pi G}\,. \tag{1.20}$$

Eq. (1.20) is also called the Raychaudhuri equation, and it can also be trivially derived from Eqs. (1.18) and (1.19).

The Hubble parameter H and the conformal time τ are defined as

$$H = \frac{\dot{a}}{a}\,, \tag{1.21}$$

$$\frac{d\tau}{dt} = \frac{1}{a}\,. \tag{1.22}$$

Then the conformal Hubble parameter is given by

$$\mathscr{H} = \frac{a'}{a} = aH\,, \tag{1.23}$$

where the dot denotes differentiation with respect to proper time, and the prime differentiation with respect to conformal time. Static solutions of Eqs. (1.19)-(1.20) correspond to $\dot{a} = \ddot{a} = 0$, and various solutions have been proposed: the Einstein Universe ($K = 1$, $p = 0$), the de Sitter Universe ($K = \rho = p = 0$) [26] and others proposed by Alexander Friedmann [24], and Georges Lemaître [25].

The observed expansion of the Universe [27–29] made cosmologists to abandon the static solutions. By introducing an equation of state

$$p = w\rho\,, \tag{1.24}$$

where w is a constant, in the case of $K = \Lambda = 0$, the solutions to the Friedmann equations take a simple form [10]

$$\rho = \frac{\rho_0}{a^{3w+1}}\,, \tag{1.25}$$

$$a = \left(\frac{t}{t_0}\right)^{2/(3w+1)}\,. \tag{1.26}$$

The radiation-dominated era corresponds to $w = 1/3$ and the matter-dominated one to $w = 0$, yielding the following solutions for the scale-factor:

$$a(t) \propto t^{1/2} \propto \tau(\text{ radiation era})\,, \tag{1.27}$$

$$a(t) \propto t^{2/3} \propto \tau^2(\text{ matter era})\,. \tag{1.28}$$

1.2 The formation of structures

In Subchapter 1.1, we have derived the Friedmann equations in a homogeneous universe. This is however not the case in reality and moreover we are interested in analysing the formation and evolution of large-scale structures within the expanding universe. In this Subchapter, we discuss how small fluctuations around the homogeneous background described in Subchapter 1.1 can produce large-scale structures through gravitational instability. Here, we use a full general-relativistic approach, although some of the results can be derived in the more intuitive Newtonian approximation. In the Newtonian approximation, results are only valid on scales smaller than the Hubble radius, and moreover they are not valid for relativistic fluids, such

as photons and neutrinos. We start with the flat FLRW metric ($k = 0$) expressed in terms of conformal coordinates:

$$ds^2 = a^2(\tau)\left(-d\tau^2 + \delta_{ij}dx^i dx^j\right) . \tag{1.29}$$

For this flat metric, the Friedmann Equations (1.19) and (1.20) can be re-written in terms of conformal time coordinates

$$\mathscr{H}^2 = \frac{1}{3}\left(\rho + 8\pi G\Lambda\right) , \tag{1.30}$$

$$\dot{\mathscr{H}} = \frac{1}{3}a^2\left[\Lambda - 8\pi G(\rho + 3p)\right] . \tag{1.31}$$

We consider small perturbations around this metric (1.29), which in the most general case produce the line element

$$ds^2 = a^2\left[-(1+2A)d\tau^2 - 2B_i dx^i d\tau + (\delta_{ij} + h_{ij})dx^i dx^j\right] , \tag{1.32}$$

where A, B_i and h_{ij} are functions of time and position and we denote with $g_{\mu\nu}$ the resulting metric tensor. Moreover, the linear perturbation degrees of freedom can be decomposed further, into scalar, vector and tensor parts (SVT decomposition):

$$B_i = \partial_i B + B_i^V , \tag{1.33}$$

$$h_{ij} = 2C\delta_{ij} + \left(\partial_i\partial_j - \frac{1}{3}\delta_{ij}\nabla^2\right)E + \frac{1}{2}(\partial_i E_j^V + \partial_j E_i^V) + E_{ij}^T , \tag{1.34}$$

where B, C and E are scalar components, B_i^V and E_i^V are vector components and E_{ij}^T are tensor components and $\partial^i B_i^V = \partial^i E_i^V = \partial^i E_{ij}^T = 0$ and $E_i^{iT} = 0$. We note that there are 10 degrees of freedom, out of which there are 4 scalars (A, B, C and E), 4 vectors and 2 tensors (in the case of vectors and tensors there were 6 and 6 degrees of freedom respectively, but these were reduced by using symmetry, divergenceless and traceless properties).

These perturbations introduce unphysical degrees of freedom which must be dealt with. We start by studying how the perturbation variables transform under a small change of coordinate system. These transformations are called *gauge transformations*.

1.2.1 Gauge transformations

We consider two coordinate systems for the same spacetime, with metrics $g_{\mu\nu}$ and $\tilde{g}_{\mu\nu}$, and with coordinates X and $\tilde{X}$ respectively, such that

$$\tilde{X}^\mu = X^\mu + \xi^\mu \,, \tag{1.35}$$

where $\xi^0 \equiv T$ and $\xi^i \equiv L^i = \partial^i L + L^{iV}$ are functions of space and time and $\partial_i L^{iV} = 0$. Then the line element is the same in both frames and therefore the spacetime can be expressed as

$$ds^2 = g_{\mu\nu}(X) dX^\mu dX^\nu = \tilde{g}_{\mu\nu}(\tilde{X}) d\tilde{X}^\mu d\tilde{X}^\nu \,, \tag{1.36}$$

and the transformation law between the frames is

$$g_{\mu\nu}(X) = \frac{\partial \tilde{X}^\alpha}{\partial X^\mu} \frac{\partial \tilde{X}^\beta}{\partial X^\nu} \tilde{g}_{\alpha\beta}(\tilde{X}) \,. \tag{1.37}$$

By considering the perturbed metric of Eq. (1.32) and its tilded counterpart and plugging them both in Eq. (1.37), and then considering the 00, $0i$ and ij components of the equations at first order, we obtain the gauge transformations of the perturbations:

$$\tilde{A} = A - T' - \mathscr{H} T \,, \tag{1.38}$$

$$\tilde{B}_i = B_i + \partial_i T - L_i' \,, \tag{1.39}$$

$$\tilde{h}_{ij} = h_{ij} - \partial_i L_j - \partial_j L_i - 2\mathscr{H} T \delta_{ij} \,. \tag{1.40}$$

The SVT-decomposed quantities transform as:

$$\tilde{B} = B + T - L' \,, \tag{1.41}$$

$$\tilde{B}_i^V = B_i^V - L_i^{V\prime} \,, \tag{1.42}$$

$$\tilde{C} = C - \mathscr{H} T - \frac{1}{3} \nabla^2 L \,, \tag{1.43}$$

$$\tilde{E} = E - L \,, \tag{1.44}$$

$$\tilde{E}_i^V = E_i^V - L_i^V \,, \tag{1.45}$$

$$\tilde{E}_{ij}^T = E_{ij}^T \,. \tag{1.46}$$

One procedure for solving the redundancy in the number of degrees is called *gauge fixing*. Two popular gauge choices that are used for studying linear perturbations in cosmology are:

The synchronous gauge

This gauge is characterised by $A = B_i = 0$, *i.e.* the only perturbations are in the spatial part of the metric. This is achieved in the tilded basis by solving the differential equation (1.38) for T and then by solving Eqs. (1.41) and (1.42) for L and L_i^V respectively. This gauge is the most widespread and has been used in numerical codes such as CMBFAST [30] and CAMB [31, 32]. With the synchronous gauge, we must be careful because not all gauge modes are fixed.

The conformal Newtonian gauge

The conformal Newtonian gauge is characterised by setting the scalar B and E terms to 0. This can be achieved by considering in the gauge transformation equations (1.38)-(1.46), $L = E$, $T = L' - B$. Then in the tilded basis, $\tilde{E} = \tilde{B} = 0$. The canonical form of the metric for scalar perturbations in this gauge is obtained by taking $\psi = A$ and $\phi = -C$:

$$ds^2 = a^2(\tau)\left[-(1+2\psi)d\tau^2 + (1-2\phi)\delta_{ij}dx^i dx^j\right]. \tag{1.47}$$

After the gauge has been set, the perturbations in both the matter and the metric have to be included. Another possibility is to choose gauge-invariant perturbation variables such that they remain unchanged by gauge transformations. This idea was first proposed by Bardeen in Ref. [33]. In subsequent parts of this thesis, we choose to fix the gauge to the synchronous gauge and study the cosmological perturbations there.

1.2.2 Synchronous gauge perturbations

By choosing the synchronous gauge, the line element (1.32) is given by

$$ds^2 = a^2\left[-d\tau^2 + (\delta_{ij} + h_{ij})dx^i dx^j\right]. \tag{1.48}$$

As the metric is already perturbed, we have to consider perturbations to the energy-momentum tensor (1.9). Starting from the energy-momentum tensor of a fluid (1.8) and perturbing the density ρ, pressure p and velocity u^μ, we find

$$\delta T^\mu{}_\nu = (\delta\rho + \delta p)u^\mu u_\nu + (\rho + p)(u^\mu \delta u_\nu + \delta u^\mu u_\nu) + \delta p \delta^\mu_\nu + \Sigma^\mu{}_\nu, \tag{1.49}$$

where $\Sigma^\mu{}_\nu$ is the anisotropic stress, which can be taken to have only spatial components and be traceless $\Sigma^0{}_0 = \Sigma^i{}_0 = \Sigma^0{}_i = \Sigma^i{}_i = 0$. In the unperturbed metric, the fluid velocity of a

comoving observer is

$$u^\mu = \left(\frac{1}{a}, 0, 0, 0\right). \tag{1.50}$$

In the perturbed frame, the 4-velocity vector $u^\mu + \delta u^\mu$ must still be a unit 4-vector, *i.e.* it must satisfy $(u^\mu + \delta u^\mu)(u_\mu + \delta u_\mu) = 1$ and hence at linear order δu^μ has to have the following form:

$$\delta u^\mu = \left(0, \frac{1}{a}\mathrm{v}_i\right), \tag{1.51}$$

where $\mathrm{v}^i \equiv \frac{dx^i}{d\tau}$ represents the coordinate velocity. Then Eqs. (1.9) and (1.49) together with Eqs. (1.50) and (1.51) yield the energy-momentum tensor in the perturbed frame:

$$T^0{}_0 = -\bar{\rho}(1+\delta\rho) \equiv -\bar{\rho}(1+\delta), \tag{1.52}$$

$$T^i{}_0 = -(\rho + p)v^i, \tag{1.53}$$

$$T^i{}_j = (\bar{p} + \delta p)\delta^i_j + \Sigma^i_j. \tag{1.54}$$

Here each of the quantities on the right side of the equation represent the matter perturbations of all the matter in the Universe. Before trying to solve the Einstein Equation (1.1), it is useful to first convert the equations into Fourier space and then decompose all the tensors involved into scalar, vector and tensor parts, similarly to the real-space decomposition (1.34). The advantage of such a procedure is that in Fourier space the equations describing each of the three types of perturbations decouple and can be treated separately. A general tensor $T_{\mu\nu}$ can be split as

$$T_{ij} = \frac{1}{3}\delta_{ij}T + \left(\hat{k}_i\hat{k}_j - \frac{1}{3}\delta_{ij}\right)T^S + \left(\hat{k}_i T^V_j + \hat{k}_j T^V_i\right) + T^T_{ij}, \tag{1.55}$$

with T and T^S being the scalar parts of the perturbation - the trace and the anisotropic scalar respectively, while T^V_i is the vector part and T^T_i is the tensor part respectively. The vector components are transverse, *i.e.* $k^i T^V_i = 0$, and the tensor components are traceless and transverse $k^i T^T_{ij} = k^j T^T_{ij} = 0$ and $T^{Ti}_i = 0$.

By considering only up to first order perturbations to the Einstein Equation (1.1) we obtain at 0^{th} order the Friedmann Equations (1.30)-(1.31), while at first order we derive the evolution equations for the metric perturbations,

$$h'' + \frac{a'}{a}h' = -8\pi G a^2(\delta\rho + 3\delta p), \tag{1.56}$$

$$h^{S\prime\prime} + 2\frac{a'}{a}h^{S\prime} + \frac{1}{3}k^2(h - h^S) = 16\pi G a^2 p\Sigma^S, \tag{1.57}$$

$$h_i^{V\prime\prime} + 2\frac{a'}{a}h_i^{V\prime} = 16\pi G a^2 p\Sigma_i^V \,, \tag{1.58}$$

$$h_\varepsilon^{T\prime\prime} + 2\frac{a'}{a}h_\varepsilon^{T\prime} + k^2 h_\varepsilon^T = 16\pi G a^2 p\Sigma_\varepsilon^T \,, \tag{1.59}$$

where the index i in the case of the vectors and ε for the tensor modes correspond to the two possible polarisations. Because the synchronous gauge is not completely specified, there are also constraint equations, given by

$$k^2(h - h^S) + 3\frac{a'}{a}h' = 24\pi G a^2 \delta\rho \,, \tag{1.60}$$

$$k^2(h - h^{S\prime}) = -24\pi G a^2(\rho + p)\theta \,, \tag{1.61}$$

$$kh_i^{V\prime} = 16\pi G(P_i^V - a^2(\rho + p)\mathrm{v}_i^V) \,, \tag{1.62}$$

where θ is the velocity divergence. By considering the energy momentum conservation $\nabla^\nu T_{\mu\nu} = 0$,

$$\delta' = -(1+w)\left(\theta + \frac{h'}{2}\right) - 3\frac{a'}{a}\left(\frac{\delta p}{\delta\rho} - w\right)\delta \,, \tag{1.63}$$

$$\theta' = -\frac{a'}{a}(1-3w)\theta - \frac{w'}{1+w}\theta + \frac{\delta p/\delta\rho}{1+w}k^2\delta + \frac{2}{3}\frac{w}{1+w}k^2\Sigma^S \,, \tag{1.64}$$

$$\mathrm{v}_i^{V\prime} = -\frac{a'}{a}(1-3w)\mathrm{v}_i^V - \frac{w'}{1+w}\mathrm{v}_i^V - \frac{w}{1+w}k\Sigma_i^V \,. \tag{1.65}$$

The equations above are valid for uncoupled fluids and therefore they have to evaluated for each of the components of interest. In order to solve numerically for the perturbation equations described here, they need to be coupled to the moments of the brightness function, which are described in Subchapter 1.3.

We will discuss in what follows the evolution of the cold dark matter (CDM) fluctuations in the radiation, matter and Λ epochs and how structures are formed. We consider a universe where the cosmological constant has been included in the density and pressure terms and does not appear explicitly in the Friedmann equations (1.30)-(1.31).

1.2.3 Growth of structure

For simplicity, we consider a universe consisting of only radiation and CDM. We use the subscripts r and c to refer to radiation and CDM quantities respectively. The CDM particles are considered to be pressureless dust ($w_c = c_{s(c)}^2 = 0$) with no peculiar velocity ($\theta_c = \Sigma_c^S = 0$).

Then, Eq. (1.63) becomes simply

$$\delta_c' = -\frac{h'}{2}\,. \tag{1.66}$$

Radiation is characterised by $w_r = c^2_{s(r)} = 1/3$ and, by neglecting the shear stress ($\Sigma^S_r = 0$) we can combine Eqs. (1.63)-(1.64) into

$$\delta_r'' + \frac{k^2}{3}\delta_r + \frac{2}{3}h'' = 0\,. \tag{1.67}$$

Eqs. (1.66)-(1.67) then yield

$$\delta_r'' + \frac{k^2}{3}\delta_r - \frac{4}{3}\delta_c'' = 0\,. \tag{1.68}$$

By using the Friedmann Equation (1.30), Eq. (1.56) for the scalar perturbation can be expressed in terms of the density fractions Ω_i of the various components i of the universe as

$$h'' + \frac{a'}{a}h' = -3\mathscr{H}^2\sum_i \Omega_i(1+3w_i)(1+\delta_i)\,, \tag{1.69}$$

where

$$\Omega_i = \frac{8\pi G\rho_i}{3H^2}\,. \tag{1.70}$$

Then the differential equation for h in this two-component universe becomes

$$h'' + \frac{a'}{a}h' = -3\left(\frac{a'}{a}\right)^2(2\Omega_r\delta_r + \Omega_c\delta_c)\,. \tag{1.71}$$

CDM perturbations in the radiation era

In the radiation era the density of radiation dominates over the CDM density and hence $\Omega_r \approx 1$ and $a \propto \tau$ (Eq. (1.27)). Moreover, on super-horizon scales ($k\tau \ll 2\pi$) the perturbations are chosen to be adiabatic (as predicted by single-field inflationary models), and therefore the radiation and CDM perturbations satisfy the relation

$$\delta_r = \frac{4}{3}\delta_c\,. \tag{1.72}$$

Hence, from Eq. (1.71) together with Eq. (1.66), we obtain the following equation for the CDM,

$$\delta_c'' + \frac{1}{\tau}\delta_c' - \frac{4}{\tau^2}\delta_c = 0\,, \tag{1.73}$$

which has power-like solutions of the form

$$\delta_c(\mathbf{k},\tau) = A(\mathbf{k})\left(\frac{\tau}{\tau_i}\right)^2 + B(\mathbf{k})\left(\frac{\tau}{\tau_i}\right)^{-2}, \tag{1.74}$$

where A and B are arbitrary functions of $\mathbf{k}$ and τ_i is a constant conformal time. The first term represents CDM perturbations modes that are growing in the radiation era on very large scales, $\delta_c \propto a^2$, while the second term is quickly decaying.

On sub-horizon scales, where $k\tau \gg 2\pi$, pressure effects make the third term of Eq. (1.68) negligible with respect to the second one, and therefore we have to solve a harmonic oscillator equation for δ_r. This has oscillatory solutions of the form

$$\delta_r(\mathbf{k},\tau) = C(\mathbf{k})\cos(k\tau/\sqrt{3}) + D(\mathbf{k})\sin(k\tau/\sqrt{3})\,. \tag{1.75}$$

These oscillations are rapid with respect to the gravitational collapse time of CDM and they average to 0. The CDM perturbations can be treated separately. From Eq. (1.71), combined with Eq. (1.66), we find the equation for the evolution of the CDM:

$$\delta_c'' + \frac{1}{\tau}\delta_c = 0\,, \tag{1.76}$$

with solutions of the form

$$\delta_c(\mathbf{k},\tau) = E(\mathbf{k})\log\left(\frac{\tau}{\tau_i}\right) + F(\mathbf{k})\,. \tag{1.77}$$

This growth is much slower than the expansion of the universe and therefore, in the radiation era there is only very mild growth on sub-horizon scales.

CDM perturbations in the matter era

During this epoch, the CDM component of the universe dominates over radiation ($\Omega_c \approx 1$), and by using Eqs. (1.66) and (1.71), we obtain the time evolution equation of CDM as

$$\delta_c'' + \frac{a'}{a}\delta_c' - \frac{3}{2}\left(\frac{a'}{a}\right)^2\delta_c = 0\,. \tag{1.78}$$

Considering the growth rate $a \propto \tau^2$ (Eq. 1.28)) in the matter era, the above equation has solutions of the form

$$\delta_c(\mathbf{k},\tau) = A(\mathbf{k})\left(\frac{\tau}{\tau_i}\right)^2 + B(\mathbf{k})\left(\frac{\tau}{\tau_i}\right)^{-3}. \tag{1.79}$$

The first term represents the growing mode solution $\delta_c \propto a$, while the second term is a decaying mode that can be safely neglected. In this case, the solutions are valid on all scales.

CDM perturbations in the cosmological constant era

During the cosmological constant era, $a \propto \exp(H_0 t)$ and the CDM is diluted away. Then, the last term of Eq. (1.78) is negligible compared to the other two and we are left with the perturbation equation

$$\delta_c'' + \frac{a'}{a}\delta_c' = 0\,, \tag{1.80}$$

which has solutions of the form:

$$\delta_c(\mathbf{k},\tau) = A(\mathbf{k}) + B(\mathbf{k})\exp(-2H_0 t)\,. \tag{1.81}$$

This result shows that linear perturbations do not grow during this fast expansion era. Hence, in the linear theory, matter perturbations grow in the radiation era, on super-horizon scales, and in the matter era on all scales.

1.3 The Boltzmann Equation

The primordial fluctuations were created in the early Universe, but we can only observe their implications today. Therefore, we consider the trajectories of photons from the early Universe until today. We denote the photon trajectory by the unit vector $\hat{\mathbf{n}}$. We consider the seven-dimensional phase space defined by the position 4-vector x^μ and momentum $p^\mu = \frac{dx^\mu}{d\lambda}$, such that $p_\mu p^\mu = 0$, called the *phase space*. The particle position vector satisfies the geodesic equation,

$$\frac{d^2x^\mu}{d\lambda^2} + \Gamma^\mu_{\nu\rho}\frac{dx^\nu}{d\lambda}\frac{dx^\rho}{d\lambda} = 0\,, \tag{1.82}$$

and the momentum p^μ satisfies

$$\frac{dp^\mu}{d\lambda} + \Gamma^\mu_{\nu\rho}p^\nu p^\rho = 0. \tag{1.83}$$

By considering a comoving observer with velocity $u^\mu = (1/a, \mathbf{0})$ (Eq. (1.50)), orthogonal to the hypersurface given by (x^μ, p^μ), the number of worldlines intersecting the volume dV is given by

$$dN = f(x,p)(-u_\mu p^\mu) dV dV_p \,, \tag{1.84}$$

where the function f is the phase space distribution of the particles and dV and dV_p represent the volume elements in real and momentum space respectively. The function f is invariant under canonical transformations, and the zeroth order phase distribution is given by the Fermi-Dirac and Bose-Einstein distributions. These distributions are given by the following expressions:

$$f_0(\varepsilon) = \frac{g_s}{h^3} \frac{1}{e^{\varepsilon/k_B T_0} \pm 1} \,, \tag{1.85}$$

where the plus sign corresponds to the Fermi-Dirac distribution and the minus sign corresponds to the Bose-Einstein distribution, ε is the energy of the state, g_s is the spin degeneracy, h and k_B are the Planck and Boltzmann constants, $T_0 = aT$ is the temperature of the particles today. The Boltzmann equation describes the distribution of particles in phase space,

$$\frac{df}{d\lambda} = \frac{\partial f}{\partial \lambda} + \frac{dx^i}{d\lambda}\frac{\partial f}{\partial x^i} + \frac{dq}{d\lambda}\frac{\partial f}{\partial q} + \frac{d\hat{n}_i}{d\lambda}\frac{\partial f}{\partial \hat{n}_i} = C[f] \tag{1.86}$$

where $C[f]$ is a term quantifying the interactions. In the absence of collisions, *i.e.* when $C[f] = 0$, the phase space distribution of particles is conserved.

For photons with direction of propagation $\hat{\mathbf{n}}$, the 4-momentum can be expressed as

$$p^\mu = (p^0, |\mathbf{p}|\hat{n}^i) \,. \tag{1.87}$$

Using Eqs. (1.50) and (1.87), the energy of such a photon is given by:

$$E = -u_\mu p^\mu = a p^0 \equiv p \,. \tag{1.88}$$

The photon spectrum is given by the Bose-Einstein distribution (1.85), which is isotropic. It is helpful to define a new variable,

$$q \equiv ap = a^2 p^0 \,, \tag{1.89}$$

such that the isotropic Planck spectrum can be simply expressed as $f_0(q)$.

From the geodesic equation (1.83) it can be shown that

$$\frac{dq}{d\tau} = -\frac{1}{2} q h'_{ij} \hat{n}_i \hat{n}_j \,, \tag{1.90}$$

$$\frac{d\hat{n}_i}{d\tau} = \mathscr{O}(h) \,. \tag{1.91}$$

Using the Planck spectrum described above, a general (non-isotropic) distribution can be split into the isotropic part f_0 and a remainder part f_1 which has temporal and directional dependencies:

$$f(x,p,\tau) \equiv f(x,q,\hat{\mathbf{n}},\tau) = f_0(q) + f_1(x,q,\hat{\mathbf{n}},\tau) \,. \tag{1.92}$$

By substituting Eqs. (1.92), (1.90) and (1.91) into the collisionless Boltzmann equation (1.86), and neglecting second-order terms, we obtain a partial differential equation for f_1:

$$\frac{\partial f_1}{\partial \tau} + \hat{n}^i \frac{\partial f_1}{\partial x^i} = \frac{1}{2} q \frac{df_0}{dq} h'_{ij} \hat{n}_i \hat{n}_j \,, \tag{1.93}$$

which in Fourier-space satisfies the equation

$$\frac{\partial f_1}{\partial \tau} + ik\mu f_1 = \frac{1}{2} q \frac{df_0}{dq} h'_{ij} \hat{n}_i \hat{n}_j \,, \tag{1.94}$$

where $\mu = \hat{k} \cdot \hat{n}$.

We consider a local inertial frame for the particle. In this frame, the metric is locally flat, and the momentum of the particle is given by

$$\tilde{p}^\mu = (\tilde{p}^0, \tilde{\mathbf{p}}) = \left(a p^0, a \left(\delta_{ij} + \frac{1}{2} h_{ij} p^j \right) \right) . \tag{1.95}$$

The spatial and temporal magnitudes are the same, *i.e.*, $\tilde{p}^0 = |\tilde{\mathbf{p}}| = p$ (from Eq. (1.88)). As the volume element dV_p is frame-invariant, we can express it in terms of this new variable in the local inertial frame

$$dV_p = \frac{1}{a^2} q dq d\Omega \,, \tag{1.96}$$

where $d\Omega$ represents the angular variables of integration.

The energy-momentum tensor of the photons can be expressed in terms of the distribution function in phase space,

$$T^{\mu\nu} = \int p^\mu p^\nu f(x,p,\tau) dV_p \,. \tag{1.97}$$

Then using Eqs. (1.50) and (1.96), the energy density becomes

$$\rho = u_0 u_0 T^{00} = \frac{1}{a^4}\int q^3 (f_0 + f_1) dq d\Omega \equiv \bar{\rho}_\gamma (1+\delta_\gamma)\,, \tag{1.98}$$

where $\bar{\rho}_\gamma$ and δ_γ represent the background energy density of photons and a perturbation to it respectively; they have the following expressions:

$$\bar{\rho}_\gamma = \frac{4\pi}{a^4}\int q^3 f_0 dq\,, \tag{1.99}$$

$$\delta_\gamma = \frac{1}{a^4\bar{\rho}_\gamma}\int q^3 f_1 dq d\Omega\,. \tag{1.100}$$

Also,

$$T^{0i} = \frac{1}{a^6}\int q^3 \hat{n}^i f_1 dq d\Omega = \frac{1}{a^2}\frac{4}{3}\bar{\rho}_\gamma i k_i \theta_\gamma\,. \tag{1.101}$$

We note that in Eq. (1.94) there is no term $\partial f_1/\partial q$ and so we consider an ansatz for the solution of the form

$$\begin{aligned} f(\mathbf{x},\mathbf{p},\tau) &= f_0\left(\frac{p}{T(\mathbf{x},\hat{\mathbf{n}},\tau)}\right) = f_0\left(\frac{\bar{T}q}{T}\right) = f_0\left(\frac{q}{1+\Delta T/T}\right) \\ &\approx f_0(q) - q\frac{df_0}{dq}\frac{\Delta T}{T}(\mathbf{x},\hat{\mathbf{n}},\tau) \\ &= f_0 + f_1\,. \end{aligned} \tag{1.102}$$

Integrating this equation for f_1 by parts with respect to q and using Eq. (1.99) we obtain

$$\int f_1 q^3 dq = 4\frac{\Delta T}{T}\int f_0 q^3 dq = 4\frac{\Delta T}{T}\frac{a^4\bar{\rho}_\gamma}{4\pi}\,. \tag{1.103}$$

By defining the brightness as $\Delta \equiv \frac{4\Delta T}{T}$ and integrating in a similar fashion Eq. (1.94), together with (1.103) and (1.99) we obtain a differential equation for Δ:

$$\Delta' + ik\mu\Delta = -2h'_{ij}\hat{n}^i\hat{n}^j\,, \tag{1.104}$$

which is the *brightness equation* for photons in the absence of collisions. In order to obtain the full evolution equation for the brightness Δ we must consider photon collisions. Before decoupling, the photons interact with electrons and baryons via Compton scattering. These interactions modify Eq. (1.104) to

$$\Delta' + ik\mu\Delta = -2h'_{ij}\hat{n}^i\hat{n}^j + a\sigma_T n_e(\delta_\gamma + 4\hat{\mathbf{n}}\cdot\mathbf{v}_e - \Delta)\,, \tag{1.105}$$

where σ_T is the Thomson scattering cross-section (and is constant), n_e is the density of free electrons and $\mathbf{v}_e$ is the velocity of electrons. This equation can be solved directly by first multiplying it by $e^{ik\tau}$ and observing that the left hand side becomes a total derivative. Then the solution can be expressed as

$$\Delta(k,\mu,\tau_0) = \int_{\tau_a}^{\tau_0} d\tau e^{-\kappa} e^{-ik\mu(\tau_0-\tau)} \left[|\dot{\kappa}| \left(\frac{1}{4}\delta_\gamma(k,\tau) + 4\mu \mathbf{k}\cdot\mathbf{v}_e \right) - 2h'_{ij}\hat{n}^i\hat{n}^j \right], \quad (1.106)$$

where

$$\kappa(\tau) = \int_{\tau}^{\tau_0} a n_e \sigma_T d\tau' \quad (1.107)$$

is the optical depth and τ_a is a sufficiently early time, $\tau_a \ll \tau_{\rm dec}$.

When the optical depth falls to zero sufficiently rapidly through $\tau_{\rm dec}$ compared to the perturbation length scale $1/k$, $|\dot{\kappa}|e^{-\kappa} \approx \delta_D(\tau - \tau_{\rm dec})$, and by ignoring the quadrupole at last scattering and then converting to real space, we obtain the Sachs-Wolfe formula for the anisotropies today

$$\frac{\Delta T}{T}(\mathbf{x},\hat{\mathbf{n}}) = \frac{1}{4}\delta_\gamma(\mathbf{x},\tau_{\rm dec}) + \hat{\mathbf{n}}\cdot\mathbf{v}_e(\mathbf{x},\tau_{\rm dec}) - \frac{1}{2}\int_{\tau_{\rm dec}}^{\tau_0} h'_{ij}\hat{n}^i\hat{n}^j d\tau\,. \quad (1.108)$$

The first term represents the intrinsic photon density fluctuations, the second one the Doppler shifts and the integral is the integrated Sachs-Wolfe effect.

The brightness function can be expanded into moments Δ_l using Legendre polynomials P_l as

$$\Delta(\mathbf{k},\mu,\tau) = \sum_l (-i)^l (2l+1)\Delta_l(\mathbf{k},\mu,\tau)P_l(\mu)\,. \quad (1.109)$$

The recurrence differential equations for the moments are obtained by using the recurrence relation for Legendre polynomials, together with the expansion (1.109) and the differential equation (1.105). The moments are thus obtained by using the orthogonality properties of the Legendre polynomials:

$$\Delta_l(\mathbf{k},\mu,\tau) = \frac{i^l}{4\pi}\int \Delta(\mathbf{k},\mu,\tau)P_l(\mu)d\Omega\,. \quad (1.110)$$

Hence the first three moments yield

$$\Delta_0 = \delta_\gamma, \quad (1.111)$$

$$\Delta_1 = \frac{4}{3}i\hat{\mathbf{k}}\cdot\mathbf{v} = -\frac{4}{3}k\theta_\gamma, \quad (1.112)$$

$$\Delta_2 = 2\sigma_\gamma\,. \quad (1.113)$$

By considering only scalar perturbations for the metric and using Eqs. (1.111)-(1.113) the recurrence relations for the metric take the form

$$\delta'_\gamma - \frac{4}{3}k^2\theta_\gamma = -\frac{2}{3}h' \,, \tag{1.114}$$

$$\theta'_\gamma + \frac{1}{4}\delta_\gamma - \sigma_\gamma = -an_e\sigma_T\frac{\theta_\gamma - \theta_b}{k^2} \,, \tag{1.115}$$

$$\sigma'_\gamma + \frac{4}{15}k^2\theta_\gamma + \frac{3}{10}k\Delta_3 = \frac{2}{15}h'_s - an_e\sigma_T\sigma_\gamma \,, \tag{1.116}$$

$$\Delta'_l = \frac{k}{2l+1}\left[l\Delta_{l-1} - (l+1)\Delta_{l+1}\right] - an_e\sigma_T\Delta_l \,, \text{for } l \geq 3 \,. \tag{1.117}$$

The moments Δ_l can be used to calculate the Cosmic Microwave Background (CMB) power spectrum, which will be treated in the next subchapter.

1.4 The Cosmic Microwave Background

One of the most important discoveries of cosmology is the CMB by Penzias and Wilson [34, 35] in 1964 with a temperature of around 3K. It has been predicted by Gamow [12] and is produced by photons interacting electromagnetically and gravitationally with the other species which travel freely across space after they decoupled. Thus they were produced from recombination, and provide us with an image of the Universe at redshift 1000. At that time, the level of inhomogeneity in the Universe was around one part in 10^5. In fact, observations of the CMB frequency spectrum and its anisotropies in both temperature and polarisation channels have played a very important role in the development of modern cosmology and of our understanding of the early Universe. In order to characterise mathematically the general temperature anisotropies in the sky one decomposes them in terms of spherical harmonics using the parametrisation of a unit vector $\hat{\mathbf{n}} = (\theta, \phi)$ [36, 37],

$$\frac{\Delta T}{T}(\theta,\phi) = \sum_{l=0}^{\infty}\sum_{m=-l}^{l} a_{lm}Y_{lm}(\theta,\phi) \,. \tag{1.118}$$

The properties of the spherical harmonic functions can be used to express the coefficients a_{lm}:

$$a_{lm} = \int \frac{\Delta T}{T}Y^*_{lm}(\hat{n})d\Omega \,. \tag{1.119}$$

Due to statistical isotropy they satisfy the relation

$$\langle a_{lm}a^*_{l'm'}\rangle = C_l\delta_{ll'}\delta_{mm'} \,, \tag{1.120}$$

where C_l is the *angular power spectrum*. Then, the ensemble average power is given by

$$C_l = \langle |a_{lm}|^2 \rangle. \tag{1.121}$$

Because we only have one realisation of the Universe, an estimator of the angular power spectrum becomes

$$\hat{C}_l = \frac{1}{2l+1} \sum_{m=-l}^{l} |a_{lm}|^2 . \tag{1.122}$$

Then the multipoles C_l can be recast into a simple form,

$$C_l = \frac{2}{\pi} \int dk k^2 P(k) \left| \frac{\Delta_l(\mathbf{k}, \eta_0)}{\delta(\mathbf{k})} \right|^2 , \tag{1.123}$$

where

$$\langle \delta(\mathbf{k}) \delta^*(\mathbf{k}') \rangle = P(k) \delta_D(\mathbf{k} - \mathbf{k}') . \tag{1.124}$$

Here δ_D is the Dirac delta function and $P(k)$ is the power spectrum. Eq. (1.108) can be integrated by parts and recast in Fourier space into

$$\begin{aligned} \frac{\Delta T}{T}(\mathbf{k}, \mu, \tau_0) = &\left[\frac{1}{4}\delta_\gamma + \frac{3i\mu}{4k}\delta_\gamma' - \frac{i\mu}{2k}(h' - h_s') - \frac{h_s''}{2k^2} \right]_{\tau=\tau_{\rm dec}} e^{-ik\mu(\tau_0 - \tau_{\rm dec})} \\ &- \int_{\tau_{\rm dec}}^{\tau_0} d\tau e^{ik\mu(\tau - \tau_0)} \left[\frac{1}{6}(h' - h_s') - \frac{h_s'''}{2k^2} \right] . \end{aligned} \tag{1.125}$$

On large scales ($k \to 0$), in a matter dominated universe:

$$h^- = h - h_s = \text{const.} , \tag{1.126}$$

$$h_s \propto \tau^2 , \tag{1.127}$$

$$\delta_\gamma \propto k^2 . \tag{1.128}$$

Hence, using the growing mode solution from Eq. (1.79), the only non-vanishing term in Eq. (1.125) is

$$-\frac{h_s''}{2k^2} = \frac{\delta_c}{k^2} \equiv \frac{2A}{(k\tau_i)^2} . \tag{1.129}$$

It follows that the large-angle temperature fluctuations can be written as a Fourier expansion

$$\frac{\Delta T}{T}(\mathbf{x}, \hat{\mathbf{n}}) = \int \frac{d^3\mathbf{k}}{(2\pi)^3} \frac{2A(\mathbf{k})}{(k\tau_i)^2} e^{i\mathbf{k}\cdot\hat{\mathbf{n}}\tau_0} , \tag{1.130}$$

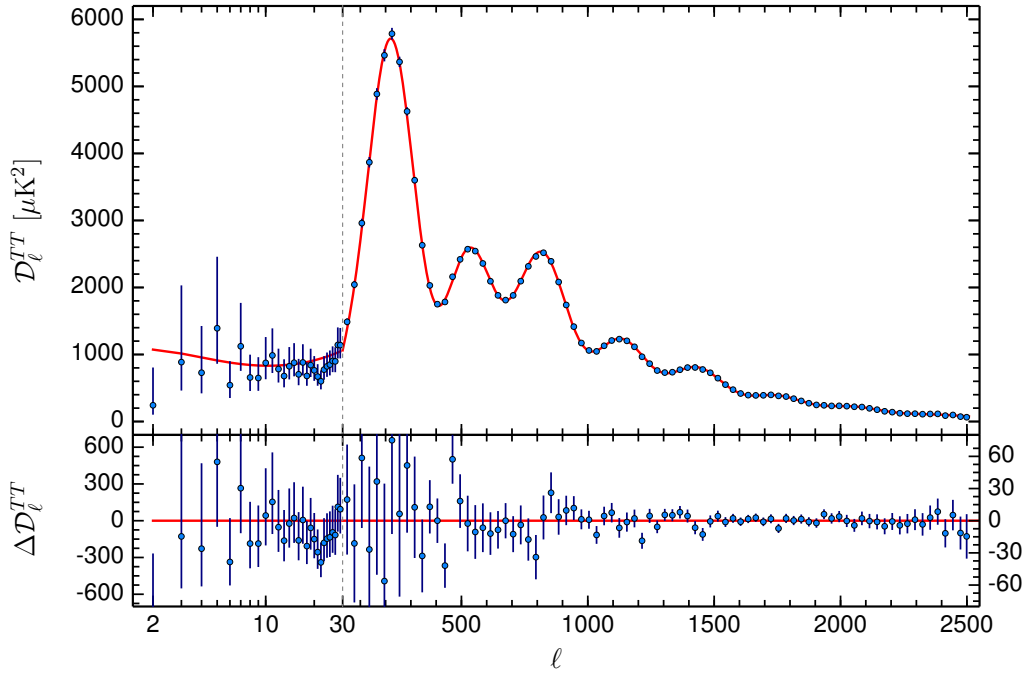

Fig. 1.2 Temperature power spectrum as measured by the Planck Collaboration (blue data points) with the maximum likelihood temperature power spectrum (top panel). The bottom panel represents residuals with respect to the red curve. This plot is Fig. 1 of Ref. [7].

where we have used $\tau_0 - \tau_{\rm dec} \approx \tau_0$. By using the relations between Legendre polynomials P_l, spherical harmonics Y_{lm} and spherical Bessel functions j_l,

$$P_l(\hat{\mathbf{n}}\cdot\hat{\mathbf{n}}') = \frac{4\pi}{2l+1}\sum_m Y_{lm}(\hat{\mathbf{n}})Y^*_{lm}(\hat{\mathbf{n}}')\,, \tag{1.131}$$

$$e^{i\mathbf{k}\cdot\hat{\mathbf{n}}\tau} = \sum i^l(2l+1)\,j_l(k\tau)P_l(\hat{\mathbf{k}}\cdot\hat{\mathbf{n}})\,, \tag{1.132}$$

we obtain the following expression for the a_{lm} at small l:

$$a_{lm} = 8\pi\int\frac{d^3\mathbf{k}}{(2\pi)^3}\frac{A(\mathbf{k})}{(k\tau_i)^2}i^l\,j_l(k\tau_0)Y^*_{lm}(\mathbf{k})\,. \tag{1.133}$$

Assuming a scale invariant power spectrum $P \propto k$, the power spectrum multipoles can be expressed as

$$C_l = \frac{4B}{\pi l(l+1)}\,, \tag{1.134}$$

where B is a constant representing the primordial power spectrum amplitude. Hence, on large scales $l(l+1)C_l$ is constant, and represents the Sachs-Wolfe plateau. On small angular scales, corresponding to $l > 200$, we use the flat-sky approximation: $k \propto l$. The main contributions are given by:

- intrinsic photon density fluctuations $\sigma_I \sim \frac{k^3}{2\pi^2}\langle\left|\frac{1}{4}\delta_\gamma\right|^2\rangle$;
- Sachs-Wolfe plateau $\sigma_{S-W} \sim \frac{k^3}{2\pi^2}\langle\left|\frac{h_s''}{2k^2}\right|^2\rangle$;
- Doppler effects $\sigma_V \sim \frac{k^3}{2\pi^2}\langle\left|\frac{3i\mu\delta_\gamma'}{4k}\right|^2\rangle$.

Qualitatively, on superhorizon scales, only the Sachs-Wolfe term is important (σ_{S-W}), while on subhorizon scales, corresponding to $l > 400$,

$$\sigma_I \approx \frac{8\pi^2}{9}B\cos^2\left(\frac{k\tau}{\sqrt{3}}\right)\exp\left(-\frac{2k^2}{k_D^2}\right)\,, \tag{1.135}$$

$$\sigma_V \approx \frac{8\pi^2}{9}B\sin^2\left(\frac{k\tau}{\sqrt{3}}\right)\exp\left(-\frac{2k^2}{k_D^2}\right)\,, \tag{1.136}$$

where k_D is the diffusion wavenumber. In Figure 1.2 we have plotted the temperature exhibiting these features, as measured by the Planck Collaboration.

1.5 Outline of the Thesis

In this thesis we analyse two classes of cosmological topics constrained by observations of the CMB and large-scale structure. In the first part (Chapters 2-4), we discuss anisotropies produced by topological defects, in particular cosmic strings (Chapter 3) and domain walls (Chapter 4). These topological features are predicted at cosmological phase transitions and so are relevant to many inflationary models. In the last few decades more and more stringent bounds have been determined for the cosmic strings parameters, but in many cases these bounds have relied on using a string power spectrum calculated by using an implementation of a simple phenomenological model (unconnected segment model). In this thesis, we develop the formalism for determining the CMB power spectrum of cosmic strings using accurate unequal-time correlators (UETCs) directly obtained from the energy-momentum tensor of an evolving defect simulation. We use this formalism to calculate the CMB power

spectrum of Nambu-Goto cosmic strings from simulations. We then use this power spectrum to find constraints on the cosmic string tension in different inflationary scenarios. This allows us to explore degeneracies between the cosmic string tension and various non-minimal parameters (running of the spectral index, sterile neutrinos, $N_{\rm eff}$, primordial tensor modes).

We modify the formalism developed for cosmic strings in order to be able to calculate the CMB power spectrum obtained from domain wall networks and we use the power spectrum to determine the first-ever quantitative constraint on the energy scale of formation of domain walls. The detailed calculation provides a basis for the original Zel'dovich bound [38].

The second major topic of the thesis is represented by the matter bispectrum of LSS (Chapters 5-6). In Chapter 5, we provide a review of the different LSS models from the literature, split into perturbative approaches (standard perturbation theory, effective field theory, renormalised perturbation theory, resummed Lagrangian perturbation theory) and phenomenological models (standard halo model, improved halo model). We also calculate for the first time the two-loop bispectrum in the renormalised perturbation theory (MPTBREEZE approach) by moving all the leading divergences in the integrals to a single point. In Chapter 6, we compare the predictions of the different models considered with N-body numerical simulations for low redshifts and we show on which scales and for which redshifts each of them is accurate. We identify the shapes that characterise the three components of the halo model with the flat, squeezed and constant bispectrum shapes. We show that all the perturbative theories (up to one-loop) have a flattened shape as the tree-level bispectrum. Moreover, we develop a new phenomenological model, based on the above-mentioned shapes, that provides a very good fit to the numerical simulations by calibrating a few parameters, pointing towards a simple quantitative 'HALOFIT' approach for future bispectrum measurements and comparisons.

CHAPTER 2

COSMIC DEFECTS

2.1 Introduction

Topological defects were first proposed by Skyrme [39] in the context of particle excitations, but it was realised that they appear during the spontaneous symmetry breaking of fields. This idea has been applied to cosmology: in the early Universe, during the cooling-down phase, the Universe experiences a series of phase transitions, where field symmetries describing the Universe are spontaneously broken. Then, topological defects may form: textures, monopoles, strings, and domain walls (for a review see Ref. [40]). Their characteristics and evolution have been studied in analogy with condensed matter physics [41] and particularly solid state physics [42].

In cosmology, the production of topological defects is associated with the cooling of the Universe. They are not predicted by the Standard Model of particle physics, but defects appear in many of its extensions, notably in unified theories. Initially, the temperature of the Universe was high enough so that it was in an unbroken symmetry state. As it cooled down, the Universe suffered a series of phase transitions where topological defects may have formed. The symmetry breaking phases are associated with the formation of matter and with the separation of the fundamental forces: the electromagnetic force, the weak nuclear force, the strong nuclear force and gravity. The energy scale when the symmetry breaking phase occurs imprints different characteristics to the topological defects, and has observational consequences as well. If the broken symmetry is a global one, the defects are called *global* defects, while if the symmetry is local involving a gauge vector field they are called *local* defects.

Apart from being predicted by grand unification theories, the popularity of defects was influenced by the possibility of explaining the anisotropies in the CMB with cosmic strings.

Indeed, in the 1980s theories have been developed where the galaxies were formed from cosmic string seeds [43, 44]. A more recent motivation comes from fundamental theory where the cosmic strings stretching across the Universe could be superstrings, that is, direct relics from a higher-dimensional epoch in the early history of the Universe [45].

A simple model illustrating the symmetry breaking process has been studied by Goldstone [46]. We consider a complex field ϕ with complex conjugate $\bar{\phi}$ and a Mexican-hat potential $V(\phi)$ with two real positive parameters λ and η:

$$V(\phi) = \frac{1}{4}\lambda(\bar{\phi}\phi - \eta^2)^2 . \tag{2.1}$$

This has the Lagrange density

$$\mathscr{L} = \partial_\mu \bar{\phi}\partial^\mu \phi - V(\phi) , \tag{2.2}$$

which is invariant under the global gauge transformation:

$$\phi(x) \to e^{i\alpha}\phi(x) . \tag{2.3}$$

The minima of the potential $V(\phi)$ lie on a circle defined by $|\phi| = \eta$. Therefore, the theory has an infinite number of vacuum states characterised by

$$\langle 0|\phi|0\rangle = \eta e^{i\theta} , \tag{2.4}$$

where θ is an arbitrary phase. However, by considering the global gauge transformation (2.3), the ground state of Eq. (2.4) changes to $\eta e^{i(\theta+\alpha)}$, which signifies that the symmetry is broken under such a transformation. However, as all the vacua are equivalent, we are free to choose the most convenient one, corresponding to $\theta = 0$. Then we can also perform a change of variable and re-express the field ϕ by deviations from the vacuum state η, in terms of two real fields ϕ_1 and ϕ_2, which have 0 expectations values

$$\phi = \eta + \frac{1}{\sqrt{2}}(\phi_1 + i\phi_2) , \tag{2.5}$$

$$\bar{\phi} = \eta + \frac{1}{\sqrt{2}}(\phi_1 - i\phi_2) . \tag{2.6}$$

Substituting the above expressions into Eq. (2.2), the Lagrangian becomes

$$\mathscr{L} = \frac{1}{2}(\partial_\mu \phi_1)^2 - \frac{1}{2}\lambda\eta^2\phi_1^2 + \frac{1}{2}(\partial_\mu \phi_2)^2 + \mathscr{O}(\phi_1^3, \phi_2^3) . \tag{2.7}$$

Thus, we have now expressed the Lagrangian system as a sum of the contributions of the Lagrangians corresponding to two scalar fields, ϕ_1 and ϕ_2 respectively, the first (radial) of which carries a mass $\sqrt{\lambda}\eta$ and the second (azimuthal) is massless and has periodic symmetry. The cosmic string solution is due to a nontrivial winding in this second massless field.

Classes of defects

Let $\mathscr{M}$ be a manifold. The topology of the manifold can be characterised by the *homotopy group*. If we consider maps from the n-sphere S^n to the manifold $\mathscr{M}$ having a common base point x_0, then two maps that can be continuously deformed into one another are considered topologically equivalent. Thus, the set of maps $S^n \to \mathscr{M}$ can be split into equivalence classes, such that the maps in each class are topologically equivalent. These equivalence classes form a group, the homotopy group π_n. The topological defects can be classified in terms of their homotopy group. In Table 2.1, we show the four main types of topological defects, their homotopy groups and their dimensionality.

Table 2.1 Classification of topological defects by homotopy group of the manifold and dimensionality.

Topological defect	Homotopy group	Dimensionality
Domain walls	$\pi_0(\mathscr{M})$	2
Strings	$\pi_1(\mathscr{M})$	1
Monopoles	$\pi_2(\mathscr{M})$	0
Textures	$\pi_3(\mathscr{M})$	–

In the next part of this Chapter, we will summarize the basic properties of each of the defects, and analyse their cosmological consequences.

2.2 Domain walls

Domain walls are the simplest cosmological defects, as they can be described by a single scalar field ϕ. A comprehensive introduction to this class of cosmic defects can be found in Refs. [40, 47]. One starts with the Lagrangian describing a discrete broken symmetry, that can be written as

$$\mathscr{L} = \frac{1}{4\pi}\left[\frac{1}{2}\phi_{,\alpha}\phi^{,\alpha} - V(\phi)\right], \tag{2.8}$$

where the field ϕ is real and the potential V has at least two degenerate minima [48]. A very simple model in one spatial dimension and one time dimension is obtained by considering ϕ to be a real field in one dimension, with a potential given in the Goldstone model (Eq. 2.1). The potential $V(\phi)$ is plotted in Fig. 2.1 and has minima at $\phi = \pm\eta$. The discrete symmetry of the system is $\phi \to -\phi$, with $V(\phi) = V(-\phi)$.

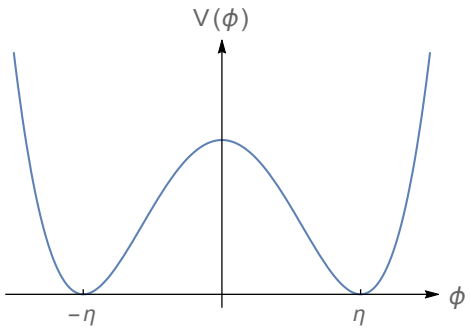

Fig. 2.1 Potential $V(\phi)$ characterising the formation of domain walls.

The equation of motion obtained from the Lagrangian (2.8),

$$\frac{\partial^2\phi}{\partial t^2} - \frac{\partial^2\phi}{\partial x^2} + \lambda(\phi^2 - \eta^2)\phi = 0 \tag{2.9}$$

has trivial solutions $\phi = \pm\eta$ which have zero energy and are therefore stable. From the symmetry of the system one can see that these two solutions are equally preferred. Hence there would be regions in the Universe (sufficiently far apart in space such that they would not be in causal contact), which would choose one of the minima and others which would choose the other one [47, 49]. However, as the field must be a continuous function, ϕ has to be interpolated between the regions with different zero-energy solutions. Such an interpolating solution is given by

$$\phi(x) = \eta \tanh(\sqrt{\lambda/2}\eta x), \tag{2.10}$$

which represents a Z_2 kink around $x = 0$ and is plotted in left panel of Fig. 2.2.

By looking at the energy density of this system (right panel of Fig. 2.2), we see that in order to pass from one minimum to the other, the field must go through a point where $\phi = 0$, corresponding to the maximum of the potential. The "jump" from one minimum to the other is represented by the domain wall, which stores the energy of the system. As the two regions are disconnected, the domain wall must be infinite.

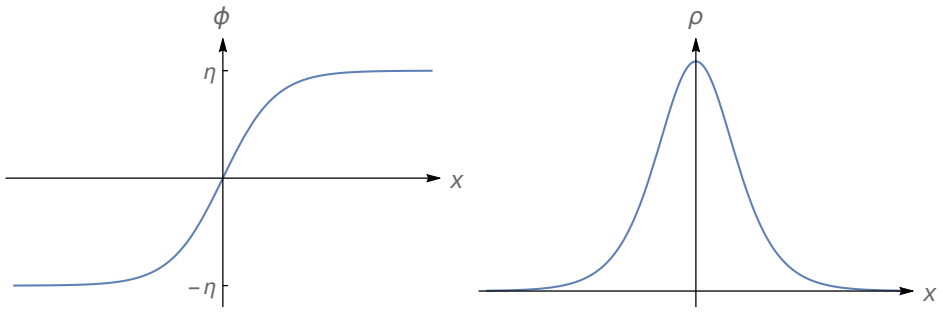

Fig. 2.2 Static solution of Eq. (2.9) illustrating the formation of domain walls (left) and energy density of this solution (right).

A generalisation of this simple model is obtained by considering a potential with N minima,

$$V(\phi) = \frac{1}{4}\lambda(\bar{\phi}\phi - \eta^2)^2 - 2m^2\eta^2\frac{\cos(N\theta)-1}{N^2}, \tag{2.11}$$

where ϕ is a complex field of phase θ. In this theory, there are N vacua, corresponding to the minima of the potential, which can be separated by domain walls.

As we shall see in Chapter 4 for domain wall scaling solutions, the energy density of walls grows faster than that of the background radiation and matter as the Universe expands. Eventually the walls will become the dominant part of the energy of the Universe making the evolution highly anisotropic [38, 50]. For this reason, their symmetry breaking scale is believed to be constrained to around 1 MeV because of the effect on the CMB. Nevertheless, their existence is predicted by various cosmological models which have discrete broken symmetries [51, 52]. In Chapter 4, we will derive a quantitative bound on the energy scale of formation of the domain walls using current CMB measurements.

2.3 Cosmic strings

Cosmic strings are one-dimensional line-like defects, characterised by their tension μ. Their existence was first proposed by Kibble [53], in analogy with the symmetry breaking which occurs in ferromagnets. Of the topological defects considered, cosmic strings are the most studied because they appear in a wide class of theories arising from string and supersymmetric theories.

The formation of cosmic strings can be explained in a similar way to that of domain walls. The Mexican hat potential described in Eq. (2.1) is illustrated in Fig. 2.3.

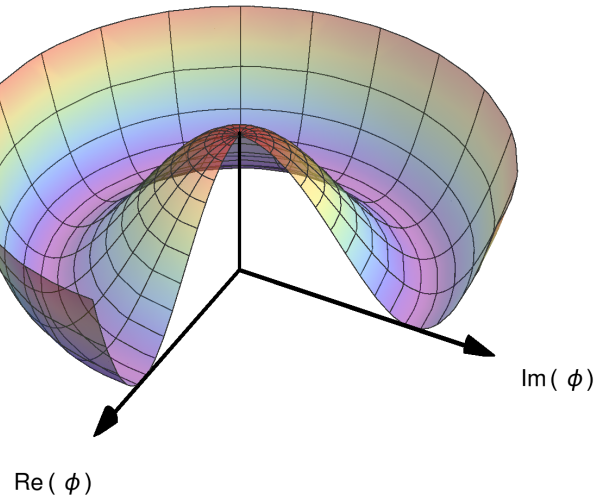

Fig. 2.3 Mexican hat potential $V(\phi)$ characterising the formation of cosmic strings.

Similarly to the case of domain walls, for strings the different states of minimum energy described in Eq. (2.4) can appear randomly in different patches of the Universe [49, 54]. By considering a loop in space, in which the phase of the minimum is modified by 2π, by continuity of the field, there must be a point inside the loop where $\phi = 0$ – that is the core of the cosmic string. As in the case of domain walls, it corresponds the fact that ϕ must pass over the maximum of the potential.

From a historical point of view, cosmic strings were once considered to be the primary source of anisotropies in the CMB [40, 55] that generated the growth of structures. However, it has been shown that the characteristics of the power spectrum they produce does not match the one observed in the CMB using the COBE mission and Boomerang [56], WMAP and *Planck* probes. The cosmic string temperature power spectrum is smooth and has a unique peak, and hence it does not match the observed CMB power spectrum. In the meantime, a good agreement in the power spectrum has been obtained from the inflationary scenarios, effectively ruling out topological defects as the primary source of anisotropies [9]. Cosmic strings can nevertheless still be present and models of brane inflation predict their formation [57, 58]. Current observational data allow a maximum of 3% of the observed power to be due to cosmic strings [9]. Initially it was expected that the energy scale of formation of the strings was in the region of $\eta \sim 10^{16}$ GeV, which is the Grand Unification Theory scale, which corresponds to $G\mu/c^2 \sim 10^{-6}$ via

$$\frac{G\mu}{c^2} = \left(\frac{\eta}{m_{\rm pl}c^2}\right)^2 . \tag{2.12}$$

Such high energy is impossible to probe with terrestrial experiments, and identifying the existence of cosmic strings at these energies would offer a very interesting connection with particle physics. It would be possible to test particle collision patterns at very high energies and to identify signatures of extra dimensions from string theory [9, 59].

More recent studies in string theory have shown that their tension could in fact be as low as the electroweak scale [60]. In this case, the allowed limit for the string tension would be $10^{-11} < G\mu/c^2 < 10^{-6}$ [45]. The more recent work is based on superstring theories and new methods of string compactification with large extra dimensions and/or large warp factors. These ideas are presented in detail in Refs. [61, 62]. Another option, which relies on supersymmetry, is presented in Ref. [63].

Very recently, various cosmic string models [2, 64, 65] have been discussed in trying to explain the BB polarisation obtained by the BICEP2 experiment [66] as well as large-scale anomalies in the CMB, such as the cold spot [67].

String networks are formed of long strings and finite loops. When long strings intersect, there are two possibilities: they either pass through one another as if there were no collision, or they disconnect and reconnect again in a different way. Loops can be formed in the latter case. When a string self-intersects, the reconnection probability is one for classical cosmic strings [68]. They then collapse inward and decay. During the decay process, their energy is converted into gravitational waves. The recent detection of gravitational waves from the merger of two black holes [69] represents a significant milestone and revives the possibility that these could be measured from the effects of cosmic strings in the future.

There are two approaches for studying the evolution of cosmic strings: the Abelian-Higgs field theory model and the Nambu-Goto effective action. A detailed study of cosmic strings can be found in Refs. [40, 70] and a recent short review of the field in Ref. [54]. We will present the approaches for both cases in Chapter 3.

Macroscopically, cosmic strings are characterised by their energy per unit length, μ. Its large value is expected to give rise to observable effects, such as gravitational lensing and gravitational waves. They induce temperature linelike discontinuities, thus giving a characteristic signature in the cosmic microwave background (CMB) power spectrum [71, 72].

2.4 Monopoles

Monopoles are point-like defects and they arise when a sphere of infinite radius cannot be smoothly contracted to a point. Their existence was first proposed by Dirac [73] as magnetic

monopoles. In the context of symmetry breaking, an example of monopole production is through the $SU(2) \to U(1)$ phase transition [74, 75]. The Lagrangian density for a triplet of real fields ϕ

$$\mathscr{L} = \mathscr{D}_\mu \phi \cdot \mathscr{D}^\mu \phi - \frac{1}{4} G_{\mu\nu} \cdot G^{\mu\nu} - V(\phi) \tag{2.13}$$

is considered with the potential

$$V(\phi) = \frac{1}{4}\lambda(\phi^a \phi^a - \eta^2)^2 , \tag{2.14}$$

where

$$G^{\mu\nu} = \nabla^\mu \mathbf{W}^\nu - \nabla^\nu \mathbf{W}^\mu - e\mathbf{W}^\mu \wedge \mathbf{W}^\nu , \tag{2.15}$$

$$\mathscr{D}^\mu \phi = \nabla^\mu \phi - e\mathbf{W}^\mu \wedge \phi \tag{2.16}$$

and $\mathbf{W}^\mu$ is the gauge potential. Then the monopole solution is given by

$$\phi^a = \eta h(r) \frac{x^a}{r} , \tag{2.17}$$

with the gauge field satisfying

$$A_0^a = 0 , \tag{2.18}$$

$$A_i^a = -(1 - K(r)) \varepsilon^{aij} \frac{x^j}{er^2} , \tag{2.19}$$

and the functions h and K satisfy $h(0) = 0$, $K(0) = 1$ and $h(\infty) = 1$ and $K(\infty) = 0$.

The production of such magnetic monopoles is a generic prediction of GUT theories and they are expected to have a typical mass of ten times the GUT scale. This can be used to predict the density of the monopoles. However, this is in complete disagreement with observational bounds. This discrepancy is solved by inflation, as monopoles which have formed before inflation are diluted away and those being produced later in the form of monopole-antimonopole pairs are suppressed by a Boltzmann factor.

2.5 Textures

Textures represent more complicated field configurations and can only be stable in at least four dimensions [76]. An example of a model where textures can form in four dimensions is

given by the Lagrangian [40]

$$\mathscr{L} = \frac{1}{2}\partial_\mu \phi_i \partial^\mu \phi_i - \frac{1}{4}\lambda(\phi_i\phi_i - \eta^2)\,. \tag{2.20}$$

In this case there is a $SO(4)$ symmetry broken to $SO(3)$. One can parametrise this three-sphere representing the vacuum manifold with three angular variables

$$\phi_i = \eta(\sin\zeta\sin\xi\cos\gamma, \sin\zeta\sin\xi\sin\gamma, \sin\zeta\cos\xi, \cos\zeta)\,. \tag{2.21}$$

The Lagrangian (2.20) with the parametrisation (2.21) gives rise to the effective action

$$S = \frac{1}{2}\eta^2 \int d^4x\sqrt{-g}\left[(\partial_\mu\zeta)^2 + \sin^2\zeta\left[(\partial_\mu\xi)^2 + \sin^2\xi(\partial_\mu\gamma)^2\right]\right]\,. \tag{2.22}$$

A spherically symmetric texture would correspond to

$$\zeta = \zeta(t,r)\,, \tag{2.23}$$

$$\xi = \theta\,, \tag{2.24}$$

$$\gamma = \phi\,, \tag{2.25}$$

with ζ a continuous function and $\zeta(r=0)=0$ and $\zeta(r=\infty)=\pi$. By considering a flat spacetime, and using the above spherically symmetric ansatz for the texture, one can simplify the action (2.22), yielding a very simple solution for ζ:

$$\zeta = 2\cot^{-1}(-t/r), \quad t<0\,. \tag{2.26}$$

Cosmologically, textures are expected to create temperature anisotropies and to be seen as cold or hot points on the sky. Attempts have been made to explain the cold spot of the CMB with textures [77] and an analysis with the WMAP data has shown that at most six textures can be present in the sky [78]. Textures have also been proposed as sources of the structure in the Universe by using their instability to generate fluctuations that eventually grow into structures [79].

CHAPTER 3

COSMIC STRINGS

3.1 Cosmic string models

The CMB is a powerful method for distinguishing between early Universe models. Results from the *Planck* Collaboration [17] provide strong constraints on cosmic strings, instead giving robust support for a nearly scale-invariant inflationary model with the standard six parameters. At present, however, cosmic string constraints are determined not from direct Nambu-Goto string simulations but from either a phenomenological string model, the unconnected segment model (USM) [80], or from field theory simulations of the Abelian-Higgs model of increasing, but still limited, resolution [81]. The resulting CMB constraints are different, so there is good motivation for determining the Nambu-Goto results directly, which can also improve the calibration of the USM model.

A different approach for detecting cosmic strings has also been investigated, which is based on detecting non-Gaussian signatures generated by cosmic strings through CMB maps using higher-order correlation functions such as the bispectrum [82–84]. These methods have yielded weaker constraints on the cosmic strings tension so far.

In addition, pulsar timings have been used to constrain the gravitational wave background, which in turn places stringent constraints on cosmic strings [85, 86]. These methods provide an independent bound on the cosmic string tension to the CMB one, and in the future they can be significantly improved by new constraints on gravitational waves.

In this Subchapter we present the two different models mentioned above for studying the evolution of cosmic strings: the Abelian-Higgs field theory model and the Nambu-Goto effective action.

3.1.1 Abelian-Higgs model

The Abelian-Higgs model is the relativistic extension of the Ginsburg-Landau theory and has the action [40]

$$S = \int d^4y(\partial_\mu + ieA_\mu)\bar{\phi}(\partial^\mu - ieA^\mu)\phi - \frac{1}{4}F_{\mu\nu}F^{\mu\nu} - \frac{1}{4}\lambda(|\phi|^2 - \eta^2)^2\,, \tag{3.1}$$

where ϕ is a complex scalar field, λ and e are coupling constants, and A_μ is a four-dimensional U(1) gauge field satisfying $F_{\mu\nu} = \partial_\mu A_\nu - \partial_\nu A_\mu$. Using $D_\mu = \partial_\mu - ieA_\mu$, the equations of motion become

$$D_\mu D^\mu \phi = -\frac{\lambda\phi}{2}(|\phi|^2 - \eta^2)\,, \tag{3.2}$$

$$\partial_\nu F^{\nu\mu} = 2e\Im(\phi^\star D^\mu \phi)\,. \tag{3.3}$$

The action described in Eq. (3.1) has vortex-type solutions [87, 88], which are static and cylindrically symmetric,

$$\phi_s(\mathbf{r}) = e^{in\theta} f(r)\,, \tag{3.4}$$

$$A_{sa}(\mathbf{r}) = \varepsilon_{ab}x_b\frac{n}{er^2}\alpha(r)\,, \tag{3.5}$$

with $a,b = 1,2$ representing two Cartesian coordinates and ε being an antisymmetric tensor. Fixing suitable boundary conditions, the large r asymptotic solutions to these equations can be obtained in terms of modified Bessel functions of the second kind,

$$\alpha(r) = 1 - rK_1\left(\sqrt{2}er\right)\,, \tag{3.6}$$

$$f(r) = 1 - K_0\left(\sqrt{\lambda}r\right)\,. \tag{3.7}$$

In the case of a curved string, one can express any point near the string world sheet in terms of tangent vectors to the world sheet and normal vectors

$$y^\mu(\xi) = x^\mu(\zeta) + \rho^A n_A^\mu(\zeta)\,, \tag{3.8}$$

where n_A^μ are the normal vectors, $x_{,a}^\mu$ are the tangent vectors, y^μ is a point near the world sheet and $\xi^\mu = (\zeta^a, \rho^A)$. The approximate solution is thus

$$\phi\left(y(\xi)\right) = \phi_s(r)\,, \tag{3.9}$$

$$A^{\mu}\left(y(\xi)\right) = n_B^{\mu}(\zeta) A_{sB}(r)\,, \tag{3.10}$$

where $r^2 = (\rho^1)^2 + (\rho^2)^2$. When rewriting the action in terms of these new coordinates, one needs to calculate the Jacobian of the transformation from the y to ξ coordinates. This is given by the square root of the modulus of the determinant of the world sheet metric $M_{\alpha\beta}$, which can be expressed as

$$M_{\alpha\beta} = \mathrm{diag}\left(\gamma_{ab}, -\delta_{AB} + \mathscr{O}(r/R)\right)\,, \tag{3.11}$$

where

$$\gamma_{ab} = g_{\mu\nu} x^{\mu}_{,a} x^{\nu}_{,b} \tag{3.12}$$

and R is the curvature radius of the string. The integration over the normal coordinates ρ^A can be performed, yielding just the constant μ. The asymptotic solutions (3.7) decaying exponentially, the correction is reduced to $\mathscr{O}(\delta/R)$. Hence, if one considers the string thickness to be small with respect to its curvature radius, the Nambu-Goto action is obtained as the first-order approximation [40]. It will be discussed in the next subchapter.

3.1.2 Nambu-Goto model

A one-dimensional reduction of the Abelian-Higgs action gives rise to the Nambu-Goto action, described below (see Refs. [40, 70]). Hence, the Nambu-Goto strings have just one dimension (zero width) and live in a two-dimensional space-time parametrised by $X^{\mu} = X^{\mu}(\zeta^a)$ with $a = 0, 1$. The physical motivation for using this approximation is that higher-order corrections are small when strings are considered to be long enough compared to their width [89]. Nambu-Goto strings are solutions of the Nambu-Goto action

$$S = -\mu \int \sqrt{-\gamma}\, d^2\zeta\,, \tag{3.13}$$

where $\gamma_{ab} = g_{\mu\nu}\partial_a X^{\mu}\partial_b X^{\nu}$ is the two-dimensional world sheet metric and $\gamma = \det(\gamma_{\mu\nu})$ [same as Eq. (3.12), with $x^{\mu} \to X^{\mu}$].

(ζ^0, ζ^1) is an arbitrary parametrisation of the string world sheet, with one of the parameters timelike and the other spacelike. Hence, in an expanding universe, one may choose to take $\zeta^0 \equiv \tau$ (conformal time) and $\zeta^1 \equiv \sigma$ (the spacelike parameter of the string).

Simulations usually start with Vachaspati-Vilenkin initial conditions [90], which will be discussed in Subchapter 3.2. When two strings segments meet, they split and then reconnect the other way (intercommutation). In this process, loops are being formed and they decay and

radiate energy. In the time evolution of the cosmic string network, the strings are expected to reach a scaling solution, *i.e.* the number of cosmic strings crossing each horizon volume is fixed [91]. This energy loss mechanism in fact makes cosmic strings cosmologically viable (otherwise cosmic strings would eventually dominate the Universe) [53] and also the initial conditions considered for the simulations become less important. In Fourier space, the energy-momentum tensor arising from action (3.13) can be expressed as

$$\Theta_{\mu\nu}(\mathbf{k},\tau) = \int d^3\mathbf{x} e^{i\mathbf{k}.\mathbf{x}} \Theta_{\mu\nu}(\mathbf{x},\tau) = \mu \int d\sigma e^{i\mathbf{k}.\mathbf{X}(\sigma,\tau)} \left(\varepsilon \dot{\mathbf{X}}^{\mu} \dot{\mathbf{X}}^{\nu} - \varepsilon^{-1} \mathbf{X}'^{\mu} \mathbf{X}'^{\nu} \right) , \quad (3.14)$$

where the prime denotes differentiation with respect to σ and dot denotes differentiation with respect to τ and $\varepsilon = \sqrt{\mathbf{X}'^2/(1-\dot{\mathbf{X}}^2)}$ represents the energy density along the string. For the Nambu-Goto strings, a good phenomenological model is given by the velocity-dependent one-scale (VOS) model [92–94]. This model assumes that the string population is formed by long strings (denoted by ∞) and small loops (denoted by l). The long strings are characterised by the correlation length L and by the root-mean-square velocity v,

$$\mathrm{v}^2 = \frac{\int \dot{X}^2 \varepsilon d\sigma}{\int \varepsilon d\sigma} . \quad (3.15)$$

The averaged energy density of the long strings is

$$\rho_{\infty} = \frac{\mu}{L^2} \quad (3.16)$$

and the parameter $\tilde{c}$ is a constant which expresses the loop production rate and is defined by the following formula:

$$\frac{d\rho_{\infty}}{dt} = \tilde{c}\mathrm{v}\frac{\rho_{\infty}}{L} . \quad (3.17)$$

The evolution equations for the correlation length L and for the velocity of long strings v can be derived from the microscopic equations of motion and Newton's second law:

$$2\frac{dL}{dt} = 2HL(1+\mathrm{v}^2) + \tilde{c}\mathrm{v} \quad (3.18)$$

$$\frac{d\mathrm{v}_{\infty}}{dt} = (1-\mathrm{v})\left(\frac{k}{L} - 2H\mathrm{v}\right) , \quad (3.19)$$

where k is a parameter which characterises the small scale structure of the string network and which expresses the loop production rate [92],

$$k = \frac{\langle (1-\dot{\mathbf{x}})(\dot{\mathbf{x}}\cdot\mathbf{u})\rangle}{\mathrm{v}(1-\mathrm{v}^2)\mathrm{u}}, \tag{3.20}$$

with $\mathbf{u}$ the curvature radius vector. For the relativistic regimes considered in the case of cosmic strings, a suitable asymptotic ansatz is

$$k_{\mathrm{rel}} = \frac{2\sqrt{2}}{\pi}\cdot\frac{1-8\mathrm{v}^6}{1+8\mathrm{v}^6}, \tag{3.21}$$

while in the nonrelativistic limit a consistent asymptotic limit is found [94]:

$$k_{\text{non-rel}} = \frac{2\sqrt{2}}{\pi}. \tag{3.22}$$

Numerical simulations have fixed $\tilde{c} = 0.23$ regardless of epoch. Scale-invariant solutions, which are characterised by $\mathrm{v} =$ constant and $L \propto t$ exist only when the scale factor is evolving as a power law.

Phenomenological unconnected segment model

For Nambu-Goto strings, the USM model has been devised, as described in Refs. [80, 95–97]. In the this model, the cosmic string network is described by a Brownian network which is formed from a set of independent, uncorrelated straight segments with random velocities. All segments are produced early in the evolution of the Universe, and then, at each epoch, part of the strings decay such that scaling is preserved throughout the history of the Universe. Each segment has comoving length equal to the correlation length, and its position is randomly chosen, in such a way such that the equations of motion (3.18) and (3.19) are satisfied for each particular string segment. Hence, the magnitude of the velocity is determined by these equations, but its orientation is arbitrary and is taken from a flat distribution.

As the model is made from straight segments, the small scale structure of the strings is not taken into account. This has been adjusted phenomenologically, by adding a new "wiggliness" parameter α [98], which, however, describes only the macroscopic evolution of the strings. This modifies the energy momentum tensor (3.14) to

$$\Theta_{\mu\nu}(\mathbf{k},\tau) = \mu\int d\sigma e^{i\mathbf{k}.\mathbf{X}(\sigma,\tau)}\left(\varepsilon\alpha\dot{\mathbf{X}}^{\mu}\dot{\mathbf{X}}^{\nu} - \frac{1}{\varepsilon\alpha}\mathbf{X}'^{\mu}\mathbf{X}'^{\nu}\right). \tag{3.23}$$

The string segment decay is realised through a function T^{off} that is a smooth approximation to the Heaviside function, such that after a certain time the particular string segment

disappears and similarly for the appearance of the segment through a similar function $T^{\rm on}$. The total stress-energy tensor is calculated as the sum of the individual components for the segments,

$$\Theta_{\mu\nu}(\mathbf{k},\tau) = \sum_m \Theta^m_{\mu\nu}(\mathbf{k},\tau) T^{\rm off}\left(\tau,\tau^{\rm off}_m\right) T^{\rm on}\left(\tau,\tau^{\rm on}_m\right) \,. \tag{3.24}$$

The energy-momentum tensor of one segment is of the form of Eq. (3.23):

$$\Theta_{\mu\nu}(\mathbf{k},\tau) = \mu \int_{-l/2}^{l/2} d\sigma e^{i\mathbf{k}\cdot\mathbf{X}} (\varepsilon\alpha \dot{X}^\mu \dot{X}^\nu - \frac{1}{\varepsilon\alpha} X'^\mu X'^\nu) \,, \tag{3.25}$$

where l is the comoving correlation length $l = L/a$. The number of string segments N at each particular time satisfies

$$N(\tau) \propto \frac{1}{\tau^3} \tag{3.26}$$

and hence scaling is preserved [96]. However, in this case in order to have one string segment today, one would need at least 10^{12} initial string segments, which is not possible numerically. The problem was overcome by considering only one of the segments decaying at each particular time and multiplying it by a suitable weighting function, chosen such that scaling is preserved. An equation for the evolution of the wiggliness parameter α is used [91]:

$$\alpha(\tau) = 1 + \frac{0.9}{H\tau} \,, \tag{3.27}$$

such that it satisfies the expected behaviour in the radiation, matter and cosmological constant eras.

As the equations describing the matter perturbations and the power spectra do not depend on the direction of the wave-vector $\mathbf{k}$, this can be taken to be along the $k_3 = k_z$ axis. Thus, the energy-momentum tensor components become

$$\Theta_{00} = \frac{\mu\alpha}{\sqrt{1-\mathrm{v}^2}} \frac{\sin(k\hat{X}'_3 l/2)}{k\hat{X}'_3/2} \cos(k\cdot X_0 + k\hat{X}_3 v\tau) \tag{3.28}$$

$$\Theta_{ij} = \left[\mathrm{v}^2 \hat{\dot{X}}_i \hat{\dot{X}}_j - \frac{(1-\mathrm{v}^2)}{\alpha^2} \hat{X}'_i \hat{X}'_j\right] \Theta_{00} \,, \tag{3.29}$$

while Θ_{0i} can be expressed using the conservation of the stress-energy tensor $\Theta_{\mu\nu}$. With this choice of the wave vector, the components required for the Boltzmann integrator CMBACT [99], which in turn is based on CMBFAST [30] are:

$$\Theta^S = (2\Theta_{33} - \Theta_{11} - \Theta_{22})/2 \,, \tag{3.30}$$

$$\Theta^V = \Theta_1^V = \Theta_{13}\,, \tag{3.31}$$

$$\Theta^T = \Theta_{12}^T = \Theta_{12}\,, \tag{3.32}$$

$$\Theta = \Theta_{ii}\,, \tag{3.33}$$

$$\Theta^D = \Theta_{03}\,. \tag{3.34}$$

These are the anisotropic scalar, the vector component, the tensor component, the trace and the velocity field.

This model has been used to mimic the behaviour of Abelian-Higgs strings, by tuning its parameters. The results are in good agreement with the field theory simulations [59].

CMB comparison for Abelian-Higgs and Nambu-Goto simulations

As described in the previous subchapters, field theory simulations have a much lower dynamical range than Nambu-Goto simulations. They are, however, able to resolve scales of sizes comparable to the string width, and the decay products appear naturally out of the simulation. For Nambu-Goto simulations, the intersection of two different strings forms a loop. This must be specified in the simulation algorithm, such that the loop is cut off from the long strings, which then reconnect again [40]. In the case of Nambu-Goto simulations, loops are clearly visible, but in field theory simulations, energy moves directly into massive modes of the fields because of the limited dynamical range. A comparison between the two types of simulations appears in Fig. 1 of Ref. [8] and is reproduced in Fig. 3.1.

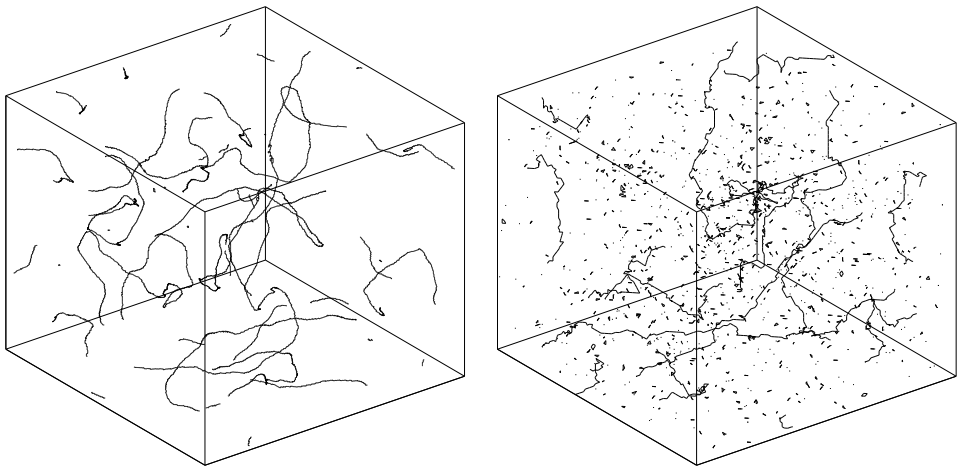

Fig. 3.1 Comparison of AH (left) and Nambu-Goto (right) cosmic string simulations, taken from Ref. [8].

This can be illustrated by the different shapes and amplitudes of the temperature power spectra determined from these two models, as it can be seen in Fig. 3 of Ref. [9]. These plots were created with the standard parameters from the code CMBACT [99] for the USM (Nambu) and AH mimic and with field theory simulations for the Abelian-Higgs cosmic strings. A similar comparison is shown later in the Chapter (Fig. 3.14).

The difference may be due to the fact that the USMs are not able to model the velocity correlations between the strings, but also to the fact that the field theory simulations rely on extrapolation over many orders of magnitude [81]. Even though extensive simulations have been performed for the Abelian-Higgs model, the Nambu-Goto strings have mostly been described using the simplified USM model.

3.2 Cosmic string simulations

In order to analyse the consequences of cosmic strings on the CMB, we had to first determine the power spectrum they produce from Nambu-Goto simulations. We have used the Allen and Shellard code [100] to generate the string networks with Vachaspati-Vilenkin initial conditions [40, 90] and to evolve them in time in different epochs of the Universe.

At the initial time of the simulation, the cubic simulation box is discretised as a lattice. For each of the vertices of this lattice, the magnitude of the field ϕ is assumed to be constant, while its phase takes one of three distinct values, which are randomly assigned. At most one string is allowed to pass through the face of a cubic cell. Whether this happens or not is determined by looking at the winding number of the phase of the field around the centre of the cell - if it is nonzero, then a string is passing through it. By applying this procedure to the whole box, the strings segments can form long strings (which have ends on the faces of the exterior of the lattice) or closed loops.

To obtain an accurate prediction for the cosmic string power spectrum, we have used three simulations, covering in total a redshift range from 5900 to 0 as follows. The first simulation (Simulation 1) starts deep into the radiation era, goes through radiation-matter transition, and ends in the matter era, corresponding to redshifts from 5900 to 700. The second simulation lies entirely in the matter era, with redshifts from 860 to 37. The third simulation starts in the matter era (redshift 48) and goes into the cosmological constant future, to $z = 0$. All three simulations had earlier initial times, but we have removed around 1.5% of the time steps of each of them in order to remove the excessive correlations in the initial conditions. The important quantity in this context is the dynamical range of the simulations. After removing these initial time steps, we decrease the dynamical range of each of the

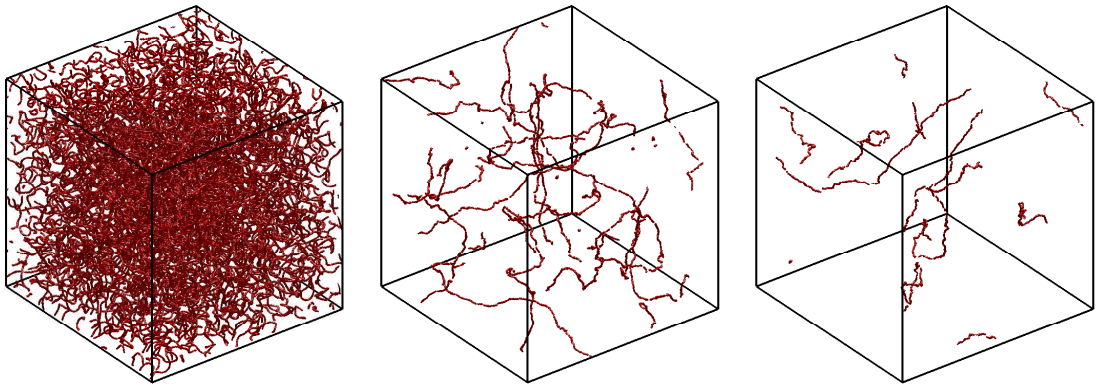

Fig. 3.2 Evolution of the string network in the simulation covering the matter era (redshift range 945 to 37.2, from left to right).

simulations by roughly 15%. In Fig. 3.2 the time evolution of the string network simulation covering the matter epoch is shown by plotting the energy component for the strings at three time steps corresponding the first, middle and last time used in the calculation of the UETCs. The density of strings is decreasing with the expansion of the Universe, such that scaling is preserved during the evolution of the simulation. The scaling behaviour of the simulations has been shown in detail in Ref. [101]. The simulations have an initial string resolution of 24 points per correlation length and have been evolved at fixed comoving resolution. The background cosmology for the evolution of the networks has been taken to be the ΛCDM, with WMAP 5-year best-fit parameters: $\Omega_c = 0.214$, $\Omega_b = 0.044$, $\Omega_\Lambda = 0.742$, $H_0 = 71.9$. These simulation have also been used in a different context in Ref. [102].

The three simulations cover the entire cosmological history of the Universe which is of interest when determining the CMB power spectrum. One can see that the network is initially very dense (Fig. 3.2) in each of the simulations, and Vachaspati-Vilenkin initial conditions are used.

Large loops are kept in the simulation and contribute to the total energy-momentum tensor of the network. In a physical context, small loops decay into gravitational radiation. Those that are smaller than the resolution of the simulation are not resolved and hence could be treated as point mass sources. Their effect on the overall string network is negligible in linear theory and therefore are neglected in practice because it accelerates the network simulation to remove very small nonintersecting loops. These tiny loops were also found to have a small effect in Refs. [103, 104]. By ignoring these small loops, we obtain a conservative bound on cosmic strings. An alternative simulation technique has been developed in Refs. [105, 106]

where the evolution of these small loops can be more efficiently continued during network evolution.

The string code outputs the cosmic string parameters for all the points from the string network at each time. Another code is used to read in all the parameters for all points at a particular time step, evaluate the local energy-momentum tensor using the real-space version of Eq. (3.14) and then interpolate it on a three dimensional grid of chosen size. The outcome of this is an energy-momentum tensor for the whole network at a specific time evaluated on a 3D grid. This is Fast Fourier Transformed, and it is then decomposed into scalar, vector, and tensor parts (SVT decomposition) in order to determine the components required [107].

The first code treats each time step separately. It reads the coordinates of each point and the data required to calculate the energy-momentum tensor at that particular place according to Eq. (3.14). This energy-momentum tensor is interpolated on a given grid, user-specified according to the resolution required, using a triangular cloud-in-cell interpolation method. This method interpolates each of the given points onto the 27 closest neighbours on the three-dimensional grid (weighted appropriately according to the distance to each point and ensuring energy conservation in this process), and the results are added up. Thus, the full stress-energy tensor is created on the grid at that particular time in real space. Then the full 3D matrix is converted to Fourier space using a Fast Fourier Transform routine. The new grid, now in Fourier space, is smoothed out by multiplying it with a Gaussian and then the energy-momentum tensor is split into scalar, vector, and tensor parts. For the scalar parts, we have chosen to output the Θ_{00} (energy density) and Θ^S (anisotropic scalar) components, but other choices can be made according to what one needs; for the vector parts, we have output two of the vector components and similarly for tensors.

3.3 Unequal-time correlator approach

Cosmic strings are active sources. This means that unlike primordial perturbations, which are seeded at the end of inflation, cosmic strings continuously seed perturbations throughout the history of the Universe [108]. The presence of cosmic strings modifies the usual energy-momentum tensor of the radiation and matter contents of the Universe, by adding a term corresponding to the cosmic strings. We consider uniform energy density and space curvature as initial conditions in the Einstein-Boltzmann equations (1.56)-(1.59) and (1.114)-(1.117). In this case, to first order in perturbation theory, by integrating the full Boltzmann equations with these initial conditions one we obtain directly the string multipoles $C_l^{\rm string}$, decoupled from the power spectrum of the other components of the Universe. This is due to the fact

that the active sources are uncorrelated with the primordial fluctuations and thus the total angular power spectrum can be expressed as

$$C_l = C_l^{\text{inflationary}} + C_l^{\text{string}} . \tag{3.35}$$

In the present case, we are only interested in calculating the power spectrum from the cosmic defects, as the inflationary power spectrum is already precisely determined (Ref. [17]).

To do the integration, there are two methods: (1a) ignore the full Boltzmann hierarchy and use Green's functions (e.g. Refs. [82, 109]) or (1b) use a first-order equivalent to Greens's functions and treat the full Boltzmann hierarchy (Ref. [107]); and (2) use UETCs. Indeed, Eqs. (1.56)-(1.59) are linear and their homogeneous part only depends on the magnitude of the wave vector, which makes it possible to use the UETC approach.

In general, to calculate the CMB power spectrum [110] from active sources, one has to solve an equation of the form

$$\mathscr{D}X = S_T , \tag{3.36}$$

where $\mathscr{D}$ is a differential operator and S_T is the active source. The power spectrum is then a quadratic quantity which has the general form

$$\left\langle X_i(\tau_0,\mathbf{k}) X_j^*\left(\tau_0,\mathbf{k}'\right)\right\rangle . \tag{3.37}$$

This can be expressed in terms of Green's functions G as follows:

$$\left\langle X_i(\tau_0,\mathbf{k}) X_j^*\left(\tau_0,\mathbf{k}'\right)\right\rangle = \int_{\tau_{in}}^{\tau_0} d\tau G_{im}(\tau,k) \int_{\tau_{in}}^{\tau_0} d\tau' G_{jn}^*\left(\tau',k'\right) \left\langle S_m(\tau,\mathbf{k}) S_n^*\left(\tau',\mathbf{k}'\right)\right\rangle \tag{3.38}$$

where τ_{in} is some initial time. Hence, to calculate the influence of strings on the CMB power spectrum, only the following quantity is needed: $\left\langle S_m(\tau,\mathbf{k}) S_n^*\left(\tau',\mathbf{k}'\right)\right\rangle$, which is called the UETC of the sources. In particular, the string energy-momentum tensor UETC can be written as

$$\langle \Theta_{\mu\nu}(\mathbf{k},\tau)\Theta_{\rho\sigma}(-\mathbf{k},\tau')\rangle = X_{\mu\nu,\rho\sigma}(k,\tau,\tau')\delta_D(0) . \tag{3.39}$$

Using scaling, one can re-express this correlation function as [109]

$$X_{\mu\nu,\rho\sigma}(k,\tau,\tau') = \frac{c_{\mu\nu,\rho\sigma}(k\tau,k\tau')}{\sqrt{\tau\tau'}} . \tag{3.40}$$

This new UETC matrix $c_{\mu\nu,\rho\sigma}(k\tau,k\tau')$ is obtained as the expectation value of a squared quantity and hence is positive definite [108]. It is thus diagonalisable and can be expressed in terms of its eigenvalues and eigenvectors [111, 112],

$$c_{\mu\nu,\rho\sigma}(k\tau,k\tau') = \sum_i \lambda_i \mathrm{v}^{(i)}_{\mu\nu}(k\tau)\mathrm{v}^{(i)T}_{\rho\sigma}(k\tau')\,, \tag{3.41}$$

where v_i are the a set of orthonormal eigenvectors of the matrix c.

The eigenmodes are coherent [111] and hence each of them can be fed individually into a Boltzmann equation solver yielding the angular power spectrum $C_l^{(i)}$ and then the total angular power spectrum can be expressed as

$$C_l^{\mathrm{string}} = \sum_i \lambda_i C_l^{(i)}\,. \tag{3.42}$$

As the unequal time correlators have been multiplied by $\sqrt{\tau\tau'}$, the source terms in the Boltzmann equation are substituted as

$$\Theta(k\tau) \to \frac{\mathrm{v}^{(i)}(k\tau)}{\sqrt{\tau}}\,. \tag{3.43}$$

To calculate the power spectrum of the cosmic strings, one has to modify the source of the energy-momentum tensor of the Einstein equations by adding the contribution from the strings as sources [107]:

$$T_{\mu\nu} \to T_{\mu\nu} + \Theta_{\mu\nu}\,. \tag{3.44}$$

The contribution to the total energy-momentum tensor due to the active sources is considered small compared to stress-energy tensor of the background and hence by considering the cosmic string sources as perturbations to the matter terms, the perturbations to Eqs. (1.52)-(1.54) are modified to

$$\delta T^0_0 = -\delta\rho + \Theta^0_0\,, \tag{3.45}$$

$$\delta T^0_i = (\rho + P)\,\mathrm{v}_i + \Theta^0_i\,, \tag{3.46}$$

$$\delta T^i_j = \delta P \delta^i_j + p\Sigma^i_j + \Theta^i_j\,. \tag{3.47}$$

Using the Einstein equation (1.1) and its conservation $\nabla^\nu G_{\mu\nu} = 0$, the equations for the perturbations (1.56)-(1.59), as well as the constraints (1.60)-(1.62) are modified to

accommodate the energy-momentum tensor of cosmic strings to:

$$h'' + \frac{a'}{a}h' = -8\pi G[a^2(\delta\rho + 3\delta p) + \Theta_{00} + \Theta], \tag{3.48}$$

$$k\bar{\eta}' = 4\pi G a^2 \sum_i (\rho_i + p_i)\,\mathrm{v}_i - \frac{4\pi G}{k}\Theta^D, \tag{3.49}$$

$$h^{S\prime\prime} + 2\frac{a'}{a}h^{S\prime} - 2k^2\eta = 16\pi G\left(a^2 p\Sigma^S + \Theta^S\right), \tag{3.50}$$

$$h_i^{V\prime\prime} + 2\frac{a'}{a}h_i^{V\prime} = 16\pi G\left(a^2 p\Sigma_i^{\mathrm{v}} + \Theta_i^{\mathrm{v}}\right), \tag{3.51}$$

$$h^{T\prime\prime} + 2\frac{a'}{a}h^{T\prime} + k^2 h^T = 16\pi G\left(a^2 p\Sigma^T + \Theta^T\right), \tag{3.52}$$

where $\bar{\eta} = \frac{h-h^S}{6}$ and an additional constraint equation for Θ^D is

$$\Theta^{D\prime} = \Theta^D\left(-2\frac{a'}{a} - \frac{k^2 a}{3a'}\right) - \frac{k^2}{3}\left(2\Theta^S - \Theta_{00} - \frac{a\Theta_{00}'}{a'}\right). \tag{3.53}$$

The metric variables used for the actual computation are taken to be $\bar{\eta}$, h^S, h^V and h^T and hence equations (3.49)-(3.52) have been implemented into a Boltzmann solver (CMBFAST), by modifying the relevant equations to accommodate the cosmic string sources. The energy-momentum tensor of the cosmic strings needed to be substituted with the relevant eigenvector, as described in Eq. (3.43).

For the scalar part of the power spectrum, one requires the components Θ_{00} and Θ^S. In this situation, it is not possible to diagonalise each of the UETC matrices corresponding to $\langle\Theta_{00}\Theta_{00}\rangle$ and $\langle\Theta^S\Theta^S\rangle$ separately because the cross-correlator $\langle\Theta_{00}\Theta^S\rangle$ is nonzero. One has to build the block matrix

$$\begin{pmatrix} \langle\Theta_{00}\Theta_{00}\rangle & \langle\Theta_{00}\Theta^S\rangle \\ \langle\Theta^S\Theta_{00}\rangle & \langle\Theta^S\Theta^S\rangle \end{pmatrix} \tag{3.54}$$

and to diagonalize it. The first half of each of the eigenvectors would correspond to Θ_{00}, and the second half would correspond to Θ^S. The eigenvalues are common to both.

In the case of vectors and tensors, the situation is different. The two vector modes Θ^{V1} and Θ^{V2} evolve independently, but their autocorrelators are the same,

$$\langle\Theta^V\Theta^V\rangle \equiv \langle\Theta^{V1}\Theta^{V1}\rangle = \langle\Theta^{V2}\Theta^{V2}\rangle \tag{3.55}$$

and their cross-correlators vanish $\langle\Theta^{V1}\Theta^{V2}\rangle = 0$, due to statistical isotropy [81]. The same is true for the two tensor modes. Furthermore, the mixed scalar/vector, scalar/tensor and

vector/tensor UETCs also vanish. We will discuss the results that we obtained using this method in Subchapter 3.6.

We have used the decomposition section of the Landriau and Shellard code [107] to calculate the energy-momentum components of the UETCs. The energy-momentum tensor of the string network has been interpolated on a 3D grid in Fourier space, and it has been decomposed into scalar, vector and tensor parts. The relevant UETCs described in the previous paragraphs were then calculated.

3.4 Evolution of the UETCs and resolution effects

The most important aspect when calculating the UETCs is to make sure that the resolution considered is high enough so that it can capture all the physical scales of relevance for sourcing the main CMB signal. A first step in order to achieve this was to analyse the energy density of the string network in real space at a given time for a range of grid resolutions. Boxes of 128^3, 256^3, 512^3, 768^3, 1024^3, and 1536^3, respectively, points have been chosen. In Fig. 3.3 the energy density of the string network for time 384 out of 1536 for the simulation in the radiation era has been plotted for these resolutions, for cubes of a quarter of the side of the simulation box.

For the lowest two resolutions considered, important information is smoothed out, and the strings do not have a threadlike appearance. As the resolution is increased, the strings become thinner as one would expect with better grid sampling. However, one cannot increase the resolution indefinitely because, after getting in the vicinity of the resolution of the simulation itself, the network would appear as made up of disconnected bulbs. The effect of resolution on a string network is especially apparent at earlier times (as shown in Fig. 3.3), when the string density is much higher. However, when one is interested in ray tracing through the simulation, e.g. to compute CMB maps [102], the difference in resolution does not affect the results at early times because of the very high string density but will cause the late-time features to have increasing levels of sharpness; however, as we shall now show, adequate resolution is critical for the accurate computation of UETCs.

Even though in recent years the computational capacity has radically increased, it is still challenging to go to very high resolutions in simulations. Increasing by a factor of 2 the linear grid resolution increases each file size by a factor of 8 and the time required by a similar amount. Due to these time and disk space considerations, we chose to use a grid size of 1024^3 for the simulations. The huge grid size limits, however, our possibility of using a very high time resolution as well, and for each of the simulations, we use around 100

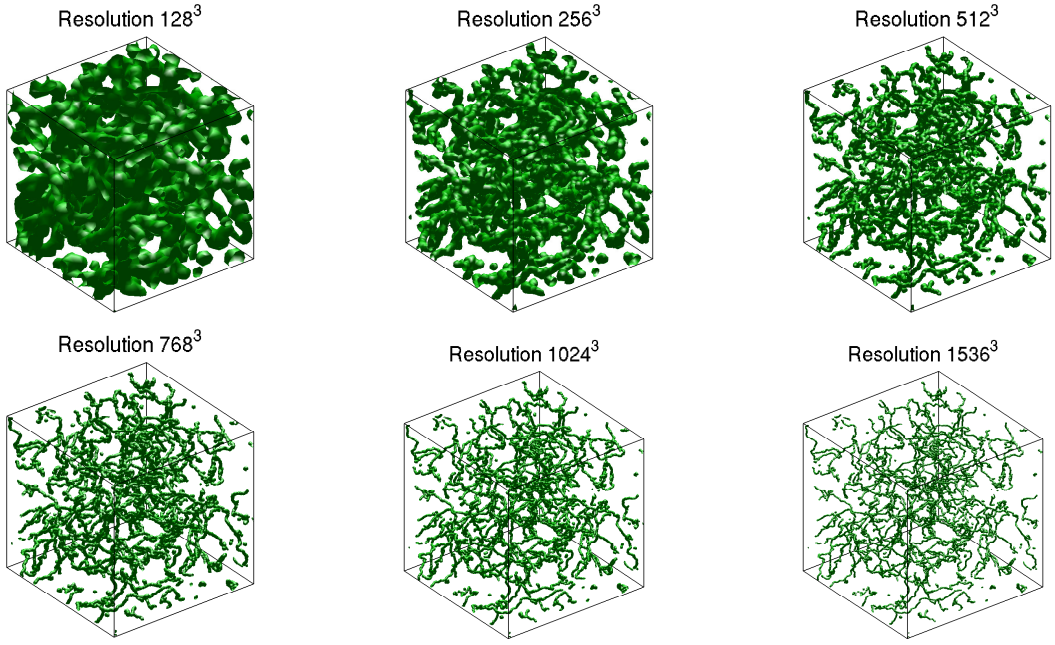

Fig. 3.3 Energy density component of the string network in real space evaluated at time 384 out of 1536 for the simulation in the radiation era for the six resolutions considered: 128^3, 256^3, 512^3, 768^3, 1024^3 and 1536^3 points.

time steps. We have checked that the time sampling does not modify the UETCs noticeably. To ensure the symmetry of the UETCs, we are using the same sampling for τ_1 and τ_2 for the computations. An alternative approach is being developed, which uses a lower spatial resolution but a greater time resolution. To obtain the full UETCs at a resolution of 1024^3, a total CPU time of approximately 20000 h is required using 200 Intel Xeon processors with a clock speed of 2.6GHz. We have performed all the calculations on the COSMOS supercomputer. Typical UETCs obtained at resolution of 1024^3 are plotted in Figs. 3.4 and 3.5 from the simulation covering the matter era.

At resolutions greater than or equal to 512^3, spurious peaks appear in the UETCs if the first 1% of the time steps of the simulation is considered. This is due to the appearance of loops over the length scale of the resolution size, *i.e.* excessive correlation in the Vachaspati-Vilenkin initial conditions. In Fig. 3.6, we have represented the initial appearance of the string network, both as a 3D view and a projection of the energy density to illustrate the correlation between the segments forming the string network. To get accurate predictions for the UETCs, the first time steps should be discarded, as they represent only the effect of the initial conditions and not of the physics involved.

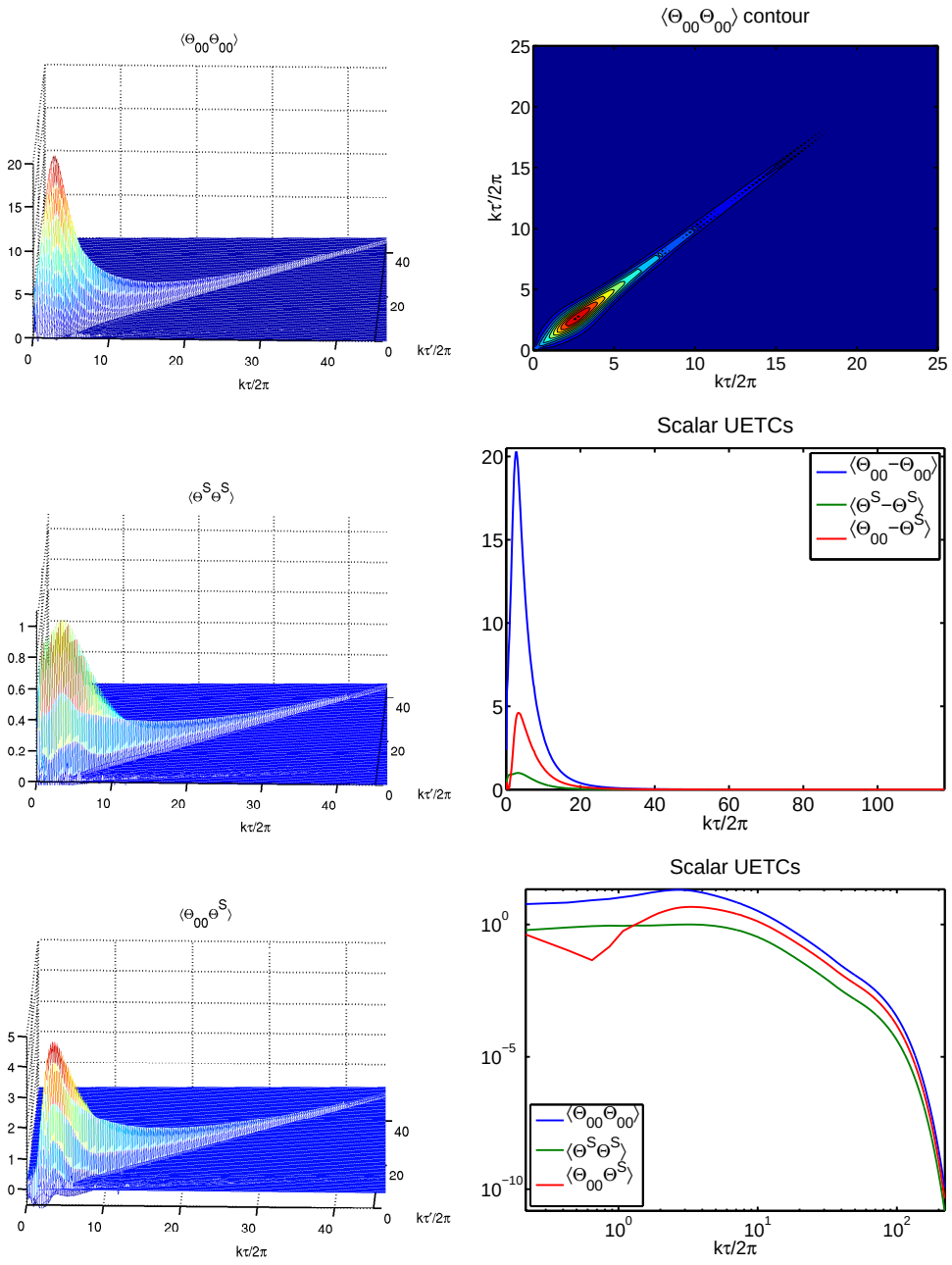

Fig. 3.4 Scalar UETCs obtained from a grid resolution of 1024^3: the figures of the left represent oblique 3D views of the three scalar UETCs ($\langle\Theta_{00}\Theta_{00}\rangle(k\tau,k\tau')$ - top, $\langle\Theta^S\Theta^S\rangle(k\tau,k\tau')$ - middle and $\langle\Theta_{00}\Theta^S\rangle(k\tau,k\tau')$ - bottom), the top right plot represents a contour plot of $\langle\Theta_{00}\Theta_{00}\rangle$ in linear scale and two bottom right plots represent the three scalar equal time correlators in linear and logarithmic scales.

Another important feature that needs to be checked is the scale invariance of the UETCs. This can be checked by verifying whether the shape of the UETC depends on which part of

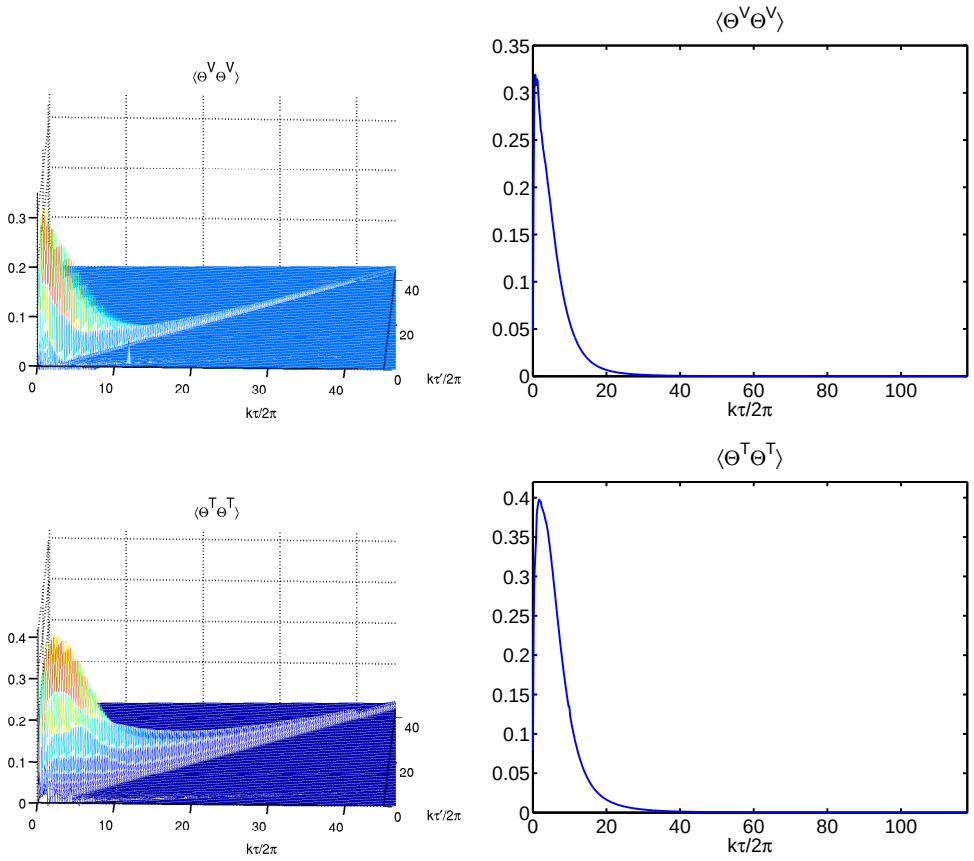

Fig. 3.5 Vector and tensor UETC components obtained from a grid resolution of 1024^3: oblique 3D views of $\langle \Theta^V \Theta^V \rangle(k\tau, k\tau')$ and $\langle \Theta^T \Theta^T \rangle(k\tau, k\tau')$ (left) and the corresponding equal time correlators (right).

the simulation is used (after discarding the initial conditions). The UETCs in Figs. 3.4-3.5 are scale-invariant. They are almost independent of the starting time of the simulation. We have illustrated this behaviour by plotting the $\langle \Theta_{00} \Theta_{00} \rangle$ UETC between three times (64, 140, and 220) and all times between 32 and 223 and 64 and 223 (Fig. 3.7). The plots have been zoomed in around the peak in order to show the scale invariance.

In the case of the 3D plot, the differences in terms of starting time are imperceptible, and hence only the one with the starting time 32 is represented. When correlating components of the energy-momentum tensor from early times with all the corresponding components from a certain time until the end of the simulation, there appears to be a small difference in the UETC corresponding to that starting point. If we choose, however, a later time to correlate with all the others, the difference becomes imperceptible. This is due to the fact that for earlier times there is more information in the string network due to the higher string

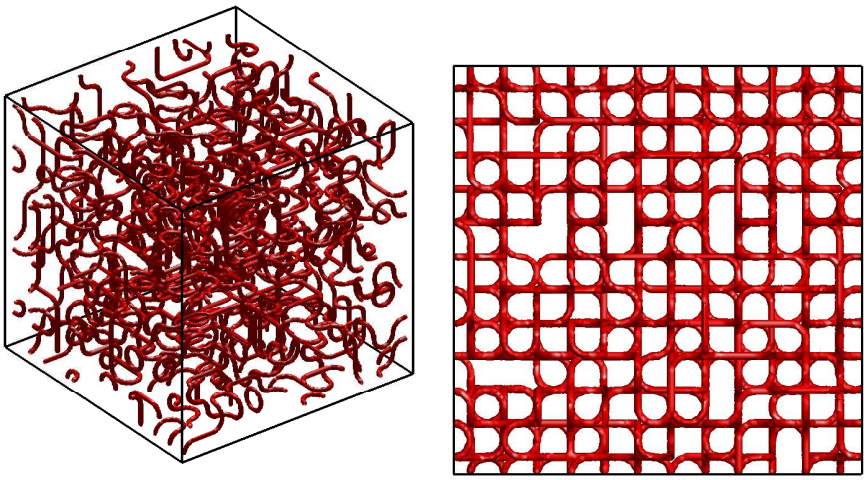

Fig. 3.6 Network correlation in the initial conditions from the simulation covering the matter era: left - oblique 3D view, right - front view.

density. The string network becomes less dense with the expansion of the Universe. This can be seen in the fact that the correlators in Fig. 3.7 have slightly lower amplitudes from top to bottom as the time used for correlations increases. Nevertheless, scale invariance is a good approximation just throughout each of the simulations; the string network is not scale-invariant throughout the history of the Universe, as the UETCs are not identical in the three simulations.

Resolution convergence

We have studied the convergence of both the shape and the amplitude of the UETCs in terms of the resolution of the grid. To illustrate this, we have chosen the simulation in the matter era. In Fig. 3.8, we have plotted the equal time correlator (diagonal component of the UETC) of the energy density for the various resolutions considered, from 128^3 until 1280^3. The peak is still increasing as the resolution is increased, but one can observe that relative differences from consecutive resolutions are getting smaller. However, technical constraints do not allow us yet to increase the resolution further and get the results in a reasonable amount of time. Currently the full simulation at a resolution of 1280 takes around 40000 CPU hours on Intel Xeon processors with a clock speed of 2.6GHz on the COSMOS supercomputer.

From Fig. 3.8 it can be seen that the two lowest resolutions do not give accurate results. This was expected since the string network is not properly resolved at this resolution (see Fig. 3.3). The behaviour of the other correlators that were calculated is similar and has not been

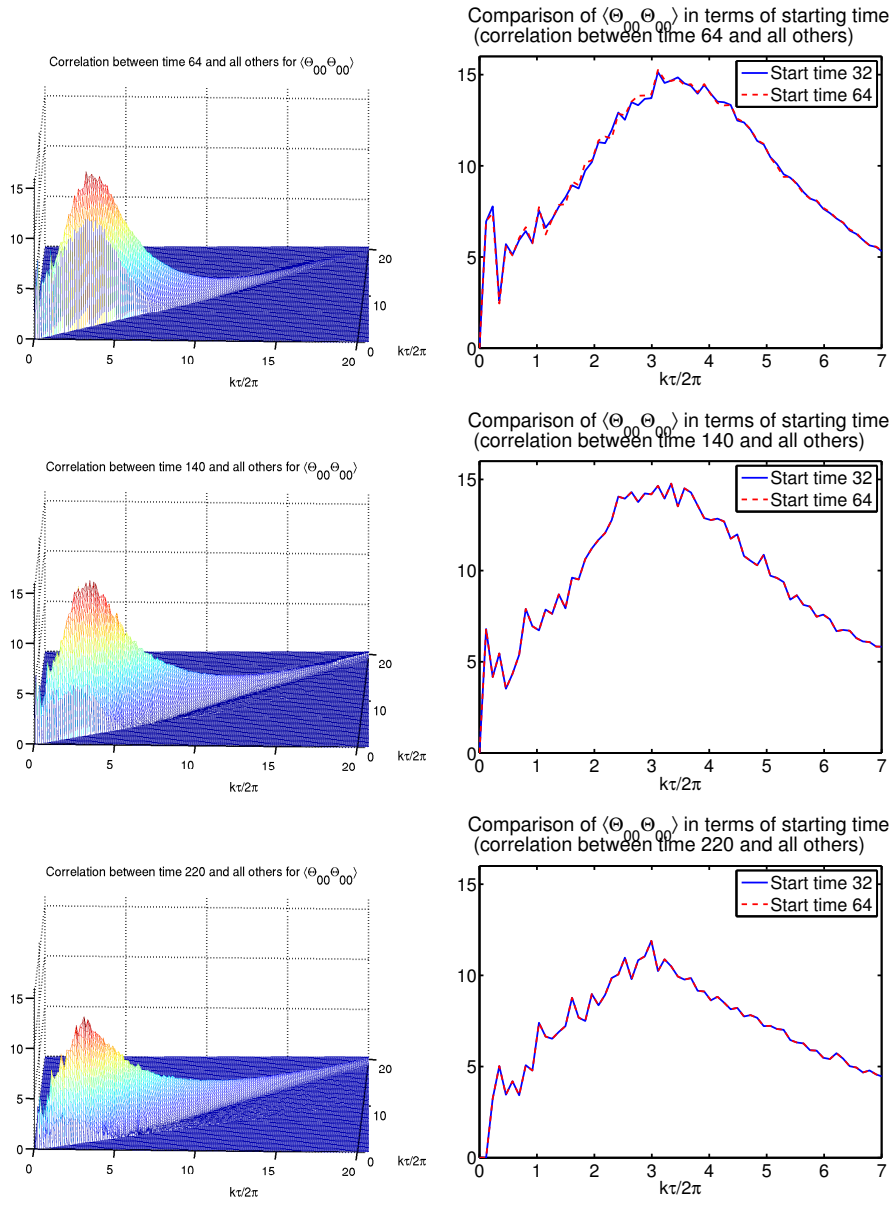

Fig. 3.7 $\langle\Theta_{00}\Theta_{00}\rangle$ UETCs calculated between one snapshot of the simulation and the whole simulation from different starting point, exhibiting scale invariance. In the bottom two rhs plots, the two plotted curves are indistinguishable. Scaling can be observed between the figures despite the correlation time used.

plotted. We have used the UETCs obtained at resolutions of 128^3, 256^3, 512^3, 768^3, 1024^3 and 1280^3 and we have determined the correlations between them in terms of the *shape* and *amplitude correlators* defined by the two formulae

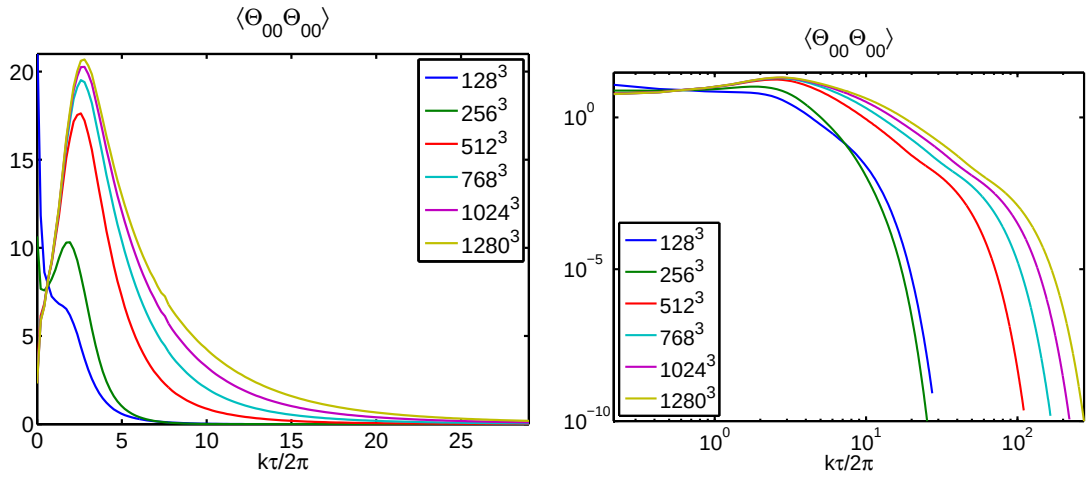

Fig. 3.8 $\langle\Theta_{00}\Theta_{00}\rangle$ equal time correlators at different resolutions.

$$s^{(c)}_{A,B} = \frac{\sum_i \sum_j U^A(i,j)U^B(i,j)}{\sqrt{\sum_{i,j}(U^A(i,j))^2}\sqrt{\sum_{i,j}(U^B(i,j))^2}}, \tag{3.56}$$

$$r^{(c)}_{A,B} = \frac{\sqrt{\sum_{i,j}(U^A(i,j))^2}}{\sqrt{\sum_{i,j}(U^B(i,j))^2}}, \tag{3.57}$$

where (c) is taken to be $\langle\Theta_{00}\Theta_{00}\rangle$, $\langle\Theta^S\Theta^S\rangle$, $\langle\Theta_{00}\Theta^S\rangle$, $\langle\Theta^V\Theta^V\rangle$, and $\langle\Theta^T\Theta^T\rangle$, respectively. These represent measures of the goodness of fit between the different simulations considered in terms of their shapes and amplitudes respectively. We have taken A to be the simulation at a resolution of 1280^3, and for B we took in turn each of the simulations from resolutions of 128^3, 256^3, 512^3, 768^3, and 1024^3 respectively. The results obtained are shown in Table 3.1, and the convergence trend is displayed in Fig. 3.9.

As the grid resolution is increased to 1280^3, Fig. 3.9 and Table 3.1 show very good convergence in both the shape and the amplitude for all the UETCs. The shape correlator is better than 99.6% for the 1024^3 resolution for all the correlators considered, while the difference in the amplitude correlators is better than 8%. The convergence at approximately 5% is limited by numerical constraints. However, from Fig. 3.8, one can see that, although we are approaching convergence with the correlators, this has not been yet achieved. Between $70 < k\tau < 80$, the energy density UETC decays by 2 to 3 orders of magnitude compared to $k\tau = \mathcal{O}(1)$ and hence it would make a comparatively small contribution to the power

Table 3.1 Shape and amplitude correlators of the UETCs at different simulation resolutions and the UETC at resolution 1280^3

UETC	Correlator	128^3	256^3	512^3	768^3	1024^3
$\langle\Theta_{00}\Theta_{00}\rangle$	Shape	0.6048	0.7783	0.9735	0.9939	0.9991
	Amplitude	3.0939	2.4376	1.2889	1.1123	1.0384
$\langle\Theta^S\Theta^S\rangle$	Shape	0.5628	0.6026	0.9192	0.9750	0.9952
	Amplitude	3.7040	2.6621	1.5079	1.2220	1.0831
$\langle\Theta_{00}\Theta^S\rangle$	Shape	0.6072	0.6377	0.949	0.9851	0.9971
	Amplitude	5.7650	4.1559	1.4993	1.1968	1.0696
$\langle\Theta^V\Theta^V\rangle$	Shape	0.6587	0.7381	0.9335	0.9795	0.9962
	Amplitude	2.4435	1.8765	1.3244	1.1524	1.0593
$\langle\Theta^T\Theta^T\rangle$	Shape	0.5632	0.6011	0.9180	0.9772	0.9961
	Amplitude	3.5414	2.8519	1.5209	1.2278	1.0833

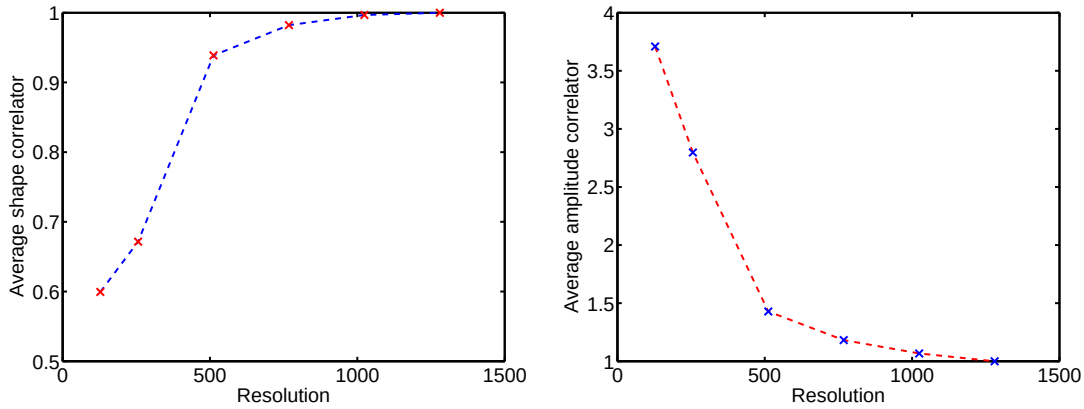

Fig. 3.9 Evolution of the averaged shape and amplitude correlators.

spectrum. For the region $k\tau < 70$, there is a definite sign that the graphs are approaching convergence, though it is not completely achieved.

3.5 Analytic UETC model

An analytic model for the calculation of UETCs based on the phenomenological USM model for Nambu-Goto strings has been developed in Ref. [97]. The correlation length can be expressed in terms of a new parameter ξ defined as $\xi = \frac{L}{a\tau}$.

Using Eqs. (3.28) and (3.29), as well as the SVT decomposition, the relevant UETCs are obtained analytically by integrating over the string network, separately for each stress-energy

component of interest:

$$\langle\Theta(k,\tau_1)\Theta(k,\tau_2)\rangle = \\ = \frac{2f(\tau_1,\tau_2,\xi,L_f)}{16\pi^3}\int_0^{2\pi}d\phi\int_0^{\pi}\sin\theta\,d\theta\int_0^{2\pi}d\psi\int_0^{2\pi}d\chi\,\Theta(k,\tau_1)\Theta(k,\tau_2)\ , \tag{3.58}$$

where the function f quantifies the decrease in the number of segments by string decay. The four angles of integration represent: ξ the orientation of one string segment with respect to the k_z axis, θ and ϕ the usual position angles in spherical polar coordinates and ψ the angle between the position vector and the velocity vector. The anisotropic scalar, vector and tensor components are given in this case by Eqs. (3.30)-(3.32). The UETCs that are computed are compared with simulations produced with the CMBACT code for different values of the parameters.

The final results have only three free parameters: v, α, and ξ. They can be obtained by integrating Eq. (3.58) and depend on integral expressions I_i,

$$\langle\Theta(k,\tau_1)\Theta(k,\tau_2)\rangle = \frac{f(\tau_1,\tau_2,\xi,L_f)\mu^2}{k^2\,(1-\mathrm{v}^2)}\sum_{i=1}^{6}A_i\left[I_i(x_-,\rho)-I_i(x_+,\rho)\right]\ , \tag{3.59}$$

where $\rho = k|\tau_1-\tau_2|\mathrm{v}$, $x_\pm = k\xi\,(\tau_1\pm\tau_2)/2$ and the expressions A_i depend again on the three parameters and can be found together with the expressions for I_i in the Appendix of Ref. [97].

Fit to the analytic model

To be able to compare the simulated UETCs with the analytical ones from Ref. [97], we have added the two vector and two tensor components and we have obtained the five functions used in Ref. [97]. The analytical model depends on three parameters, v, α, and ξ. The parameters have the following ranges: v varies between 0 and 1, α is in the interval [1, 2] and ξ is positive. We use again the *shape* [see Eq. (3.56)] and *amplitude correlators* [Eq. (3.57)], this time with A representing the analytical UETC and B representing the simulated one. The s's and r's have been tabulated for parameters in the permitted ranges and the values of the shape correlators have been maximised. The amplitude correlators have been chosen to be as close to one another as possible (due to different normalisation factors).

The best-fit parameters are as follows: $\xi = 0.2$ for the first two simulations and $\xi = 0.3$ for the third; while v is 0.5, 0.1, and 0.6, respectively; and α is 1.5, 1.3, and 1.3. The best results obtained for the three simulations for the shape and amplitude correlators are

presented in Table 3.2. We note that the mixed scalar correlator $\langle \Theta_{00}\Theta^S \rangle$ exhibits poor correlation between the UETCs calculated from the USM model and the simulated ones. This happens because the USM is unable to capture all the physical correlations between the strings, due to the oversimplified model. Hence the position of the peak of the USM UETC is both shifted and is too low with respect to the simulated one. We will show a comparison between these "best fit" power spectra and the ones that we have obtained using the eigenvectors in Subchapter 3.6.

Table 3.2 Shape and amplitude correlators for UETCs in the three simulations

Simulation	Correlator	$\langle \Theta_{00}\Theta_{00} \rangle$	$\langle \Theta^S\Theta^S \rangle$	$\langle \Theta_{00}\Theta^S \rangle$	$\langle \Theta^V\Theta^V \rangle$	$\langle \Theta^T\Theta^T \rangle$
Radiation era	Shape	0.710	0.841	0.188	0.815	0.738
	Amplitude	1.009	0.985	0.338	0.656	0.932
Matter era	Shape	0.667	0.801	0.132	0.744	0.663
	Amplitude	1.000	0.978	0.343	0.693	1.086
Matter + Λ eras	Shape	0.751	0.820	0.212	0.803	0.718
	Amplitude	0.998	1.094	0.365	0.746	0.928

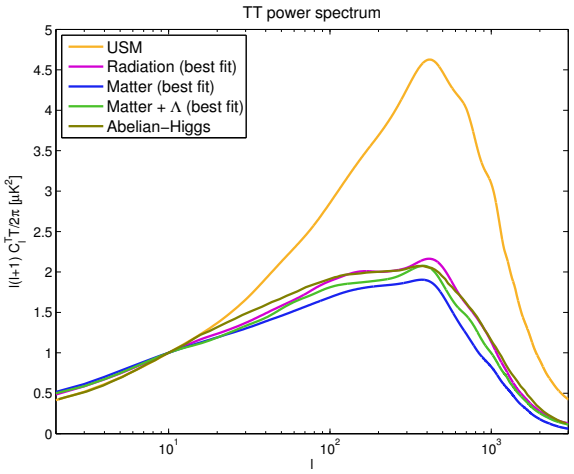

Fig. 3.10 Comparison between the TT power spectrum for USM , Abelian-Higgs and Nambu-Goto simulated strings. Simulation 1 covers the radiation era, Simulation 2 the matter era, and Simulation 3 matter and cosmological constant eras. The USM and Abelian-Higgs power spectra are the standard results used in the *Planck* cosmic defects paper [9]. All power spectra are normalised to $C_{10}^{\text{strings}} = 1$.

We have updated CMBACT with the *Planck* parameters [18] of the 2013 data release, and we have taken $G\mu = 2.07 \times 10^{-6}$, as in Ref. [97]. We then ran the code with 500 string

segments and 400 realisations with the parameters found for the best fit. We have obtained these values of the parameters by fixing the values of v, α, and ξ on all scales. Otherwise, the parameters are just initial conditions for the differential equations in the VOS model, and hence the results vary only weakly with them. The cosmological parameters chosen were the *Planck+WP+high L+BAO* parameters from the 2013 *Planck* results [17]. For comparison, we have also run the default CMBACT [99] with default initial parameters ($v = 0.65$, $\alpha = 1.9$, $\xi = 0.13$) with *Planck* cosmology. We have taken the Abelian-Higgs power spectrum data from Ref. [113], and we have plotted in Fig. 3.10 all three power spectra from simulations on the same graph in terms of the multipole l, in logarithmic scales, together with the USM and Abelian-Higgs ones.

The power spectrum for the Nambu-Goto strings, obtained from simulations, is situated between the power spectra of the USM and the Abelian-Higgs models. This was expected, as the USM model is unable to capture very accurately the entire small scale behaviour of the cosmic strings, while the Abelian-Higgs model does not have enough dynamic range. It can be seen that the position of the peak corresponds to approximately the same l in all cases and that the power spectrum in the three cases is very similar for $l < 30$. The matter era spectrum has a smaller peak amplitude and is straighter for large l. The CMB power spectra obtained from the simulations are very similar because of the fact that we are only using CMBACT with different parameters to obtain them. In the next subchapter we will describe the power spectrum obtained using UETCs directly.

3.6 Power spectrum obtained from eigendecomposition of UETCs

Using the formulae in Subchapter 3.3, we have run our code and we have computed the power spectra from the three simulations that span the whole cosmological time. The power spectra have been calculated first by using each of the individual simulations and extending their validity to the whole cosmological time by assuming scaling. For example, even though we have determined the UETCs using just cosmic strings that have evolved in the radiation era, we assume that the UETCs would be valid for all times. The matrices corresponding to them have been diagonalised, and their corresponding eigenvectors have been sorted in terms of the magnitude of their eigenvalues (from largest to lowest). We determined the power spectra from each of the eigenvectors and then we summed up the results. Although in principle all the eigenvectors have to be used in order to obtain an exact result, in practice

using Eq. (3.42) it can be noticed that for very small eigenvalues the contribution to the overall angular power spectra becomes insignificant. We have analysed this problem in detail and it turns out that for all four power spectra considered using roughly 200 eigenvectors gives a very good convergence for the power spectra. We have checked this in all our results. This is illustrated in Fig. 3.11 with the power spectra that we have obtained in the radiation era. The power spectra obtained from the scalar, vector and tensor components have been plotted on separate figures, and the convergence in terms of the number of eigenvectors used has been shown. In the case of the vectors, for the TT and TE power spectra we get excellent convergence using just 100 eigenvectors. For the EE and BB vector power spectra as for all tensor components we need 200 eigenvectors to get a very good convergence.

Later (see Fig. 3.13), we will show a comparison between the results that we have obtained by assuming scale invariance throughout the history of the Universe vs. scale invariance in each of the cosmological eras (radiation, matter, and Λ domination).

From the comparison of the results obtained from the simulations with the ones found by fitting the three parameters in CMBACT we notice that, unfortunately, the fits do not match the results from the simulations very well. The comparison between the simulations and the fits in the case of the temperature power spectrum is illustrated in Fig. 3.12. The standard USM and Abelian-Higgs power spectra are also plotted for comparison.

We used the three simulations separately, assuming their validity in the redshift range in which they were run, and we calculated the relevant C_l's in each case, and then we added the results up. We will show the methodology used for combining the results from the three simulations for calculating the total combined angular power spectrum in the following paragraph.

Combining the simulations

We consider the collisional Boltzmann equation for the brightness (1.105), derived in Subchapter 1.3 for the cosmic defects. In this case we have to analyse separately the scalar, vector and tensor equations of the brightness. We assume that the cosmic string energy-momentum tensor (in this case the corresponding eigenvector) is nonzero only in a conformal time interval $(\tau^{(A)}, \tau^{(B)})$. We will show that the time derivative of h^{α} tends to zero outside this interval. Equations. (3.49)-(3.52) are linear and their initial conditions are $h^{\alpha} = \dot{h}^{\alpha} = 0$ at $\tau = 0$, with α corresponding to the scalars, vectors, and tensors. Hence, $h^{\alpha}(\tau) = \dot{h}^{\alpha}(\tau) = 0$ for $\tau < \tau^{(A)}$. For $\tau > \tau^{(B)}$, there is no longer any source present, and hence $h^{(\alpha)}$ would at most remain constant while its time derivative would quickly decay. Hence, $\Delta = 0$ in the absence of cosmic strings (due to the suitable initial conditions). We denote $S = S(\dot{h}^{\alpha})$ be

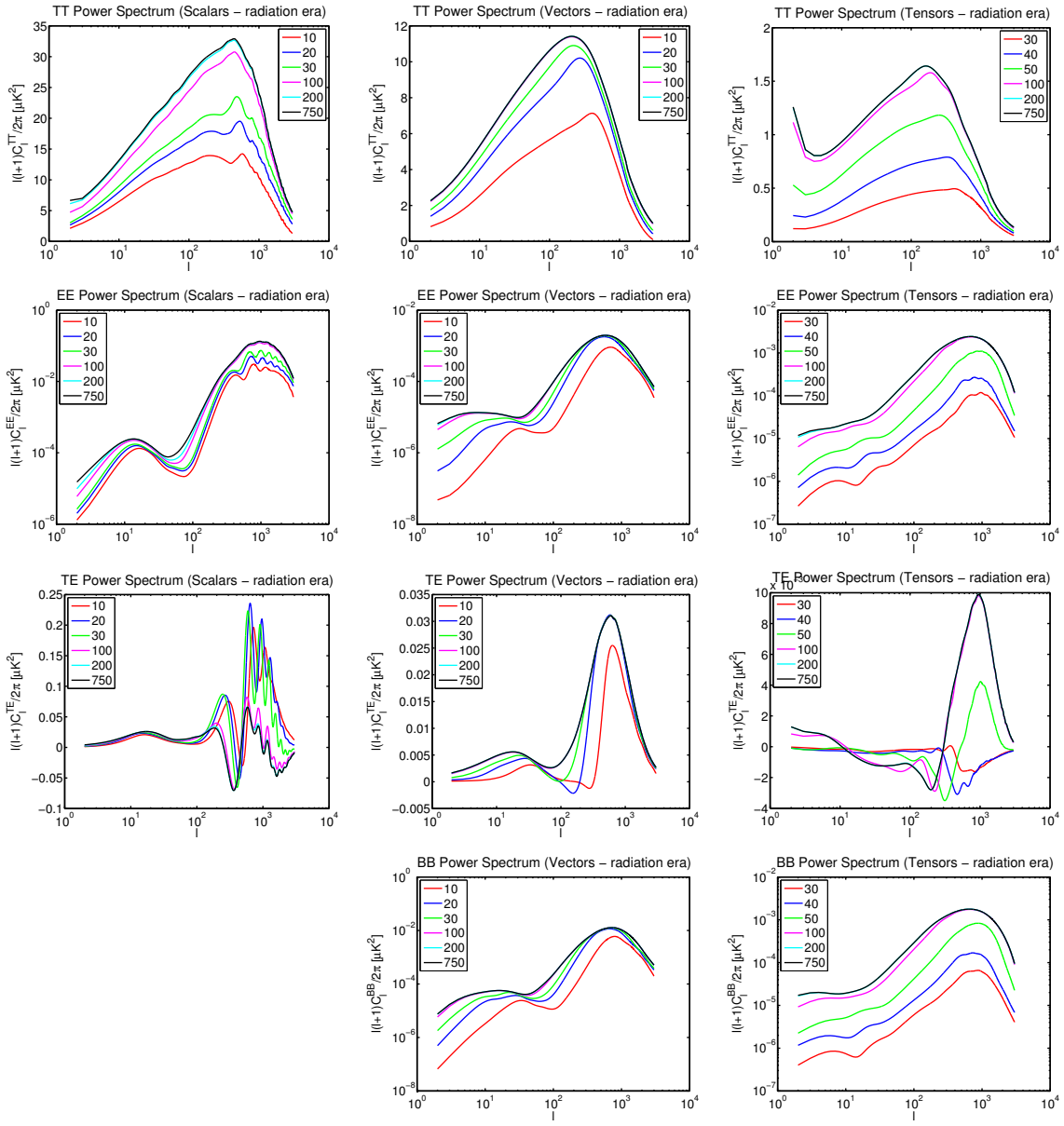

Fig. 3.11 Power spectra of the cosmic strings obtained from the simulations in the radiation era assuming scale invariance. From left to right: scalar, vector, and tensor power spectra; from top to bottom: TT, EE, TE, and BB power spectra ($G\mu = 1.5 \times 10^{-7}$). The numbers in the legend represent the number of eigenvectors used. The colours in the tensor spectra plots represent different numbers of eigenvectors used compared to the scalar and vector spectra.

the source function due to strings in each of the cases above and we consider the moments of the Boltzmann equation (1.110) and we use the integral identities involving the Legendre polynomials and the spherical Bessel functions:

$$\int_{-1}^{1} P_m(x)P_n(x)dx = \frac{2}{2n+1}\delta_{mn} \tag{3.60}$$

$$\frac{i^l}{2}\int_{-1}^{1} P_l(\mu)e^{ik\mu(\tau-\tau_0)}d\mu = j_l(k(\tau_0-\tau)) \tag{3.61}$$

to obtain

$$\Delta_l(\mathbf{k},\tau_0) = \int_0^{\tau_0} d\tau S(\mathbf{k},\tau) j_l(k(\tau_0-\tau))\,. \tag{3.62}$$

The angular power spectrum for this source term can be expressed as in Eq. (1.123).

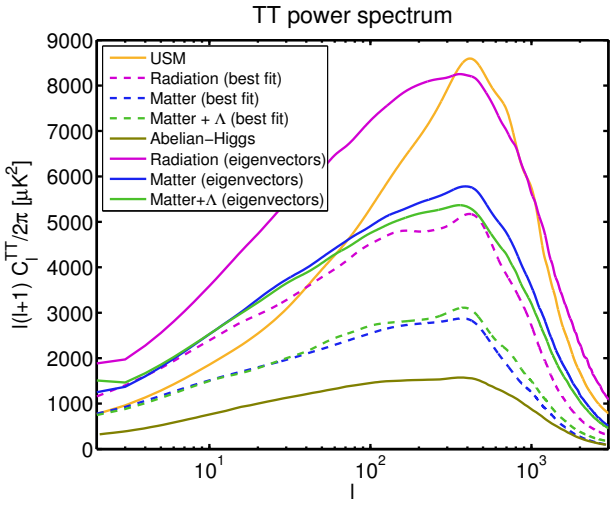

Fig. 3.12 Comparison between the TT power spectra obtained through the best fit method and using eigenvectors ($G\mu = 2.07\times10^{-6}$).

Each of the simulations considered is valid in a different time range. In the previous subchapter we have extended the validity of the simulations by assuming scaling. However, scaling is not perfect throughout the history of Universe, as can be seen from the power spectra that we have obtained by making this assumption (Fig. 3.13). If scaling were perfect, the power spectra from the three simulations would have to be identical. We express the energy-momentum tensor in the three epochs considered as follows:

$$\Theta(k,\tau) \to \begin{cases} \frac{v_{\text{radiation}}(k\tau)}{\sqrt{\tau}} & \text{if } \tau \in \text{radiation era} \\ \frac{v_{\text{matter}}(k\tau)}{\sqrt{\tau}} & \text{if } \tau \in \text{matter era} \\ \frac{v_{\text{matter+}\Lambda}(k\tau)}{\sqrt{\tau}} & \text{if } \tau \in \Lambda \text{ era} \end{cases} . \tag{3.63}$$

Equation (1.105) is a differential equation which is linear in the cosmic string sources and hence Eq. (3.62) has the same property for all values of l. This shows that splitting the sources into three parts, computing the moments Δ_l separately, and then summing up the results would not change the integral. We will now consider that the string sources only act in the time interval where they are defined and we will split the calculation into three parts, corresponding to each of the epochs. For example, for the radiation era, we shall take the energy momentum-tensor from Eq. (3.63) as

$$\Theta(k,\tau) \to \begin{cases} \frac{\mathrm{v}_{\mathrm{radiation}}(k\tau)}{\sqrt{\tau}} & \text{if } \tau \in \text{radiation era} \\ 0 & \text{if } \tau \notin \text{radiation era} \end{cases} . \tag{3.64}$$

In the general case, an arbitrary source S from Eq. (3.62) can be written in terms of its constituents as

$$S(k,\tau) = \sum S_i(k,\tau)\,, \tag{3.65}$$

where each of the $S_i's$ is defined on an interval $(\tau_i^{(A)}, \tau_i^{(B)})$. These intervals are disjoint. This is possible because the differential involved for Δ_l and h are linear. However, in the expression for C_l there is a square of Δ_l. So we can re-express Eq. (1.123) as

$$C_l = \sum_i C_l^i + \frac{4}{\pi}\sum_{i<j}\int_0^\infty dk k^2 \int_0^{\tau_0} d\tau_1 \int_0^{\tau_0} d\tau_2 S_i(k,\tau_1) S_j(k,\tau_2)\, j_l(k(\tau_0-\tau_1))\, j_l(k(\tau_0-\tau_2))\,, \tag{3.66}$$

where C_l^i represents the contribution to the angular power spectrum obtained only from source i (e.g. only radiation era). We will now show that the last sum of integrals from Eq. (3.66) is negligible compared to each of the terms in the first sum. We note that the sources S oscillate much less in k compared to the Bessel functions and hence, after changing the order of integration, a typical integral term from this sum can be written as

$$\begin{aligned} &\int_0^{\tau_0} d\tau_1 \int_0^{\tau_0} d\tau_2 S_i(k,\tau_1) S_j(k,\tau_2) \int_0^\infty dk k^2\, j_l(k(\tau_0-\tau_1))\, j_l(k(\tau_0-\tau_2)) \\ \sim &\int_0^{\tau_0} d\tau_1 \int_0^{\tau_0} d\tau_2 S_i(k,\tau_1) S_j(k,\tau_2)\delta(\tau_2-\tau_1) = \int_0^{\tau_0} d\tau_1\; S_i(k,\tau_1) S_j(k,\tau_1) \end{aligned} \tag{3.67}$$

by using the properties of the spherical Bessel functions. We now assume $i<j$ and we take into account that the cosmic strings only source the perturbation equations in the intervals $(\tau_i^{(A)}, \tau_i^{(B)})$ and $(\tau_j^{(A)}, \tau_j^{(B)})$. The contribution from the first source will only start at $\tau_i^{(A)}$ and end at $\tau_i^{(B)}$. Hence, S_1 will be zero before $\tau_i^{(A)}$ and start decaying after $\tau_i^{(B)}$. The decay of the sources after there are no strings is exponential in time. A similar behaviour is expected

from the second cosmic string region. Hence, the integral (3.67) will only have a nonzero contribution in the region where the contribution of the first source has not completely decayed and the second source has an increasing contribution. As this contribution is suppressed due to the time decay of the sources S_i, this last integral will give a very small contribution and we will neglect it.

The results that we obtained show that, in the TT spectrum, the cosmological constant era contributes at $l < 100$ with a peak at $l = 30$, the matter era contributes in the range $50 < l < 400$, and the radiation simulation for $l > 200$, as expected. The total power spectrum converges to the matter and Λ era result for low l and the radiation era one at high l. The final results resemble most the extrapolated matter era simulation, in agreement with the results reported in Ref. [110]. The other three spectra (TE, EE, and BB) exhibit a similar behaviour but the signal is dominated by the one from the radiation era. The individual results are shown in Fig. 3.13. We have used 200 eigenvectors for each of the lines in the plots.

In Fig. 3.14 we show the final TT power spectrum obtained from the three Nambu-Goto simulations (combined), together with the USM and Abelian-Higgs ones. In addition, we also plot the results obtained with the fourth version of the code CMBACT [99], in which the author has corrected various bugs but also updated the VOS model. This new version gives a lower amplitude for the temperature power spectrum and its overall shape resembles more the Abelian-Higgs one. Using our simulations, we obtain an even lower amplitude for the power spectrum. The peak remains at roughly the same position as in the USM case. The shape of our TT power spectrum is more similar in terms of amplitude to the USM result, but its shape resembles more the Abelian-Higgs spectrum.

3.7 String tension constraints

3.7.1 Background on methods

In this subchapter we discuss the implications of the presence of the cosmic strings on the CMB, at the level of the power spectrum. In the previous subchapter we have calculated the power spectrum induced by the cosmic strings on their own, but we are also interested in the way the other parameters describing the Universe may be modified by the presence of cosmic strings. The most straightforward way is to consider the standard 6-parameter ΛCDM model, together with a parameter quantifying the presence of cosmic strings. In addition to this very simple scenario, in this subchapter we consider the degeneracies that can be induced be

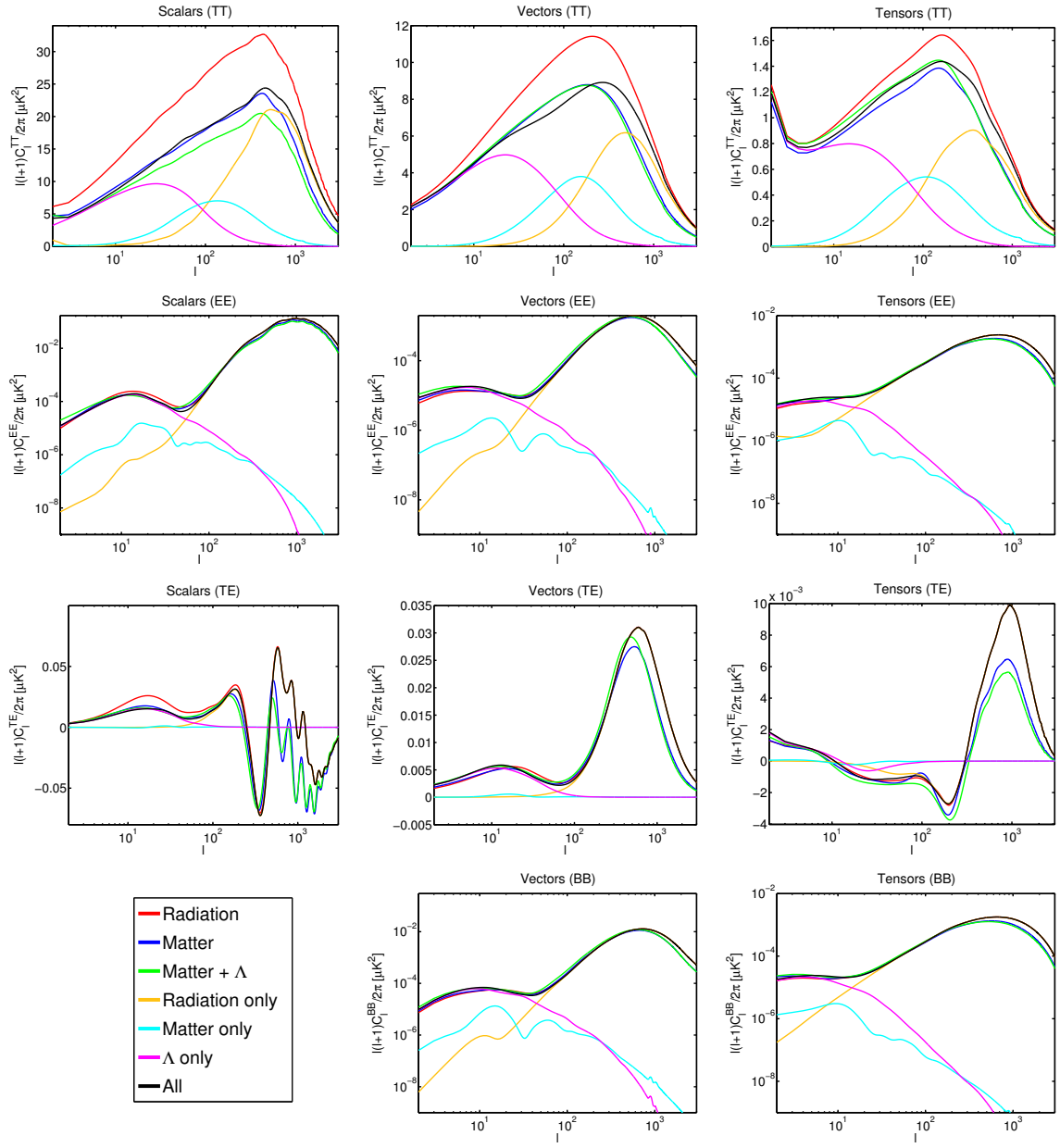

Fig. 3.13 Power spectra of the cosmic strings obtained by using each of the three sets of UETCs and assuming scaling for the whole history of the Universe. The red, green, and blue show the power spectra considering the extrapolation of the results obtained in the radiation, matter, and matter + Λ epochs. The contributions from the UETCs from just the time interval where they are valid are plotted in the yellow, cyan, and magenta curves, and their sum is in black. The black curve represents the final overall power spectrum obtained. From left to right: The scalar, vector, and tensor power spectra; from top to bottom the TT, EE, TE, and BB power spectra ($G\mu = 1.5 \times 10^{-7}$).

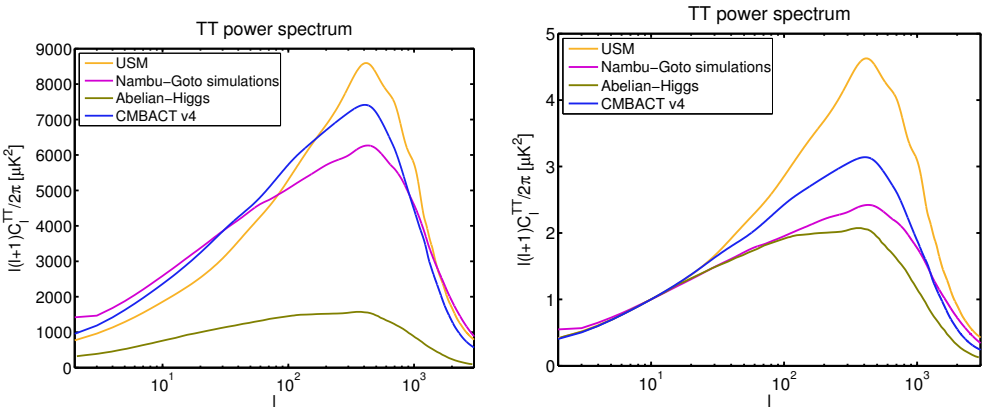

Fig. 3.14 Comparison between the TT power spectra obtained using the three simulations and the USM, Abelian-Higgs (standard results) and CMBACT version 4. In the left plot, the string tension is $G\mu = 2.07 \times 10^{-6}$, showing that the USM and the Nambu-Goto strings have different amplitudes compared to the Abelian-Higgs ones; in the right plot, amplitudes are normalised to $C_{10}^{\text{strings}} = 1$, emphasising the similar shapes of the power spectra considered.

considering various non-minimal cosmological parameters, such as tensor modes, running of the spectral index, increasing the number of effective degrees of freedom and adding a massive sterile neutrino. Part of this detailed analysis has been motivated by the claims of the BICEP2 Collaboration of the discovery of tensor modes [66]. To constrain the power spectrum contribution from the Nambu-Goto string simulations, we have used a Markov chain Monte Carlo method, using a modified version of the COSMOMC code [114, 115]. This method involves evaluating the power spectrum each time the parameters are modified, by calling an instance of the code CAMB [32]. The total power spectrum is obtained from the sum between the inflationary spectrum and the one obtained from cosmic strings because the cosmic string sources, which are active sources, are uncorrelated with the primordial perturbations [116]. This would in principle require the calculation of the cosmic string power spectrum many thousands of times, for each choice of cosmological parameters, which is not feasible because calculating the cosmic string power spectrum by itself requires several hours of computational work. Fortunately it has been suggested [80, 95] that it evolves much slower as a function of the parameters compared to its inflationary counterpart. In Ref. [117] it has been explicitly shown that by varying the cosmological constant, the string tension allowed by the data $G\mu/c^2$ changes with less than 10%. The cosmic strings are expected to contribute less than 5% in the total power spectrum, so as the cosmological parameters are varied in the allowed regions, the string power spectrum does not vary more than 20% [118, 119]. This gives overall better than 1% accuracy for the contribution of cosmic strings. Hence we have

calculated the cosmic string power spectrum for a particular set of cosmological parameters and we only allow the overall string contribution to vary, through the parameter f_{10}, which represents the fractional power of the cosmic strings compared to the inflationary power at the tenth multipole [9, 59],

$$f_{10} = \frac{C_{10}^{\text{string}}}{C_{10}^{\text{total}}} \,. \tag{3.68}$$

We also use the relation $f_{10} \propto (G\mu)^2$ to relate the new parameter to the string tension [120]. For this analysis, we have used the March 2014 version of the COSMOMC code. In the next subchapter, after a short introduction to the BICEP2 experiment, we analyse the degeneracies and the constraints on the cosmic string tension as well as on other cosmological parameters in two scenarios: by considering only the *Planck* likelihood (with WMAP polarisation) and adding the BICEP2 results as well.

In order to asses the likelihoods of each of the cosmological parameters considered in a model, the marginalised distributions are usually determined, where the full N-dimensional parameter space is projected onto the one-dimensional space of the parameter of interest – this can be obtained approximately from the number of samples in each parameter bin. By applying the projection, the information about the shape of the distribution in the marginalised directions is lost, and in particular whether the distribution is Gaussian or not. To check this, one can plot the mean likelihood of the samples at each value of the parameter. If the distribution is Gaussian, then the marginalised distributions and the mean likelihoods would be identical. If the two quantities are significantly different, then either the likelihood distribution is non-Gaussian or prior volume effects are important [115].

3.7.2 BICEP2 experiment

The BICEP2 announcement of the discovery of the B-mode polarisation [66] has created a huge interest in the cosmology community. This is because this discovery potentially opens a new window on the Universe, especially if the signal has a primordial origin. Such a signal cannot be explained by the standard ΛCDM cosmology, thus requiring additional parameters.

One of the simplest additions to the minimal ΛCDM is primordial tensor modes generated by inflation at a high energy scale. The BICEP2 Collaboration estimates a tensor-to-scalar ratio around $r = 0.20$ ($r = 0.16$ after foreground subtraction), but the results are in tension with the standard ΛCDM model which is also used in *Planck* papers [17]. This could suggest that additional degrees of freedom are required in order to relieve this tension [66], possibly by allowing for a scale-dependent spectral index, the running of the spectral index

($n_{run} = dn_s/dlnk$). Many different cosmological scenarios have been proposed to relieve this tension: the curvature of the Universe [121], the number of effective degrees of freedom, the sum of the neutrino masses, the Helium abundance and a sterile neutrino mass [122], running of the spectral index and dust [123].

A different type of solution to explain the *B*-mode polarisation is a signal from topological defects. Defects generate both vector and tensor modes in the *B* channel [99, 116, 124] and hence they are a natural candidate for reconciling the tension between the datasets. Many inflationary models involve a phase transition in the early Universe where cosmic strings can be formed naturally [40, 125]. Both the groups working on strings generated through the phenomenological unconnected segment model (USM) [80, 95, 97, 99] and the Abelian-Higgs cosmic strings [81, 118, 123] have analysed the possibility of using cosmic strings to explain the polarisation signal form the BICEP2 probe [64, 65]. These authors have evaluated the implications of the presence of cosmic strings and have concluded that they cannot alone explain the whole signal in the *B*-mode polarisation, though they could make some contribution.

After a lengthy debate about the origin of the signal detected by the BICEP2 Collaboration, a joined analysis with the *Planck* Collaboration has shown that all of the BICEP signal could be produced by dust and there is no strong evidence for any primordial *B*-mode polarization. [126].

3.7.3 Results for the *Planck* likelihood

In this simplest case, we have added the cosmic string coefficient f_{10} to the six ΛCDM parameters, together with the various nuisance parameters, thus performing a full likelihood calculation. We have found the constraints: $G\mu < 1.49 \times 10^{-7}$ and $f_{10} < 0.0193$ at 95% confidence level, which are comparable with the results obtained by the *Planck* Collaboration [9]. The improvement in the fit after including cosmic strings is small. There are few degeneracies with cosmic strings, and ΛCDM parameters change very little after the introduction of cosmic strings. In Figure 3.15 we plot the marginalised likelihoods in the $f_{10} - \Omega_b h^2$, $f_{10} - H_0$ and $f_{10} - n_s$ planes. Here, the two-dimensional plot is similar to Figure 10 of Ref. [9]. The constraint that we have obtained is very close to the *Planck* one ($G\mu/c^2 < 1.5 \times 10^{-7}$) [9]. We have validated our formalism by obtaining the constraint for the unconnected segment model power spectrum. Therefore, we have concluded that this is due to the fact that our power spectrum has a different shape and more power at low multipoles.

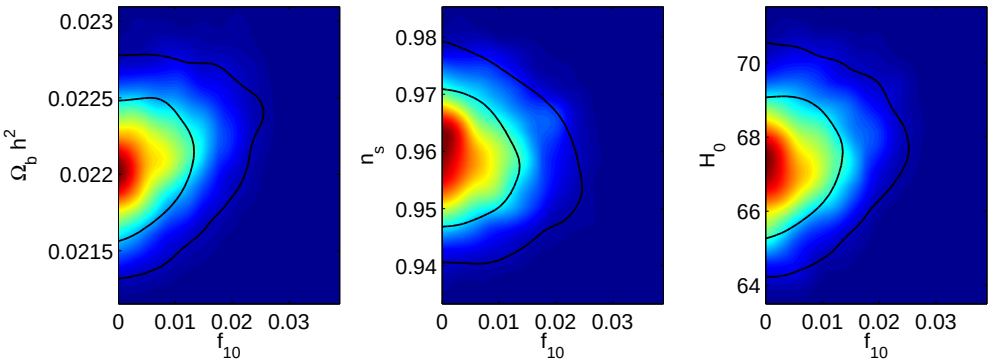

Fig. 3.15 Marginalised likelihoods in the *Planck* + WP & strings model.

In order to show the way the constraints on the parameters change due to the presence of cosmic strings, we have performed the same likelihood calculation without the defects. The comparison between the two scenarios is shown in Table 3.3.

Table 3.3 Constraints on the fitted cosmological parameters, together with 1σ error bars in a full likelihood analysis (with all relevant nuisance parameters) with and without cosmic strings in the case of *Planck* and WMAP polarisation

	Planck + WP	
Parameter	No strings	Strings
$G\mu/c^2$ (95% upper limit)	-	1.49×10^{-7}
$G\mu/c^2$ (best fit)	-	4.99×10^{-8}
H_0	67.20 ± 1.16	67.42 ± 1.20
$100\Omega_b h^2$	2.202 ± 0.027	2.209 ± 0.029
$\Omega_c h^2$	0.120 ± 0.003	0.119 ± 0.003
τ	0.089 ± 0.013	0.087 ± 0.013
$100\theta_{MC}$	1.0412 ± 0.0006	1.0412 ± 0.0006
$ln(10^{10}A_s)$	3.088 ± 0.025	3.078 ± 0.026
n_s	0.959 ± 0.007	0.958 ± 0.007

The constraint on $G\mu/c^2$ in this standard scenario is slightly weaker compared to the one expected from the USM model but tighter compared to that from the Abelian-Higgs model.

Apart from this simple scenario we have also considered adding different non-minimal parameters to the model and we have looked at the degeneracies that appeared. The parameters we have considered adding are the following:

- r, which is the tensor-to-scalar ratio evaluated at $k = 0.002$ Mpc^{-1}. This also enforces the relation $n_t = -r/8$ for the tensor spectral index n_t;
- *running* of the spectral index;
- $N_{\rm eff}$, the effective number of neutrino-like relativistic degrees of freedom. The minimal case corresponds to $N_{\rm eff}$=3.046 and the additional degrees of freedom are quantised by the parameter $\Delta N_{\rm eff} = N_{\rm eff} - 3.046$;
- $m^{\rm eff}_{\nu,{\rm sterile}}$, the mass of a *sterile neutrino*. The sterile neutrinos are motivated by the discovery of neutrino oscillations (e.g. Ref. [127]).

The most interesting results that we have obtained are shown in Tables 3.4-3.5.

We have observed that $N_{\rm eff}$ is in most cases very degenerate with cosmic strings and hence it allows it to attain huge values. For example, looking just at the second row of Table 3.4, we observe that the preferred values for $N_{\rm eff}$ increase after adding cosmic strings, to $\Delta N_{\rm eff} > 1$. The error bar also increases, suggesting the fact that there is a degeneracy appearing after adding the parameter f_{10}. The error bar also increases considerably on the baryon contribution, H_0 and n_s. The value of the Hubble constant is increased massively from the ΛCDM result. We have explored ways in order to fix this, by adding additional likelihoods. We first added SPT/ACT (HighL), which didn't change the values of the parameters much and didn't reduce the error bars either. Adding in addition BAO reduced the error bars and shifted the values of the parameters back to the values prior to the introduction of cosmic strings and $N_{\rm eff}$. This however reduced the allowed contribution from cosmic strings as well.

In terms of the degeneracies that appear, the most interesting case is the one with $N_{\rm eff}$ and tensor modes. In this case the data suggest as a best fit $r = 0.12 \pm 0.09$, so it is non-zero at 1σ level. The Hubble constant is increased as well to $H_0 = 80.59 \pm 6.57$. This is in fact due to the degeneracies introduced by cosmic strings, which are illustrated in Figure 3.16. The allowed value of the string tension is quite large as well, $G\mu/c^2 < 2.49 \times 10^{-7}$. This degeneracies disappear however after adding BAO, reducing the cosmic string contribution to $G\mu/c^2 < 1.69 \times 10^{-7}$ at 95% confidence level.

The same situation is true when adding other parameters such as running parameter in addition to $N_{\rm eff}$ and strings. This also allows the contribution from cosmic strings to increase, up to $G\mu/c^2 = 2.49 \times 10^{-7}$ in the $N_{\rm eff}$ & r option. The results with just $N_{\rm eff}$ added (and no strings) can be restored by adding HighL and BAO data. In this case, from the one-dimensional likelihood plots we see that the cosmic strings contribution is reduced, but a non-zero value is favoured (Figure 3.17). The values of the cosmological parameters which

Table 3.4 Values of the cosmological parameters when considering only the *Planck* likelihoods with 1σ error bars, obtained by considering a full likelihood analysis (all cases also include the *Planck* nuisance parameters)

Parameter	strings, n_{run}	strings, r, $N_{\rm eff}$	$N_{\rm eff}$ (*Planck*)
$G\mu/c^2$ (95% upper limit)	1.88×10^{-7}	2.49×10^{-7}	-
$G\mu/c^2$ (best fit)	8.23×10^{-8}	1.09×10^{-8}	-
n_{run}	-0.020 ± 0.010	-	-
r	-	0.12 ± 0.09	-
$\Delta N_{\rm eff}$	-	1.574 ± 0.748	0.563 ± 0.316
H_0	67.46 ± 1.22	80.59 ± 6.57	71.34 ± 2.66
$100\Omega_b h^2$	2.237 ± 0.034	2.354 ± 0.077	2.243 ± 0.037
$\Omega_c h^2$	0.120 ± 0.003	0.135 ± 0.008	0.127 ± 0.0047
τ	0.098 ± 0.016	0.100 ± 0.016	0.095 ± 0.015
$100\theta_{MC}$	1.0413 ± 0.0007	1.0402 ± 0.0007	1.0405 ± 0.0007
$ln(10^{10}A_s)$	3.101 ± 0.032	3.123 ± 0.033	3.117 ± 0.031
n_s	0.952 ± 0.008	1.017 ± 0.027	0.980 ± 0.014
$-ln\mathscr{L}$	4902.0	4902.5	4902.0

Parameter	strings, $N_{\rm eff}$ (*Planck*)	strings, $N_{\rm eff}$ (*Planck* + HighL)	strings, $N_{\rm eff}$ (*Planck* + HighL + BAO)
$G\mu/c^2$ (95% upper limit)	2.28×10^{-7}	1.80×10^{-7}	1.58×10^{-7}
$G\mu/c^2$ (best fit)	7.35×10^{-8}	1.77×10^{-7}	1.34×10^{-7}
$\Delta N_{\rm eff}$	1.072 ± 0.564	1.186 ± 0.528	0.658 ± 0.304
H_0	75.96 ± 4.84	76.46 ± 4.45	71.51 ± 1.95
$100\Omega_b h^2$	2.305 ± 0.062	2.302 ± 0.054	2.243 ± 0.030
$\Omega_c h^2$	0.132 ± 0.006	0.134 ± 0.07	0.129 ± 0.05
τ	0.098 ± 0.015	0.097 ± 0.015	0.090 ± 0.013
$100\theta_{MC}$	1.0404 ± 0.0007	1.0402 ± 0.0007	1.0404 ± 0.0007
$ln(10^{10}A_s)$	3.117 ± 0.034	3.121 ± 0.033	3.104 ± 0.029
n_s	0.996 ± 0.020	0.997 ± 0.019	0.976 ± 0.010
$-ln\mathscr{L}$	4902.6	5255.3	5256.1

Parameter	n_{run} (*Planck*)	n_{run}, $N_{\rm eff}$, strings (*Planck*)	n_{run}, $N_{\rm eff}$, strings (*Planck* + HighL)
$G\mu/c^2$ (95% upper limit)	-	2.28×10^{-7}	2.06×10^{-7}
$G\mu/c^2$ (best fit)	-	1.03×10^{-7}	1.75×10^{-7}
n_{run}	-0.015 ± 0.009	-0.054 ± 0.015	-0.008 ± 0.015
$\Delta N_{\rm eff}$	-	0.935 ± 0.713	0.969 ± 0.733
H_0	67.00 ± 1.20	74.84 ± 5.87	74.73 ± 5.92
$100\Omega_b h^2$	2.215 ± 0.030	2.300 ± 0.062	2.294 ± 0.058
$\Omega_c h^2$	0.121 ± 0.027	0.130 ± 0.008	0.131 ± 0.008
τ	0.097 ± 0.015	0.099 ± 0.016	0.099 ± 0.016
$100\theta_{MC}$	1.0412 ± 0.0006	1.0405 ± 0.0008	1.0404 ± 0.0008
$ln(10^{10}A_s)$	3.108 ± 0.030	3.117 ± 0.034	3.122 ± 0.033
n_s	0.954 ± 0.008	0.989 ± 0.028	0.986 ± 0.028
$-ln\mathscr{L}$	4901.7	4902.2	5255.6

Table 3.5 Values of the cosmological parameters when considering only the *Planck* and WP likelihoods with 1σ error bars, obtained by considering a full likelihood analysis

Parameter	n_{run}, $N_{\rm eff}$, strings (*Planck* + HighL + BAO)	strings, r	strings, r, running
$G\mu/c^2$ (95% upper limit)	1.95×10^{-7}	1.42×10^{-7}	1.99×10^{-7}
$G\mu/c^2$ (best fit)	3.57×10^{-8}	5.09×10^{-8}	8.39×10^{-9}
n_{run}	-0.014 ± 0.011	-	-0.029 ± 0.012
r	-	0.039 ± 0.036	0.11 ± 0.09
$\Delta N_{\rm eff}$	0.386 ± 0.289	-	-
H_0	70.21 ± 1.87	67.59 ± 1.21	67.92 ± 1.31
$100\Omega_b h^2$	2.258 ± 0.032	2.211 ± 0.029	2.254 ± 0.038
$\Omega_c h^2$	0.125 ± 0.005	0.119 ± 0.003	0.119 ± 0.003
τ	0.097 ± 0.015	0.087 ± 0.013	0.101 ± 0.016
$100\theta_{MC}$	1.0408 ± 0.0007	1.0413 ± 0.0006	1.0415 ± 0.0007
$ln(10^{10}A_s)$	3.108 ± 0.031	3.077 ± 0.025	3.105 ± 0.032
n_s	0.967 ± 0.012	0.960 ± 0.007	0.953 ± 0.009
$-ln\mathscr{L}$	5257.8	4903.2	4902.0
Parameter	$N_{\rm eff}$ (*Planck* + HighL)	$N_{\rm eff}$ (*Planck* + HighL + BAO)	$N_{\rm eff}$, $m^{\rm eff}_{\nu,\rm sterile}$
$\Delta N_{\rm eff}$	0.669 ± 0.323	0.531 ± 0.255	0.535 ± 0.306
$m^{\rm eff}_{\nu,\rm sterile}$ [eV]	-	-	0.261 ± 0.222
H_0	71.86 ± 2.76	70.61 ± 1.68	69.14 ± 2.74
$100\Omega_b h^2$	2.241 ± 0.038	2.227 ± 0.028	2.233 ± 0.035
$\Omega_c h^2$	0.129 ± 0.005	0.128 ± 0.004	0.127 ± 0.005
τ	0.095 ± 0.015	0.092 ± 0.013	0.095 ± 0.015
$100\theta_{MC}$	1.0404 ± 0.0007	1.0405 ± 0.0007	1.0405 ± 0.0007
$ln(10^{10}A_s)$	3.120 ± 0.032	3.112 ± 0.027	3.117 ± 0.032
n_s	0.980 ± 0.014	0.974 ± 0.010	0.975 ± 0.014
$-ln\mathscr{L}$	5255.3	5258.58	4902.5
Parameter	strings, $N_{\rm eff}$, $m^{\rm eff}_{\nu,\rm sterile}$	strings, r, $N_{\rm eff}$, $m^{\rm eff}_{\nu,\rm sterile}$	strings, $N_{\rm eff}$, r (*Planck* + HighL + BAO)
$G\mu/c^2$ (95% upper limit)	2.36×10^{-7}	2.57×10^{-7}	1.56×10^{-7}
$G\mu/c^2$ (best fit)	9.17×10^{-8}	1.44×10^{-7}	
r	-	0.11 ± 0.90	0.05 ± 0.04
$\Delta N_{\rm eff}$	1.055 ± 0.535	1.522 ± 0.725	0.696 ± 0.308
$m^{\rm eff}_{\nu,\rm sterile}$ [eV]	0.36 ± 0.32	0.38 ± 0.35	-
H_0	72.71 ± 4.79	76.69 ± 6.48	71.79 ± 2.00
$100\Omega_b h^2$	2.293 ± 0.058	2.338 ± 0.078	2.244 ± 0.030
$\Omega_c h^2$	0.132 ± 0.007	0.136 ± 0.008	0.130 ± 0.005
τ	0.097 ± 0.015	0.099 ± 0.016	0.089 ± 0.012
$100\theta_{MC}$	1.0402 ± 0.0008	1.0399 ± 0.0008	1.0403 ± 0.0007
$ln(10^{10}A_s)$	3.111 ± 0.033	3.120 ± 0.027	3.103 ± 0.028
n_s	0.989 ± 0.020	1.010 ± 0.027	0.978 ± 0.010
$-ln\mathscr{L}$	4902.6	4902.3	5259.6

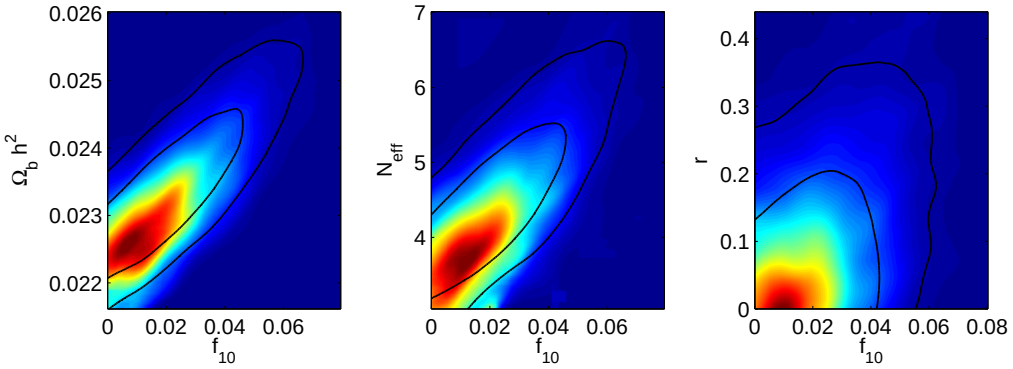

Fig. 3.16 Marginalised likelihoods obtained when adding cosmic strings, $N_{\rm eff}$ and tensor modes (r).

became very large drop considerably after adding the SPT/ACT likelihoods and the BAO. This one-dimensional plot is illustrative for the influence of the BAO in returning cosmological parameters close to their standard ΛCDM + $N_{\rm eff}$ values by suppressing degeneracies. Hence, in the simplest ΛCDM & strings model, the degeneracies between cosmic strings and other parameters are small, and BAO has a very small influence on cosmic strings. The same outcome appears when we additionally add tensor modes. For all the scenarios with $N_{\rm eff}$ the values of the parameters increase massively after adding cosmic strings. The case with $N_{\rm eff}$, r and strings is a bit different compared to the others allowing additional degrees of freedom, in the sense that after adding BAO the contribution from cosmic strings is again consistent with zero, just as in the ΛCDM + strings scenario. The process of the increase of the values of the parameters in a scenario with additional degrees of freedom is illustrated in Figure 3.18.

The degeneracies between $N_{\rm eff}$ and cosmic strings have been studied in the context of the Abelian-Higgs cosmic string model [128] and the authors have obtained a similar conclusion.

3.7.4 Results for the *Planck* & BICEP2 likelihoods

After the release of the BICEP2 data, we have tried to explain the signal that has been detected using our Nambu-Goto cosmic strings. However, due to the amplitude of the signal, if one would try to fit the data only with cosmic strings would require a tension of $G\mu = 8.8 \times 10^{-7}$. Such a high value of $G\mu$ is not allowed by the stronger constraints from the TT power spectrum [9] and is at the limit of the constraints from the bispectrum. However, with the new BICEP2 data the allowed contribution from the cosmic strings is increased compared to

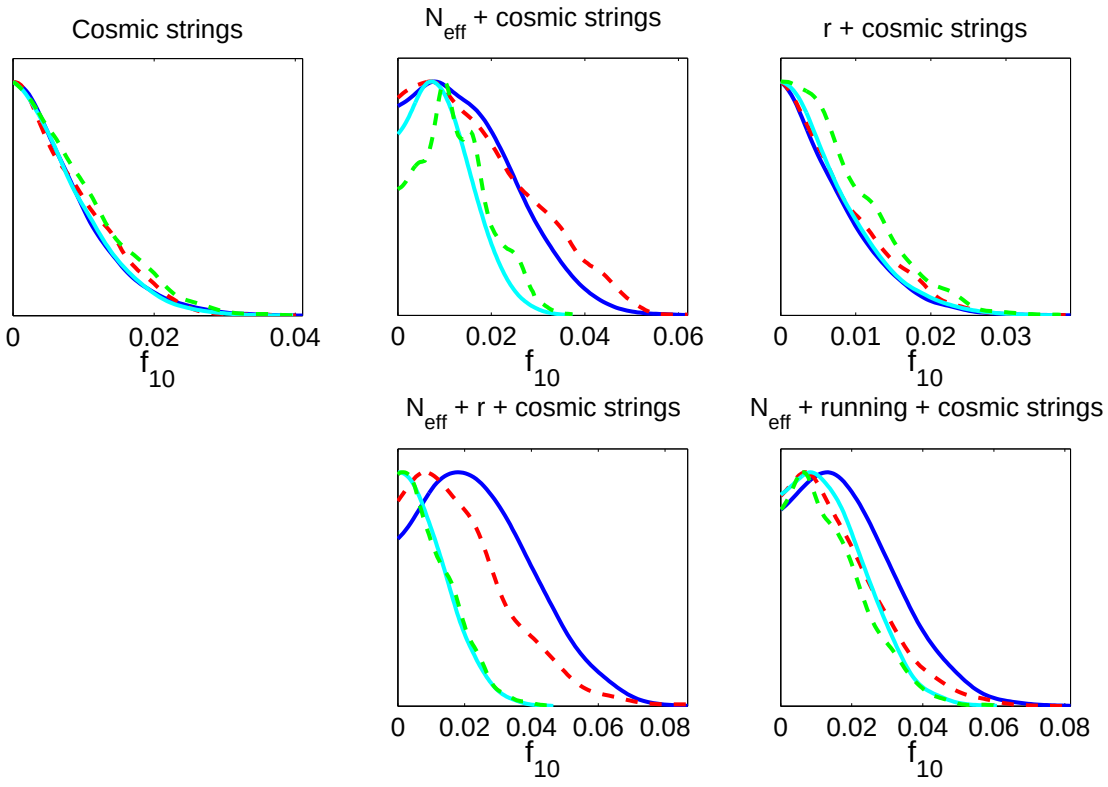

Fig. 3.17 Mean likelihoods of the samples (red dotted lines) and marginalised probabilities (blue solid lines) for parameter f_{10} in the following situations (from left to right and top to bottom): *Planck* & strings; *Planck* & strings & $N_{\rm eff}$; *Planck* & strings & r; *Planck* & strings & $N_{\rm eff}$ & r, *Planck* & $N_{\rm eff}$ & running & cosmic strings. The green and cyan curves respectively represent the mean likelihoods and marginalised probabilities of the samples after the introduction of HighL & BAO.

using *Planck* data alone, because these are a source of BB polarisation. Using full likelihood calculations, we have found an increase of about 16% in the string tension by adding the BICEP2 likelihoods compared to using only *Planck* data (but without adding additional parameters), to $G\mu$ to 1.74×10^{-7}. The other cosmological parameters are not significantly affected by the inclusion of cosmic strings (see later), but the BB power spectrum is not fitted very well, as it can be observed in Figure 3.19.

We have considered various possibilities of fitting the data without tensor modes ($r = 0$), but the fit values did not improve. The easiest option was to introduce the tensor modes together with cosmic strings. In that situation we have obtained a value of $r = 0.15 \pm 0.04$ and $G\mu < 1.44 \times 10^{-7}$ with $f_{10} < 0.026$ at 95% confidence level. In this case, the tensor-

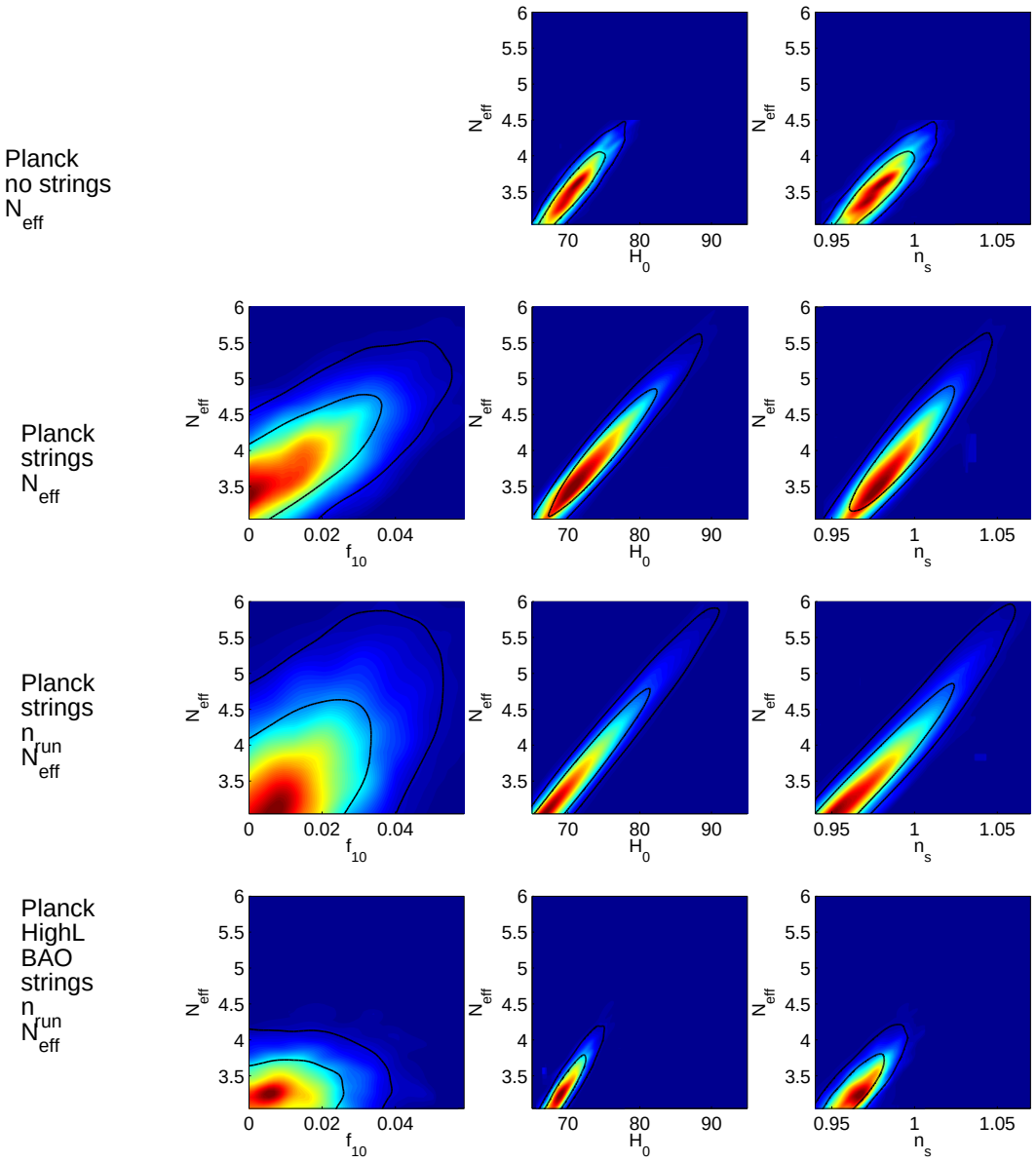

Fig. 3.18 Two-dimensional marginalised likelihoods in the f_{10}-$N_{\rm eff}$, H_0-$N_{\rm eff}$ and n_s-$N_{\rm eff}$ planes in the following cases (top to bottom): $N_{\rm eff}$ only (no strings), $N_{\rm eff}$ and cosmic strings, $N_{\rm eff}$, running and cosmic strings, $N_{\rm eff}$, running and cosmic strings, with SPT/ACT and BAOs.

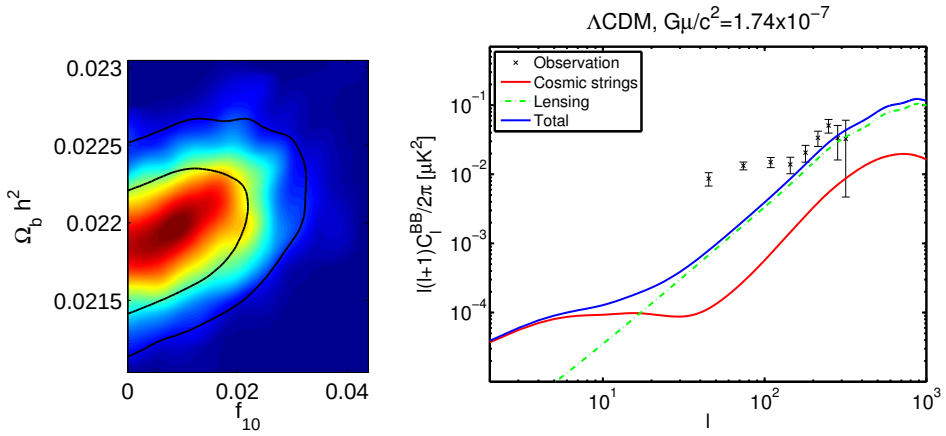

Fig. 3.19 Marginalised likelihoods in the f_{10}-$\Omega_b c^2$ plane (left) and best fit of the BB power spectrum using the *Planck* and BICEP2 likelihoods with cosmic strings at $G\mu = 1.74 \times 10^{-7}$ (right) and ΛCDM.

to-scalar ratio is decreased compared to the best-fit obtained by the BICEP2 team, but it is closer to value they have obtained after subtracting the dust foregrounds. There is no sign of degeneracy with any of the parameters. The data is fitted much better, but the string contribution is small (Figure 3.20).

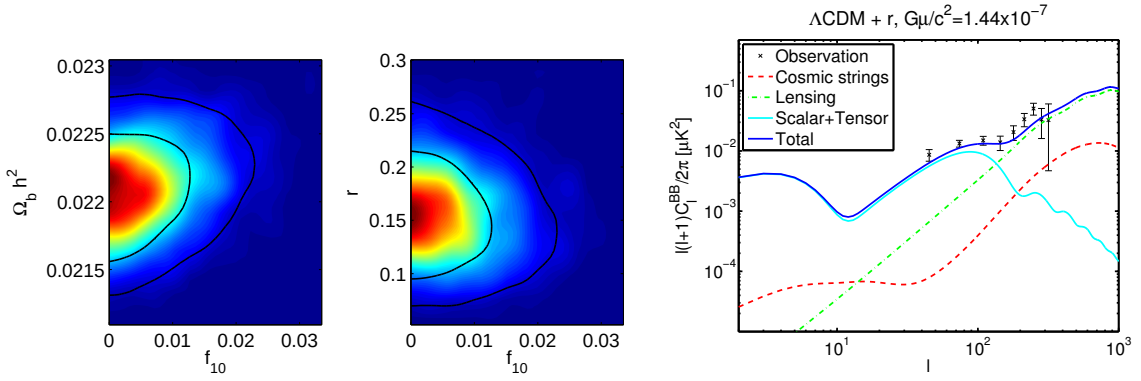

Fig. 3.20 Marginalised likelihoods in the f_{10}-$\Omega_b c^2$ and f_{10}-r planes for BICEP2 likelihoods with strings and tensor modes (left) and best fit of the BB power spectrum using the *Planck* and BICEP2 likelihoods with cosmic strings at $G\mu = 1.44 \times 10^{-7}$, ΛCDM and r (right).

In Table 3.6, we present the results that we have obtained using the *Planck*, WMAP polarisation and BICEP2 likelihoods, with and without tensor modes and with and without cosmic strings.

Table 3.6 Values of the cosmological parameters in the *Planck* + WP + BICEP2 likelihoods case with 1σ error bars, obtained by considering a full likelihood analysis (all cases also include the *Planck* nuisance parameters) obtained when considering tensor modes and cosmic strings

Parameter	ΛCDM	strings	r	strings, r
$G\mu/c^2$ (95% upper limit)	-	1.74×10^{-7}	-	1.44×10^{-7}
$G\mu/c^2$ (best fit)	-	8.46×10^{-8}	-	8.30×10^{-8}
r	-	-	0.16 ± 0.04	0.15 ± 0.04
H_0	66.26 ± 1.15	66.76 ± 1.20	67.72 ± 1.10	67.95 ± 1.20
$100\Omega_b h^2$	2.183 ± 0.27	2.197 ± 0.030	2.203 ± 0.028	2.210 ± 0.029
$\Omega_c h^2$	0.122 ± 0.003	0.121 ± 0.003	0.119 ± 0.003	0.118 ± 0.003
τ	0.093 ± 0.013	0.090 ± 0.013	0.089 ± 0.013	0.088 ± 0.013
$100\theta_{MC}$	1.041 ± 0.0006	1.0411 ± 0.0007	1.0413 ± 0.0006	1.0414 ± 0.0007
$ln(10^{10}A_s)$	3.101 ± 0.00255	3.084 ± 0.027	3.085 ± 0.025	3.075 ± 0.025
n_s	0.954 ± 0.0070	0.953 ± 0.007	0.964 ± 0.007	0.964 ± 0.007
$-ln\mathscr{L}$	4946.7	4946.1	4926.5	4926.6

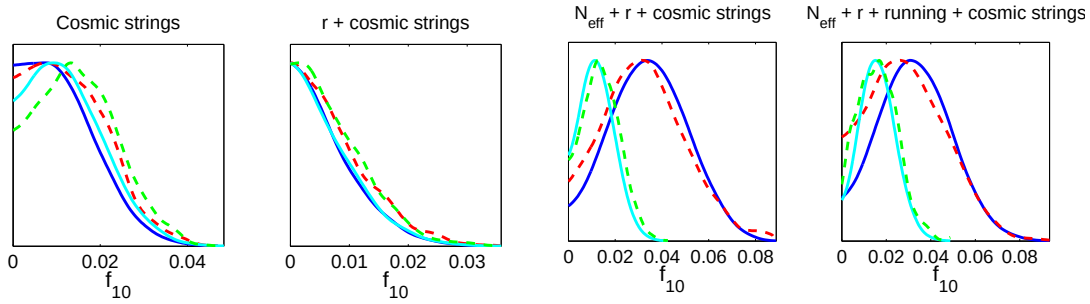

Fig. 3.21 Mean likelihoods of the samples (red dotted lines) and marginalised probabilities (blue solid lines) for parameter f_{10} in the following situations (from left to right and top to bottom): *Planck* & BICEP & strings; *Planck* & BICEP & strings & r; *Planck* & BICEP & strings & $N_{\rm eff}$ & r, *Planck* & BICEP & $N_{\rm eff}$ & running & r & cosmic strings. The green and cyan curves respectively represent the mean likelihoods and marginalised probabilities of the samples after the introduction of HighL & BAO.

We note that in the absence of tensor modes a non-zero contribution from cosmic strings is favoured, but this disappears as soon as r is introduced. This is due to the fact that although cosmic strings cannot explain the BB polarisation signal by having the wrong shape (even if we allow arbitrary large $G\mu/c^2$) they are still able to help fitting the BICEP2 data point in the absence of tensor modes. As the tensor modes are introduced, they take over the string contribution by giving the correct shape in the polarisation domain. This is illustrated clearly

by the one-dimensional likelihood plots for f_{10} in the two left plots of Figure 3.21. Baryon acoustic oscillations do not change the result significantly in the case with tensors. However, for the string-only one, they fix the contribution from strings to a non-zero value.

Table 3.7 Values of the cosmological parameters in the *Planck* + WP + BICEP2 likelihoods case with 1σ error bars, obtained by considering a full likelihood analysis (all cases also include the *Planck* nuisance parameters)

Parameter	$N_{\rm eff}$, r	$N_{\rm eff}$, r, strings (*Planck*)	$N_{\rm eff}$, r, strings (*Planck* + HighL)	$N_{\rm eff}$, r, strings (*Planck* + HighL + BAO)
$G\mu/c^2$ (95% upper limit)	-	2.72×10^{-7}	2.47×10^{-7}	1.70×10^{-7}
$G\mu/c^2$ (best fit)	-	1.96×10^{-7}	1.68×10^{-7}	1.43×10^{-7}
n_{run}	-	-	-	-
r	0.20 ± 0.05	0.23 ± 0.06	0.22 ± 0.06	0.16 ± 0.04
$\Delta N_{\rm eff}$	1.1061 ± 0.42	2.19 ± 0.69	2.234 ± 0.637	0.908 ± 0.331
H_0	76.14 ± 3.52	85.86 ± 6.06	85.72 ± 5.42	73.21 ± 2.11
$100\Omega_b h^2$	2.287 ± 0.044	2.408 ± 0.073	2.398 ± 0.062	2.255 ± 0.031
$\Omega_c h^2$	0.132 ± 0.006	0.141 ± 0.007	0.143 ± 0.007	0.133 ± 0.006
τ	0.101 ± 0.015	0.135 ± 0.016	0.104 ± 0.016	0.089 ± 0.013
$100\theta_{MC}$	1.0403 ± 0.0007	1.0400 ± 0.0007	1.0399 ± 0.0007	1.0401 ± 0.0007
$ln(10^{10}A_s)$	3.136 ± 0.033	3.132 ± 0.034	3.137 ± 0.034	3.107 ± 0.028
n_s	1.006 ± 0.017	1.039 ± 0.023	1.037 ± 0.022	0.986 ± 0.011
$-ln\mathscr{L}$	4923.15	4922.6	5275.4	5279.0
Parameter	n_{run}, r	r, n_{run}, strings	r, n_{run}, $N_{\rm eff}$, strings	r, n_{run}, $N_{\rm eff}$, strings (*Planck* + HighL + BAO)
$G\mu/c^2$ (95% upper limit)	-	2.07×10^{-7}	2.65×10^{-7}	1.88×10^{-7}
$G\mu/c^2$ (best fit)	-	9.42×10^{-8}	1.28×10^{-7}	1.08×10^{-7}
n_{run}	-0.028 ± 0.010	-0.036 ± 0.011	-0.012 ± 0.02	-0.031 ± 0.012
r	0.19 ± 0.04	0.22 ± 0.05	0.23 ± 0.06	0.22 ± 0.05
$\Delta N_{\rm eff}$	-	-	1.426 ± 0.927	0.448 ± 0.310
H_0	67.72 ± 1.23	68.27 ± 1.28	82.03 ± 7.61	70.79 ± 1.98
$100\Omega_b h^2$	2.234 ± 0.315	2.262 ± 0.037	2.384 ± 0.077	2.271 ± 0.031
$\Omega_c h^2$	0.119 ± 0.003	0.119 ± 0.003	0.136 ± 0.010	0.126 ± 0.005
τ	0.104 ± 0.016	0.103 ± 0.016	0.105 ± 0.017	0.102 ± 0.1053
$100\theta_{MC}$	1.0414 ± 0.0007	1.0420 ± 0.0007	1.0403 ± 0.0008	1.0409 ± 0.0007
$ln(10^{10}A_s)$	3.121 ± 0.031	3.108 ± 0.033	3.131 ± 0.035	3.121 ± 0.032
n_s	0.958 ± 0.008	0.954 ± 0.008	1.020 ± 0.033	0.967 ± 0.012
$-ln\mathscr{L}$	4922.9	4922.8	4922.0	5276.5

Table 3.8 Values of the cosmological parameters in the *Planck* + WP + BICEP2 likelihoods case with 1σ error bars, obtained by considering a full likelihood analysis

Parameter	n_{run}, strings	r, $N_{\rm eff}$, n_{run}, strings (*Planck* + HighL)	$N_{\rm eff}$, strings, $m^{\rm eff}_{\nu,{\rm sterile}}$	r, $N_{\rm eff}$, strings, $m^{\rm eff}_{\nu,{\rm sterile}}$
$G\mu/c^2$ (95% upper limit)	2.25×10^{-7}	2.41×10^{-7}	2.99×10^{-7}	2.85×10^{-7}
$G\mu/c^2$ (best fit)	1.56×10^{-8}	1.96×10^{-7}	2.36×10^{-7}	1.53×10^{-7}
n_{run}	-0.025 ± 0.010	-0.012 ± 0.017	-	-
r	-	0.23 ± 0.06	-	0.22 ± 0.06
$\Delta N_{\rm eff}$	-	1.703 ± 0.910	1.87 ± 0.67	2.21 ± 0.073
$m^{\rm eff}_{\nu,{\rm sterile}}$ [eV]	-	-	0.20 ± 0.19	0.30 ± 0.25
H_0	66.92 ± 1.28	81.61 ± 7.31	80.00 ± 5.92	83.15 ± 6.62
$100\Omega_b h^2$	2.236 ± 0.036	2.373 ± 0.067	2.369 ± 0.072	2.402 ± 0.076
$\Omega_c h^2$	0.122 ± 0.003	0.137 ± 0.010	0.142 ± 0.008	0.142 ± 0.008
τ	0.100 ± 0.016	0.106 ± 0.016	0.103 ± 0.016	0.103 ± 0.016
$100\theta_{MC}$	1.0413 ± 0.0007	1.0403 ± 0.0008	1.0397 ± 0.0007	1.0397 ± 0.0007
$ln(10^{10}A_s)$	3.104 ± 0.033	3.137 ± 0.034	3.127 ± 0.035	3.129 ± 0.034
n_s	0.944 ± 0.008	1.017 ± 0.033	1.013 ± 0.022	1.035 ± 0.024
$-ln\mathscr{L}$	4943.6	5275.7	4943.1	4922.2

The most interesting cases are described in Tables 3.7-3.8. As in the *Planck* case, interesting degeneracies appear due to $N_{\rm eff}$ and a similar outcome can also be observed.

The cosmic strings contribution is very large with the *Planck* & BICEP2 likelihoods, but the Hubble constant and $N_{\rm eff}$ are also very big (see Table 3.7 and Figure 3.22). Adding ACT/SPT and BAO recovers the ΛCDM values for the cosmological parameters and reduces the contribution from cosmic strings. Nevertheless, a non-zero contribution is still preferred (two right panels of Figure 3.21). In both the scenarios of cosmic strings & $N_{\rm eff}$ & r and cosmic strings & $N_{\rm eff}$ & r & n_{run} the preferred value of f_{10} is non-zero and the distribution is wide. Adding SPT/ACT and BAO reduces the preferred value for f_{10}, but also narrows the distribution. This can be compared to Figure 3.17, but here the BICEP2 polarisation data favours more a non-zero contribution of cosmic strings.

When considering the scenario with cosmic strings, $N_{\rm eff}$ and $m^{\rm eff}_{\nu,{\rm sterile}}$, we obtain a non-zero best-fit value for the cosmic string parameter. The best fit value is $G\mu/c^2 = 2.36\times10^{-7}$ and the constraint is $G\mu/c^2 < 2.99\times10^{-7}$ at 2σ level. Both the Hubble constant and $N_{\rm eff}$ have big values and the fit is not very good not having tensor modes.

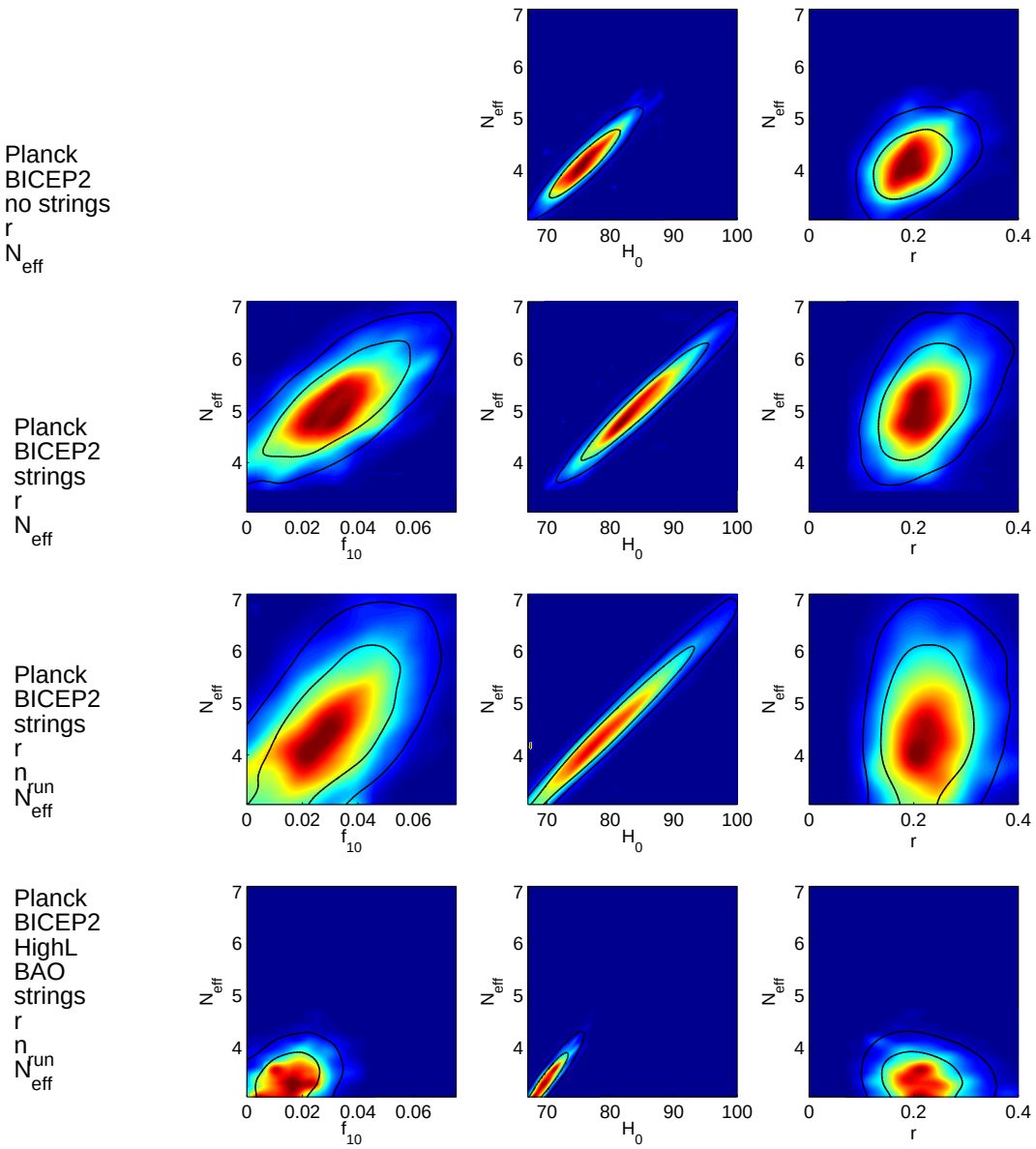

Fig. 3.22 Two-dimensional marginalised likelihoods in the f_{10}-$N_{\rm eff}$, H_0-$N_{\rm eff}$ and n_s-$N_{\rm eff}$ planes in the following cases (top to bottom): $N_{\rm eff}$ only (no strings), $N_{\rm eff}$ and cosmic strings, $N_{\rm eff}$, running and cosmic strings, $N_{\rm eff}$, running and cosmic strings, with SPT/ACT and BAOs.

3.8 Discussion and conclusions

In this Chapter we have studied the consequences of Nambu-Goto cosmic strings on the CMB, through the power spectrum. We have used high-resolution Nambu-Goto cosmic string simulation obtained from the Allen and Shellard code and we have used them to determine the energy-momentum tensor of the string network. We have decomposed the energy-momentum tensor of the network into its corresponding scalar, vector and tensor parts and we have used these to determine the UETCs for the three epochs of interest: the radiation era, the matter era and matter to cosmological constant era. We have performed eigendecompositions of the UETCs thus obtained and we have used the eigenvectors as sources for an Einstein-Boltzmann solver. We have modified the standard CMBFAST code to incorporate the sources generated by the cosmic strings. We have determined the power spectra from each of the three epochs and we have devised a method to combine them together to obtain an overall power spectrum.

We have used the obtained power spectrum to constrain the string tension magnitude by adding cosmic strings to the standard 6-parameter ΛCDM model [17]. In this simplest model, we obtained a string tension constraint of $G\mu/c^2 < 1.49 \times 10^{-7}$ (95% confidence), using the *Planck* likelihood and WMAP polarisation. This result is comparable to the value obtained by the *Planck* team [9]. In this case, the string tension $G\mu/c^2$ does not introduce extra degeneracies between ΛCDM parameters. However, by allowing $N_{\rm eff}$ to vary, the string constraint gets much weaker ($G\mu/c^2 < 2.28 \times 10^{-7}$) and the Hubble constant increases to $H_0 = 75.96$, with a significant degeneracy between f_{10} and H_0. This degeneracy disappears however by adding BAOs and HighL contributions. In that case, the string tension reverts close to its previous value, $G\mu/c^2 < 1.58 \times 10^{-7}$. We note that BAOs are the key ingredient for breaking the degeneracies as HighL data cannot alone solve the problem. The same behaviour is observed when allowing tensor modes in addition to $N_{\rm eff}$, where the constraint on $G\mu/c^2$ shifts from 2.49×10^{-7} to 1.56×10^{-7} with BAOs. These degeneracies can be more easily interpreted visually (see Figs. 3.15 and 3.16). By adding running in addition to cosmic strings, the string constraint becomes slightly weaker ($G\mu/c^2 < 1.88 \times 10^{-7}$), but does not induce significant degeneracies. In addition, we have also analysed the contribution of an additional sterile neutrino and we have found no significant differences to the parameter values.

We have performed a similar analysis by considering the BICEP2 data in addition to *Planck* likelihoods and WMAP polarisation. In this case, the string tension constraints loosen, but the new polarisation signal cannot be explained solely by cosmic strings with no

contribution from primordial tensor modes. This is due to the fact that cosmic strings are tightly constrained by the temperature data. Hence, in a pure ΛCDM and strings scenario, the 95% confidence level constraint on the string tension only rises to $G\mu/c^2 < 1.74 \times 10^{-7}$ (Figure 3.19). By adding tensor modes, we note that the model prefers a value of $r = 0.15$ and $G\mu/c^2 < 1.44 \times 10^{-7}$ and strings are not favoured. Adding additionally $N_{\rm eff}$ greatly increases the allowed amount of cosmic strings to 2.72×10^{-7}, but the values of r, of the Hubble constant and of $\Delta N_{\rm eff}$ are increased as well, 0.20 to 85.86 and 2.19 respectively. This is due to the same degeneracies that appear. BAOs and SPT/ACT likelihoods again revert the situation to ΛCDM with $G\mu/c^2 < 1.70 \times 10^{-7}$, $r = 0.16$ $\Delta N_{\rm eff} = 0.908$ and $H_0 = 73.21$. We note again that the SPT/ACT likelihoods make little difference to the results (Table 3.7). By also allowing for a non-zero running of the spectral index we see from Table 3.7 that running in itself allows for more cosmic strings ($G\mu/c^2 < 2.07 \times 10^{-7}$) and tensor modes ($r = 0.22$) but the degeneracies are modest and the Hubble constant keeps its usual value ($H_0 = 68.27$). $N_{\rm eff}$, when added to this model, induces huge degeneracies and shifts the Hubble parameter but again this problem is cured with BAOs.

For the time being, the CMB power spectrum represents the most powerful method for constraining extensions to the 6-parameter ΛCDM model. The current data does not presently exclude the presence of cosmic strings, but they are severely constrained. Because the fluctuations generated by cosmic strings are non-Gaussian, their signal can be detected in principle using higher order correlations, such as the bispectrum and trispectrum [84, 102, 129, 130], but the constraints are not yet competitive with the power spectrum ones. The constraints obtained in this work could be drastically improved in the future using different approaches. The 21 cm hydrogen line [131] is expected to improve the constraints with at least three orders of magnitude compared to the CMB power spectrum, gravitational waves [86, 132] and lensing surveys [133] with two orders of magnitude.

CHAPTER 4

DOMAIN WALLS

4.1 Domain walls equations of motion

As discussed in Chapter 2, domain walls are the simplest cosmological defects, as they can be described by a single scalar field ϕ. One starts with the Lagrangian (2.8), describing a discrete broken symmetry, with a potential having al least two degenerate minima [48]. The energy-momentum tensor of the walls network can then be expressed in terms of this Lagrangian as follows:

$$\Theta_{\mu\nu} = \frac{1}{4\pi}\left[\phi_{,\mu}\phi_{,\nu} - g_{\mu\nu}\left[\frac{1}{2}\phi_{,\alpha}\phi^{,\alpha} + V(\phi)\right]\right]. \tag{4.1}$$

We consider a flat FLRW metric [Eq. (1.7)], with scale factor a, as described in Chapter 1, where the 0^{th} dimension corresponds to conformal time. With respect to this metric, the components of the energy-momentum tensor become

$$\Theta_{00} = \frac{1}{4\pi}\left[\frac{1}{2}\phi'^2 + \frac{1}{2}(\nabla\phi)^2 + a^2V(\phi)\right], \tag{4.2}$$

$$\Theta_{0i} = \frac{1}{4\pi}\left[\phi'\partial_i\phi\right], \tag{4.3}$$

$$\Theta_{ij} = \frac{1}{4\pi}\left[\partial_i\phi\partial_j\phi + \delta_{ij}\left(\frac{1}{2}\phi'^2 - \frac{1}{2}(\nabla\phi)^2 - a^2V(\phi)\right)\right], \tag{4.4}$$

where prime denotes a derivative with respect to conformal time and the gradients are with respect to comoving coordinates. By applying the standard variational technique,

$$\frac{1}{\sqrt{-g}}\partial_\mu\left(\sqrt{-g}\frac{\partial\mathscr{L}}{\partial\left(\partial_\mu\phi\right)}\right) = \frac{\partial\mathscr{L}}{\partial\phi} \tag{4.5}$$

for the Lagrange density (2.8), the equation of motion for ϕ is obtained:

$$\frac{\partial^2\phi}{\partial\tau^2}+2\left(\frac{d\ln a}{d\ln\tau}\right)\frac{1}{\tau}\frac{\partial\phi}{\partial\tau}-\nabla^2\phi=-a^2\frac{\partial V}{\partial\phi}\,, \tag{4.6}$$

where τ is the conformal time. In the case of a constant power-law expansion of the Universe, $a\propto t^{\lambda}$ and $\frac{d\ln a}{d\ln\tau}=\frac{\lambda}{1-\lambda}$ has the value 1 in the radiation era and 2 in the matter era.

In order to calculate the stress-energy tensor components one has to first solve equation of motion (4.6) and then to substitute the solution into the corresponding equations (4.2)-(4.4). However in the comoving coordinates described above, the thickness of the walls decreases as a^{-1} and, as Eq. (4.6) has to be solved numerically on a grid, the wall thickness quickly becomes smaller than the grid spacing. This problem can be overcome [48] by modifying Eq. (4.6) to

$$\frac{\partial^2\phi}{\partial\tau^2}+\alpha\left(\frac{d\ln a}{d\ln\tau}\right)\frac{1}{\tau}\frac{\partial\phi}{\partial\tau}-\nabla^2\phi=-a^{\beta}\frac{\partial V}{\partial\phi}\,. \tag{4.7}$$

The unmodified equation of motion corresponds to $\alpha=\beta=2$. However, taking the coefficients to be $\alpha=3$ and $\beta=0$, one solves the problem of wall thinning, as the walls would have constant thickness in comoving coordinates (by modifying β) and would also maintain energy-momentum conservation (by modifying α as well). The procedure is called the Press-Ryden-Spergel (PRS) algorithm, after the names of the authors in [48].

In practical terms, the main effect of the PRS algorithm is to change the wall thickness. We know on physical grounds that the physical thickness of the walls can't affect their dynamics (at least once they are formed and reasonably well separated from each other), since a wall's integrated surface density and surface tension are independent of the thickness - see for example chapter 13 of Ref. [40].

Moreover, the original PRS paper [48] shows that this algorithm preserves the behaviour of two key dynamical effects in the evolution of wall networks: the rate at which the Hubble damping localises the scalar field into the minima of the potential, and the momentum conservation law (describing how a wall slows down due to the Hubble flow). More recently, these results have been confirmed by additional analytic arguments [134] and by extensive numerical tests [135]. We are therefore confident that the algorithm retains the relevant dynamics.

Equation (4.7) can now be solved numerically on a grid using a finite difference scheme as follows:

$$\delta \equiv \frac{1}{2}\alpha \frac{\Delta\tau}{\tau}\frac{d\ln a}{d\ln\tau}\,, \tag{4.8}$$

$$\begin{aligned}\left(\nabla^2\phi\right)_{ijk} = &\left[\phi_{i+1,j,k}+\phi_{i-1,j,k}+\phi_{i,j+1,k}+\right.\\ &\left.+\phi_{i,j-1,k}+\phi_{i,j,k+1}+\phi_{i+1,j,k-1}-6\phi_{i,j,k}\right]\Delta_x^2\,,\end{aligned} \tag{4.9}$$

$$\dot{\phi}_{ijk}^{n+\frac{1}{2}} = \frac{(1-\delta)\,\dot{\phi}_{ijk}^{n-\frac{1}{2}} + \Delta\tau\left(\nabla^2\phi_{ijk}^{n} - a^{\beta}\frac{\partial V}{\partial\phi_{ijk}^{n}}\right)}{1+\delta}\,, \tag{4.10}$$

$$\phi_{ijk}^{n+1} = \phi_{ijk}^{n} + \Delta\tau\dot{\phi}_{ijk}^{n+\frac{1}{2}}\,. \tag{4.11}$$

These equations use the assumption that the domain walls always have a small contribution on the overall energy density of the Universe. This assumption is based on the fact that no direct signs of domain walls have been observed. Hence their contribution to the matter perturbations can be treated as a first order approximation in perturbation theory. Therefore, at this order, their evolution does not significantly affect the expansion of the Universe and hence we can safely use a power law expansion rate for radiation and matter epochs.

4.2 Formalism for calculating the power spectrum

In order to calculate the power spectrum of fluctuations generated by domain walls, we proceed in a similar manner to the case of cosmic strings, described in detail in Chapter 3. We first solve Eqs. (4.8)-(4.11) numerically to obtain the field ϕ and its time derivative, and then we use Eqs. (4.2)-(4.4) to calculate the energy-momentum tensor. We project it onto a three-dimensional grid as in Chapter 3 and we decompose it into its scalar, vector and tensor parts, and as in the case of the strings. The components chosen are the same as in the case of cosmic strings.

As it is the case of cosmic strings, domain walls are active sources, and they continuously source the metric perturbations. As domain walls have a different scaling law compared to cosmic strings, the UETCs computed directly are non-scaling even in a purely radiation or matter epoch. Therefore, in order to be able to use them in a Boltzmann code, we have to fix the scaling. In each epoch, the scaling behaviour is achieved by considering the quantity

$$C\left(k\tau_1,k\tau_2\right)\delta_D(0) = \frac{1}{\sqrt{\tau_1\tau_2}}\langle\Theta^*(\mathbf{k},\tau_1)\Theta(\mathbf{k},\tau_2)\rangle\,, \tag{4.12}$$

where Θ corresponds to a generic component of the energy-momentum tensor. For the cases considered, these are positive definite functions, and hence they can be expressed in terms of their eigenvectors and positive eigenvalues as follows:

$$C(k\tau_1, k\tau_2) = \sum_i \lambda_i \mathrm{v}_i(k\tau_1)^T \mathrm{v}_i(k\tau_2) = \sum_i w_i(k\tau_1)^T w_i(k\tau_2)\,, \tag{4.13}$$

with $w_i = \sqrt{\lambda_i}\mathrm{v}_i$. Then one would have to substitute the energy-momentum tensor component with

$$\Theta(\mathbf{k}, \tau) \to \sqrt{\tau} w_i(k\tau) = \sqrt{\tau}\sqrt{\lambda_i} v_i(k\tau) \tag{4.14}$$

due to the fact that we have divided by $\sqrt{\tau}$ in Eq. (4.12). Hence, we have arrived at an equation which is analogous to Eq. (3.43) for cosmic strings. We now proceed in exactly the same way as for cosmic strings, with the only difference being in the sources.

We determine the UETCs and then the corresponding power spectra in similar fashion to the cosmic strings, by using two simulations - one in the radiation era and one in the matter era. In order to obtain an overall power spectrum, we use the summing procedure that we have explained in Chapter 3, but we also need to make the assumption that the matter era UETCs are also valid after the end of the matter era, *i.e.* during the fast expansion rate of the Universe in the cosmological constant epoch. This is not entirely satisfactory, because we know that the energy density of the domain walls is greater than the background and therefore their power spectrum will be dominated by the late-time contribution. On the other hand, in the cosmological constant era we cannot use the exponential expansion directly, because the expansion rate does not have a simple form as in the radiation and matter eras. Therefore, we propose an approximation to the cosmological constant epoch by considering the Universe to be expanding with an effective power law, and we determine the power λ of an expansion rate $a \propto t^{\lambda}$ that has the same slope today, as the actual expansion rate of the Universe. We then create a simulation with this expansion rate and we then include it in our formalism. We use both the two- and three-era calculations to determine the constraints on the domain walls, and then show that the change due to the last epoch is small.

4.3 Simulations

For our domain wall numerical simulations we use a code based on the PRS algorithm [48] with the diagnostic tools introduced in [136]. This has been successively parallelised and optimised to exploit recent high-performance computing developments; the more recent version of the code is described in [135], and a forthcoming publication will describe further developments.

In order to solve Eqs. (4.8)-(4.11), we assume the following numerical values of the parameters involved:

$$\alpha = 3\,, \tag{4.15}$$

$$\beta = 0\,, \tag{4.16}$$

$$V(\phi) = \frac{\pi^2}{50}\left(\phi^2 - 1\right)^2\,. \tag{4.17}$$

This corresponds to an initial wall thickness of $W_0 = 10$. The evolution of such a domain wall network is illustrated in Fig. 4.1, by plotting the energy density component at different times of the evolution of the Universe. Initially, the network is very dense due to the random initial conditions in the code. As the Universe is expanding, the effect of the initial conditions is no longer important. At the end of simulation, the walls disappear completely.

The grid spacing is taken to be $\Delta_x = 1$ and the initial conditions are such that ϕ is taking random values on the grid between -1 and 1 and $\dot{\phi} = 0$ everywhere. We ran 3 three-dimensional simulations, with a box size of 1024^3 points, one in radiation era ($\lambda = 1/2$), one in the matter era ($\lambda = 2/3$) and one in late-time Λ-dominated era.

The energy-momentum tensor of the domain wall network can be evaluated at any time, but we are only interested in the scaling regime of the simulation for the calculation of UETCs. The regime where the network exhibits such behaviour has been investigated in detail in [135, 137]. In Figure 4.2 we show the peaks of the $\langle\Theta_{00}\Theta_{00}\rangle$ unequal time correlators (*i.e.* the value of the maximum of the equal-time correlator) calculated using Eq. (4.12), with each of them centred around the value on the x-axis. This shows how good the scaling is in this regime.

In Figure 4.3 we have plotted four 2-dimensional slices through the domain wall network at different times of the simulation, and these show how the network becomes less dense over time.

For the Λ-era, taking into account that the contribution today would be the most important, we consider a simulation with $\lambda = H_0 t_0$, where t_0 is the age of the Universe and H_0 is the

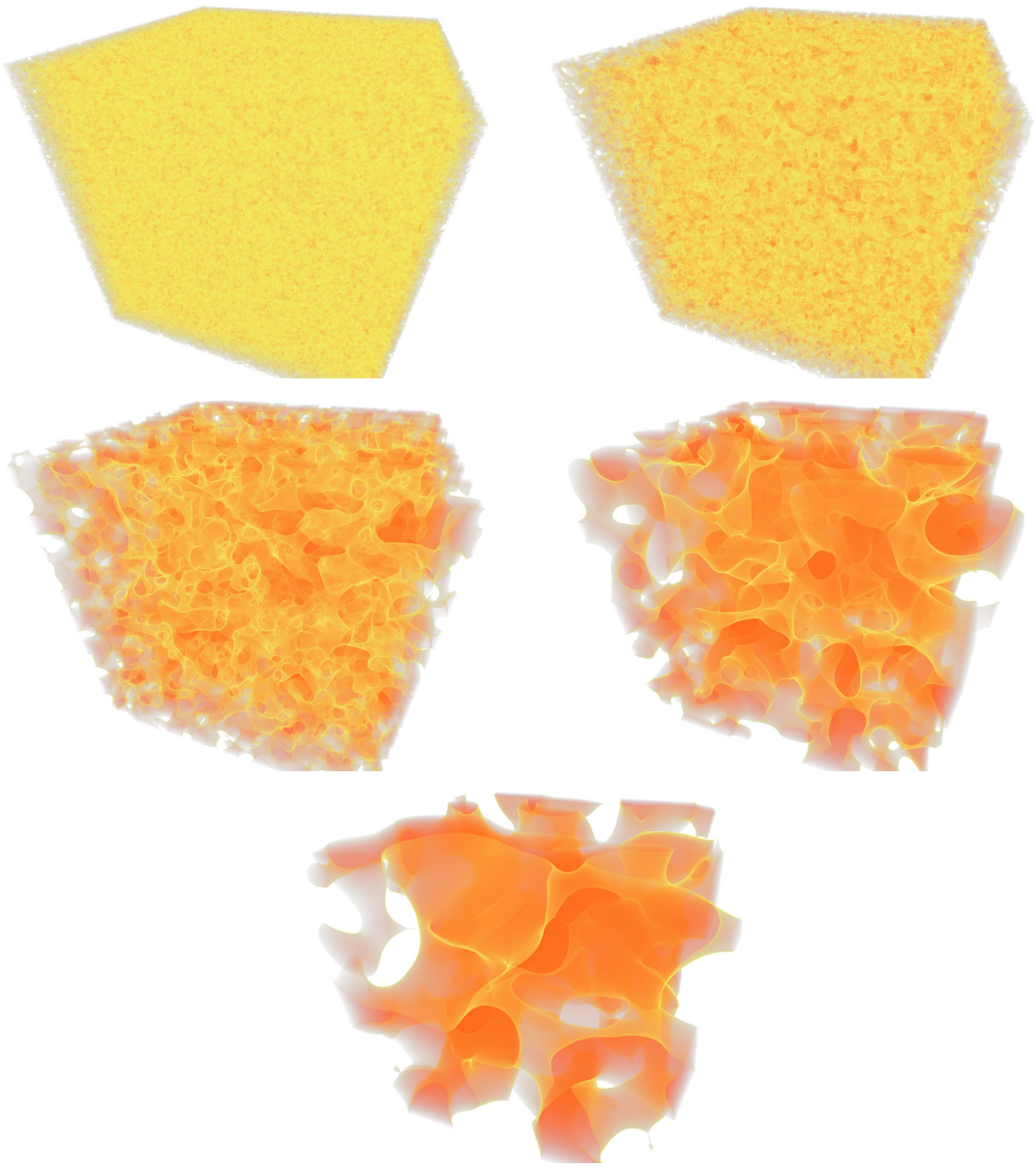

Fig. 4.1 Three-dimensional plots of the energy density component of the energy-momentum tensor of the domain wall network at five times through the simulation (left to right and top to bottom).

Hubble expansion rate today. Using the values of the cosmological parameters from Ref. [17], we take an average value of $\lambda = 0.95$ between various likelihoods.

In a universe with $a \propto t^{\lambda}$, the scalefactor can be expressed as

$$a = \frac{ct}{(1-\lambda)\tau}. \tag{4.18}$$

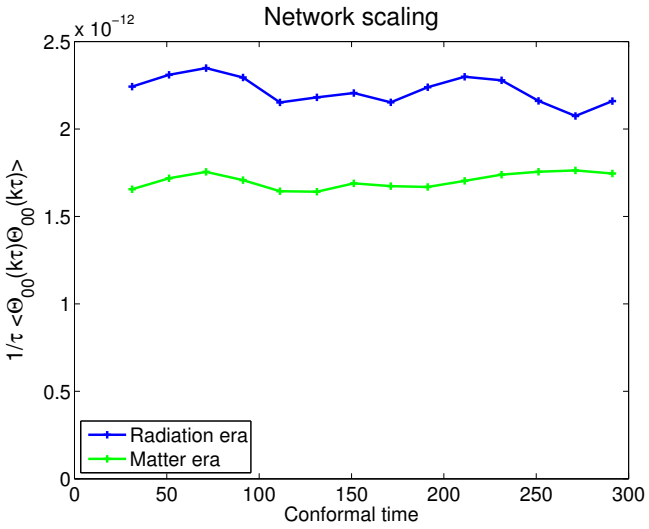

Fig. 4.2 Scaling behaviour of the UETC in the radiation (blue) and matter (green) eras.

Then, if A is the comoving area of the walls, V is the volume of the simulation box and σ is the surface tension of the domain walls (*i.e.* energy per area), the physical density of domain walls can be expressed as

$$\rho = \frac{\sigma A a^2}{V a^3} = (1-\lambda)\left(\frac{A\tau}{V}\right)\frac{\sigma}{ct}\,. \tag{4.19}$$

The numerical value of the product of the first two brackets in Eq. (4.19) is obtained directly from the simulations. The domination of the power spectrum by the contribution from the matter era makes it possible to safely use $\lambda = \frac{2}{3}$ without introducing significant errors. In the matter era, for the scaling regime we took $\frac{A\tau}{V} = 1.93$. Using Eq. (4.19) and the fact that the background density of the Universe is given by $\bar{\rho} = \frac{1}{6\pi G t^2}$, the numerical coefficient required to multiply the power spectrum today in order to restore physical units is given by $\left(\frac{6\pi G t_0 \sigma}{c}\right)^2$.

4.4 Results

We have calculated the power spectra for the domain walls in the temperature and polarisation channels for the radiation and matter era simulations separately and then by combining the two simulations together. We have also realised this in the three-simulations scenario.

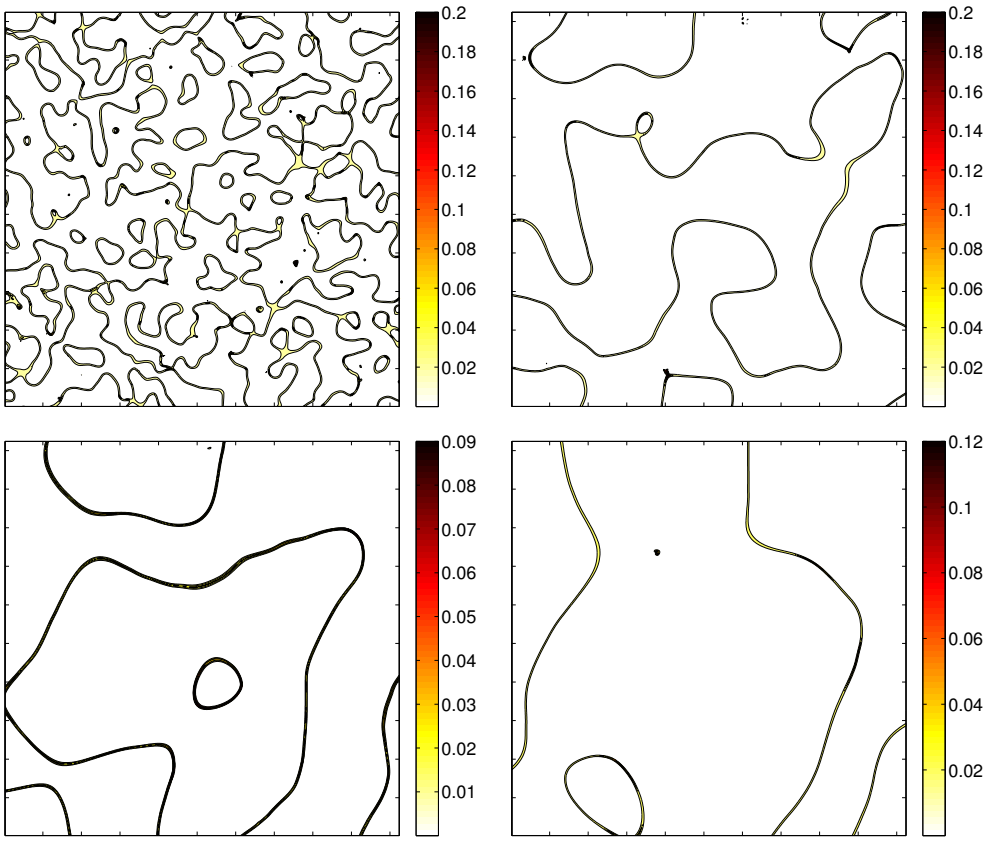

Fig. 4.3 Two-dimensional slices through the domain wall network showing the energy density of the walls in the matter era during the scaling regime of the simulation. The four panels represent snapshots taken at roughly equal conformal time steps between the beginning and end of the simulation (from left to right and top to bottom). The colour bars show the magnitude of the energy density of the network in the units of the simulation.

The results show that the radiation era contribution has a subdominant effect. This was expected, because the growth of the density of domain walls over time would mean that their most significant contribution is at late times. Indeed, as the matter era results completely dominate the power spectra, the errors from the procedure of combining the simulations become completely negligible. In Figure 4.4 we have plotted separately the contributions from the radiation and matter epochs to the power spectra in the temperature and polarisation channels showing how the matter era dominates on all the scales of interest. Only in the scalar TE plot one can see a more important effect of the radiation era. Hence, a simulation with a higher expansion rate than the one in the matter epoch is desirable, because this would be a much better approximation to the expansion rate today.

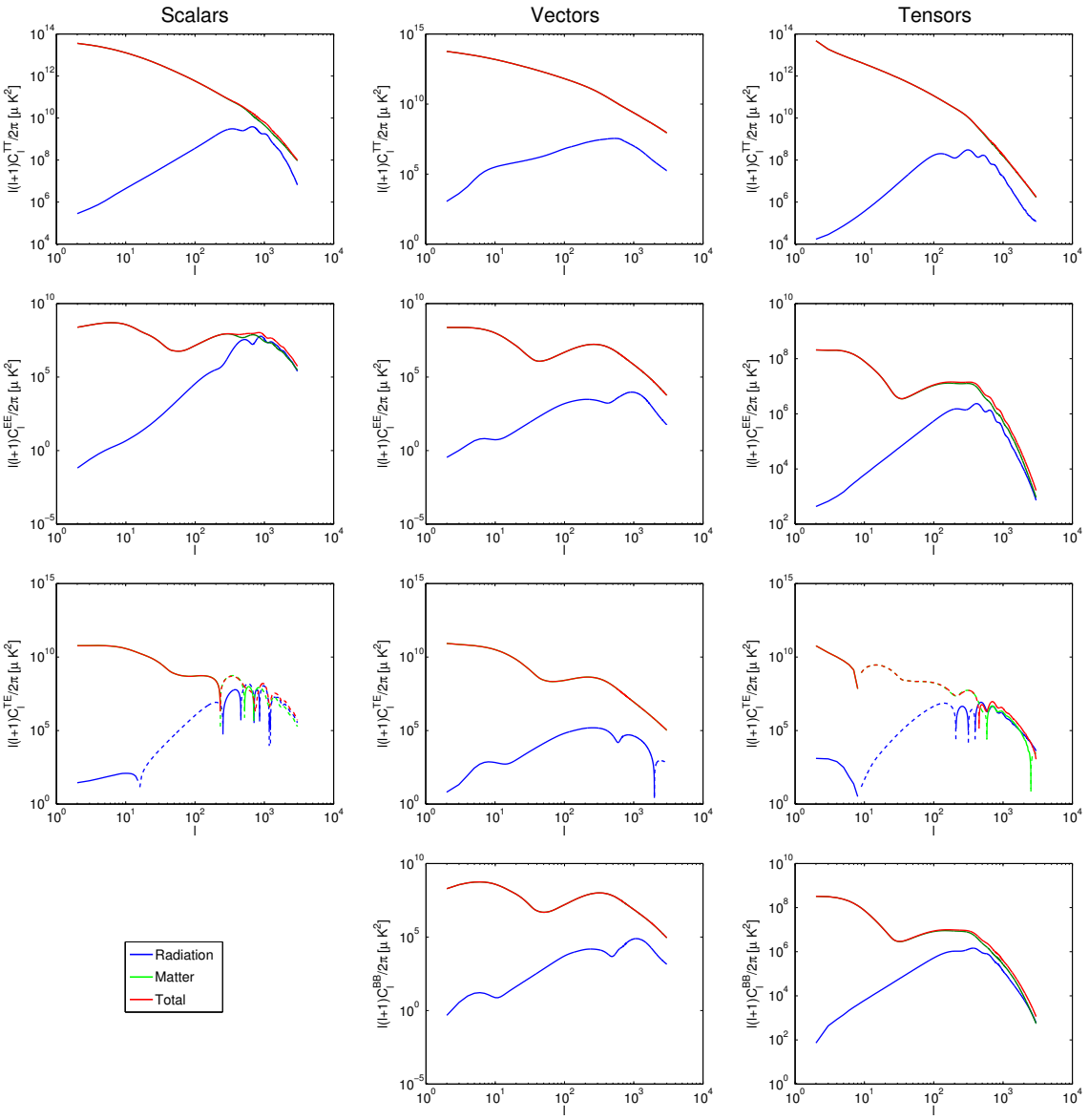

Fig. 4.4 Power spectra of domain walls showing the individual results from the radiation (in blue) and matter (in green) eras as well as total power spectra for scalars, vectors and tensors in the temperature and polarisation (EE, TE and BB) channels. In the case of the TE polarisation we have plotted the negative parts with dashed lines in the same colours as their positive counterparts. In the plots $\sigma/t_0 = 1.5 \times 10^{-7}$.

By adding the late-time simulation, the peak of the curves at $l = 2$ drops by about one third in all four power spectra considered (Fig. 4.5). In that case, the expansion rate of the Universe is faster than the growth of the domain wall density and hence the power is leaking to intermediate scales, keeping an approximately constant integrated power spectrum. As a

consequence there is only a small change in the CMB constraint on domain walls in the two scenarios.

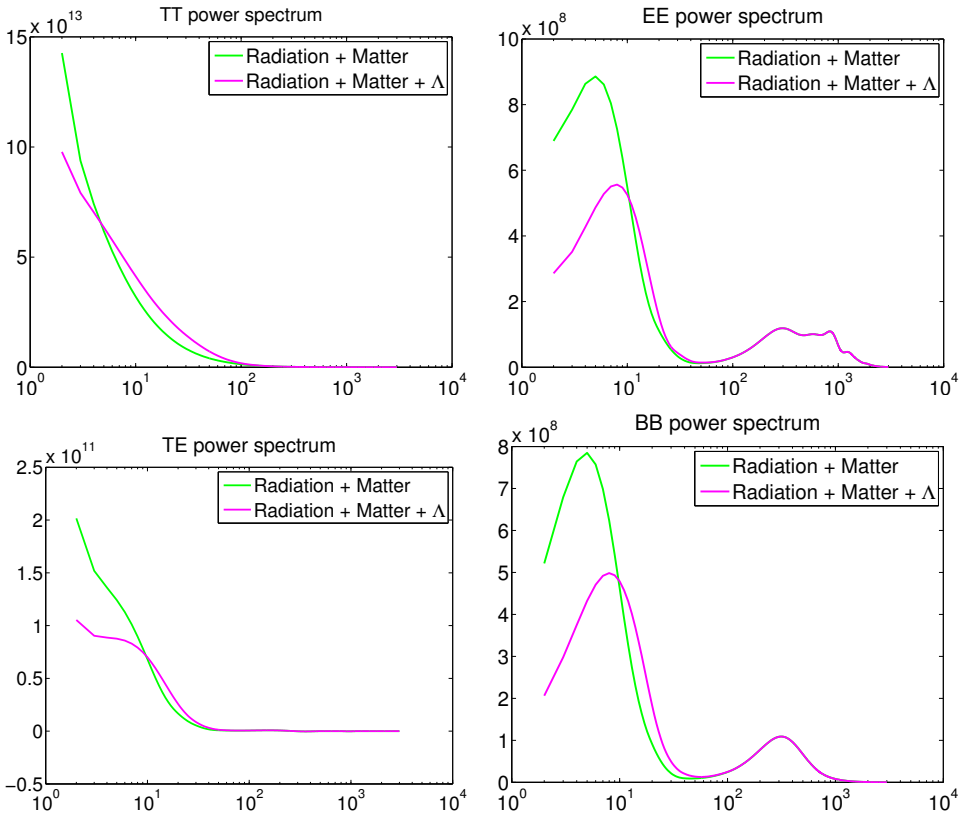

Fig. 4.5 Comparison between the domain walls power spectra from radiation & matter eras and radiation, matter & Λ eras. In the plots $\sigma/t_0 = 1.5 \times 10^{-7}$.

4.5 CMB constraints on domain walls

We used the March 2014 version of the COSMOMC code [115] which is based on a Markov chain - Monte Carlo method to obtain constraints on the allowed contribution of the domain walls to the CMB power spectrum. We had to modify the code to accommodate the power spectrum from the domain walls. As the domain wall matter perturbations are uncorrelated to the primordial fluctuations, their power spectrum can be calculated separately. This is very helpful, because although their spectrum would depend on the cosmological parameters, the relative change to the inflationary spectrum would be small, as it happens for cosmic strings. Domain walls are tightly constrained by their TT power spectrum shape and hence the parameter variation impact would not be very significant. We have used the standard

ΛCDM six-parameter model, together with a parameter quantifying the amplitude of the spectrum of the walls together with the Planck likelihoods of the 2013 data release.

We have analysed the radiation and matter scenarios, and also one involving a late-time cosmological constant epoch. For the radiation and matter scenario, we have obtained a constraint on the surface density of the domain walls of $\sigma < 4.22 \times 10^{-9}$ kg/m^2 (at 95% confidence level), which corresponds to an energy scale of formation for domain walls of 0.96 MeV [40].

By considering in addition the cosmological constant era, the constraints become $\sigma < 3.85 \times 10^{-9}$ kg/m^2 and 0.93 MeV. Both are in very good agreement with very rough observational constraints based just on the anisotropy constraint $\delta T/T \leq 10^{-5}$, which suggest that their energy scale should be less then 1 MeV (the original Zel'dovich bound) [38].

Even though intuitively one may expect the constraint to weaken by adding the cosmological constant era (due to the fact that there is less power on very large scales), this does not happen because there is additional power on intermediate scales. There are large error bars for small l and beyond $l = 10$ the integrated power spectra are almost equivalent.

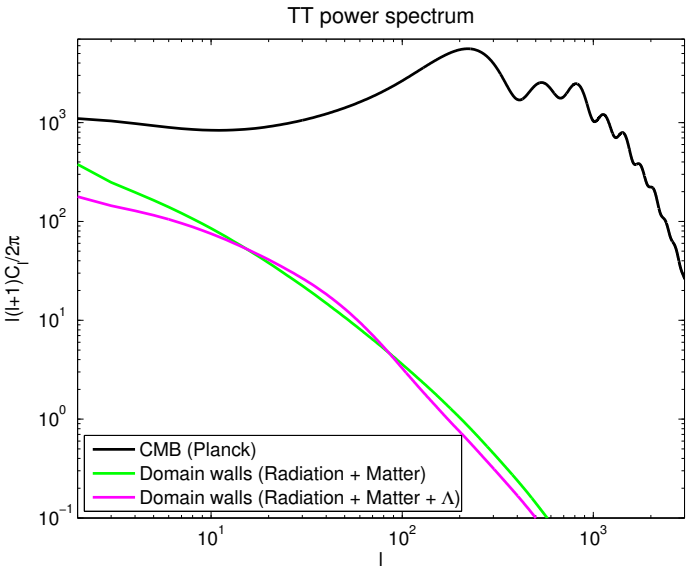

Fig. 4.6 Comparison between the CMB power spectrum (from Planck) and the power spectrum from domain walls (normalised at the 2σ value of the energy scale) in the two scenarios considered.

The values of the ΛCDM parameters do not shift significantly from the standard best fit ΛCDM *Planck* values, without domain walls. This is illustrated in Table 4.1. This is due to

the fact that the allowed contribution of domain walls is very small, because of the different shape of their temperature power spectrum.

Table 4.1 Constraints on the fitted cosmological parameters, together with 1σ error bars in a full likelihood analysis (with all relevant nuisance parameters) with and without domain walls in the case of *Planck* and WMAP polarisation in the two domain walls scenarios considered.

Parameter	No Walls	Walls (radiation & matter)	Walls (radiation, matter & Λ)
$\sigma <$ (95%)	-	0.96	0.93
H_0	67.20 ± 1.16	67.25 ± 1.18	67.31 ± 1.18
$100\Omega_b h^2$	2.202 ± 0.027	2.201 ± 0.028	2.203 ± 0.028
$\Omega_c h^2$	0.120 ± 0.003	0.119 ± 0.003	0.119 ± 0.003
τ	0.089 ± 0.013	0.088 ± 0.013	0.088 ± 0.013
$100\theta_{MC}$	1.0412 ± 0.0006	1.0412 ± 0.0006	1.0412 ± 0.0006
$\ln(10^{10} A_s)$	3.088 ± 0.025	3.085 ± 0.025	3.086 ± 0.024
n_s	0.959 ± 0.007	0.960 ± 0.007	0.960 ± 0.007

Using these values of the energy scale, we have plotted on the same graph in logarithmic scale the standard CMB *Planck* power spectrum [17] and the domain walls power spectra, normalised at the 95% confidence level for its surface density (Fig. 4.6). The plot shows that indeed the domain walls only contribute on large scales as their power spectrum is quickly decaying in l-space.

4.6 Conclusions

In this Chapter we have used high-resolution simulations based on the PRS algorithm to evaluate the energy-momentum tensor of a network of domain walls in an expanding universe, covering the radiation, matter and late-time Λ-domination eras. We have analysed how the wall network scales and we have seen that the scaling law is different to cosmic strings. We have then evaluated its unequal time correlator components in each epoch. We have used the rescaled eigenvectors and eigenvalues obtained from these correlators as sources into an Einstein-Boltzmann solver and we have thus determined the power spectrum of the domain wall network. The temperature power spectrum of the domain walls is quickly decreasing as a function of l and has its maximum where the CMB measurements have large error bars. This allows the presence of some domain walls even though the shape of their power spectrum is completely different to the one of the CMB.

We have analysed two scenarios: one where only radiation and matter eras are considered and one which involves in addition a fast-expansion rate. We have shown that although there are noticeable changes in the obtained power spectra, the CMB constraints vary insignificantly.

We have used the CMB power spectrum to find the first precise quantitative constraint on the domain wall surface density, with an energy scale of 0.93 MeV at the 95% CL for the standard Λ-cosmology. It is interesting to note that the result we have obtained is very close to the qualitative Zel'dovich bound [38].

CHAPTER 5

PERTURBATIVE AND HALO MODELS FOR THE LARGE SCALE STRUCTURE OF THE UNIVERSE

5.1 Introduction

In the previous Chapters we have been studying topological defects and their effects on the CMB. We have seen that, due to the ever-increasing accuracy of CMB experiments, cosmic defects have been severely constrained. The ΛCDM model has so far been successful in describing the properties of the Universe, as recently confirmed by the latest *Planck* satellite results [6, 7]. The initial conditions of this model are based on the assumption that all the structure in the Universe was generated by quantum fluctuations at primordial times, during an inflationary phase [138, 139]. The physics of inflation has been extensively studied in recent years and many scenarios have been proposed [140–144]; distinguishing between the numerous existing models is one of the ultimate goals of cosmology. This problem can be tackled observationally by studying the properties of the perturbations at later times: the cosmic microwave background (CMB) and the large-scale structure of the Universe (LSS).

CMB anisotropies have provided in the past two decades a wealth of cosmological information, which has been exploited with increasing efficiency by subsequent observational campaigns, up to the exquisite accuracy of the latest results from the *Planck* satellite [7]. The CMB has also provided some of the strongest constraints on inflation. On the one hand, the shape of the CMB two-point statistics (power spectrum) is directly related to the power spectrum of perturbations at the end of inflation, whose parameters and features can thus be accurately constrained [145]. On the other hand, many inflationary models predict a significant non-Gaussian component in the distribution of primordial perturbations [146]: higher-order statistics of the CMB anisotropies, such as the three-point correlation function (bispectrum) have provided strict constraints on such models [147].

Nevertheless, the CMB can primarily supply only two-dimensional data from the surface of last scattering due to its projected nature, which in temperature has been already almost fully exploited to the limit of cosmic variance by *Planck*. The LSS, traced by current and upcoming galaxy surveys, contains much more information than the CMB, due to its three-dimensional nature (the late time matter distribution as a function of redshift), and it can thus provide further complementary insight on cosmology across cosmic time. In principle, there is roughly a 1000-fold increase in the number of modes available compared to the CMB [148], but this information is more challenging to extract due to the more limited theoretical understanding of the LSS physics in the low-redshift Universe, where additional complexity is added by non-linear structure formation, the relationship between dark and visible matter (galaxy bias), and redshift-space effects [149]. Nonetheless, galaxy surveys like SDSS [150] and BOSS [151, 152] have dramatically increased our understanding of the Universe. On-going and future surveys, like DES [153, 154], LSST [155], *Euclid* [156], DESI [157], *WFIRST* [158] and the proposed SPHEREX mission [159] are expected to increase the precision of the measurements even further.

To date, most cosmological implications from large-scale structure data have been drawn from the power spectrum of the density fluctuations. At linear level, this observable encodes all the information available if the primordial random fluctuations are Gaussian. The power spectrum is also sensitive to some classes of primordial non-Gaussianity (PNG) via the scale-dependent galaxy bias [160, 161], which has been widely used to obtain competitive PNG constraints [162–167].

However, in order to fully exploit the LSS information and to test all types of PNG, it is important to also study higher-order statistics, such as the bispectrum [168–174]. Even for Gaussian initial conditions, where the primordial bispectrum is zero, non-linear coupling between Fourier modes produces a non-zero bispectrum due to gravitational collapse [175]. This gravitational bispectrum must be well understood in order to be able to separate the primordial component and to constrain the physics of inflation. At the same time, it can provide additional cosmological information [176], for example on the growth of structure [177–179], and bias parameters [177, 180–185].

Modelling the evolution of matter density perturbations beyond linear scales is a complex problem. On relatively large scales, in the quasi-linear regime, significant progress has been made using perturbative methods. Arguably, the most common procedure is Eulerian standard perturbation theory (SPT) [186–189], where the growth of structure is described by a set of differential equations in terms of the present-time density perturbations, expanded to the desired order. Alternatively, in Lagrangian perturbation theory (LPT) [190–196] the

fluid equations are written in terms of the initial density perturbations via a displacement field, which reduces to the Zel'dovich approximation at linear order [197]. Both methods have advantages and shortcomings [198–201]; in particular, SPT has a narrow range of validity at low redshift, and its series expansion shows poor convergence properties. LPT has the additional drawback that its perturbative approach can not predict clustering beyond shell crossing. For these reasons, the recent years have seen a proliferation of further developments: SPT has been re-formulated in the language of field theory by Ref. [202–207], re-organising the series expansion in terms of vertices and propagators, and improving its convergence properties (renormalised perturbation theory, RPT); this has been later simplified to the MPTBREEZE scheme [208]. Related developments include the large-N expansion [209], the closure theory [210], and renormalisation group approaches [211, 212]. A resummation technique in Lagrangian space (RLPT) was developed by Ref. [213]; subsequent extensions were developed by Refs. [213–220]. Most recently, the effective field theory of LSS (EFTofLSS) has been developed by Refs. [148, 221–228], based on the idea that the contribution of small-scale physics to the quasi-linear perturbations can be encapsulated into an set of additional, unknown source terms in the equations of motion, whose value can be fixed by comparison with N-body simulations.

In the fully non-linear regime, perturbation theories necessarily break down and numerical N-body simulations have to be used to calibrate phenomenological models of gravitational clustering, such as the halo model [229–231]. This formalism is based on the approximation that all matter in the Universe is in the form of halos, and it can be used to describe the matter power spectrum and bispectrum relatively accurately (typically better than 10% at $k < 1\,h/\mathrm{Mpc}$ at $z = 0$) [232]. It is however difficult to significantly improve the halo model accuracy beyond the limits set by its underlying assumptions, especially on intermediate scales. For this reason, Refs. [218, 233, 234] combined a revised version of the halo model, valid on small scales, with perturbative recipes that are more accurate on quasi-linear scales. A more drastic approach was introduced by Refs. [235, 236], where the physically-motivated small-scale one-halo term was replaced with a series expansion in the even powers of k, with free parameters to be calibrated on N-body simulations. It is possible to extend these ideas even further into the direction of phenomenology at the cost of a reduced physical understanding: the HALOFIT method [237, 238] achieves a higher accuracy matter power spectrum by combining halo model-inspired templates with numerous heuristic parameters fit to N-body simulations while, in the ultimate numerical and agnostic approach, matter clustering is directly calculated by interpolating over a grid of N-body simulations spanning

a range of different cosmologies [239]. No bispectrum counterpart exists to date for these numerical methods.

At the same time, there has been progress in N-body simulations studies and bispectrum estimators [173, 176, 240–243]. In contrast with the standard brute-force method of measuring the bispectrum for all possible triangular configurations, Refs. [242, 244] applied to the LSS the modal decomposition of the bispectrum introduced for CMB studies by Refs. [173, 245], thus developing a significantly faster and more efficient estimator. A simplified version tailored to estimating the projection of the simulation bispectrum on the tree-level prediction was presented in Ref. [243].

Relatively few measurements of the bispectrum from galaxy surveys exist [246–253]. The state of the art results have recently been obtained by Ref. [254, 255] from the BOSS luminous red galaxies. These data have been used to improve the power spectrum constraints on galaxy bias and structure growth; however, to date no primordial non-Gaussianity constraints exist from the LSS bispectrum.

In the literature various models for describing the LSS on mildly non-linear scales have been proposed. There are perturbative methods that try to expand the solutions of the differential equations around the linear solution. They perform well close to the linear regime, but are expected to diverge soon after.

Based on the perturbative methods, there have been various approaches that have tried to solve the problems appearing in the standard perturbation theory methods, related to poorly converging perturbative series, ultraviolet divergences etc., and that have managed to improve the range of validity of the perturbative methods.

A completely different model is the halo model, which is a phenomenological model based on the spherical gravitational collapse model. This model is only moderately accurate on large scales, but it is expected to give reliable results on smaller scales, as it models the physical phenomena involved.

In this Chapter, various models will be introduced, and their prediction for the matter power spectrum and bispectrum will be discussed, in the absence of primordial non-Gaussianity.

5.2 Perturbation theory models of Large Scale Structure

Although the structures that we observe today in the Universe are clearly not homogeneous or isotropic, on very large scales the matter density becomes almost uniform in space and hence, on these scales, a good approximation can be made by considering small perturbations to the

density and velocity fields (as discussed in Subchapter 1.2). These very large scales where structures are homogeneous represent the linear regime, and by considering perturbations to these quantities we are able to predict the matter evolution outside these regime. These methods are therefore very useful on certain scales, but eventually the perturbative expansions are no longer valid and we have to rely on either using N-body simulations, or phenomenological models calibrated to simulations in order to be able to describe the observations. A first step for the perturbative approaches is represented by the Eulerian standard perturbation theory (SPT), which is discussed in the next subchapter.

5.2.1 Standard Perturbation Theory

As the equations governing the growth of structure are non-linear and hence very difficult to solve, the perturbative approach has been developed. It consists of linearising the equations involved and then considering small perturbations around these linearised solutions. The cosmological model assumes that the large-scale structure in the Universe today is obtained as a result of the growth of primordial fluctuations through gravitational instability. These particles are non-relativistic on scales much smaller than the Hubble radius and hence they obey Newtonian equations of motion. It is also assumed that the distribution of particles is described by the Boltzmann equation. For deriving the various properties of dark matter, the following notation will be used: δ_D for the Dirac-delta function, $\mathscr{H}$ for the conformal Hubble constant. A detailed description and derivation of the perturbation theory formalism can be found in Ref. [189].

The density contrast δ and the peculiar velocity $\mathbf{u}$ are defined in terms of the average density $\bar{\rho}$ and velocity $\mathbf{v}$ as

$$\rho(\mathbf{x},\tau) = \bar{\rho}(\tau)\left[1+\delta(\mathbf{x},\tau)\right], \tag{5.1}$$

$$\mathbf{v}(\mathbf{x},\tau) = \mathscr{H}\mathbf{x} + \mathbf{u}(\mathbf{x},\tau). \tag{5.2}$$

Then the cosmological gravitational potential Φ satisfies the Poisson equation

$$\nabla^2\Phi(\mathbf{x},\tau) = \frac{3}{2}\Omega_m(\tau)\mathscr{H}^2(\tau)\delta(\mathbf{x},\tau). \tag{5.3}$$

The particle number density in phase space $f(\mathbf{x},\mathbf{p},\tau)$ satisfies the Vlasov equation

$$\frac{df}{d\tau} = \frac{\partial f}{\partial \tau} + \frac{\mathbf{p}}{ma} \cdot \nabla f - am \nabla \Phi \cdot \frac{\partial f}{\partial \mathbf{p}} = 0 \,, \tag{5.4}$$

where $\mathbf{p}$ is the momentum.

In order to obtain the spatial distribution of the particles, the moments of Eq. (5.4) can be taken by appropriate integration in momentum space. The first three momenta of interest are:

$$\int d^3\mathbf{p} f(\mathbf{x}, \mathbf{p}, \tau) = \rho(\mathbf{x}, \tau) \,, \tag{5.5}$$

$$\int d^3\mathbf{p} \frac{\mathbf{p}}{am} f(\mathbf{x}, \mathbf{p}, \tau) = \rho(\mathbf{x}, \tau) \mathbf{u}(\mathbf{x}, \tau) \,, \tag{5.6}$$

$$\int d^3\mathbf{p} \frac{p_i p_j}{am} f(\mathbf{x}, \mathbf{p}, \tau) = \rho(\mathbf{x}, \tau) u_i(\mathbf{x}, \tau) u_j(\mathbf{x}, \tau) + \sigma_{ij}(\mathbf{x}, \tau) \,. \tag{5.7}$$

Eq. (5.5) gives the continuity equation and Eqs. (5.6)-(5.7) give the Euler equation, in analogy to fluid mechanics [256]:

$$\frac{\partial \delta(\mathbf{x}, \tau)}{\partial \tau} + \nabla \cdot [(1 + \delta(\mathbf{x}, \tau)) \mathbf{u}(\mathbf{x}, \tau)] = 0 \,, \tag{5.8}$$

$$\frac{\partial \mathbf{u}(\mathbf{x}, \tau)}{\partial \tau} + \mathscr{H} \mathbf{u}(\mathbf{x}, \tau) + \mathbf{u}(\mathbf{x}, \tau) \cdot \nabla \mathbf{u}(\mathbf{x}, \tau) = -\nabla \Phi(\mathbf{x}, \tau) - \frac{1}{\rho} \nabla_j \left(\rho \sigma_{ij} \right) \,. \tag{5.9}$$

On large scales, the Universe is expected to be smooth and hence Eqs. (5.8) and (5.9) can be linearised. By defining the divergence and vorticity of the velocity field as

$$\theta(\mathbf{x}, \tau) = \nabla \cdot \mathbf{u}(\mathbf{x}, \tau) \,, \tag{5.10}$$

$$\mathbf{w}(\mathbf{x}, \tau) = \nabla \times \mathbf{u}(\mathbf{x}, \tau) \,, \tag{5.11}$$

they satisfy the following differential equations:

$$\frac{\partial \delta(\mathbf{x}, \tau)}{\partial \tau} + \theta(\mathbf{x}, \tau) = 0 \,, \tag{5.12}$$

$$\frac{\partial \theta(\mathbf{x}, \tau)}{\partial \tau} + \mathscr{H}(\tau) \theta(\mathbf{x}, \tau) + \frac{3}{2} \Omega_m(\tau) \mathscr{H}^2(\tau) \delta(\mathbf{x}, \tau) = 0 \,, \tag{5.13}$$

$$\frac{\partial \mathbf{w}(\mathbf{x}, \tau)}{\partial \tau} + \mathscr{H}(\tau) \mathbf{w}(\mathbf{x}, \tau) = 0 \,, \tag{5.14}$$

in the absence of velocity dispersion or pressure, which is the case for cold dark matter ($\sigma_{ij} = 0$). The vorticity quickly decays in time due to the expansion of the Universe and hence it can be ignored.

In SPT, the assumption made is that the density and velocity fluctuations can be expanded in terms of the linear solution as

$$\delta(\mathbf{x},\tau) = \sum_{n=1}^{\infty} \delta^{(n)}(\mathbf{x},\tau) \,, \tag{5.15}$$

$$\theta(\mathbf{x},\tau) = \sum_{n=1}^{\infty} \theta^{(n)}(\mathbf{x},\tau) \,, \tag{5.16}$$

where $\delta^{(n)}$ and $\theta^{(n)}$ are functions of the n^{th} power of δ and θ respectively.

Taking the Fourier Transform of Eqs. (5.8) and (5.9) (and the divergence for the latter with Eq. (5.10)) and using the expansions (5.15) and (5.16), the following equations are obtained:

$$\frac{\partial\tilde{\delta}(\mathbf{k},\tau)}{\partial\tau} + \tilde{\theta}(\mathbf{k},\tau) = -\int d^3\mathbf{k}_1\mathbf{k}_2\delta_D(\mathbf{k}-\mathbf{k}_{12})\alpha(\mathbf{k}_1,\mathbf{k}_2)\,\tilde{\theta}(\mathbf{k}_1,\tau)\,\tilde{\delta}(\mathbf{k}_2,\tau) \,, \tag{5.17}$$

$$\frac{\partial\tilde{\theta}(\mathbf{k},\tau)}{\partial\tau} + \mathscr{H}\tilde{\theta}(\mathbf{k},\tau) + \frac{3}{2}\Omega_m\mathscr{H}^2\tilde{\delta}(\mathbf{k},\tau) = -\int d^3\mathbf{k}_1\mathbf{k}_2\delta_D(\mathbf{k}-\mathbf{k}_{12})\,\beta(\mathbf{k}_1,\mathbf{k}_2)\tilde{\theta}(\mathbf{k}_1,\tau)\,\tilde{\theta}(\mathbf{k}_2,\tau) \,, \tag{5.18}$$

where $\mathbf{k}_{12} = \mathbf{k}_1 + \mathbf{k}_2$ and

$$\alpha(\mathbf{k}_1,\mathbf{k}_2) = \frac{\mathbf{k}_{12}\cdot\mathbf{k}_1}{k_1^2} \,, \tag{5.19}$$

$$\beta(\mathbf{k}_1,\mathbf{k}_2) = \frac{k_{12}(\mathbf{k}_1\cdot\mathbf{k}_2)}{2k_1^2k_2^2} \,. \tag{5.20}$$

In a ΛCDM universe, Eqs. (5.17) and (5.18) can be solved with the expansions

$$\tilde{\delta}(\mathbf{k},\tau) = \sum_{n=1}^{\infty} D^n(a)\,\delta_n(\mathbf{k}) \,, \tag{5.21}$$

$$\tilde{\theta}(\mathbf{k},\tau) = -\mathscr{H}\sum_{n=1}^{\infty} D^n(a)\,\theta_n(\mathbf{k}) \,, \tag{5.22}$$

with $D(a)$ the linear growth factor and δ_n and θ_n given in terms of the expansions:

$$\delta_n(\mathbf{k}) = \int d^3\mathbf{q}_1\cdots\int d^3\mathbf{q}_n F_n(\mathbf{q}_1\cdots\mathbf{q}_n)\,\delta_1(\mathbf{q}_1)\cdots\delta_1(\mathbf{q}_n)\,\delta_D(\mathbf{k}-\mathbf{q}_1-\cdots-\mathbf{q}_n) \,, \tag{5.23}$$

$$\theta_n(\mathbf{k}) = \int d^3\mathbf{q}_1\cdots\int d^3\mathbf{q}_n G_n(\mathbf{q}_1\cdots\mathbf{q}_n)\,\delta_1(\mathbf{q}_1)\cdots\delta_1(\mathbf{q}_n)\,\delta_D(\mathbf{k}-\mathbf{q}_1-\cdots-\mathbf{q}_n) \,. \tag{5.24}$$

The time dependence of Eqs. (5.21) and (5.22) is only exact in an Einstein-de Sitter Universe, with $\Omega_m = 1$ and $\Omega_\Lambda = 0$. Nevertheless, the approximation is still accurate within a few percent for a more realistic universe [189]. In what follows, $D(a)$ and $D(z)$ will be used interchangeably, using the relation between the scalefactor and redshift $1+z = \frac{1}{a}$. The functions F_n and G_n are called kernels. They are homogeneous functions of the wavevectors and are given in terms of Eqs. (5.19) and (5.20) in the following recurrence relations:

$$F_1 = 1\,, \tag{5.25}$$

$$G_1 = 1\,, \tag{5.26}$$

$$\begin{aligned} F_n(\mathbf{q}_1,\cdots,\mathbf{q}_n) &= \sum_{m=1}^{n-1} \frac{G_m(\mathbf{q}_1,\cdots,\mathbf{q}_m)}{(2n+3)(n-1)} \\ &\times \left[(2n+1)\,\alpha(\mathbf{k}_1,\mathbf{k}_2)\,F_{n-m}(\mathbf{q}_{m+1},\cdots,\mathbf{q}_n) + 2\beta(\mathbf{k}_1,\mathbf{k}_2)\,G_{n-m}(\mathbf{q}_{m+1},\cdots,\mathbf{q}_n)\right], \end{aligned} \tag{5.27}$$

$$\begin{aligned} G_n(\mathbf{q}_1,\cdots,\mathbf{q}_n) &= \sum_{m=1}^{n-1} \frac{G_m(\mathbf{q}_1,\cdots,\mathbf{q}_m)}{(2n+3)(n-1)} \\ &\times \left[3\alpha(\mathbf{k}_1,\mathbf{k}_2)\,F_{n-m}(\mathbf{q}_{m+1},\cdots,\mathbf{q}_n) + 2n\beta(\mathbf{k}_1,\mathbf{k}_2)\,G_{n-m}(\mathbf{q}_{m+1},\cdots,\mathbf{q}_n)\right], \end{aligned} \tag{5.28}$$

with $\mathbf{k}_1 = \mathbf{q}_1 + \cdots + \mathbf{q}_m$ and $\mathbf{k}_2 = \mathbf{q}_{m+1} + \cdots + \mathbf{q}_n$. For the correlation functions, the symmetrised versions of these functions are required,

$$F_n^{(s)}(\mathbf{q}_1,\cdots,\mathbf{q}_n) = \frac{1}{n!} \sum_{\text{permutations}} F_n(\mathbf{q}_1,\cdots,\mathbf{q}_n)\,. \tag{5.29}$$

In up to one-loop calculations for the power and bispectrum, only the expressions up to $n = 4$ for F_n are required. The explicit expressions for F_3 and F_4 are given in Ref. [187]. For F_2, the expression is:

$$F_2^{(s)}(\mathbf{q}_1,\mathbf{q}_2) = \frac{5}{7} + \frac{1}{2}\frac{\mathbf{q}_1\cdot\mathbf{q}_2}{q_1 q_2}\left(\frac{q_1}{q_2}+\frac{q_2}{q_1}\right) + \frac{2}{7}\frac{(\mathbf{q}_1\cdot\mathbf{q}_2)^2}{q_1^2 q_2^2}\,. \tag{5.30}$$

$F_2^{(s)}$ kernel calculation

Here we show how the expression for the kernel $F_2^{(s)}$ can be derived from first principles. Considering a matter-only universe, with $\Omega_m = 1$, $a = \tau^2$ and $\mathscr{H} = \frac{2}{\tau}$, Eqs. (5.17, 5.18) become

$$\delta' + \theta = -I_1[\delta,\theta]\,, \tag{5.31}$$

$$\theta' + \frac{2}{\tau}\theta + \frac{6}{\tau^2}\delta = -I_2[\delta, \theta]\,, \tag{5.32}$$

where I_1 and I_2 are the expressions on the r.h.s. of Eqs. (5.17, 5.18). Expanding δ and θ to second order, one obtains the following equations:

$$\delta = \tau^2\delta_1 + \tau^4\delta_2\,, \tag{5.33}$$
$$\delta' = 2\tau\delta_1 + 4\tau^3\delta_2\,, \tag{5.34}$$
$$\theta = -2\tau\theta_1 - 2\tau^3\theta_2\,, \tag{5.35}$$
$$\theta' = -2\theta_1 - 6\tau^2\theta_2\,. \tag{5.36}$$

For $n = 1$, I_1 and I_2 are second-order quantities and hence Eqs. (5.31, 5.32) are solved by $\theta_1 = \delta_1$. For $n = 2$, one has to use the first-order solutions for the integrals on the r.h.s. of the expressions, and the following equations are obtained:

$$4\tau^3\delta_2 - 2\tau^3\theta_2 = -I_1[\tau^2\delta_1, -2\tau\delta_1]\,, \tag{5.37}$$
$$-10\tau^2\theta_2 + 6\tau^2\delta_2 = -I_2[\tau^2\delta_1, -2\tau\delta_1]\,. \tag{5.38}$$

By solving the above equations for δ_2 and substituting the integral expressions I_1 and I_2 and α (Eq. 5.19) and β (Eq. 5.20), one finds the integral expression

$$\delta_2(\mathbf{k}) = \int d^3\mathbf{q}_1 \int d^3\mathbf{q}_2 \delta_D(\mathbf{k} - \mathbf{q}_1 - \mathbf{q}_2) \left[\frac{5}{7} + \frac{2}{7}\frac{(\mathbf{q}_1\cdot\mathbf{q}_2)^2}{q_1^2 q_2^2} + \frac{\mathbf{q}_1\cdot\mathbf{q}_2}{7}\left(\frac{6}{q_1^2} + \frac{1}{q_2^2}\right)\right]. \tag{5.39}$$

The expression of $F_2^{(s)}$ from Eq. (5.30) is finally obtained by symmetrisation over the arguments $\mathbf{q}_1$ and $\mathbf{q}_2$.

One-loop power spectrum and bispectrum contributions

The 2- and 3-point correlation functions are defined as

$$\langle \delta(\mathbf{k}_1)\,\delta(\mathbf{k}_2)\rangle = (2\pi)^3\,\delta_D(\mathbf{k}_1 + \mathbf{k}_2)\,P(k)\,, \tag{5.40}$$
$$\langle \delta(\mathbf{k}_1)\,\delta(\mathbf{k}_2)\,\delta(\mathbf{k}_3)\rangle = (2\pi)^3\,\delta_D(\mathbf{k}_1 + \mathbf{k}_2 + \mathbf{k}_3)\,B(k_1, k_2, k_3)\,. \tag{5.41}$$

In order to obtain the required contributions to the power spectrum and bispectrum, one needs to plug in the expansion (5.23) into (5.21) and then the final result into Eq. (5.40) and (5.41) respectively. The full expansion is then grouped according to the number of δ_1's involved. The loop expansion is in analogy with the loop diagrams from quantum field theory.

It represents an intuitive manner of determining all the contributions at each order in the expansion. In this diagrammatic expansion, the exterior lines represent the arguments of the correlation function, vertices where n lines meet are the kernels F_n, and the interior lines represent wavevectors which are integrated over. As usual, the sum of wavevectors into any vertex should be 0 and numerical factors in front of each diagram represents its symmetry. The numbers appearing in the name of each contribution represents the number of interior lines in each of its vertices. In the next few paragraphs, we show the expressions for the power spectrum and bispectrum up to one loop, in the absence of primordial non-Gaussianity.

In the case of the power spectrum, the one-loop contribution has been obtained in Ref. [188]. The 0-loop contribution is simply the linear power spectrum,

$$P_{\text{0-loop}}(k,z) = P_{11}(k,z) = D^2(z) P_{\text{lin}}(k) . \tag{5.42}$$

It can be evaluated by evolving the primordial fluctuations through the Boltzmann equations through codes such as CAMB [31]. The 1-loop contribution can be obtained from two diagrams and has the following expansion:

$$P_{\text{1-loop}}(k,z) = P_{13}(k,z) + P_{22}(k,z) , \tag{5.43}$$

where the two contributions have the following expressions:

$$P_{13}(k,z) = D^4(z) \int \frac{d^3q}{(2\pi)^3} 6 P_{\text{lin}}(k) P_{\text{lin}}(q) F_3^{(s)}(\mathbf{k},\mathbf{q},-\mathbf{q}) , \tag{5.44}$$

$$P_{22}(k,z) = D^4(z) \int \frac{d^3q}{(2\pi)^3} 2 P_{\text{lin}}(q) P_{\text{lin}}(|\mathbf{k}-\mathbf{q}|) \left[F_2^{(s)}(\mathbf{q},\mathbf{k}-\mathbf{q})\right]^2 . \tag{5.45}$$

For the 2-loop power spectrum there are 4 terms, which involve kernels up to F_5. The expressions involved are shown in detail in Refs. [224, 257].

For the bispectrum, the lowest order contribution, corresponding to no loops is called the tree-level bispectrum and has the following expression:

$$B_{\text{tree}}(k_1,k_2,k_3) = D^4(z) P_{\text{lin}}(k_1) P_{\text{lin}}(k_2) F_2^{(s)}(\mathbf{k}_1,\mathbf{k}_2) + 2 \text{ permutations} . \tag{5.46}$$

For the 1-loop bispectrum, there are 4 diagrams that can be drawn,

$$B_{\text{1-loop}} = B_{222} + B_{321}^{(I)} + B_{321}^{(II)} + B_{411} . \tag{5.47}$$

These have the following expressions:

$$B_{222}(k_1,k_2,k_3) = 8D^6(z)\int_{\mathbf{q}} P_{\rm lin}(q)\,P_{\rm lin}(|\mathbf{k}_2-\mathbf{q}|) \times P_{\rm lin}(|\mathbf{k}_3+\mathbf{q}|)\,F_2^{(s)}(-\mathbf{q},\mathbf{k}_3+\mathbf{q})\,F_2^{(s)}(\mathbf{k}_3+\mathbf{q},\mathbf{k}_2-\mathbf{q})\,F_2^{(s)}(\mathbf{k}_2-\mathbf{q},\mathbf{q})\,, \tag{5.48}$$

$$B_{321}^{(I)}(k_1,k_2,k_3) = 6D^6(z)\,P_{\rm lin}(k_3)\int_{\mathbf{q}} P_{\rm lin}(|\mathbf{k}_2-\mathbf{q}|) \times P_{\rm lin}(q)\,F_3^{(s)}(-\mathbf{q},-\mathbf{k}_2+\mathbf{q},-\mathbf{k}_3)\,F_2^{(s)}(\mathbf{k}_2-\mathbf{q},\mathbf{q}) + 5\text{ permutations}\,, \tag{5.49}$$

$$B_{321}^{(II)}(k_1,k_2,k_3) = 6D^6(z)\,P_{\rm lin}(k_2)\,P_{\rm lin}(k_3)\,F_2^{(s)}(\mathbf{k}_2,\mathbf{k}_3) \times \int_{\mathbf{q}} P_{\rm lin}(q)\,F_3^{(s)}(\mathbf{k}_3,\mathbf{q},-\mathbf{q}) + 5\text{ permutations}\,, \tag{5.50}$$

$$B_{411}(k_1,k_2,k_3) = 12D^6(z)\,P_{\rm lin}(k_2)\,P_{\rm lin}(k_3) \times \int_{\mathbf{q}} P_{\rm lin}(q)\,F_4^{(s)}(\mathbf{q},-\mathbf{q},-\mathbf{k}_2,-\mathbf{k}_3) + 2\text{ permutations}\,, \tag{5.51}$$

where $\int_{\mathbf{q}} = \int \frac{d^3q}{(2\pi)^3}$. The actual numerical evaluation of the integrals (5.44)-(5.51) is non-trivial because the kernels may diverge. It has been shown [258, 259] that the divergences exactly cancel each other when summing the whole one-loop contributions together, both in the power spectrum and bispectrum, provided that the linear power spectrum grows slowly enough on very large scales. However, for the numerical evaluation, a method to remove the divergences must be used. For the power spectrum at one loop only, a convenient split of the integration regions has been used in Ref. [188] which solves the divergence problems. More recently, both the power spectrum and bispectrum divergences have been eliminated in Refs. [223, 224, 260]. Their method will be briefly explained in the next paragraphs.

For Eqs. (5.44)-(5.51) it can be easily seen that the divergences appear at 0 and $\pm\mathbf{k}_i$. The basic idea of the method is to first perform a convenient change of variable in order to first move all the divergences to 0 and then, as the variable of integration spans all space, to do a symmetrisation in $\mathbf{q} \leftrightarrow -\mathbf{q}$. For the power spectrum, this method yields

$$\begin{aligned} P_{\text{1-loop}}(k,z) = D^4(z)\int \frac{d^3q}{(2\pi)^3}\Big[&6P_{\rm lin}(k)\,P_{\rm lin}(q)\,F_3^{(s)}(\mathbf{k},\mathbf{q},-\mathbf{q}) \\ &+ 2P_{\rm lin}(q)\,P_{\rm lin}(|\mathbf{k}-\mathbf{q}|)\left[F_2^{(s)}(\mathbf{q},\mathbf{k}-\mathbf{q})\right]^2\Theta(|\mathbf{k}-\mathbf{q}|-q) \\ &+ 2P_{\rm lin}(q)\,P_{\rm lin}(|\mathbf{k}+\mathbf{q}|)\left[F_2^{(s)}(-\mathbf{q},\mathbf{k}+\mathbf{q})\right]^2\Theta(|\mathbf{k}+\mathbf{q}|-q)\Big]\,, \end{aligned} \tag{5.52}$$

where Θ is the Heaviside step function. For the bispectrum, $B_{321}^{(II)}$ and B_{411} only have divergences at 0 and hence do not need any change of variable. The integrand b_{222} of B_{222} needs to be re-expressed in the following manner [260]:

$$\begin{aligned}
b_{222}^{(k_3>k_1)} =& 8P_{\rm lin}(q)P_{\rm lin}(|\mathbf{k}_2-\mathbf{q}|)P_{\rm lin}(|\mathbf{k}_3+\mathbf{q}|)F_2^{(s)}(-\mathbf{q},\mathbf{k}_3+\mathbf{q})F_2^{(s)}(\mathbf{k}_3+\mathbf{q},\mathbf{k}_2-\mathbf{q}) \\
&\times F_2^{(s)}(\mathbf{k}_2-\mathbf{q},\mathbf{q})\Theta(|\mathbf{k}_2-\mathbf{q}|-q)\Theta(|\mathbf{k}_3+\mathbf{q}|-q) \\
&+8P_{\rm lin}(|\mathbf{k}_3+\mathbf{q}|)P_{\rm lin}(|-\mathbf{k}_1+\mathbf{q}|)P_{\rm lin}(q)F_2^{(s)}(\mathbf{k}_3+\mathbf{q},-\mathbf{q})F_2^{(s)}(-\mathbf{q},-\mathbf{k}_1+\mathbf{q}) \\
&\times F_2^{(s)}(-\mathbf{k}_1+\mathbf{q},-\mathbf{q}-\mathbf{k}_3)\Theta(|-\mathbf{k}_1+\mathbf{q}|-|\mathbf{k}_3+\mathbf{q}|)\Theta(|\mathbf{k}_3+\mathbf{q}|-q) \\
&+8P_{\rm lin}(|\mathbf{k}_2-\mathbf{q}|)P_{\rm lin}(q)P_{\rm lin}(|\mathbf{k}_1+\mathbf{q}|)\times F_2^{(s)}(-\mathbf{k}_2+\mathbf{q},-\mathbf{k}_1-\mathbf{q})F_2^{(s)}(-\mathbf{k}_1-\mathbf{q},\mathbf{q}) \\
&\times F_2^{(s)}(\mathbf{q},\mathbf{k}_2-\mathbf{q})\Theta(|\mathbf{k}_2-\mathbf{q}|-q)\Theta(|\mathbf{k}_1+\mathbf{q}|-|\mathbf{k}_2-\mathbf{q}|) \\
&+8P_{\rm lin}(|\mathbf{k}_2-\mathbf{q}|)P_{\rm lin}(\mathbf{q})P_{\rm lin}(|\mathbf{k}_1+\mathbf{q}|)F_2^{(s)}(-\mathbf{k}_2+\mathbf{q},-\mathbf{k}_1-\mathbf{q}) \\
&\times F_2^{(s)}(-\mathbf{k}_1-\mathbf{q},\mathbf{q})F_2^{(s)}(\mathbf{q},\mathbf{k}_2-\mathbf{q})\Theta(|\mathbf{k}_2-\mathbf{q}|-q)\Theta(|\mathbf{k}_2-\mathbf{q}|-|\mathbf{k}_1+\mathbf{q}|) \quad (5.53)
\end{aligned}$$

$$b_{222}^{(k_3<k_1)} = b_{222}^{(k_3>k_1)}\Big|_{\mathbf{k}_1\leftrightarrow\mathbf{k}_3} , \quad (5.54)$$

with the note that this expression is only valid under the integral sign due to the various remapping. Similarly, b_{321}^I becomes:

$$b_{321}^I \to 2b_{321}^I\Theta\left(|\mathbf{k}_2-\mathbf{q}|-q\right) . \quad (5.55)$$

The sum of the 4 contributions is then calculated by performing the integrals directly. They can be calculated numerically fast using the multi-dimensional integrator CUBA [261].

5.2.2 Effective Field Theory

The SPT approach has so far been successful in describing the evolution of perturbations close to the linear scale at just 1- and 2-loop level. However, going to a higher number of loops may not allow us to go more into the non-linear regime. At non-linear level the Fourier modes no longer evolve independently, and hence small scale fluctuation can influence much larger scales. Moreover, the SPT expansion can only be expected to work when the density contrast is small, $|\delta| \ll 1$. Even when this condition is not satisfied, the gravitational potential is still small and can be used to produce a valid perturbative expansion. In order to cure these issues, the Effective Field Theory of LSS (EFTofLSS) has been developed in Refs. [148, 221].

The method consists of adding an effective stress-energy tensor $\tau_{\mu\nu}$, induced by short wavelength modes. This has the effect of adding corrections to the fluid equations, with terms corresponding to the speed of sound, viscosity and stochastic pressure. The equations governing this effective field theory are obtained by considering the collisionless Boltzmann equation in an expanding universe and smoothing it on a lengthscale Λ^{-1}. Hence, the theory is determined by the equations of motion of the long-wavelength modes, sourced by a stress-energy tensor. In the absence of the stress-energy tensor, the SPT equations (5.12)-(5.14) are recovered.

The linearised equations of motion become:

$$\nabla^2\phi_l = \frac{3}{2}H_0^2\Omega_m\frac{\delta_l}{a}\,, \tag{5.56}$$

$$\dot{\delta}_l = -\frac{1}{a}\partial_i\left[(1+\delta_l)\,\mathrm{v}_l^i\right]\,, \tag{5.57}$$

$$\dot{\mathrm{v}}_l^i + H\mathrm{v}_l^i + \frac{1}{a}\mathrm{v}_l^j\partial_j\mathrm{v}_l^i + \frac{1}{a}\partial^i\phi_l = -\frac{1}{a}\left(\partial\tau\right)^i_{\rho_l}\,, \tag{5.58}$$

where $(\partial\tau)^i_{\rho_l} = \frac{1}{\delta_l}\partial_j\tau^{ij}$. The velocity field v_l is however not the physical field, and is sensitive to short distance physics. Therefore it has to be renormalised by adding suitable counterterms, otherwise correlation functions involving it may get arbitrary large contributions.

In order to simplify the calculation, it is convenient to decompose the velocity into its divergence (θ) and curl (ω_i) parts,

$$\mathrm{v}^i = \frac{\partial^i}{\partial^2}\theta - \varepsilon^{ijk}\frac{\partial_j}{\partial^2}\omega_k\,. \tag{5.59}$$

By re-expressing the velocity using Eq. (5.59) in Eqs. (5.56)-(5.58), it is shown that the linear solution for ω decays in time as the scale factor, and hence it can be safely ignored. By expressing the equations in Fourier space and the derivatives in terms of the scale factor a, the equations became:

$$a\mathscr{H}\delta'(a,\mathbf{k}) + \theta(a,\mathbf{k}) = -\int\frac{d^3q}{(2\pi)^3}\alpha(\mathbf{q},\mathbf{k}-\mathbf{q})\delta(a,\mathbf{k}-\mathbf{q})\theta(a,\mathbf{q})\,, \tag{5.60}$$

$$\begin{aligned} a\mathscr{H}\theta'(a,\mathbf{k}) + \mathscr{H}\theta(a,\mathbf{k}) + \frac{3}{2}\mathscr{H}_0^2\Omega_m\frac{1}{a}\delta(a,\mathbf{k}) = \\ -\int\frac{d^3q}{(2\pi)^3}\beta(\mathbf{q},\mathbf{k}-\mathbf{q})\theta(a,\mathbf{k}-\mathbf{q})\theta(a,\mathbf{q}) - ik_i(\partial\tau)^i_{\rho_l}(\mathbf{k})\,, \end{aligned} \tag{5.61}$$

where the functions α and β are the ones from Eqs. (5.19)-(5.20). By writing the term involving $\partial\tau$ using the Poisson equation, full details being given in Refs. [148, 224, 260],

these equations can be solved similarly to their SPT counterparts:

$$\delta(a,\mathbf{k}) = \sum_{n=1}^{\infty} D^n(a)\delta^{(n)}(\mathbf{k}) + \sum_{n=1}^{\infty} D^{n+\zeta}(a)\tilde{\delta}^{(n)}(\mathbf{k}), \tag{5.62}$$

$$\theta(a,\mathbf{k}) = \sum_{n=1}^{\infty} D^n(a)\theta^{(n)}(\mathbf{k}) + \sum_{n=1}^{\infty} D^{n+\zeta}(a)\tilde{\theta}^{(n)}(\mathbf{k}), \tag{5.63}$$

where $\delta^{(n)}$ and $\theta^{(n)}$ can be expressed in terms of the kernels F_n and G_n (Eqs. 5.23-5.28), while the tilded expressions can be expressed similarly, but $\tilde{F}_n$ and $\tilde{G}_n$ satisfy slightly more complicated expressions:

$$\tilde{F}_1 = 1, \tag{5.64}$$

$$\tilde{G}_1 = 1, \tag{5.65}$$

$$\tilde{F}_n(\mathbf{q}_1,\cdots,\mathbf{q}_n) = \frac{1}{(n-1+\zeta)(n+\frac{3}{2}+\zeta)} \times \left\{-\xi\bar{c}_n k^2 F_n(\mathbf{q}_1,\cdots,\mathbf{q}_n) + \right.$$
$$\left. \sum_{m=1}^{n-1}\left[\left(n+\frac{1}{2}+\zeta\right)\alpha(\mathbf{k}_1,\mathbf{k}_2)\mathscr{A}_m(\mathbf{q}_1,\cdots,\mathbf{q}_n) + \beta(\mathbf{k}_1,\mathbf{k}_2)\mathscr{B}_m(\mathbf{q}_1,\cdots,\mathbf{q}_n)\right]\right\}, \tag{5.66}$$

$$\tilde{G}_n(\mathbf{q}_1,\cdots,\mathbf{q}_n) = \frac{1}{(n-1+\zeta)(n+\frac{3}{2}+\zeta)} \times \left\{-\xi(n+\zeta)\bar{c}_n k^2 F_n(\mathbf{q}_1,\cdots,\mathbf{q}_n) + \right.$$
$$\left. \sum_{m=1}^{n-1}\left[\frac{3}{2}\alpha(\mathbf{k}_1,\mathbf{k}_2)\mathscr{A}_m(\mathbf{q}_1,\cdots,\mathbf{q}_n) + (n+\zeta)\beta(\mathbf{k}_1,\mathbf{k}_2)\mathscr{B}_m(\mathbf{q}_1,\cdots,\mathbf{q}_n)\right]\right\}, \tag{5.67}$$

where the functions $\mathscr{A}_m$ and $\mathscr{B}_m$ are given recursively by

$$\mathscr{A}_m(\mathbf{q}_1,\cdots,\mathbf{q}_m) = \tilde{G}_m(\mathbf{q}_1,\cdots,\mathbf{q}_m)F_{n-m}(\mathbf{q}_{m+1},\cdots,\mathbf{q}_n)$$
$$+G_m(\mathbf{q}_1,\cdots,\mathbf{q}_m)\tilde{F}_{n-m}(\mathbf{q}_{m+1},\cdots,\mathbf{q}_n), \tag{5.68}$$

$$\mathscr{B}_m(\mathbf{q}_1,\cdots,\mathbf{q}_m) = \tilde{G}_m(\mathbf{q}_1,\cdots,\mathbf{q}_m)G_{n-m}(\mathbf{q}_{m+1},\cdots,\mathbf{q}_n)$$
$$+G_m(\mathbf{q}_1,\cdots,\mathbf{q}_m)\tilde{G}_{n-m}(\mathbf{q}_{m+1},\cdots,\mathbf{q}_n) \tag{5.69}$$

and $\bar{c}_n$, ζ and ξ are constants. ξ is a multiplicative factor for $\bar{c}_n$ and hence it can be set to a convenient value, while the numerical value of ζ can be chosen on physical grounds. In order to keep the theory local in time, $\bar{c}_n = \bar{c}_1$ for all n, which is proportional to the sound speed $c^2_{s(1)}$. The lowest level counterterm that appears in the matter power spectrum is the 2-point correlation function between $\delta^{(1)}$ and $\tilde{\delta}^{(1)}$. Setting $\xi = \zeta(\zeta+5/2)$, this lowest order counterterm can be expressed in terms of a single free parameter, the sound speed $c^2_{s(1)}$.

The linear and SPT 1-loop contribution remain, and one term is added [224],

$$-2\left(2\pi\right)c_{s(1)}^{2}\frac{k^{2}}{k_{\mathrm{NL}}^{2}}D^{2+\zeta}\left(z\right)P_{\mathrm{lin}}\left(k\right). \tag{5.70}$$

The free parameter is fixed by fitting the 1-loop EFT power spectrum to the non-linear power spectrum at a low value of k, where the SPT result is still valid, while ζ is fixed by looking at the redshift-evolution of the power spectrum, and a value of $\zeta = 3.1$ is found to best fit simulations as well as scaling properties of the Universe.

For the bispectrum, the coefficient described in the previous paragraph describes the tree level counter-term, which has the following expression:

$$\begin{aligned} B_{c_s}\left(k_1,k_2,k_3\right) = D\left(z\right)^{2+\zeta}\Big[&2P_{\mathrm{lin}}\left(k_1\right)P_{\mathrm{lin}}\left(k_2\right)\tilde{F}_2^{(s)}\left(\mathbf{k}_1,\mathbf{k}_2\right) + 2 \text{ permutations} \\ &-2\bar{c}_1 k_1^2 P_{\mathrm{lin}}\left(k_1\right)P_{\mathrm{lin}}\left(k_2\right)F_2^{(s)}\left(\mathbf{k}_1,\mathbf{k}_2\right) + 5 \text{ permutations}\Big], \end{aligned} \tag{5.71}$$

where $\bar{c}_1 = 2\pi\frac{c_{s(1)}^2}{k_{\mathrm{NL}}}$.

5.2.3 Renormalised Perturbation Theory

Formalism

The Renormalized perturbation theory (RPT) model has been developed in Refs. [203–208]. The method uses the formalism of the SPT and re-organises the infinite expansion differently using an idea presented in Ref. [202]. SPT is not a classical type of perturbation theory, as its coupling constant may be large, and hence the range of scales where it is valid depends on number of factors, such as the redshift, the primordial perturbation spectrum and the order of the correlation functions of interest. Hence, using the notation from SPT and defining $\eta = \log a\left(\tau\right)$, the following 2-component vector is defined:

$$\Psi\left(\mathbf{k},\eta\right) = \left(\delta\left(\mathbf{k},\eta\right), -\theta\left(\mathbf{k},\eta\right)/\mathscr{H}\right). \tag{5.72}$$

Then Eqs. (5.17)-(5.18) can be recast in the following matrix notation:

$$\partial_\eta\Psi_a\left(\mathbf{k},\eta\right) + \Omega_{ab}\Psi_b\left(\mathbf{k},\eta\right) = \gamma_{abc}^{(s)}\left(\mathbf{k},\mathbf{k}_1,\mathbf{k}_2\right)\Psi_b\left(\mathbf{k}_1,\eta\right)\Psi_c\left(\mathbf{k}_2,\eta\right), \tag{5.73}$$

where repeated Fourier arguments (here $\mathbf{k}_1$ and $\mathbf{k}_2$) are integrated over,

$$\Omega_{ab} = \begin{pmatrix} 0 & -1/2 \\ -3/2 & 1/2 \end{pmatrix} \tag{5.74}$$

and $\gamma^{(s)}_{abc}$ is a symmetrised vertex matrix which has the following non-zero components:

$$\gamma^{(s)}_{121}(\mathbf{k},\mathbf{k}_1,\mathbf{k}_2) = \delta_D(\mathbf{k}-\mathbf{k}_1-\mathbf{k}_2)\,\alpha(\mathbf{k}_1,\mathbf{k}_2)/2, \tag{5.75}$$

$$\gamma^{(s)}_{112}(\mathbf{k},\mathbf{k}_1,\mathbf{k}_2) = \delta_D(\mathbf{k}-\mathbf{k}_1-\mathbf{k}_2)\,\alpha(\mathbf{k}_2,\mathbf{k}_1)/2, \tag{5.76}$$

$$\gamma^{(s)}_{222}(\mathbf{k},\mathbf{k}_1,\mathbf{k}_2) = \delta_D(\mathbf{k}-\mathbf{k}_1-\mathbf{k}_2)\,\beta(\mathbf{k}_1,\mathbf{k}_2)\,, \tag{5.77}$$

and the following symmetry:

$$\gamma^{(s)}_{abc}(\mathbf{k},\mathbf{k}_i,\mathbf{k}_j) = \gamma^{(s)}_{acb}(\mathbf{k},\mathbf{k}_j,\mathbf{k}_i)\,. \tag{5.78}$$

A solution to Eq. (5.73) can be given in terms of an inverse Laplace transform,

$$\Psi_a(\mathbf{k},\eta) = g_{ab}(\eta)\,\phi_b(\mathbf{k}) + \int_0^\eta d\eta' g_{ab}(\eta-\eta')\,\gamma^{(s)}_{bcd}(\mathbf{k},\mathbf{k}_1,\mathbf{k}_2)\,\Psi_c(\mathbf{k}_1,\eta')\,\Psi_d(\mathbf{k}_2,\eta')\,, \tag{5.79}$$

where

$$\phi_a(\mathbf{k}) \equiv \Psi_a(\mathbf{k},\eta=0) \tag{5.80}$$

and

$$\sigma_{ab}(\omega) = \frac{1}{(2\omega+3)(\omega-1)}\begin{pmatrix} 2\omega+1 & 2 \\ 3 & 2\omega \end{pmatrix} \tag{5.81}$$

and g_{ab} is the linear propagator, defined for positive η as

$$g_{ab}(\eta) = \oint_{c-i\infty}^{c+i\infty}\frac{d\omega}{2\pi i}\sigma_{ab}(\omega)\,e^{\omega\eta} = \frac{e^\eta}{5}\begin{pmatrix} 3 & 2 \\ 3 & 2 \end{pmatrix} - \frac{e^{-3\eta/2}}{5}\begin{pmatrix} -2 & 2 \\ 3 & -3 \end{pmatrix} \tag{5.82}$$

and $g_{ab}(\eta) = 0$ for $\eta < 0$ and $g_{ab}(\eta) \to \delta_{ab}$ as $\eta \to 0^+$. The initial field $\phi_a(\mathbf{k})$ can be expressed in terms of a two-component vector u_a as

$$\phi_a(\mathbf{k}) = u_a\delta(\mathbf{k},\eta=0)\,, \tag{5.83}$$

corresponding to the usual case where $\theta(\mathbf{k},\eta=0) \propto \delta(\mathbf{k},\eta=0)$. The first part of the solution depends on initial conditions. The second (integral) term corresponds to the nonlinear interactions. Then Eq. (5.79) is solved as a series expansion

$$\Psi_a(\mathbf{k},\eta) = \sum_{n=1}^{\infty} \Psi_a^{(n)}(\mathbf{k},\eta)\,, \tag{5.84}$$

where

$$\Psi_a^{(n)}(\mathbf{k},\eta) = \int \delta_D(\mathbf{k}-\mathbf{k}_{1\cdots n})\,\mathscr{F}^{(n)}_{aa_1\cdots a_n}(\mathbf{k}_1,\cdots,\mathbf{k}_n;\eta)\,\phi_{a_1}(\mathbf{k}_1)\cdots\phi_{a_n}(\mathbf{k}_n) \tag{5.85}$$

and $\mathbf{k}_{1\cdots n} = \mathbf{k}_1 + \cdots \mathbf{k}_n$. The kernel function $\mathscr{F}$ satisfies recurrence relations that are analogous to Eqs. (5.27) and (5.28), and indeed for the growing mode solutions these are obtained. By using the expressions for $\mathscr{F}_a^{(n)}$s it is possible to obtain the solutions for $\Psi_a^{(n)}$s. This is how the solutions are obtained in SPT. Here, the ingredients from the theory are represented by Feynman diagrams, easing the calculation of the $\Psi_a^{(n)}$s and allowing for a simplified formalism. The basic rules are described in detail in Ref. [203]. The solutions thus expressed permit the calculation of the correlation function between $\Psi_a^{(i)}$s for any number of loops.

Non-linearities modify however both the linear propagator (5.82) and the vertex function (5.75)-(5.77). Thus the fully non-linear propagator is defined as

$$G_{ab}(k,\eta)\,\delta_D\left(\mathbf{k}-\mathbf{k}'\right) = \left\langle \frac{\delta\Psi_a(\mathbf{k},\eta)}{\delta\phi_b(\mathbf{k}')} \right\rangle . \tag{5.86}$$

This represents the response of the final density and velocity fields to variations in initial conditions. Using the series expansion (5.84) it can be expressed in terms of the linear propagator as

$$G_{ab}(k,\eta) = g_{ab}(k,\eta) + \sum_{n=2}^{\infty} \left\langle \frac{\delta\Psi_a^{(n)}(\mathbf{k},\eta)}{\delta\phi_b(\mathbf{k}')} \right\rangle . \tag{5.87}$$

The symmetric full vertex function is defined in terms of the fully non-linear propagator by

$$\begin{aligned}\left\langle \frac{\delta^2\Psi_a(\mathbf{k},\eta)}{\delta\phi_e(\mathbf{k}_1)\delta\phi_f(\mathbf{k}_2)} \right\rangle = 2\int_0^\eta ds \int_0^s ds_1 \int_0^s ds_2 G_{ab}(\eta-s) \\ \times\Gamma^{(s)}_{bcd}(\mathbf{k},s;\mathbf{k}_1,s_1;\mathbf{k}_2,s_2)\,G_{ce}(s_1)G_{df}(s_2)\,.\end{aligned} \tag{5.88}$$

Hence, the vertex function $\gamma^{(s)}$ is the first term in an expansion of Γ. Now both the vertex function and the non-linear propagator can be expanded and also expressed in terms of

Feynman diagrams. For the nonlinear propagator, Dyson's formula is thus obtained,

$$G_{ab}(\mathbf{k},\eta) = g_{ab}(\eta) + \int_0^\eta ds_1 \int_0^{s_1} ds_2 g_{ac}(\eta - s_1)\,\Sigma_{cd}(\mathbf{k}, s_1, s_2)\,G_{db}(\mathbf{k}, s_2)\,, \tag{5.89}$$

where Σ represents the sum of the principal path irreducible diagrams (diagrams that cannot be split into disjoint pieces by removing a linear propagator from the principal path).

In the small-scale limit, the infinite series for the propagator can be resummed after a lengthy computation to [204]

$$G_{ab}(k,a) = g_{ab}(a)\exp\left(-\frac{k^2\sigma_d^2}{2}\right), \tag{5.90}$$

where $\sigma_d^2 = \frac{(a-1)^2}{3}\int \frac{d^3q}{2\pi^3}\frac{P_{\rm lin}}{q^2}$.

This method permits the calculation of the n-point correlation function in the RPT for arbitrary number of loops. Explicit expressions for the power spectrum and bispectrum are showed in Ref. [206]. Compared to SPT, this method has the advantage that all the contributions involved are positive and the resummation of the propagator terms gives a well-defined perturbative expansion in the non-linear regime. However, the expressions involved are complicated and the solutions are computationally demanding, requiring to solve numerically a set of integro-differential equations. Moreover, more than one loop is required to obtain an accurate result, even on mildly non-linear scales.

In order to solve these problems, in Refs. [206, 208] the authors propose a method that simplifies the calculation dramatically. The scheme is called MPTBREEZE and in this formalism only the late time propagator is calculated and hence no time integrations are required. First, the nonlinear propagator is generalised to an arbitrary number of points. The $(p+1)$-point propagator $\Gamma^{(p)}$ has been defined as:

$$\frac{1}{p!}\left\langle \frac{\delta^p \Psi_a(\mathbf{k},a)}{\delta\phi_{b_1}(\mathbf{k}_1)\cdots\delta\phi_{b_p}(\mathbf{k}_p)}\right\rangle = \delta_D\left(\mathbf{k}-\mathbf{k}_{1\cdots p}\right)\Gamma^{(p)}_{ab_1\cdots b_p}(\mathbf{k}_1,\cdots,\mathbf{k}_p,a)\,, \tag{5.91}$$

where $\mathbf{k}_{1\cdots p} = \mathbf{k}_1 + \cdots + \mathbf{k}_p$. In this framework, the power spectrum can be expressed as

$$P(k,z) = \sum_{r\geq 1} r! \int \delta_D(\mathbf{k}-\mathbf{q}_{1\cdots r})\left[\Gamma^{(r)}(\mathbf{q}_1,\cdots,\mathbf{q}_r,z)\right]^2 P_{\rm lin}(q_1)\cdots P_{\rm lin}(q_r)d^3q_1\cdots d^3q_r\,. \tag{5.92}$$

In the two limits of interest, of small and large ks, the multi-point propagator behaves as

$$\begin{aligned}\Gamma_a^{(n)} &\sim a^n \left(F_n\left(\mathbf{k}_1,\cdots,\mathbf{k}_n\right), G_n\left(\mathbf{k}_1,\cdots,\mathbf{k}_n\right)\right) \text{ as } k\to 0\,,\\ \Gamma_a^{(n)} &\to \mathscr{F}_a^n \exp\left(-\frac{1}{2}k^2\sigma_d^2\right) \text{ as } k\to\infty\,.\end{aligned} \tag{5.93}$$

For intermediate scales an integral solution is obtained for each propagator. If only the growing mode initial conditions are considered, the following very simple expression for the growing mode solutions is obtained,

$$\Gamma_\delta^{(n)}\left(\mathbf{k}_1,\cdots,\mathbf{k}_n;z\right) = D_+^n\left(z\right) F_n^{(s)}\left(\mathbf{k}_1,\cdots,\mathbf{k}_n\right) \exp\left[f(k)D_+^2(z)\right]\,, \tag{5.94}$$

where the function f depends only on the linear power spectrum today:

$$\begin{aligned}f\left(k\right) = \int \frac{d^3q}{(2\pi)^3}\frac{P_{\rm lin}\left(q,z=0\right)}{504k^3q^5}\Big[&6k^7q - 79k^5q^3 + 50q^5k^3\\ &-21kq^7 + \frac{3}{4}\left(k^2-q^2\right)^3\left(2k^2+7q^2\right)\log\frac{|k-q|^2}{|k+q|^2}\Big]\,.\end{aligned} \tag{5.95}$$

This method agrees very well with the results of the more exact method *RegPT* [262].

Using this formalism, the power spectrum up to two loops can be expressed as follows:

$$P_{\rm tree}\left(k,z\right) = \left[\Gamma^{(1)}\left(k;z\right)\right]^2 P_{\rm lin}\left(k\right)\,, \tag{5.96}$$

$$P_{\text{1-loop}}\left(k,z\right) = 2\int\frac{d^3q}{(2\pi)^3}\left[\Gamma^{(2)}\left(\mathbf{k}-\mathbf{q},\mathbf{q};z\right)\right]^2 P_{\rm lin}\left(|\mathbf{k}-\mathbf{q}|\right)P_{\rm lin}\left(q\right)\,, \tag{5.97}$$

$$P_{\text{2-loop}}\left(k,z\right) = 6\int\frac{d^3q_1}{(2\pi)^3}\int\frac{d^3q_2}{(2\pi)^3}\left[\Gamma^{(3)}\left(\mathbf{k}-\mathbf{q}_{12},\mathbf{q}_1,\mathbf{q}_2;z\right)\right]^2 P_{\rm lin}\left(|\mathbf{k}-\mathbf{q}_{12}|\right)P_{\rm lin}\left(q_1\right)P_{\rm lin}\left(q_2\right)\,. \tag{5.98}$$

Using Eq. (5.94) and Eqs. (5.42) and (5.45) from Subchapter 5.2.1 and Eq. (97) from Ref. [224] , the MPTBREEZE contributions can be expressed in terms of their SPT counterparts as follows:

$$P_{\rm tree}^{\rm MPTbreeze}\left(k,z\right) = P_{11}\left(k,z\right)\exp\left[2f(k)D_+^2(z)\right]\,, \tag{5.99}$$

$$P_{\text{1-loop}}^{\rm MPTbreeze}\left(k,z\right) = P_{22}\left(k,z\right)\exp\left[2f(k)D_+^2(z)\right]\,, \tag{5.100}$$

$$P_{\text{2-loop}}^{\rm MPTbreeze}\left(k,z\right) = P_{22}^{II}\left(k,z\right)\exp\left[2f(k)D_+^2(z)\right]\,. \tag{5.101}$$

The bispectrum contributions can be treated in a similar manner [207], and the result up to one loop is (5.48), (5.49)

$$B^{\text{MPTbreeze}}(k_1,k_2,k_3,z) = \left(B_{\text{tree}} + B_{222} + B^I_{321}\right)(k_1,k_2,k_3,z) \times \exp\left[\left(f(k_1)+f(k_2)+f(k_3)\right)D^2_+(z)\right] . \tag{5.102}$$

This prescription allows a very easy computation of the power spectrum and bispectrum for this method once the SPT counterparts have been determined, as only one integral function (f) needs to be evaluated, the other terms being calculated in SPT. Unfortunately, this theory is only expected to give a reliable prediction for the bispectrum up to $k_{\text{max}} = 0.15\,\text{Mpc}^{-1}$. Therefore, it is desirable to go to the 2-loops in order to increase the range of ks. This has not been calculated so far, not even at the theory level, due to the lengthy computation.

Two-loop bispectrum calculation

The tree-level and one-loop bispectrum in this theory have been discussed above, and hence we proceed directly to the two-loop terms. The generating function for the RPT bispectrum is given by Eq. (59) of Ref. [206]. At two loops, using the notation from Ref. [206], we need to take $r+s+t=4$. As only one of these numbers can be 0, there are only three choices for r, s and t (plus permutations) giving non-vanishing contributions, which we will treat in turn:

(a) $r=3$, $s=1$, $t=0$ (+ 5 perms.);

(b) $r=2$, $s=2$, $t=0$ (+2 perms.);

(c) $r=1$, $s=1$, $t=2$ (+2 perms.).

In all these three cases, the expressions involved will depend on the functions $\Gamma^{(n)}$ only up to $\Gamma^{(4)}$, which in turn can be expressed in terms of the corresponding kernel functions $F_n^{(s)}$ through Eq. (5.94). Even though the expressions that we obtained for the MPTBREEZE two-loop bispectra are relatively simple, they cannot be integrated directly because they have various poles where at least one of the arguments of $F_n^{(s)}$ vanishes. However, we know that the divergences between the various terms must cancel exactly after performing the integration, but numerically this is an issue because the divergent parts are expected to be much bigger than the finite result and thus the numerical result may not be reliable. In order to solve this problem, we will use the methods developed in Refs. [223, 260, 263]. Compared to SPT, where some of the terms involve the kernel $F_6^{(s)}$, the expressions appearing in this

method represent a significant simplification. We note that from Eq. (5.94) all expressions will have a prefactor

$$D^8(z)\exp\left[(f(k_1)+f(k_2)+f(k_3))\,D^2(z)\right], \tag{5.103}$$

and therefore in the following paragraphs we will omit this factor because it does not affect the calculation. We will denote the three integrals by B_a, B_b and B_c and the integrands with the corresponding lowercase letters. Then the final two-loop MPTBREEZE bispectrum is

$$\begin{aligned}B^{\text{MPTbreeze}}_{\text{2-loop}}(k_1,k_2,k_3,z) = D^8(z)\exp\left[(f(k_1)+f(k_2)+f(k_3))\,D^2(z)\right]\\ \times\left[B_a(k_1,k_2,k_3)+B_b(k_1,k_2,k_3)+B_c(k_1,k_2,k_3)\right].\end{aligned} \tag{5.104}$$

The expressions for the three bispectra are as follows:

$$\begin{aligned}B_a(k_1,k_2,k_3) &= 24\int\frac{d^3q_1}{(2\pi)^3}\int\frac{d^3q_2}{(2\pi)^3}F_4^{(s)}(\mathbf{q}_1,\mathbf{q}_2,-\mathbf{k}_3-\mathbf{q}_1-\mathbf{q}_2,-\mathbf{k}_2)\\ &\quad\times F_3^{(s)}(-\mathbf{q}_1,-\mathbf{q}_2,\mathbf{k}_3+\mathbf{q}_1+\mathbf{q}_2)P_{\text{lin}}(q_1)P_{\text{lin}}(q_2)P_{\text{lin}}(k_3)P_{\text{lin}}(|\mathbf{q}_1+\mathbf{q}_2+\mathbf{k}_3|),\end{aligned} \tag{5.105}$$

$$\begin{aligned}B_b(k_1,k_2,k_3) &= 24\int\frac{d^3q_1}{(2\pi)^3}\int\frac{d^3q_2}{(2\pi)^3}F_4^{(s)}(\mathbf{q}_1,\mathbf{k}_3-\mathbf{q}_1,\mathbf{q}_2,-\mathbf{k}_2-\mathbf{q}_2)F_2^{(s)}(-\mathbf{q}_2,\mathbf{k}_2+\mathbf{q}_2)\\ &\quad\times F_2^{(s)}(-\mathbf{q}_1,\mathbf{k}_3+\mathbf{q}_1)P_{\text{lin}}(q_1)P_{\text{lin}}(q_2)P_{\text{lin}}(|\mathbf{q}_1+\mathbf{k}_3|)P_{\text{lin}}(|\mathbf{q}_2+\mathbf{k}_2|),\end{aligned} \tag{5.106}$$

$$\begin{aligned}B_c(k_1,k_2,k_3) &= 36\int\frac{d^3q_1}{(2\pi)^3}\int\frac{d^3q_2}{(2\pi)^3}F_3^{(s)}(\mathbf{q}_1,\mathbf{q}_2,\mathbf{k}_1-\mathbf{q}_1-\mathbf{q}_2)\\ &\quad\times F_2^{(s)}(-\mathbf{k}_1+\mathbf{q}_1+\mathbf{q}_2,-\mathbf{k}_3-\mathbf{q}_1-\mathbf{q}_2)F_3^{(s)}(\mathbf{k}_3+\mathbf{q}_1+\mathbf{q}_2,-\mathbf{q}_1,-\mathbf{q}_2)\\ &\quad\times P_{\text{lin}}(q_1)P_{\text{lin}}(q_2)P_{\text{lin}}(|\mathbf{k}_1-\mathbf{q}_1-\mathbf{q}_2|)P_{\text{lin}}(|\mathbf{k}_3+\mathbf{q}_1+\mathbf{q}_2|).\end{aligned} \tag{5.107}$$

We will treat each of them in turn and show how to remove the singularities before the integration.

B_a The expression for B_a has singularities when $q_1=0$, $q_2=0$ and $\mathbf{q}_1+\mathbf{q}_2=-\mathbf{k}_3$. By considering the variable $\mathbf{q}_3=-\mathbf{q}_1-\mathbf{q}_2-\mathbf{k}_3$, B_a can be re-expressed in terms of a triple integral by adding a Dirac-delta function:

$$\begin{aligned}B_a(k_1,k_2,k_3) = 24\int\frac{d^3q_1}{(2\pi)^3}\int\frac{d^3q_2}{(2\pi)^3}\int\frac{d^3q_3}{(2\pi)^3}F_4^{(s)}(\mathbf{q}_1,\mathbf{q}_2,\mathbf{q}_3)F_3^{(s)}(-\mathbf{q}_1,-\mathbf{q}_2,-\mathbf{q}_3)\\ \times\delta_D(\mathbf{q}_1+\mathbf{q}_2+\mathbf{q}_3+\mathbf{k}_3)P_{\text{lin}}(q_1)P_{\text{lin}}(q_2)P_{\text{lin}}(k_3)P_{\text{lin}}(q_3).\end{aligned} \tag{5.108}$$

This expression is now completely symmetric in $\mathbf{q}_1 \leftrightarrow \mathbf{q}_2 \leftrightarrow \mathbf{q}_3$ and hence all ordering of the magnitudes of these three wavevectors are equivalent after a suitable relabelling of the variables. As there are six possible permutations of q_1, q_2 and q_3,

$$B_a = \int\int\int \frac{d^3q_1 d^3q_2 d^3q_3}{(2\pi)^9} b_b 6\Theta(q_3 - q_2)\Theta(q_2 - q_1)\,. \tag{5.109}$$

Hence, the delta function and $\mathbf{q}_3$ can now be eliminated and the final expression is obtained,

$$\begin{aligned} B_a(k_1,k_2,k_3) = 24 \int \frac{d^3q_1}{(2\pi)^3} \int \frac{d^3q_2}{(2\pi)^3} F_4^{(s)}(\mathbf{q}_1, \mathbf{q}_2, -\mathbf{k}_3 - \mathbf{q}_1 - \mathbf{q}_2, -\mathbf{k}_2) \\ \times F_3^{(s)}(-\mathbf{q}_1, -\mathbf{q}_2, \mathbf{k}_3 + \mathbf{q}_1 + \mathbf{q}_2) P_{\rm lin}(q_1) P_{\rm lin}(q_2) P_{\rm lin}(k_3) \\ \times P_{\rm lin}(|\mathbf{q}_1 + \mathbf{q}_2 + \mathbf{k}_3|) \times 6\Theta(|\mathbf{q}_1 + \mathbf{q}_2 + \mathbf{k}_3| - q_2)\Theta(q_2 - q_1)\,. \end{aligned} \tag{5.110}$$

The expression of Eq. (5.110) has a leading divergence when $q_1 = q_2 = 0$ and a subleading divergence when $q_1 = 0$, $\mathbf{q}_2$ fixed. The two divergences corresponding to $\mathbf{q}_1 + \mathbf{q}_2 = -\mathbf{k}_3$ and $q_2 = 0$, at fixed $\mathbf{q}_1$, have disappeared because the Heaviside functions evaluate to 0 in those limits. In order to eliminate all divergences at the integrand level, we can also symmetrise in $\mathbf{q}_{1,2} \leftrightarrow -\mathbf{q}_{1,2}$:

$$b_a(\mathbf{q}_1, \mathbf{q}_2) \to \frac{1}{4}\left[b_a(\mathbf{q}_1, \mathbf{q}_2) + b_a(-\mathbf{q}_1, \mathbf{q}_2) + b_a(\mathbf{q}_1, -\mathbf{q}_2) + b_a(-\mathbf{q}_1, -\mathbf{q}_2)\right]. \tag{5.111}$$

We will use this symmetrisation for the b and c terms as well.

B_b The B_b term has divergences for $q_1 = 0$, $\mathbf{q}_1 = -\mathbf{k}_3$, $q_2 = 0$ and $\mathbf{q}_2 = -\mathbf{k}_1$. We note that b_b is symmetric under the transformations $\mathbf{q}_1 \leftrightarrow -\mathbf{k}_3 - \mathbf{q}_1$ and $\mathbf{q}_2 \leftrightarrow -\mathbf{k}_2 - \mathbf{q}_2$. We can exploit the three symmetries that now appear in the integrand by restricting the integration region to $q_1 < |\mathbf{k}_3 + \mathbf{q}_1|$ and $q_2 < |\mathbf{k}_1 + \mathbf{q}_2|$ and introducing two Heaviside functions and a factor of 2^2,

$$\begin{aligned} B_b(k_1,k_2,k_3) = 24 \int \frac{d^3q_1}{(2\pi)^3} \int \frac{d^3q_2}{(2\pi)^3} F_4^{(s)}(\mathbf{q}_1, \mathbf{k}_3 - \mathbf{q}_1, \mathbf{q}_2, -\mathbf{k}_2 - \mathbf{q}_2) F_2^{(s)}(-\mathbf{q}_2, \mathbf{k}_2 + \mathbf{q}_2) \\ \times F_2^{(s)}(-\mathbf{q}_1, \mathbf{k}_3 + \mathbf{q}_1) P_{\rm lin}(q_1) P_{\rm lin}(q_2) P_{\rm lin}(|\mathbf{q}_1 + \mathbf{k}_3|) P_{\rm lin}(|\mathbf{q}_2 + \mathbf{k}_2|) \\ \times 4\Theta(|\mathbf{k}_2 + \mathbf{q}_2| - q_2)\Theta(|\mathbf{k}_3 + \mathbf{q}_1| - q_1)\,. \end{aligned} \tag{5.112}$$

This expression is not symmetric in $\mathbf{q}_1 \leftrightarrow \mathbf{q}_2$, but we can symmetrise it by symmetrising the whole integrand (including the delta functions):

$$b_b(\mathbf{q}_1,\mathbf{q}_2) \to \frac{1}{2}\left[b_b(\mathbf{q}_1,\mathbf{q}_2)+b_b(\mathbf{q}_2,\mathbf{q}_1)\right]. \tag{5.113}$$

After the symmetrisation, we aim to restrict the integration range to $q_1 < q_2$, and we achieve this by adding an additional Θ-function, thus obtaining the final answer,

$$\begin{aligned}
B_b(k_1,&k_2,k_3) = 24\int\frac{d^3q_1}{(2\pi)^3}\int\frac{d^3q_2}{(2\pi)^3}\Theta(q_2-q_1)\times\\
&\Big[F_4^{(s)}(\mathbf{q}_1,\mathbf{k}_3-\mathbf{q}_1,\mathbf{q}_2,-\mathbf{k}_2-\mathbf{q}_2)F_2^{(s)}(-\mathbf{q}_2,\mathbf{k}_2+\mathbf{q}_2)F_2^{(s)}(-\mathbf{q}_1,\mathbf{k}_3+\mathbf{q}_1)P_{\rm lin}(q_1)P_{\rm lin}(q_2)\\
&\quad\times P_{\rm lin}(|\mathbf{q}_1+\mathbf{k}_3|)P_{\rm lin}(|\mathbf{q}_2+\mathbf{k}_2|)\times 4\Theta(|\mathbf{k}_2+\mathbf{q}_2|-q_2)\Theta(|\mathbf{k}_3+\mathbf{q}_1|-q_1)\\
&+F_4^{(s)}(\mathbf{q}_2,\mathbf{k}_3-\mathbf{q}_2,\mathbf{q}_1,-\mathbf{k}_2-\mathbf{q}_1)F_2^{(s)}(-\mathbf{q}_1,\mathbf{k}_2+\mathbf{q}_1)F_2^{(s)}(-\mathbf{q}_2,\mathbf{k}_3+\mathbf{q}_2)P_{\rm lin}(q_1)P_{\rm lin}(q_2)\\
&\quad\times P_{\rm lin}(|\mathbf{q}_2+\mathbf{k}_3|)P_{\rm lin}(|\mathbf{q}_1+\mathbf{k}_2|)\times 4\Theta(|\mathbf{k}_2+\mathbf{q}_1|-q_1)\,\Theta(|\mathbf{k}_3+\mathbf{q}_2|-q_2)\Big].
\end{aligned} \tag{5.114}$$

Hence all the leading and subleading divergences have been moved to $q_1 = q_2 = 0$ and $q_1 = 0$, at $\mathbf{q}_2$ fixed. For all the other poles in the kernels, the Heaviside functions vanish.

B_c The expression for B_c has only one direct symmetry $\mathbf{q}_1 \leftrightarrow \mathbf{q}_2$, but this is not enough. Therefore we introduce the following notation:

$$\mathbf{q}_3 = \mathbf{k}_1 - \mathbf{q}_1 - \mathbf{q}_2\,, \tag{5.115}$$

$$\mathbf{q}_4 = \mathbf{k}_1 + \mathbf{k}_2 - \mathbf{q}_1 - \mathbf{q}_2\,, \tag{5.116}$$

and we then add two additional integrations over $\mathbf{q}_3$ and $\mathbf{q}_4$ and two Dirac delta functions imposing the above constraints. The integral becomes

$$\begin{aligned}
B_c(k_1,&k_2,k_3) = 36\int\int\int\int\frac{d^3q_1d^3q_2d^3q_3d^3q_4}{(2\pi)^{12}}F_3^{(s)}(\mathbf{q}_1,\mathbf{q}_2,\mathbf{q}_3)\\
&\times F_2^{(s)}(-\mathbf{q}_3,\mathbf{q}_4)F_3^{(s)}(-\mathbf{q}_4,-\mathbf{q}_1,-\mathbf{q}_2)\\
&\times P_{\rm lin}(q_1)P_{\rm lin}(q_2)P_{\rm lin}(q_3)P_{\rm lin}(q_4)\,\delta_D(\mathbf{k}_1-\mathbf{q}_1-\mathbf{q}_2-\mathbf{q}_3)\delta_D(\mathbf{k}_2+\mathbf{q}_3-\mathbf{q}_4).
\end{aligned} \tag{5.117}$$

This expression is already symmetric in $\mathbf{q}_1 \leftrightarrow \mathbf{q}_2$, and we symmetrise it in all the other variables, obtaining 12 possible permutations and a fully symmetric expression. We can now introduce an ordering of the four variables in terms of their magnitude (e.g. $q_4 \geq q_3 \geq q_2 \geq q_1$), knowing that all the other orderings can be obtained by a suitable re-labelling of the variables. There are $4! = 24$ permutations of the four variables and, keeping only

one of the permutations, we need to multiply it by the product of Heaviside functions $24\Theta(q_4-q_3)\Theta(q_3-q_2)\Theta(q_2-q_1)$.

There are now 12 summands, and each of them involves integrals over $\mathbf{q}_1$, $\mathbf{q}_2$, $\mathbf{q}_3$ and $\mathbf{q}_4$, three Heaviside functions and two delta functions. The aim is now to perform two of the integrations, in order to eliminate the delta functions. In ten of the terms, it turns out that it is possible integrate over $\mathbf{q}_3$ and $\mathbf{q}_4$. In the other two, $\mathbf{q}_3$ and $\mathbf{q}_4$ appear in the same combination in both delta functions. For those terms we integrate over $\mathbf{q}_2$ and $\mathbf{q}_4$, and then relabel $\mathbf{q}_3 \to \mathbf{q}_2$. The final expression that we thus obtain only has divergences for $q_1 = q_2 = 0$ and $q_1 = 0$, with $\mathbf{q}_2$ fixed as required:

$$
\begin{aligned}
b_c(k_1,k_2,k_3) = 36 \Big[& 2F_2^{(s)}(\mathbf{k}_2-\mathbf{q}_1,\mathbf{q}_1)F_3^{(s)}(-\mathbf{q}_1,-\mathbf{q}_2,-\mathbf{k}_1-\mathbf{k}_2+\mathbf{q}_1+\mathbf{q}_2) \\
& \times F_3^{(s)}(\mathbf{q}_1-\mathbf{k}_2,\mathbf{k}_1+\mathbf{k}_2-\mathbf{q}_1-\mathbf{q}_2,\mathbf{q}_2)P_{\rm lin}(q_1)P_{\rm lin}(|\mathbf{q}_1-\mathbf{k}_2|)P_{\rm lin}(|\mathbf{k}_1+\mathbf{k}_2-\mathbf{q}_1-\mathbf{q}_2|) \\
& \times P_{\rm lin}(q_2)\Theta(|\mathbf{k}_1+\mathbf{k}_2-\mathbf{q}_1-\mathbf{q}_2|-|\mathbf{q}_1-\mathbf{k}_2|)\Theta(|\mathbf{q}_1-\mathbf{k}_2|-q_2|)\Theta(q_2)-q_1) \\
& + 2F_2^{(s)}(-\mathbf{q}_1,\mathbf{k}_2+\mathbf{q}_1)F_3^{(s)}(-\mathbf{k}_2-\mathbf{q}_1,-\mathbf{q}_2,-\mathbf{k}_1+\mathbf{q}_1+\mathbf{q}_2)F_3^{(s)}(\mathbf{q}_1,\mathbf{k}_1-\mathbf{q}_1-\mathbf{q}_2,\mathbf{q}_2) \\
& \times P_{\rm lin}(q_1)P_{\rm lin}(|\mathbf{k}_2+\mathbf{q}_1|)P_{\rm lin}(|\mathbf{k}_1-\mathbf{q}_1-\mathbf{q}_2|)P_{\rm lin}(q_2) \\
& \times \Theta(|\mathbf{k}_1-\mathbf{q}_1-\mathbf{q}_2|)-|\mathbf{k}_2+\mathbf{q}_1|)\Theta(|\mathbf{k}_2+\mathbf{q}_1)|-q_2)\Theta(q_2-q_1) \\
& + 2F_2^{(s)}(-\mathbf{q}_1,\mathbf{k}_2+\mathbf{q}_1)F_3^{(s)}(-\mathbf{k}_2-\mathbf{q}_1,-\mathbf{q}_2,-\mathbf{k}_1+\mathbf{q}_1+\mathbf{q}_2)F_3^{(s)}(\mathbf{q}_1,\mathbf{k}_1-\mathbf{q}_1-\mathbf{q}_2,\mathbf{q}_2) \\
& \times P_{\rm lin}(q_1)P_{\rm lin}(|\mathbf{k}_2+\mathbf{q}_1|)P_{\rm lin}(|\mathbf{k}_1-\mathbf{q}_1-\mathbf{q}_2|)P_{\rm lin}(q_2) \\
& \times \Theta(|\mathbf{k}_2+\mathbf{q}_1|-|\mathbf{k}_1-\mathbf{q}_1-\mathbf{q}_2|)\Theta(|\mathbf{k}_1-\mathbf{q}_1-\mathbf{q}_2|-q_2)\Theta(q_2-q_1) \\
& + 2F_2^{(s)}(\mathbf{k}_1+\mathbf{k}_2-\mathbf{q}_1-\mathbf{q}_2,-\mathbf{k}_1+\mathbf{q}_1+\mathbf{q}_2)F_3^{(s)}(-\mathbf{q}_1,-\mathbf{q}_2,-\mathbf{k}_1-\mathbf{k}_2+\mathbf{q}_1+\mathbf{q}_2) \\
& \times F_3^{(s)}(\mathbf{q}_1,\mathbf{k}_1-\mathbf{q}_1-\mathbf{q}_2,\mathbf{q}_2)P_{\rm lin}(q_1)P_{\rm lin}(|\mathbf{k}_1-\mathbf{q}_1-\mathbf{q}_2|)P_{\rm lin}(|\mathbf{k}_1+\mathbf{k}_2-\mathbf{q}_1-\mathbf{q}_2|)P_{\rm lin}(q_2) \\
& \times \Theta(|\mathbf{k}_1+\mathbf{k}_2-\mathbf{q}_1-\mathbf{q}_2|-|\mathbf{k}_1-\mathbf{q}_1-\mathbf{q}_2|)\Theta(|\mathbf{k}_1-\mathbf{q}_1-\mathbf{q}_2|-q_2)\Theta(q_2-q_1) \\
& + 2F_2^{(s)}(\mathbf{k}_2-\mathbf{q}_1,\mathbf{q}_1)F_3^{(s)}(-\mathbf{q}_1,-\mathbf{q}_2,-\mathbf{k}_1-\mathbf{k}_2+\mathbf{q}_1+\mathbf{q}_2)F_3^{(s)}(\mathbf{q}_1-\mathbf{k}_2,\mathbf{k}_1+\mathbf{k}_2-\mathbf{q}_1-\mathbf{q}_2,\mathbf{q}_2) \\
& \times P_{\rm lin}(q_1)P_{\rm lin}(|\mathbf{q}_1-\mathbf{k}_2|)P_{\rm lin}(|\mathbf{k}_1+\mathbf{k}_2-\mathbf{q}_1-\mathbf{q}_2|)P_{\rm lin}(q_2) \\
& \times \Theta(|\mathbf{q}_1-\mathbf{k}_2|)-|\mathbf{k}_1+\mathbf{k}_2-\mathbf{q}_1-\mathbf{q}_2|)\Theta(|\mathbf{k}_1+\mathbf{k}_2-\mathbf{q}_1-\mathbf{q}_2|-q_2)\Theta(q_2-q_1) \\
& + 2F_2^{(s)}(\mathbf{k}_1+\mathbf{k}_2-\mathbf{q}_1-\mathbf{q}_2,-\mathbf{k}_1+\mathbf{q}_1+\mathbf{q}_2)F_3^{(s)}(-\mathbf{q}_1,-\mathbf{q}_2,-\mathbf{k}_1-\mathbf{k}_2+\mathbf{q}_1+\mathbf{q}_2) \\
& \times F_3^{(s)}(\mathbf{q}_1,\mathbf{k}_1-\mathbf{q}_1-\mathbf{q}_2,\mathbf{q}_2)P_{\rm lin}(q_1)P_{\rm lin}(|\mathbf{k}_1-\mathbf{q}_1-\mathbf{q}_2|)P_{\rm lin}(|\mathbf{k}_1+\mathbf{k}_2-\mathbf{q}_1-\mathbf{q}_2|)P_{\rm lin}(q_2) \\
& \times \Theta(|\mathbf{k}_1-\mathbf{q}_1-\mathbf{q}_2|-|\mathbf{k}_1+\mathbf{k}_2-\mathbf{q}_1-\mathbf{q}_2|)\Theta(|\mathbf{k}_1+\mathbf{k}_2-\mathbf{q}_1-\mathbf{q}_2|-q_2)\Theta(q_2-q_1) \\
& + 2F_2^{(s)}(\mathbf{k}_2-\mathbf{q}_2,\mathbf{q}_2)F_3^{(s)}(-\mathbf{q}_1,-\mathbf{q}_2,-\mathbf{k}_1-\mathbf{k}_2+\mathbf{q}_1+\mathbf{q}_2)F_3^{(s)}(\mathbf{q}_1,\mathbf{k}_1+\mathbf{k}_2-\mathbf{q}_1-\mathbf{q}_2,\mathbf{q}_2-\mathbf{k}_2) \\
& \times P_{\rm lin}(q_1)P_{\rm lin}(|\mathbf{k}_1+\mathbf{k}_2-\mathbf{q}_1-\mathbf{q}_2|)P_{\rm lin}(q_2)P_{\rm lin}(|\mathbf{q}_2-\mathbf{k}_2|) \\
& \times \Theta(|\mathbf{k}_1+\mathbf{k}_2-\mathbf{q}_1-\mathbf{q}_2|-q_2)\Theta(|\mathbf{q}_2-\mathbf{k}_2|-|\mathbf{k}_1+\mathbf{k}_2-\mathbf{q}_1-\mathbf{q}_2|)\Theta(q_2-q_1)
\end{aligned}
$$

$$
\begin{aligned}
&+2F_2^{(s)}(\mathbf{k}_2-\mathbf{q}_2,\mathbf{q}_2)F_3^{(s)}(-\mathbf{q}_1,-\mathbf{q}_2,-\mathbf{k}_1-\mathbf{k}_2+\mathbf{q}_1+\mathbf{q}_2)F_3^{(s)}(\mathbf{q}_1,\mathbf{k}_1+\mathbf{k}_2-\mathbf{q}_1-\mathbf{q}_2,\mathbf{q}_2-\mathbf{k}_2)\\
&\quad\times P_{\rm lin}(q_1)P_{\rm lin}(|\mathbf{k}_1+\mathbf{k}_2-\mathbf{q}_1-\mathbf{q}_2|)P_{\rm lin}(q_2)P_{\rm lin}(|\mathbf{q}_2-\mathbf{k}_2|)\\
&\quad\times\Theta(|\mathbf{k}_1+\mathbf{k}_2-\mathbf{q}_1-\mathbf{q}_2|-|\mathbf{q}_2-\mathbf{k}_2|)\Theta(|\mathbf{q}_2-\mathbf{k}_2|-q_2)\Theta(q_2-q_1)\\
&+2F_2^{(s)}(-\mathbf{q}_2,\mathbf{k}_2+\mathbf{q}_2)F_3^{(s)}(-\mathbf{q}_1,-\mathbf{k}_2-\mathbf{q}_2,-\mathbf{k}_1+\mathbf{q}_1+\mathbf{q}_2)F_3^{(s)}(\mathbf{q}_1,\mathbf{k}_1-\mathbf{q}_1-\mathbf{q}_2,\mathbf{q}_2)\\
&\quad\times P_{\rm lin}(q_1)P_{\rm lin}(|\mathbf{k}_1-\mathbf{q}_1-\mathbf{q}_2|)P_{\rm lin}(q_2)P_{\rm lin}(|\mathbf{k}_2+\mathbf{q}_2|)\\
&\quad\times\Theta(|\mathbf{k}_1-\mathbf{q}_1-\mathbf{q}_2|-q_2)\Theta(|\mathbf{k}_2+\mathbf{q}_2|-|\mathbf{k}_1-\mathbf{q}_1-\mathbf{q}_2|)\Theta(q_2-q_1)\\
&+2F_2^{(s)}(-\mathbf{q}_2,\mathbf{k}_2+\mathbf{q}_2)F_3^{(s)}(-\mathbf{q}_1,-\mathbf{k}_2-\mathbf{q}_2,-\mathbf{k}_1+\mathbf{q}_1+\mathbf{q}_2)F_3^{(s)}(\mathbf{q}_1,\mathbf{k}_1-\mathbf{q}_1-\mathbf{q}_2,\mathbf{q}_2)\\
&\quad\times P_{\rm lin}(q_1)P_{\rm lin}(|\mathbf{k}_1-\mathbf{q}_1-\mathbf{q}_2|)P_{\rm lin}(q_2)P_{\rm lin}(|\mathbf{k}_2+\mathbf{q}_2|)\\
&\quad\times\Theta(|\mathbf{k}_1-\mathbf{q}_1-\mathbf{q}_2|-|\mathbf{k}_2+\mathbf{q}_2|)\Theta(|\mathbf{k}_2+\mathbf{q}_2|-q_2)\Theta(q_2-q_1)\\
&+2F_2^{(s)}(\mathbf{k}_2-\mathbf{q}_1,\mathbf{q}_1)F_3^{(s)}(-\mathbf{q}_1,-\mathbf{q}_2,-\mathbf{k}_1-\mathbf{k}_2+\mathbf{q}_1+\mathbf{q}_2)F_3^{(s)}(\mathbf{q}_1-\mathbf{k}_2,\mathbf{k}_1+\mathbf{k}_2-\mathbf{q}_1-\mathbf{q}_2,\mathbf{q}_2)\\
&\quad\times P_{\rm lin}(q_1)P_{\rm lin}(|\mathbf{q}_1-\mathbf{k}_2|)P_{\rm lin}(|\mathbf{k}_1+\mathbf{k}_2-\mathbf{q}_1-\mathbf{q}_2|)P_{\rm lin}(q_2)\\
&\quad\times\Theta(|\mathbf{q}_1-\mathbf{k}_2|-q_1)\Theta(|\mathbf{k}_1+\mathbf{k}_2-\mathbf{q}_1-\mathbf{q}_2|-q_2)\Theta(q_2-|\mathbf{q}_1-\mathbf{k}_2|)\\
&+2F_2^{(s)}(-\mathbf{q}_1,\mathbf{k}_2+\mathbf{q}_1)F_3^{(s)}(-\mathbf{k}_2-\mathbf{q}_1,-\mathbf{q}_2,-\mathbf{k}_1+\mathbf{q}_1+\mathbf{q}_2)F_3^{(s)}(\mathbf{q}_1,\mathbf{k}_1-\mathbf{q}_1-\mathbf{q}_2,\mathbf{q}_2)\\
&\quad\times P_{\rm lin}(q_1)P_{\rm lin}(|\mathbf{k}_2+\mathbf{q}_1|)P_{\rm lin}(|\mathbf{k}_1-\mathbf{q}_1-\mathbf{q}_2|)P_{\rm lin}(q_2)\Theta(|\mathbf{k}_2+\mathbf{q}_1|-q_1)\\
&\quad\times\Theta(|\mathbf{k}_1-\mathbf{q}_1-\mathbf{q}_2|-q_2)\,\Theta(q_2-|\mathbf{k}_2+\mathbf{q}_1|)]\,. \qquad (5.118)
\end{aligned}
$$

The three long expressions can be added together with their corresponding permutations to obtain the final two-loop result, which is then free of any divergences before the integration.

Going to two-loops and estimating perturbation residuals

We present in Fig. 5.1 three triangle configurations: equilateral, squeezed and flattened, also with a comparison between all the tree-level and one-loop perturbative methods at $z=0$. The EFT bispectrum is expected to be accurate up to higher k than one-loop RPT, as discussed by Ref. [260] and as shown in Chapter 6; therefore, knowing that the RPT approach is a convergent expansion with the precision increasing as the number of loops is increased, we can estimate the range of validity of the one-loop and two-loop MPTBREEZE results by comparison with EFT.

In Fig. 5.1, we observe that the two-loop MPTBREEZE bispectrum closely follows the EFT prediction for an extra $0.04\,h/\mathrm{Mpc}$ more than the one-loop bispectrum in the equilateral and flattened cases, while the squeezed limit shows a more modest improvement. It is therefore clear that extending MPTBREEZE to two loops in the quantitative comparisons of Chapter 6 would significantly improve its range of validity, but we decide not to pursue

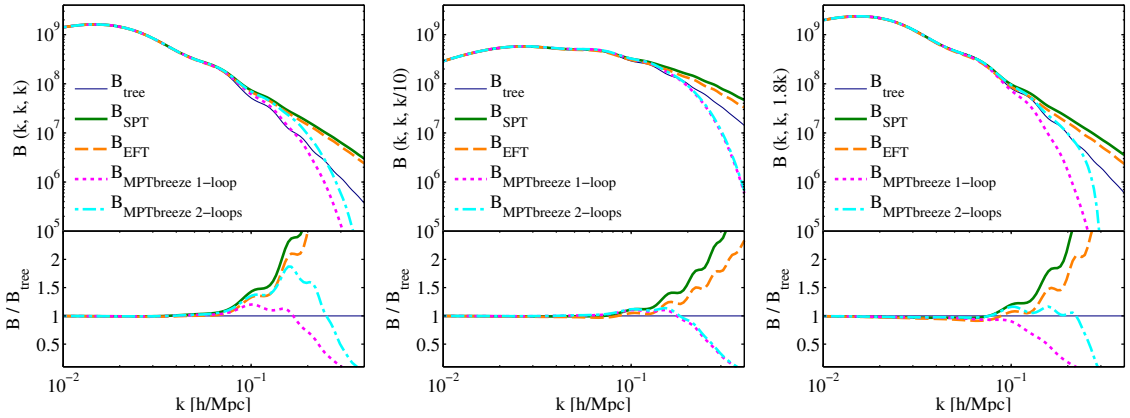

Fig. 5.1 Equilateral (*left*), squeezed (*middle*) and flattened bispectra (*right*) from perturbation theories at $z = 0$. We show the theoretical predictions of the tree-level bispectrum, SPT, EFT and the one- and two-loop MPTBREEZE bispectra. For this last model, we observe that the wavenumber at which the theory starts decaying increases significantly when adding the two-loop terms in the case of the equilateral and flattened configurations, closely following the EFT model down to smaller scales, while for the squeezed configuration the improvement is negligible. Bispectra are plotted in units of $(\mathrm{Mpc}/h)^6$ throughout the LSS chapters.

this for consistency with the other PT methods, and because of the huge analytic and numerical challenges which seem to be entailed. Controlled perturbative expansions become increasingly accurate as the number of loops is increased, so a criterion for determining where perturbation theory at a given order breaks down is to calculate the next-order contribution and find where they become significant. In Table 5.1 we show the value of the wavenumber where the higher order expansion deviates by more than 10% (20%) from the lower order. Hence, we compare SPT with tree-level, the MPTBREEZE at one loop to the tree-level and the two-loop MPTBREEZE bispectrum to its one-loop counterpart. For completeness, we also determine the effect of the counter-term in EFT which corrects SPT. At one-loop we evaluate deviations with the total correlator $\mathscr{T}$, but at two-loop order we determine the worst case amongst the three limiting configurations evaluated.

Table 5.1 indicates that the tree-level bispectrum is in fact valid only for small wavenumbers $k \lesssim 0.1\,\mathrm{Mpc}^{-1}$ at $z = 0$ and $k \lesssim 0.2\,\mathrm{Mpc}^{-1}$ at $z = 2$, with one-loop contributions apparently offering only a small incremental improvement. However, the comparison of SPT results with the EFT controlled expansion indicates that it may be possible to extrapolate perturbative expansions considerably further. As we shall see in Chapter 6, there is an unexpectedly good correspondence between some perturbative bispectra and the results of numerical simulations, going well beyond the thresholds estimated in Table 5.1.

Table 5.1 Domain of validity for perturbation theory: wavenumber $k^*_{\rm max}$ where the two perturbative expansions being compared show relative deviations greater than 10% (20%).

Perturbation theories			
Threshold 10% (20%)	$k^*_{\rm max}\,[h/{\rm Mpc}]$		
Theory	$z=0$	$z=1$	$z=2$
SPT/Tree-level	0.07 (0.08)	0.08 (0.12)	0.12 (0.14)
EFT/SPT	0.12 (0.41)	0.41 (0.93)	0.77 (1.52)
RPT 1-loop/Tree	0.08 (0.10)	0.09 (0.14)	0.13 (0.20)
RPT 2-loops/1-loop	0.09 (0.11)	0.13 (0.16)	0.19 (0.23)

5.2.4 Resummed Lagrangian perturbation theory

Alternatively, perturbation theory can be derived as a function of the Lagrangian coordinates $\mathbf{q}$, which are related to their Eulerian counterparts $\mathbf{x}$ by the displacement field $\mathbf{\Psi}$,

$$\mathbf{x}(\mathbf{q},t) = \mathbf{q} + \mathbf{\Psi}(\mathbf{q},t)\,. \tag{5.119}$$

Under the assumption that the density perturbations at initial times are negligible, Eulerian and Lagrangian coordinates are related by the continuity equation: $\rho(\mathbf{x})d^3x = \bar{\rho}d^3q$, in terms of comoving densities. Using the properties of the Dirac δ_D distribution, this leads to

$$\delta(\mathbf{x}) = \int d^3q\,\delta_D\left[\mathbf{x}-\mathbf{q}-\mathbf{\Psi}(\mathbf{q})\right] - 1\,, \tag{5.120}$$

whose Fourier transform is [264]

$$\delta(\mathbf{k}) = \int d^3q\, e^{-i\mathbf{k}\cdot\mathbf{q}}\left[e^{-i\mathbf{k}\cdot\mathbf{\Psi}(\mathbf{q})} - 1\right]\,. \tag{5.121}$$

This expression can be used to derive the observable power spectrum in Eulerian space [213, 264, 265]:

$$P(\mathbf{k}) = \int d^3\mathbf{\Delta}_{12}\, e^{-i\mathbf{k}\cdot\mathbf{\Delta}_{12}}\left\{\langle e^{-i\mathbf{k}\cdot[\mathbf{\Psi}(\mathbf{q}_1)-\mathbf{\Psi}(\mathbf{q}_2)]}\rangle - 1\right\}\,, \tag{5.122}$$

where $\mathbf{\Delta}_{ij} \equiv \mathbf{q}_i - \mathbf{q}_j$, and the expectation value only depends on the separation $\mathbf{\Delta}_{12}$ due to homogeneity. Likewise, the bispectrum can be written as [217]

$$B(k_1,k_2,k_3) = \int d^3\mathbf{\Delta}_{12} \int d^3\mathbf{\Delta}_{13}\, e^{-i\mathbf{k}\cdot(\mathbf{\Delta}_{12}+\mathbf{\Delta}_{13})} \times \left\{ \langle e^{-i\mathbf{k_2}\cdot[\mathbf{\Psi}(\mathbf{q}_1)-\mathbf{\Psi}(\mathbf{q}_2)]-i\mathbf{k_3}\cdot[\mathbf{\Psi}(\mathbf{q}_1)-\mathbf{\Psi}(\mathbf{q}_3)]}\rangle - 1 \right\}; \quad (5.123)$$

also here the expectation value only depends on the separations $\mathbf{\Delta}_{12}, \mathbf{\Delta}_{13}$. Eqs. (5.122, 5.123) relate the observable (Eulerian) density polyspectra to the displacement field $\mathbf{\Psi}$. We follow Ref. [213] and use the cumulant expansion theorem,

$$\langle e^{-iX} \rangle = \exp\left[\sum_{N=1}^{\infty} \frac{(-i)^N}{N!} \langle X^N \rangle_c \right], \quad (5.124)$$

where $\langle X^N \rangle_c$ represents the cumulant of the random variable X [189]. By applying the cumulant expansion to Eqs. (5.122, 5.123), and expanding the powers of N with the binomial theorem, two types of terms are obtained: those depending on $\mathbf{\Psi}$ at one point, and those depending on $\mathbf{\Psi}$ at two different points. Refs. [213, 217] demonstrated that, if both sets of terms are expanded to the same order, the LPT results are identical to those obtained in SPT for both power spectrum and bispectrum. However Ref. [213] found that, for large separations, the terms depending on $\mathbf{\Psi}$ at one point are much larger than those depending on $\mathbf{\Psi}$ at two points, so that the first set of terms should be kept as it is, and only the second set should be expanded. This renormalised approach is called renormalised Lagrangian perturbation theory, RLPT.

In order to derive explicit expressions for the matter power spectrum and bispectrum, we need to expand the displacement field as a function of the matter overdensity δ. The displacement field follows the equation of motion:

$$\frac{d^2\mathbf{\Psi}}{dt^2} + 2H\frac{d\mathbf{\Psi}}{dt} = -\nabla_x \phi[\mathbf{q} + \mathbf{\Psi}(\mathbf{q})], \quad (5.125)$$

where ϕ is the gravitational potential. The polyspectra of $\mathbf{\Psi}$ can be calculated by expanding it as a series of the density field:

$$\mathbf{\Psi}^{(n)}(\mathbf{p}) = \frac{iD^n}{n!} \int \frac{d^3p_1}{(2\pi)^3} ... \frac{d^3p_n}{(2\pi)^3} \delta_D \left(\sum_{j=1}^{n} \mathbf{p}_j - \mathbf{p} \right) \mathbf{L}^{(n)}(\mathbf{p}_1, ..., \mathbf{p}_n)\, \delta_1(\mathbf{p}_1) ... \delta_1(\mathbf{p}_n), \quad (5.126)$$

where δ_1 indicates the linear density perturbation at present times, and the perturbative kernels $\mathbf{L}^{(n)}$ are the analogues of the SPT kernels F_n, G_n, and are also obtained from a recursion

relation [189]. As before, the growth rate D^n is only approximate in a non-Einstein-de Sitter Universe.

This expansion leads to the RLPT power spectrum [213], and to the bispectrum [217]:

$$P^{\rm RLPT}(k) = \exp\left[-\frac{k^2}{6\pi^2}\int dp\, P_{\rm lin}(p)\right] \times \left[P_{\rm lin}(k) + P^{\rm SPT}_{\text{1-loop}}(k) + \frac{k^2}{6\pi^2}P_{\rm lin}(k)\int dp\, P_{\rm lin}(p)\right], \tag{5.127}$$

$$B^{\rm RLPT}(k_1,k_2,k_3) = \exp\left[-\frac{k_1^2+k_2^2+k_3^2}{12\pi^2}\int dp\, P_{\rm lin}(p)\right] \times \left[B^{\rm SPT}_{\rm tree} + B^{\rm SPT}_{\text{1-loop}} + \frac{k_1^2+k_2^2+k_3^2}{12\pi^2}B^{\rm SPT}_{\rm tree}\int dp\, P_{\rm lin}(p)\right], \tag{5.128}$$

where $P^{\rm SPT}_{\text{1-loop}}$ is the one-loop SPT term (without the tree-level term). From Eqs. (5.127, 5.128) it is evident that the RLPT power spectrum and bispectrum reduce back to SPT if the exponential prefactor is expanded to first order. Furthermore, this prefactor is similar to the RPT results: in both cases, the theory decays rapidly to zero outside its range of validity. Thus this method is not expected to yield realistic predictions in the fully non-linear regime where the exponential cut-off dominates, but only on quasi-linear scales.

5.2.5 Nine-parameter model

The tree-level prediction is the simplest model for the bispectrum. As its simpler counterpart, the linear power spectrum, it is only accurate for very low values of the wavevectors. One very simple improvement to this would be to substitute the linear with the non-linear power spectrum in Eq. (5.46) and another one is to modify the kernel $F_2^{(s)}$ in order to better fit simulations to $F_2^{\rm eff}$. This idea has been proposed in Ref. [266] and here we discuss a more elaborate version of it, which fits the simulation even better, from Ref. [267]. The bispectrum in this theory can then be expressed as

$$B_{\text{9-parameter}}(k_1,k_2,k_3) = P_{\rm NL}(k_1,z)\,P_{\rm NL}(k_2,z)\,F_2^{\rm eff}(\mathbf{k}_1,\mathbf{k}_2) + 2\ \text{permutations}. \tag{5.129}$$

Each of the three terms of the kernel (5.30) is modified with a function, as follows:

$$F_2^{\rm eff}(\mathbf{q}_1,\mathbf{q}_2) = \frac{5}{7}a(n_1,k_1)a(n_2,k_2) + \frac{1}{2}\frac{\mathbf{q}_1\cdot\mathbf{q}_2}{q_1 q_2}\left(\frac{q_1}{q_2}+\frac{q_2}{q_1}\right)b(n_1,k_1)b(n_2,k_2) + \frac{2}{7}\frac{(\mathbf{q}_1\cdot\mathbf{q}_2)^2}{q_1^2 q_2^2}c(n_1,k_1)c(n_2,k_2)\,. \quad (5.130)$$

The functions $a(n,k)$, $b(n,k)$, $c(n,k)$ below can be expressed in terms of 9 coefficients that are determined numerically $(a_1,\cdots a_n)$:

$$a(n,k) = \frac{1+\sigma_8^{a_6}(z)[0.7Q_3(n)]^{1/2}(qa_1)^{n+a_2}}{1+(qa_1)^{n+a_2}}\,, \quad (5.131)$$

$$b(n,k) = \frac{1+0.2a_3(n+3)(qa_7)^{n+3+a_8}}{1+(qa_7)^{n+3.5+a_8}}\,, \quad (5.132)$$

$$c(n,k) = \frac{1+4.5a_4/[1.5+(n+3)^4](qa_5)^{n+3+a_9}}{1+(qa_5)^{n+3.5+a_9}}\,. \quad (5.133)$$

The functions $n(k)$, $Q_3(n)$ and q are defined as:

$$n(k) = \frac{d\log P_{\rm lin}(k)}{d\log k}\,, \quad (5.134)$$

$$Q_3(n) = \frac{4-2^n}{1+2^{n+1}}\,, \quad (5.135)$$

$$q = \frac{k}{k_{\rm NL}}\,, \quad (5.136)$$

where $k_{\rm NL}$ is the nonlinear scale defined as the solution to the equation:

$$k_{\rm NL}^3 P_{\rm lin}(k_{\rm NL}) = 2\pi^2\,. \quad (5.137)$$

The parameters have been calibrated to give a maximum of 10% error in the matter bispectrum for $z\in[0,1.5]$ and $k\leq 0.4h/{\rm Mpc}$ and they are: $a_1=0.484$, $a_2=3.740$, $a_3=-0.849$, $a_4=0.392$, $a_5=1.013$, $a_6=-0.575$, $a_7=0.128$, $a_8=-0.722$ and $a_9=-0.926$.

5.3 Phenomenological halo models

5.3.1 Standard halo model

The halo model of large-scale structure is a relatively simple phenomenological model for describing the non-linear distribution of dark matter. It assumes that the dark matter in the Universe is clustered into dense regions called halos. This model allows us to describe the n-point correlation functions of LSS. A comprehensive review of the halo model can be found in Ref. [232]. The first use of a similar model was in Ref. [268], where the authors were interested in the distribution of galaxies. The linear and mildly non-linear scales have so far been successfully described by perturbative-type approaches, but using such methods to go further into the non-linear regime has proved to be difficult, as standard perturbation theory breaks down after a certain scale. The halo model goes further into the non-linear regime than the perturbative approaches because it models the physical phenomena happening on those scales rather than just solving the equations.

The halo model can also be used in structure formation models, as the dark matter halos could be the seeds of galaxy creation [229, 269].

In order to describe the correlation functions using this model, one has first to describe the basic properties of the halos. One starts by assuming that all the dark matter of the Universe is contained in one of the halos. Non-linear objects are assumed to have been created by spherical collapse. The spherical collapse model was first discussed in Ref. [270]. The model assumes that initially overdense regions of the Universe become less and less dense due to the expansion of the Universe until a point where they collapse due to gravitational instability. The object virialises to a sphere of radius $R_{\rm v}$, which is non-zero. Moreover, the virialised halos are $\Delta_{\rm v}$ times denser than the background and hence, in terms of this parameter, the halo mass can be expressed as

$$m = \frac{4\pi}{3} R_{\rm v}^3 \Delta_{\rm v} \bar{\rho}. \tag{5.138}$$

If the object collapses today, it must have had a critical value of the overdensity,

$$\delta_{\rm sc} = \frac{3}{5}\left(\frac{3\pi}{2}\right)^{2/3}. \tag{5.139}$$

By denoting the number density of halos at mass m and redshift z with $n(m,z)$ and the background density of the Universe with $\bar{\rho}$, the halo density is expressed in terms of a new

variable ν, called the peak height, as [229, 271]:

$$\frac{m}{\bar{\rho}} n(m,z)\, dm = f(\nu)\, d\nu\,, \tag{5.140}$$

where the function f is a universal function, (*i.e.* independent of redshift) and ν is defined in Eq. (5.144) below.

The function f is chosen in order to fit simulations. We will describe here the Sheth-Tormen [272] & Tinker [273, 274] functions.

In order to define the peak height in terms of the halo mass, the Fourier transform of the top-hat filter and the variance of the linear power spectrum are required:

$$W(x) = \frac{3\left(\sin(x) - x\cos(x)\right)}{x^3}\,, \tag{5.141}$$

$$\sigma^2(m,z) = \int_0^\infty \frac{dk}{2\pi^2} k^2 W^2(kR)\, D^2(z)\, P_{\rm lin}(k)\,. \tag{5.142}$$

The radius R is the radius of a sphere of mass m and uniform density $\bar{\rho}$: $R = \left(\frac{3m}{4\pi\bar{\rho}}\right)^{\frac{1}{3}}$, $D(z)$ is the growth function normalised to 1 today and $P_{\rm lin}(k)$ is the linear power spectrum of fluctuations today such that the linear power spectrum at redshift z is

$$P_{\rm lin}(k,z) = D^2(z)\, P_{\rm lin}(k)\,. \tag{5.143}$$

The peak function is then expressed as

$$\nu = \frac{\delta_{\rm sc}^2}{\sigma^2(m,z)}\,. \tag{5.144}$$

The internal structure of halos has been extensively studied. A widely used halo profile is the Navarro-Frenk-White (NFW) profile [275], which can be expressed in terms of two parameters, $\rho_s(m)$ and $r_s(m)$, and has the following expression:

$$\rho(r|m) = \frac{\rho_s}{\left(\frac{r}{r_s}\right)\left(1+\frac{r}{r_s}\right)^2}\,. \tag{5.145}$$

In terms of this density, the halo mass can be expressed as

$$m = \int_0^{R_{\rm v}} 4\pi r^2 \rho(r|m)\,. \tag{5.146}$$

Defining a further quantity, the concentration parameter $c(m) = \frac{R_{\rm v}}{r_s}$, for the NFW profile the mass can be re-expressed as

$$m = 4\pi\rho_s r_s^3 \left[\log(1+c) - \frac{1}{1+c}\right]. \tag{5.147}$$

Hence, ρ_s and r_s can now be specified in terms of the concentration parameter and the overdensity parameter and only the concentration parameter needs to be specified:

$$\rho_s = \frac{1}{3}\Delta_{\rm v}\bar{\rho}\frac{c^3}{\log(1+c) - \frac{1}{1+c}}, \tag{5.148}$$

$$r_s = \left(\frac{3m}{4\pi c(m)^3\Delta_{\rm v}\bar{\rho}}\right)^{1/3}. \tag{5.149}$$

The concentration parameter can be defined using a fitting function obtained from the Bolshoi simulation [276, 277], where $M_\odot$ is the Solar mass:

$$c(m,z) = 9.2\kappa(z)D(z)^{1.3}\left(\frac{m}{10^{12}h^{-1}M_\odot}\right)^{-0.09} \times \left[1 + 0.013\left(\frac{m}{10^{12}h^{-1}M_\odot}D(z)^{-\frac{1.3}{0.09}}\right)^{0.25}\right], \tag{5.150}$$

with $\kappa(z) = 1.26$ at $z = 0$ and $\kappa(z) = 0.96$ at $z \geq 1$. The final ingredient required is the normalised Fourier transform of the dark matter distribution. In the case of a spherically symmetric halo, this has the expression

$$u(k|m) = \int_0^{R_{\rm v}} dr 4\pi r^2 \frac{\sin(kr)}{kr}\frac{\rho(r|m)}{m}. \tag{5.151}$$

In the case of the NFW profile (Eq. 5.145), the integral can be calculated analytically yielding

$$u(k|m) = \frac{4\pi\rho_s r_s^3}{m}\left\{\sin(kr_s)\left[\mathrm{Si}((1+c)kr_s) - \mathrm{Si}(kr_s)\right] - \frac{\sin(kr_s)}{(1+c)kr_s} + \cos(kr_s)\left[\mathrm{Ci}((1+c)kr_s) - \mathrm{Ci}(kr_s)\right]\right\}, \tag{5.152}$$

where $\mathrm{Si}(x)$ and $\mathrm{Ci}(x)$ are the sine and cosine integral functions defined by:

$$\mathrm{Si}(x) = \int_0^x \frac{\sin(t)}{t} dt\,, \tag{5.153}$$

$$\mathrm{Ci}(x) = -\int_x^\infty \frac{\cos(t)}{t} dt\,. \tag{5.154}$$

The overdensity of halos, denoted δ_h is only equal to the matter overdensity δ as a zeroth order approximation. In order to have a more accurate relation between the two quantities, one must expand δ_h in terms of powers of δ using perturbation theory:

$$\delta_h(m,z) = \sum_{i>0} \frac{b_i(m,z)}{i!} \delta^i\,. \tag{5.155}$$

The coefficients b_i in front of the powers of δ are called bias coefficients. As this is a Taylor series in δ, it is expected to be accurate only on large scales.

These expressions assume Gaussian initial conditions. If primordial non-Gaussianity is considered, the bias coefficients will also depend on the scale k. This expansion can be plugged back into the expression of the density field,

$$\rho = \bar{\rho}(1+\delta) = \int dmmn(m)\left[1+\delta_h(m)\right] = \int dmmn(m)\left[1+\sum_{i>0}\frac{b_i(m)}{i!}\delta^i(m)\right]. \tag{5.156}$$

Identifying coefficients in the integral expressions, the following consistency conditions are obtained:

$$\int dm \frac{m}{\bar{\rho}} n(m) = 1\,, \tag{5.157}$$

$$\int dm \frac{m}{\bar{\rho}} n(m) b_1(m) = \int d\nu f(\nu) b_1(\nu) = 1\,, \tag{5.158}$$

$$\int dm \frac{m}{\bar{\rho}} n(m) b_i(m) = \int d\nu f(\nu) b_i(\nu) = 0 \tag{5.159}$$

for all $i > 1$.

Sheth-Tormen mass function

The function from Ref. [272] gives a good fit with simulations of gravitational clustering,

$$f(\nu) = A(p)\left(1+\left(q\nu^2\right)^{-p}\right)\sqrt{\frac{q\nu^2}{2\pi}}\exp\left(-q\nu^2/2\right) \tag{5.160}$$

and $\Delta_{\rm v}$ depends weakly on the cosmology through the parameter $\Omega(z) = \frac{\Omega_c(1+z)^3}{\Omega_c(1+z)^3+\Omega_\Lambda}$, with Ω_c the density of CDM and baryons today and Ω_Λ the dark energy density [278, 279]. Then,

$$\Delta_{\rm v} = \frac{18\pi^2 + 82\left(\Omega(z)-1\right) - 39\left(\Omega(z)-1\right)^2}{\Omega(z)}. \tag{5.161}$$

The 3 parameters are chosen in order to fit simulations [280]: $p = 0.3$, $A(p) = 0.3222$, $q = 0.75$.

In terms of the variable ν and the coefficients defined earlier in this subchapter (p, q), the first two bias coefficients are [272, 281, 282]:

$$b_1(\nu) = 1 + \frac{q\nu^2-1}{\delta_{\rm sc}} + \frac{2p}{\delta_{\rm sc}\left(1+(q\nu^2)^p\right)}, \tag{5.162}$$

$$b_2(\nu) = \frac{8}{21}\left[b_1(\nu)-1\right] + \frac{q\nu^2}{\delta_{\rm sc}}\frac{q\nu^2-3}{\delta_{\rm sc}} + \left(\frac{1+2p}{\delta_{\rm sc}} + 2\frac{q\nu^2-1}{\delta_{\rm sc}}\right)\frac{2p}{\delta_{\rm sc}\left(1+(q\nu^2)^p\right)}. \tag{5.163}$$

Tinker mass function

The Tinker mass function can be expressed in terms of the variable ν as follows:

$$f(\nu) = \alpha\left[1+(\beta\nu)^{-2\phi}\right]\nu^{2\eta}\exp(-\gamma\nu^2/2), \tag{5.164}$$

where $\Delta = 200$ and the coefficients β, γ, η and ϕ have the following redshift dependence:

$$\beta = \beta_0(1+z)^{0.20}, \tag{5.165}$$

$$\gamma = \gamma_0(1+z)^{-0.01}, \tag{5.166}$$

$$\eta = \eta_0(1+z)^{0.27}, \tag{5.167}$$

$$\phi = \phi_0(1+z)^{-0.08} \tag{5.168}$$

and $\alpha = 0.368$, $\beta_0 = 0.589$, $\gamma_0 = 0.864$, $\eta_0 = -0.243$ and $\phi_0 = -0.729$.

The first two bias coefficients are:

$$b_1(\nu) = \frac{2\phi}{\delta\left((\beta\nu)^{2\phi}+1\right)} + \frac{\gamma\nu^2+\delta-2\eta-1}{\delta}, \tag{5.169}$$

$$b_2(\nu) = \frac{2\left(42\gamma\nu^2\phi + 8\delta\phi - 84\eta\phi + 42\phi^2 - 21\phi\right)}{21\delta^2\left((\beta\nu)^{2\phi}+1\right)} + \frac{21\gamma^2\nu^4 + 8\gamma\delta\nu^2 - 84\gamma\eta\nu^2 - 63\gamma\nu^2}{21\delta^2} + \frac{-16\delta\eta - 8\delta + 84\eta^2 + 42\eta}{21\delta^2}\,. \quad (5.170)$$

In the numerical implementation however, the normalisation conditions (5.157)-(5.159) are not exactly satisfied, because in Eq. (5.140), $n(m) \not\to 0$ as $\nu \to 0$. In practice this is not a problem, since the halo masses won't be anyway that small and hence the normalisation is fixed by adding a numerical value to the smallest mass bin considered [283].

All these ingredients discussed so far can be used to calculate the correlation functions in the halo model. In the case of the 2-point correlation function, the power spectrum can be expressed in terms of 2 contributions, the 1-halo and 2-halo terms, which correspond to the situations where the 2 points considered belong to the same halo (1-halo) and to different halos (2-halo) respectively. Thus, the power spectrum can be expressed as

$$P(k) = P_{1h}(k) + P_{2h}(k)\,, \quad (5.171)$$

with the 1- and 2-halo contributions given by:

$$P_{1h}(k,z) = \int dm n(m) \left(\frac{m}{\bar{\rho}}\right)^2 u(k|m)^2\,, \quad (5.172)$$

$$P_{2h}(k,z) = \int dm_1 n(m_1) \left(\frac{m_1}{\bar{\rho}}\right) u(k|m_1) \int dm_2 n(m_2) \left(\frac{m_2}{\bar{\rho}}\right) u(k|m_2) P_{hh}(k|m_1,m_2)\,, \quad (5.173)$$

where the z-dependence in n and u is implicit and P_{hh} is the halo-halo power spectrum, which can be approximated at first order by:

$$P_{hh}(k|m_1,m_2) = b_1(m_1) b_1(m_2) D^2(z) P_{\rm lin}(k)\,. \quad (5.174)$$

Using Eqs. (5.173) and (5.174), the following expression is obtained for the 2-halo term:

$$P_{2h}(k,z) = \left[\int dm n(m) \left(\frac{m}{\bar{\rho}}\right) b_1(m,z) u(k|m)\right]^2 D^2(z) P_{\rm lin}(k)\,. \quad (5.175)$$

For the bispectrum, the halo model consists of three contributions, corresponding to the situations where the 3 points from the correlation function are all in the same halo (1-halo term), 2 in one halo and one in another one (2-halo term) and all 3 in different halos (3-halo term). Hence, the total bispectrum in this model, assuming no primordial non-Gaussianity

becomes

$$B(k_1,k_2,k_3) = B_{1h}(k_1,k_2,k_3) + B_{2h}(k_1,k_2,k_3) + B_{3h}(k_1,k_2,k_3)\,. \tag{5.176}$$

All three contributions can be again described using the quantities defined earlier:

$$B_{1h}(k_1,k_2,k_3) = \int dm n(m) \left(\frac{m}{\bar{\rho}}\right)^2 \prod_{i=1}^{3} u(k_i|m)\,, \tag{5.177}$$

$$\begin{aligned} B_{2h}(k_1,k_2,k_3) = &\left[\int dm_1 n(m_1) \left(\frac{m_1}{\bar{\rho}}\right) u(k_1|m_1) \times \right. \\ &\left. \int dm_2 n(m_2) \left(\frac{m_2}{\bar{\rho}}\right)^2 u(k_2|m_2)\, u(k_3|m_2)\, P_{hh}(k_1|m_1,m_2)\right] + 2 \text{ cyc.}\,, \end{aligned} \tag{5.178}$$

$$\begin{aligned} B_{3h}(k_1,k_2,k_3) = &\prod_{i=1}^{3} \left[\int dm_i n(m_i) \left(\frac{m_i}{\bar{\rho}}\right)^2 u(k_i|m_i)\right] \\ &\times \left\{ b_1(m_1)\, b_1(m_2)\, b_1(m_3)\, D^4(z)\, B_{\text{tree}}(k_1,k_2,k_3,z=0) + \right. \\ &\left. \left[b_1(m_1)\, b_1(m_2)\, b_2(m_3)\, D^4(z)\, P_{\text{lin}}(k_1)\, P_{\text{lin}}(k_2)\right] + 2 \text{ cyc.}\right\}\,, \end{aligned} \tag{5.179}$$

where B_{tree} is the tree-level bispectrum at $z = 0$ (defined in Subchapter 5.2.1).

5.3.2 Combined halo-PT model

When considering the large scale halo power spectrum, $k \to 0$, it would be expected that all the contribution would come from the 2-halo term (the points considered in the 2-point correlation function are far apart, and hence they must be in different halos). Indeed,

$$\lim_{k\to 0} u(k|m) = 1\,. \tag{5.180}$$

Using Eq. (5.175) and the normalisation condition (5.158),

$$\lim_{k\to 0} P_{2h}(k,z) = D^2(z)\, P_{\text{lin}}(k)\,, \tag{5.181}$$

as expected. However, from Eq. (5.172),

$$\lim_{k\to 0} P_{1h}(k,z) = \int dm n(m) \left(\frac{m}{\bar{\rho}}\right)^2 \neq 0\,. \tag{5.182}$$

This same phenomenon happens in the 1- and 2-halo bispectra, while the 3-halo bispectrum matches the tree-level one on large scales. This shows that the power spectrum and bispectrum

in the standard halo model is overestimated on linear scales. This is not satisfactory, since it is known that on very large scales the linear power spectrum and the tree-level bispectrum should be very accurate. This problem has been discussed in the literature: [232, 284, 285] and various solutions to it have been proposed: [205, 232–234, 237]. The solution from Refs. [233, 234] is described in this subchapter and its consequences are predicted.

It has been shown that the halo model matches simulations well at higher wavenumbers than perturbative methods for the power spectrum [232, 237, 286, 287]. Based on the observations of the above paragraph and the fact that perturbative methods work very well exactly at small wavenumbers, the authors of Refs. [233, 234] have presented a method to combine the perturbative and halo methods such that the combined theory would take the best of the perturbative theory (large scales) and halo model (mildly non-linear scales).

Working in a Lagrangian formalism, a particle trajectory is defined as $\mathbf{x}(\mathbf{q},t)$, where $\mathbf{q}$ is the initial Lagrangian coordinate. Then the power spectrum can be expressed as [264, 288]:

$$P(k) = \int d^3q \langle e^{i\mathbf{k}\cdot\Delta\mathbf{x}} - e^{i\mathbf{k}\cdot\mathbf{q}} \rangle \,, \tag{5.183}$$

where

$$\Delta\mathbf{x} = \mathbf{x}(\mathbf{q}) - \mathbf{x}(0) \tag{5.184}$$

and $\langle \cdots \rangle$ represents statistical average.

The probability that a particle $\mathbf{q}_1$ belongs to a halo with mass in $[m, m+dm]$ is

$$dF = f(\nu)\, d\nu \,. \tag{5.185}$$

Assuming that q_m is the Lagrangian radius of a halo with density $\bar{\rho}$ and mass m, the probability that a particle $\mathbf{q}_2$, at a distance $q = |\mathbf{q}_2 - \mathbf{q}_1|$ is situated in the same halo can be expressed as

$$F_m(q) = \begin{cases} \frac{(2q_m - q)^2 (4q_m + q)}{16 q_m^3} & \text{if } 0 \le q \le 2q_m \\ 0 & \text{if } q > q_m \end{cases} .$$

Then the probability that the pair $[\mathbf{q}_1, \mathbf{q}_2]$ belongs to a single halo is

$$F_{1H}(q) = \int_{\nu_{q/2}}^{\infty} d\nu f(\nu) F_m(q) \,, \tag{5.186}$$

where f is the Sheth-Tormen function (5.160). Therefore, the probability that the points belong to different halos is

$$F_{2H}(q) = 1 - F_{1H}(q) \,. \tag{5.187}$$

Hence, the 1- and 2-halo contribution can be expressed as:

$$P_{1H}(k) = \int d^3q F_{1H}(q) \langle e^{i\mathbf{k}\cdot\Delta\mathbf{x}} - e^{i\mathbf{k}\cdot\mathbf{q}} \rangle_{1H} \,, \tag{5.188}$$

$$P_{2H}(k) = \int d^3q F_{2H}(q) \langle e^{i\mathbf{k}\cdot\Delta\mathbf{x}} - e^{i\mathbf{k}\cdot\mathbf{q}} \rangle_{2H} \,, \tag{5.189}$$

where in this case the averages are conditional on the fact that the set of points must be in exactly one of the terms. The terms described in Eqs. (5.188)-(5.189) are the 1- and 2-halo terms from the halo model (Subchapter 5.3.1). By thinking of the perturbative expansions and of the expected physical behaviour of the 2 terms, $F_{1H} \equiv 0$ on all levels of perturbation theory. Hence $F_{2H} \equiv 1$ and the 2-halo contribution is completely perturbative.

At a perturbative level, the function $F_{2H}(q)$ is approximated by a typical value $F_{2H}(\frac{1}{k})$ and also the conditional average of the particles belonging to 2 halos is taken to be the value of the functions evaluated in perturbation theory. Hence,

$$P_{2H\,\text{new}}(k) = F_{2H}(1/k) P_{PT}(k) \,. \tag{5.190}$$

For the 1-halo contribution, it is assumed that the halos are fully virialised, and hence

$$\langle e^{i\mathbf{k}\cdot\Delta\mathbf{x}} \rangle_m = u(k|m)^2 \,, \tag{5.191}$$

with $u(k|m)$ given in Eq. (5.151). Substituting back the result (5.191) into (5.188) and changing the order of integration, the following expression is obtained:

$$P_{1h\,\text{new}}(k) = \int dmn(m) \left(\frac{m}{\bar{\rho}}\right)^2 \left(u(k|m)^2 - W(kq_m)^2\right) \,, \tag{5.192}$$

where $W(x)$ is the filter function defined in Eq. (5.141). This equation is very similar to Eq. (5.172), with the difference that the integral over the filter function is subtracted. This ensures that the 1-halo term would not contribute in the limit $k \to 0$ and also that it tends to P_{1h} for larger k. The perturbative power spectrum in Eq. (5.190) can be any power spectrum from perturbation theory. One can start by taking various perturbative methods like SPT and EFT and check how the result is improved.

This method can be expanded in a similar fashion to the bispectrum, though there are some differences that arise [234]. As for the power spectrum, on very large scales the only term that should contribute to the bispectrum is the 3-halo term. Hence, that is the only perturbative contribution and the 1- and 2-halo terms are non-perturbative.

In the Lagrangian formalism, the 3-point correlation function is expressed as

$$\langle \delta(\mathbf{k}_1)\,\delta(\mathbf{k}_2)\,\delta(\mathbf{k}_3)\rangle = \langle \int d^3q_1 \int d^3q_2 \int d^3q_3 \prod_{j=1}^{3} \left(e^{-i\mathbf{k}_j\cdot\mathbf{x}_j} - e^{-i\mathbf{k}_j\cdot\mathbf{q}_j} \right) \rangle \,, \tag{5.193}$$

which is then split into the 1- , 2- and 3-halo contributions. The 1-halo contribution can be expressed as:

$$\langle \delta(\mathbf{k}_1)\,\delta(\mathbf{k}_2)\,\delta(\mathbf{k}_3)\rangle_{1H} = \int d^3q^c \int dm \frac{\bar{\rho}}{m} n(m) \langle \int_{V_m} \prod_{j=1}^{3} d^3q_j \left(e^{-i\mathbf{k}_j\cdot\mathbf{x}_j} - e^{-i\mathbf{k}_j\cdot\mathbf{q}_j} \right) \rangle_{\mathbf{q}^c,m} \,, \tag{5.194}$$

where the average is conditional on the three particle positions corresponding to wavevectors $\mathbf{k}_j$ belonging to the same halo of centre $\mathbf{q}^c$, mass m and Lagrangian volume V_m. By denoting the displacement of the centre of mass of the halo with $\Psi^c = \mathbf{x}^c - \mathbf{q}^c$, the 1-halo term becomes

$$\begin{aligned} \langle \delta(\mathbf{k}_1)\,\delta(\mathbf{k}_2)\,\delta(\mathbf{k}_3)\rangle_{1H} = \int d^3q^c \int dm \frac{\bar{\rho}}{m} n(m) \left(\frac{m}{\bar{\rho}} \right)^3 \times \\ e^{-i(\mathbf{k}_1+\mathbf{k}_2+\mathbf{k}_3)\cdot\mathbf{q}^c} \prod_{j=1}^{3} d^3q_j \left(e^{-i\mathbf{k}_j\cdot\Psi^c} u\left(k_j|m\right) - W(k_j q_m) \right) . \end{aligned} \tag{5.195}$$

By performing the integration over $\mathbf{q}^c$ and by neglecting the displacement of the halos ($\Psi^c = 0$), the 1-halo bispectrum becomes:

$$B_{1h}(k_1,k_2,k_3) = \int dm n(m) \left(\frac{m}{\bar{\rho}} \right)^3 \prod_{i=1}^{3} \left[u(k_i|m) - W(k_i q_m) \right] . \tag{5.196}$$

This function has the correct behaviour on large scales.

For the 2-halo bispectrum, proceeding in a similar fashion the following expression is obtained:

$$B_{2h}(k_1,k_2,k_3) = \left[\int dm_1 n(m_1) \times \left(\frac{m_1}{\bar{\rho}}\right)[u(k_1|m_1) - W(k_1 q_{m_1})] \int dm_2 n(m_2) \times \right.$$
$$\left. \left(\frac{m_2}{\bar{\rho}}\right)^2 [u(k_2|m_2) - W(k_2 q_{m_2})]\,[u(k_3|m_2) - W(k_3 q_{m_3})]\,P_{hh}(k_1|m_1,m_2)\right] + 2 \text{ cyc}. \quad (5.197)$$

This result is however not satisfactory, because it scales as $k_1^2 P(k_1)$ as $k_1 \to 0$ and a scaling $P(k_1)$ was expected. It means that the approximation $\Psi^c = 0$ is not good enough. An approximation that scales in the correct fashion has been proposed, by taking the biases to $b_1(m) = 1$ and by removing the first bracket of $u(k_1|m_1) - W(k_1 q_{m_1})$. Hence,

$$P_{hh}(k|m_1,m_2) \approx P_{\text{lin}}(k) \quad (5.198)$$

and the 2-halo term becomes

$$B_{2h\,\text{new}}(k_1,k_2,k_3) = P_{\text{lin}}(k_1) \int dm n(m) \left(\frac{m}{\bar{\rho}}\right)^2 [u(k_2|m) - W(k_2 q_m)]$$
$$\times [u(k_3|m) - W(k_3 q_m)] + 2 \text{ cyc}. \quad (5.199)$$

As previously discussed, the 3-halo bispectrum is obtained by a perturbative approach. In a similar fashion to the 2-halo power spectrum, this contribution should match the tree-level bispectrum on very large scales. The probability that the 3 wavevectors belong to different halos can be approximated by

$$F_{3H}(k_1,k_2,k_3) = \int_0^{\nu_{k_1}} d\nu_1 \int_0^{\nu_{k_1}} d\nu_3 \int_0^{\nu_{k_1}} d\nu_3 f(\nu_1) f(\nu_2) f(\nu_3). \quad (5.200)$$

This new model for the bispectrum is expected to work better than the standard halo model and also than the perturbative approaches on the scales of interest.

CHAPTER 6

COMPARISON BETWEEN THEORETICAL LARGE SCALE STRUCTURE BISPECTRUM MODELS AND *N*-BODY SIMULATIONS

6.1 Introduction and correlators

6.1.1 Shape and amplitude correlators

In order to compare the observed or simulated bispectra with the corresponding theoretical predictions, we define the signal-to-noise weighted scalar product between two bispectrum shapes i and j [244, 289]:

$$\langle B_i, B_j \rangle \equiv \frac{V}{\pi} \int_{\mathscr{V}_B} dV_k \, \frac{k_1 k_2 k_3 \, B_i(k_1,k_2,k_3) \, B_j(k_1,k_2,k_3)}{P(k_1)P(k_2)P(k_3)} \,, \tag{6.1}$$

where the integration domain $\mathscr{V}_B$ is the tetrahedral region of volume V satisfying the triangle condition on the wavenumbers k_1, k_2 and k_3 (such that $\mathbf{k}_1 + \mathbf{k}_2 + \mathbf{k}_3 = 0$), together with a chosen resolution limit $k_1, k_2, k_3 < k_{\rm max}$. The bispectrum domain is the union of a tetrahedron with a triangular pyramid on top (denoted the 'tetrapyd') and is illustrated in Fig. 6.1. The inner product Eq. (6.1) provides a natural definition for the signal-to-noise (SN) weighted bispectrum,

$$B_i^{\rm SN}(k_1,k_2,k_3) \equiv \sqrt{\frac{k_1 k_2 k_3}{P(k_1)P(k_2)P(k_3)}} \, B_i(k_1,k_2,k_3) \,, \tag{6.2}$$

where we use the measured (or HALOFIT) power spectrum $P_{\rm NL}(k)$ for wavenumbers in the quasilinear and nonlinear regimes (rather than the linear power spectrum $P_{\rm lin}$). The SN-weighted bispectrum $B_i^{\rm SN}$ is the relevant quantity observationally if the matter bispectrum

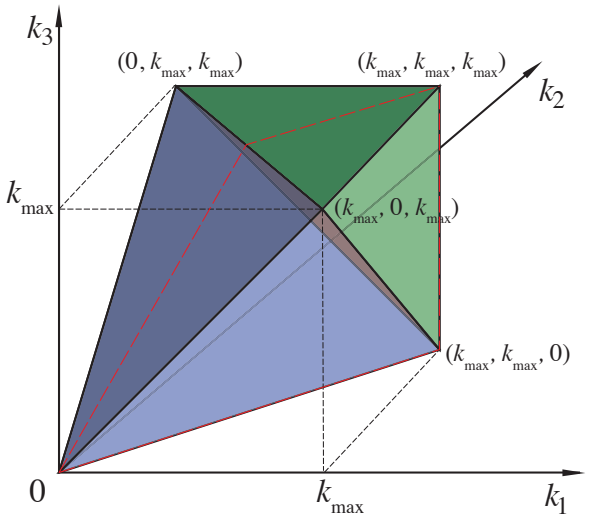

Fig. 6.1 The tetrapyd bispectrum domain consists of a tetrahedral region (blue) defined by the wavevector triangle condition in Eq. (5.41), together with a pyramidal region (green) bounded by the resolution limit $k_{\rm max}$. For the autocorrelator bispectrum this has a sixfold symmetry, so to illustrate the internal structure of the bispectrum (equilateral limit) we will split the tetrapyd across the vertical plane given by the red-dashed lines, removing the front half as shown in Fig. 6.2.

could be measured directly, providing optimal forecasts for an ideal survey (*i.e.* one without experimental noise or systematics). To develop an intuitive understanding of the distinct gravitational bispectrum contributions, we will plot the SN-weighted bispectrum in three dimensions on half the tetrapyd domain as shown in Fig. 6.2. Although the full tetrapyd has a sixfold symmetry for the isotropic bispectrum of Eq. (5.41), leaving this redundancy allows us to view $B_i^{\rm SN}$ from equilateral, flattened and squeezed limits simultaneously. (Future work will include bispectrum cross-correlators, e.g., the matter-matter-halo bispectrum where Fig. 6.2 shows the complete domain, as for recent CMB polarisation results [147].)

Based on the scalar product of Eq. (6.1), we define the *shape correlator* (or cosine) by:

$$\mathscr{S}\left(B_i, B_j\right) \equiv \frac{\langle B_i, B_j\rangle}{\sqrt{\langle B_i, B_i\rangle\langle B_j, B_j\rangle}}\,, \tag{6.3}$$

which is restricted to $-1 \leq \mathscr{S} \leq 1$. In the following, we will typically calculate the shape correlators between theoretical and simulated bispectra, to which the shapes i, j will correspond respectively.

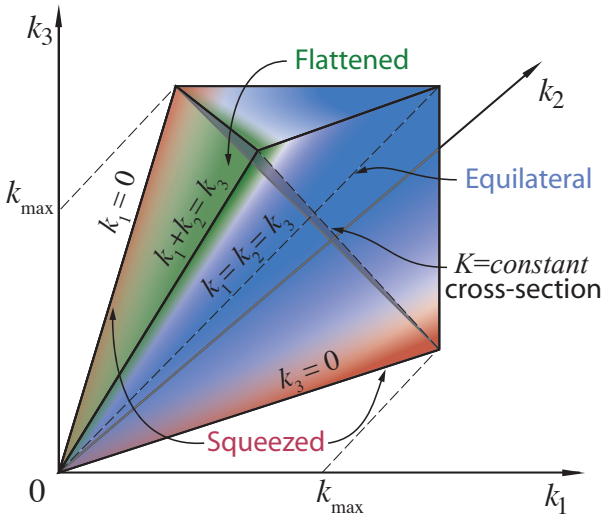

Fig. 6.2 The split 3D tetrapyd region used to illustrate the SN-weighted bispectrum showing only the back half with $k_1 < k_2$. Colour-coded regions show the location of the 'squeezed' (red), 'flattened' (green) and 'equilateral' or 'constant' (blue) shape signals. In the bispectrum ansatz Eq. (6.9) the shape $S(k_1,k_2,k_3)$ is defined on the $K \equiv k_1+k_2+k_3 = \text{const.}$ cross-sectional planes, while the scale-dependence $f(K)$ is given along the dashed diagonal $k_1 = k_2 = k_3$.

In order to measure how well the magnitude of the theoretical bispectra i fit the (simulated) data j, we define the *amplitude correlator* as:

$$\mathscr{A}\left(B_i,B_j\right) \equiv \sqrt{\frac{\langle B_i,B_i\rangle}{\langle B_j,B_j\rangle}}\,. \tag{6.4}$$

We can thus introduce a single quantity that combines the shape and amplitude information, the *total correlator*, defined as:

$$\mathscr{T}\left(B_i,B_j\right) \equiv 1 - \sqrt{\frac{\langle B_j-B_i,B_j-B_i\rangle}{\langle B_j,B_j\rangle}} \tag{6.5}$$

$$= 1 - \sqrt{1-2\mathscr{S}\left(B_i,B_j\right)\mathscr{A}\left(B_i,B_j\right)+\mathscr{A}^2\left(B_i,B_j\right)}\,. \tag{6.6}$$

This total correlator offers an excellent means by which to determine the overall goodness of fit as we essentially measure the magnitude of the residual $B_i - B_j$ relative to the measured bispectrum $|B_j|$. If $B_i = B_j$, this is zero and the total correlator is $\mathscr{T} = 1$. If B_i and B_j are misaligned ($\mathscr{S} < 1$) or differ in amplitude ($\mathscr{A} \neq 1$), the residual $B_i - B_j$ is non-zero and

the total correlator $\mathscr{T} < 1$. For increasing relative bispectrum residual, the total correlator always decreases. (Note that this is a more stringent test than the shape correlator of Eq. (6.3) alone because $\mathscr{S}$ appears under a square root in Eq. (6.6)).

It is possible to relate the total correlator $\mathscr{T}$ to the χ^2 goodness of fit determined between the theoretical bispectrum B_i and the estimated (or simulated) bispectrum B_j, as [290]:

$$\begin{aligned}\chi^2 &= \sum_{k_1,k_2,k_3} \frac{\left[B_j(k_1,k_2,k_3) - B_i(k_1,k_2,k_3)\right]^2}{\mathrm{var}(B_i)} \\ &= \langle B_j - B_i, B_j - B_i \rangle \,, \end{aligned} \tag{6.7}$$

so that χ^2 and the total correlator $\mathscr{T}$ are simply linked by:

$$\chi^2 = \left[1 - \mathscr{T}(B_i,B_j)\right]^2 \langle B_j, B_j \rangle \,. \tag{6.8}$$

As we are using a small number of simulations of limited resolution, in the following we will consider the total correlator $\mathscr{T}$ together with its uncertainty as a measurement of the goodness of fit of each model. In principle, the use of $\chi^2/\mathrm{d.o.f.}$ may be more suitable than $\mathscr{T}$ to distinguish overfitting ($\chi^2/\mathrm{d.o.f.} < 1$) from poor model performance ($\chi^2/\mathrm{d.o.f.} > 1$). However, our focus here is to determine the k_{max} at which the model starts to become a poor description of our present simulations, which corresponds to the k_{max} where $\mathscr{T}$ becomes significantly smaller than unity (given the estimated errors between simulations).

The three correlators here, $\mathscr{S}$, $\mathscr{A}$ and $\mathscr{T}$, are all cumulative functions of k_{max}, which is the resolution cut-off used in the scalar product of Eq. (6.1). We therefore obtain an overall integrated measure of how well a particular theory matches simulations (or observations) up to k_{max}.

6.1.2 Three canonical shape functions

We are able to obtain an accurate global description of the non-linear gravitational bispectrum from a sum over a limited number of simple bispectrum shapes, provided that we have the flexibility to modify an overall scale-dependent amplitude. For this reason, we consider the following non-trivial bispectrum ansatz:

$$B(k_1,k_2,k_3) = f(K)\, S(k_1,k_2,k_3) \,, \tag{6.9}$$

where $K \equiv k_1 + k_2 + k_3$, and the 'shape function' S is taken, in turn, to be a separable function of the form

$$S(k_1, k_2, k_3) = A(k_1)\, B(k_2)\, C(k_3) + \text{perms}\,. \tag{6.10}$$

This separation between transverse $K = \text{const.}$ slices and the K-dependent diagonal is illustrated in Fig. 6.2.

The separable ansatz (Eq. 6.9) is motivated in part by comparison with primordial non-Gaussian models, for which we define the shape function S by taking out an overall scaling $(k_1 k_2 k_3)^{-2}$ after which S is (almost) scale-invariant, that is, independent of the summed wavenumber K along the tetrapyd diagonal. For this reason, most primordial bispectra depend only on the two degrees of freedom transverse to the diagonal and can be completely defined by the shape S on the triangular surface $K = \text{const.}$

At late times, this simple separation of variables (Eq. 6.9) may not apply accurately because of the scale-dependent transfer functions, which means that perturbations with different wavenumbers k_i receive different amplifications. Nevertheless, this is encoded in the turnover of the late-time linear matter power spectrum $P_{\rm lin}(k)$, which can still be used to create a separable (though scale-dependent) 'shape function', e.g. as we will see for the tree-level gravitational bispectrum. For this reason, the separable description (Eq. 6.9) can still prove very useful if physically well-motivated shapes $S(k_1, k_2, k_3)$ are chosen and an overall scaling dependence $f(K)$ is allowed.

The three basic separable bispectrum shape functions $S(k_1, k_2, k_3)$ we shall employ are the constant shape [291], the squeezed (or local) shape [146, 292, 293] and the tree-level (or flattened) shape from standard perturbation theory discussed earlier. These three functions are essentially weighting functions for specific triangular configurations, that is, constant treats all triangles equally across the tetrapyd, squeezed favours those along the edges, and flattened those near the faces, as illustrated in Fig. 6.2 (qualitatively encompassing the commonly discussed equilateral, local and orthogonal shapes respectively). The constant shape is simply given by

$$S^{\rm const}(k_1, k_2, k_3) = 1\,(\text{Mpc}/h)^6. \tag{6.11}$$

Physically, the constant bispectrum is produced by a random set of point sources, together with an appropriate scaling dependence $f(K)$. It is our first approximation to the bispectrum of the non-linear virialised end products of gravitational collapse assumed in halo models, with a SN-weighted version illustrated in Fig. 6.3(a).

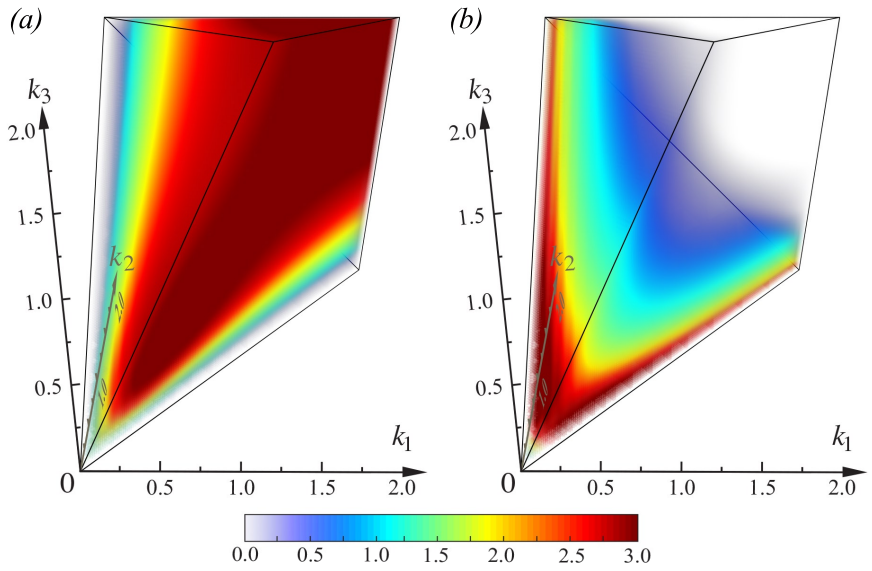

Fig. 6.3 (a) The SN-weighted 'constant' bispectrum of Eq. (6.11) with a broadly equilateral signal shown together with (b) the 'squeezed' or local model (Eq. 6.12) with high signal at the edges near $k_i \approx 0$ (shown at redshift $z = 0$). Note that the plotted 'constant' bispectrum does not have a constant cross-sectional shape because of the non-uniform signal-to-noise weighting (Eq. 6.2) particularly near the edges; here $S^{\text{const.}}$ in Eq. (6.11) is multiplied by $f(K) = K^3$ (the colour scale is normalised).

The second shape is 'squeezed' and we shall define it as

$$S^{\text{squeez}}(k_1,k_2,k_3) = \tfrac{1}{3}\left[P_{\text{lin}}(k_1)P_{\text{lin}}(k_2) + P_{\text{lin}}(k_2)P_{\text{lin}}(k_3) + P_{\text{lin}}(k_3)P_{\text{lin}}(k_1)\right], \tag{6.12}$$

which incorporates the scale dependence of the transfer functions within the linear power spectrum $P_{\text{lin}}(k)$. It is illustrated in Fig. 6.3(b). This squeezed shape is motivated by 'local' non-Gaussianity in which perturbation fields are simply squared, and where the leading contribution has a large wavelength mode affecting non-linearity on small scales (*i.e.*, for 'squeezed' triangles with $k_1 \ll k_2, k_3$). However, Eq. (6.12) regularises the related scale-invariant primordial local shape,

$$S^{\text{local}}(k_1,k_2,k_3) = \frac{1}{3}\left(\frac{k_1^2}{k_2k_3} + \frac{k_2^2}{k_3k_1} + \frac{k_3^2}{k_1k_2}\right), \tag{6.13}$$

which behaves poorly because it diverges for very squeezed triangles.

Finally, the third flattened shape is the tree-level gravitational bispectrum given by [186]

$$S^{\text{tree}}(k_1,k_2,k_3) = 2P_{\text{lin}}(k_1)P_{\text{lin}}(k_2)F_2^{(s)}(\mathbf{k}_1,\mathbf{k}_2) + 2 \text{ perms.}, \tag{6.14}$$

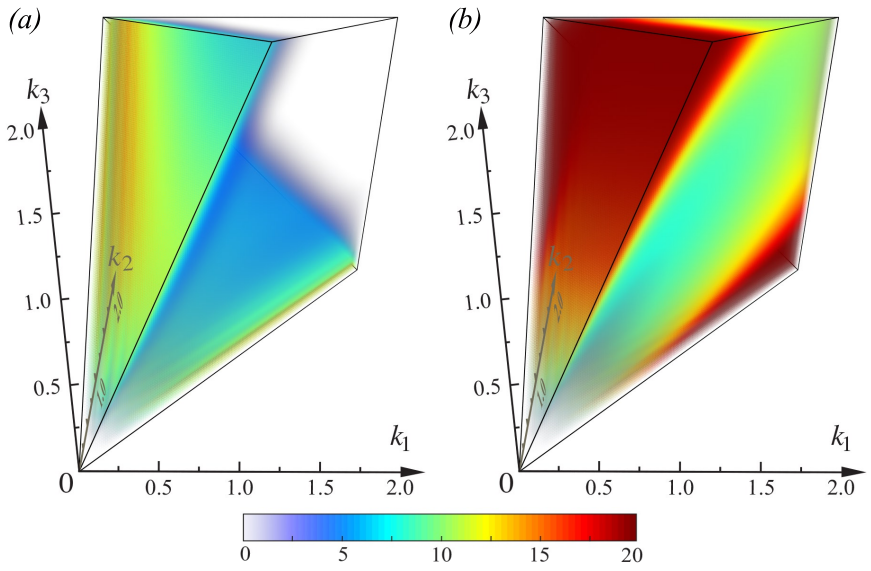

Fig. 6.4 Flattened shapes: (a) The SN-weighted tree-level bispectrum of Eq. (6.14) compared with (b) the nonlinear tree-level model (Eq. 6.15), both shown at redshift $z = 2$. Note that this flattened shape is dominated by signal on the outer tetrapyd face (front left) where $k_1 + k_2 \approx k_3$ (see Fig. 6.2 for the geometry). The nonlinear tree-level amplitude is substantially higher than the tree-level, but they share an excellent binned shape correlation (Eq. 6.17), which always remains above 99%.

where the kernel $F_2^{(s)}$ is defined in Eq. (5.30), which, although not immediately apparent, is also a separable shape of the form of Eq. (6.10). Eq. (6.14) represents the leading-order gravitational non-Gaussianity generated by non-linear terms in the equations of motion. As we shall see, the scaling dependence $f(K)$ in Eq. (6.9) allows us to approximately incorporate higher-order perturbative corrections. However, the actual gravitational bispectrum is more closely approximated if the tree-level shape (Eq. 6.14) is modified by employing the non-linear power spectrum [266], given by the HALOFIT method [237, 238]:

$$S^{\text{treeNL}}(k_1,k_2,k_3) = 2P_{\text{NL}}(k_1)P_{\text{NL}}(k_2)F_2^{(s)}(\mathbf{k}_1,\mathbf{k}_2) + 2 \text{ perms.}. \tag{6.15}$$

For this reason, we will generally employ this improved flattened bispectrum as the third shape in our subsequent modelling. Both the tree-level (Eq. 6.14) and the nonlinear tree-level (Eq. 6.15) shapes are illustrated in Fig. 6.4.

6.1.3 Scale-dependent or 'sliced' correlators

Having given the key shapes S^i that we will use to describe gravitational non-Gaussianity using the separable ansatz Eq. (6.9), we must also define a scale-dependent correlator that can be used to test the accuracy of this approximation. To determine this we need a more 'localised', binned (or 'sliced') correlator, which only integrates over the transverse degrees of freedom on the $K =$ constant surfaces, modifying Eq. (6.1) to have the restricted domain of integration,

$$\langle B_i, B_j \rangle_K^S \equiv \frac{V}{\pi} \int_{\Delta\mathscr{V}_B} dV_k \, \frac{k_1 k_2 k_3 B_i(k_1,k_2,k_3) B_j(k_1,k_2,k_3)}{P_\delta(k_1) P_\delta(k_2) P_\delta(k_3)} \,, \tag{6.16}$$

such that the integral is now evaluated in a specific thin slice of the tetrahedron with

$$K < k_1 + k_2 + k_3 < K + \Delta K \,,$$

and where the index 'S' denotes slice. Substituting the localised inner product definitions in the correlators Eq. (6.3-6.6), this allows us to define the *sliced* correlators $\mathscr{S}^S$, $\mathscr{A}^S$ and $\mathscr{T}^S$; for example, the binned shape correlator becomes

$$\mathscr{S}^S(K) \equiv \frac{\langle B_i, B_j \rangle_K^S}{\sqrt{\langle B_i, B_i \rangle_K^S \langle B_j, B_j \rangle_K^S}} \,. \tag{6.17}$$

Importantly, if we find a good binned shape correlation $S^S(K) \approx 1$ between our target model (or simulation) and the canonical shapes above (Eqs. 6.11, 6.12, 6.14), then we can use the binned amplitude correlation $\mathscr{T}^S$ to determine the overall scale-dependence $f(K)$ in our separable ansatz of Eq. (6.9). Later in Subchapter 6.4 we will combine these in a "three-shape benchmark" model and establish that it can achieve an excellent fit to simulations, thus dramatically reducing the number of degrees of freedom required to accurately describe the matter bispectrum.

6.2 Shapes of the theoretical models

6.2.1 Shapes of the perturbative bispectrum models

We conclude this subchapter by describing the shapes of the various terms appearing in the different perturbative approaches using the binned shape correlator $\mathscr{S}^S$, defined on

$K =$ const. slices in Eq. (6.16). We determine $\mathscr{S}^S$ for each perturbative model against the tree-level, squeezed and constant shapes in Subchapter 6.1.2. The results of this comparison are illustrated in Fig. 6.5. In the SPT and EFT bispectra, the tree-level term is always present, and so inevitably the 'flat' tree-level shape dominates the large-scale results. For this reason, we restrict our attention to an analysis of the one-loop SPT terms and EFT counterterms separately, in order to achieve a better understanding of the underlying shape corrections. This also simplifies the figures, because in this way there is no mixture of different powers of the growth factor and it is sufficient to test the shapes of these terms at $z = 0$. The left panel of Fig. 6.5 shows the shape correlators in scale-invariant slices of $K \equiv k_1 + k_2 + k_3 =$ constant for the sum of the positive one-loop terms of SPT (thick lines) and the negative contributions (thin lines). The central panel represents the EFT counterterm for the tree level, $-B_{c_s}$, and the right panel shows the shapes of the MPTBREEZE bispectrum. Figure 6.5 shows strong correlations with the tree-level shape in the range $0.1\,h/\mathrm{Mpc} < k < 0.5\,h/\mathrm{Mpc}$ and beyond, with only the exponential cut-off in the MPTBREEZE affecting the correlation.

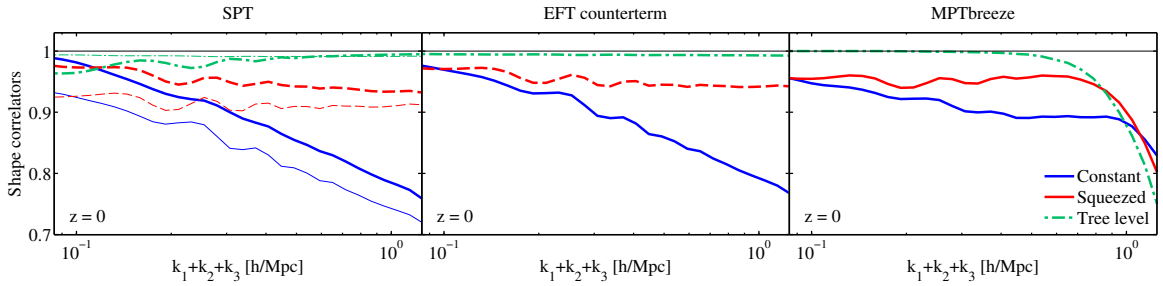

Fig. 6.5 Shapes of the perturbation theory bispectra. For each of the theoretical bispectra considered, we show the shape correlators in k slices $\mathscr{S}^S$ (Eq. 6.16) with respect to the constant, squeezed and tree-level shapes (Eqs. 6.11-6.14). The left panel shows the one-loop SPT shape correlators, the central panel shows the EFT counterterm ($-B_{c_s}$) shapes, and the right panel refers to the MPTBREEZE one-loop shapes. All panels refer to $z = 0$. In the case of SPT (left), the thick lines represent the sum of the positive terms of the one-loop expansion (B_{222} and $B^{(I)}_{321}$), while the thin lines refer to the sum of the negative terms ($B^{(II)}_{321}$ and B_{411}).

Since the tree-level shape correlator is so dominant with respect to the others, we conclude that the perturbative approaches are indistinguishable in shape from the tree-level shape Eq. (6.14) in each scale-invariant K-bin. This is for the relevant range of scales probed by this analysis, with the possible exception of some small deviations appearing in the one-loop SPT terms at small k. Overall, Fig. 6.5 implies these one-loop correction terms are not adding any qualitatively new shape degrees of freedom, thus perturbative methods can be

well-approximated in terms of the tree-level shape using the separable ansatz:

$$B_{\rm PT}(k_1,k_2,k_3) = f(K)\, S^{\rm tree}(k_1,k_2,k_3)\,, \tag{6.18}$$

where $K = k_1 + k_2 + k_3$ and $f(K)$ is an appropriate scale-dependent function defined in Eq. (6.9). We will use this result in the construction of the phenomenological benchmark model in Subchapter 6.3 below.

6.2.2 Halo model shapes

By analogy with the shape investigation of perturbation theory bispectra we described in Subchapter 6.2.1, we characterise here the shapes of the distinct halo model contributions, each of which has been evaluated numerically for a specific set of cosmological parameters (see Subchapter 6.3). In Fig. 6.6 we show the binned shape correlator results $\mathscr{S}^S$ (Eq. 6.16), by projecting the three halo model bispectrum components onto the canonical constant, squeezed and tree-level shapes (Eqs. 6.11-6.14), defined on slices of $K = k_1 + k_2 + k_3 =$ constant, for redshifts $z = \{0, 2\}$. The respective panels of Fig. 6.6 showing the one-, two-, and three-halo terms demonstrate that they are maximally correlated with the constant, squeezed, and tree-level shapes respectively, on all scales, and independently of redshift. This clear observation confirms the accuracy of the separable ansatz (Eq. 6.9) and the completeness of our canonical three shapes (Eqs. 6.11-6.14) when characterising the degrees of freedom needed to describe the standard halo bispectrum. This motivates us to find simple fitting functions $f_i(K)$ for each of the three halo model components.

One-halo term

Given the excellent shape correlation between the one-halo bispectrum (Eq. 5.177) and the constant shape (Eq. 6.11) that we observe in Fig. 6.6, we note that this term can be approximated by:

$$B_{1h}(k_1,k_2,k_3) = f_{1h}(K)\, S^{\rm const}(k_1,k_2,k_3)\,, \tag{6.19}$$

where $K \equiv k_1 + k_2 + k_3$. Because of the constant cross-sectional form of Eq. (6.19), without loss of generality we can focus exclusively on the equilateral case to find a good fit. In Fig. 6.7 (top panel) we illustrate the equilateral one-halo bispectrum obtained from Eq. (5.177) at $z = \{0, 1, 2, 3\}$, compared with the following square-Lorentzian fitting function we introduce:

$$f_{1h}(K) = \frac{A}{\left[1 + bK^2\right]^2}\,, \tag{6.20}$$

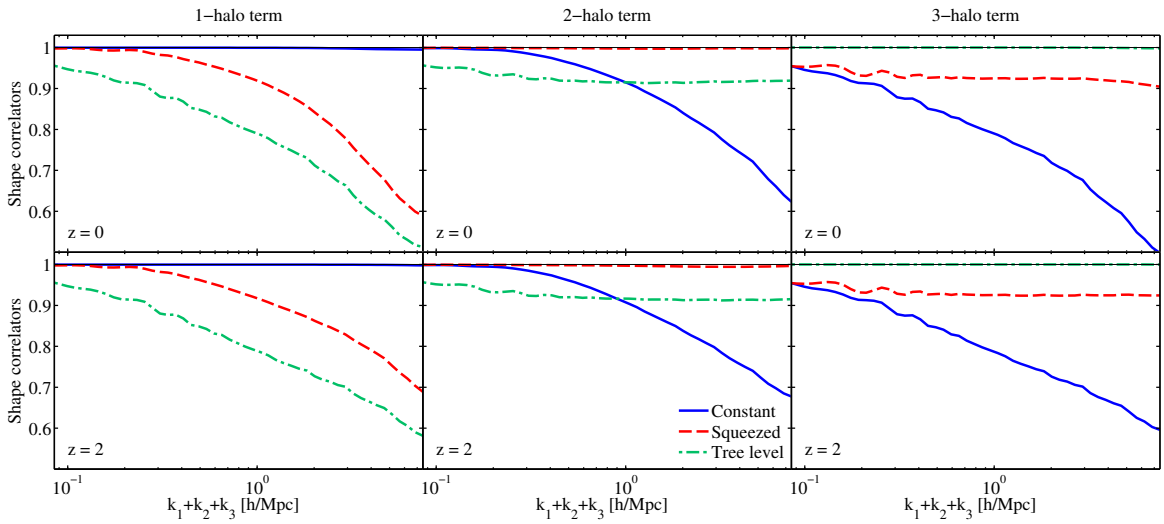

Fig. 6.6 Shapes of the halo model bispectrum. We show the correlation of the three components of the halo model with the constant, squeezed and tree-level shapes at redshifts $z = 0$ (upper panels) and $z = 2$ (lower panels). The left panels show that the one-halo term has a constant shape (Eq. 6.11), the central panels demonstrate that the two-halo term is nearly fully correlated with the squeezed shape (Eq. 6.12), and the right panels indicate that the three-halo term has the same shape as the tree-level bispectrum (Eq. 6.14). These results hold independent of scale and redshift.

where A and b are functions of redshift z through the perturbation growth factor $D(z)$. We first fit A, b for each redshift separately, and then we obtain two overall redshift-dependent fitting functions, taking account of the growth factors in the following form:

$$A = \frac{2.45 \times 10^6 D(z)^8}{0.8 + 0.2 D(z)^{-3}} \tag{6.21}$$

$$b = 0.054 D(z)^{2.2} \, h^{-2}\mathrm{Mpc}^2 \, . \tag{6.22}$$

We can see in Fig. 6.7 (top panel) for the equilateral case, and in Fig. 6.8 over the full 3D domain that this is a good approximation of the full one-halo term.

While this phenomenological fit may not be particularly well-motivated physically, it does illustrate that once the one-halo shape has been identified, then a relatively simple combination of growth factors can be used to describe the scale-dependent amplitude for the relevant wavenumber range around $K \sim 1\,h/\mathrm{Mpc}$. Alternatively, it is sufficient to model the one-halo bispectrum directly by evaluating Eq. (5.177) for equilateral values only $k_1 = k_2 = k_3$. More significantly, knowing empirically that ansatzes like Eq. (6.20) are accurate may

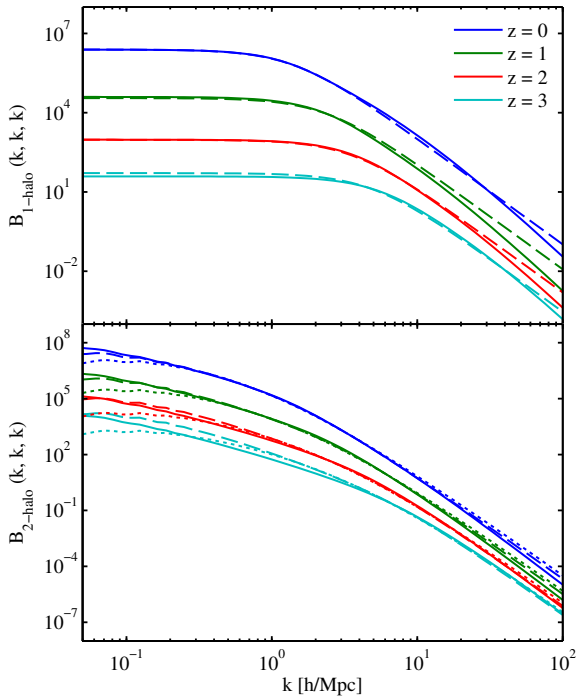

Fig. 6.7 Equilateral one-halo (top panel) and two-halo (bottom panel) bispectra at $z = \{0,1,2,3\}$ (solid lines, from top to bottom), compared with the corresponding fitting function from Eqs. (6.20, 6.24) (dashed lines). The dotted lines refer to the corrected two-halo fitting function of Eq. (6.25).

offer insight which leads to a much simpler mathematical derivation of the individual halo contributions.

Two-halo term

As seen in Fig. 6.6, the two-halo bispectrum (Eq. 5.178) is strongly correlated on all $K = \text{const.}$ slices with the squeezed shape $S^{\text{squeez}}(k_1,k_2,k_3)$ constructed from products of the power spectrum defined in Eq. (6.12). This means that we can write:

$$B_{2h}(k_1,k_2,k_3) = f_{2h}(K)\,S^{\text{squeez}}(k_1,k_2,k_3)\,. \tag{6.23}$$

In order to obtain a phenomenological fit, we consider again the equilateral configuration, which we show in Fig. 6.7 (bottom panel). From this simple analysis, we find that a useful fitting function valid for the redshift range considered is:

$$f_{2h}(K) = \frac{155}{1+26.2\,h^2\text{Mpc}^{-2}\,D(z)^{-8/3}\,K^{-2}}\,, \tag{6.24}$$

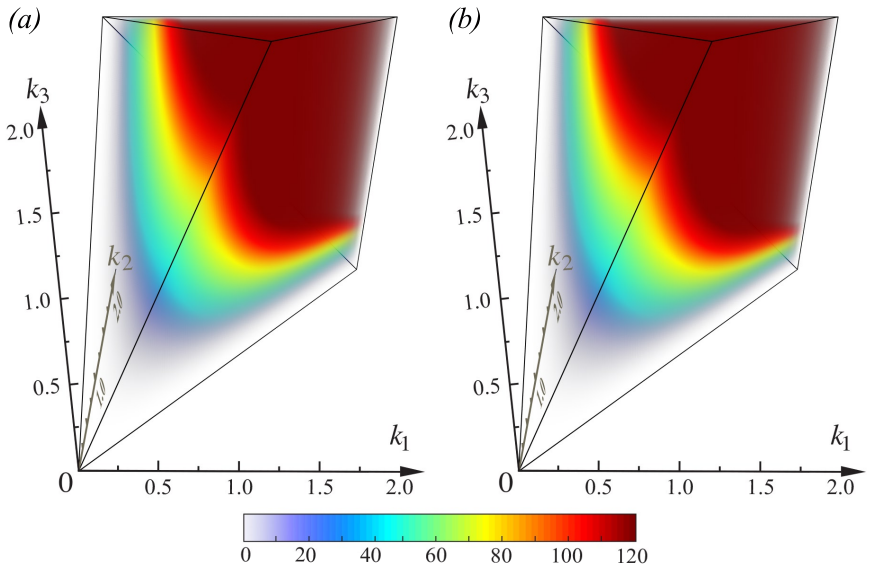

Fig. 6.8 The SN-weighted one-halo bispectrum of Eq. (5.177) (upper panel) compared at $z = 0$ with the one-halo constant shape ansatz of Eq. (6.19) with scale-dependence $f_{1h}(K)$ given by Eqs. (6.20, 6.22) (lower panel). This fit is visually hard to distinguish reflecting the high total correlation achieved over all lengthscales (and redshifts). The cross-sectional shape does not appear constant because of the SN-weighting (Eq. 6.1).

where it should be noted that the squeezed shape form already includes a $D^4(z)$ redshift dependence from the linear power spectrum in Eq. (6.12).

However, as discussed above in Subchapter 5.3.2, the standard two-halo term causes some large-scale power excess in the full bispectrum, because it does not decay appropriately as $k \to 0$; thus the full bispectrum does not recover the tree-level form on large scales. We can modify our fitting function in order to solve this issue, by considering the functional form:

$$f_{2h}(K) = \frac{C}{(1+DK^{-1})^3}\,. \tag{6.25}$$

This function is chosen to decay more rapidly on very large scales, as in that regime there should be no contribution from the two-halo term. By fitting the full two-halo term at different redshifts and considering the halo-PT VN-model, we obtain:

$$C = 240 \tag{6.26}$$

$$D = 2.5\,h\mathrm{Mpc}^{-1}\,D(z)^{-4/3}\,. \tag{6.27}$$

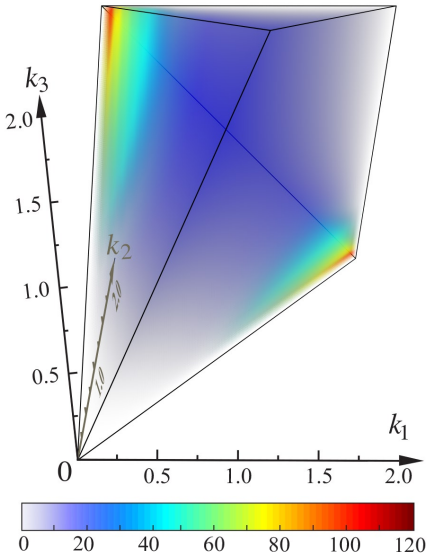

Fig. 6.9 The SN-weighted two-halo bispectrum of Eq. (5.178) at $z = 0$, showing the strongly squeezed signal. Like the one-halo bispectrum shown in Fig. 6.8, an excellent fit to this model can be obtained with the separable ansatz of Eq. (6.23) using the standard 'squeezed' shape (Eq. 6.12).

We can see in Fig. 6.7 (bottom panel) for the equilateral case, and in Fig. 6.9 over the full 3D domain that this is a good approximation of the two-halo bispectrum term.

Nevertheless, despite this improvement at $z = 0$ as $k \to 0$ we will show later that the two-halo model does not predict the appropriate growth rates at redshifts $z > 0$ when compared to simulations.

Three-halo term

The three-halo term (Eq. 5.179) has a good shape correlation with the tree-level bispectrum (Eq. 6.14), because it is essentially constructed out of this solution or its one-loop extensions, all of which share the same highly-correlated flattened shape (as discussed in Subchapter 6.2.1). Hence, as we have discussed previously, the three-halo term can be expressed again with a simple fitting function (Eq. 6.18) using the tree-level shape S^{tree}. The standard halo model effectively identifies the three-halo term with the tree-level bispectrum so we can take the fitting function to be unity. Extensions taking a perturbative result with one-loop corrections can also be described at high accuracy with Eq. (6.18) but with non-trivial scaling $f(K)$ (e.g. to simplify the halo-PT VN-model which uses B_{EFT}). Since the closely-related nonlinear tree-level bispectrum S^{treeNL} given in Eq. (6.15) provides a better approximation to

the perturbative models, we can more conveniently use this as our base tree-level ansatz:

$$B_{3h}(k_1,k_2,k_3) = f_{3h}(K)\, S^{\text{treeNL}}(k_1,k_2,k_3)\,. \tag{6.28}$$

Both tree-level and non-linear tree-level shapes are plotted in Fig. 6.4. We will employ Eq. (6.28) when developing the phenomenological three-shape model in Subchapter 6.3.

6.3 Polyspectra from simulations

6.3.1 *N*-body simulations

We use the *N*-body simulations with Gaussian initial conditions described in detail in Ref. [242]. The simulations contain 512^3 particles that are evolved from an initial redshift of $z = 49$ until today using the *N*-body GADGET-3 code [294, 295]. The simulations are run using a flat ΛCDM universe with the following WMAP7 [296] parameters: baryon energy density $\Omega_b h^2 = 0.0226$, dark matter energy density $\Omega_c h^2 = 0.11$, cosmological constant energy density $\Omega_\Lambda = 0.734$, dimensionless Hubble constant $h = 0.71$, optical depth $\tau = 0.088$, amplitude of primordial perturbations $\Delta^2_{\mathscr{R}}(k_0) = 2.43 \times 10^{-9}$ and scalar spectral index $n_s(k_0) = 0.963$, where $k_0 = 0.002\,h\,\text{Mpc}^{-1}$. We use simulations of three different box sizes of 1600, 400 and 100 Mpc$/h$ respectively; the first one has glass Gaussian initial conditions and the other two have regular grid initial conditions. We denote the simulations using their names from Ref. [242]: *G512g*, G^{512}_{400}, G^{512}_{100}. Given the fixed number of particles, the three box sizes lead to the following wavenumber ranges: $[0.0039, 0.5]\,h/\text{Mpc}$, $[0.016, 2.0]\,h/\text{Mpc}$ and $[0.062, 8.0]\,h/\text{Mpc}$ respectively. For each box size, three independent realisations are available.

We combine the power spectra and bispectra from the different simulation boxes as follows. As it can be seen in Fig. 6 of Ref. [242], where the matter power spectra from the three simulations considered are compared to the HALOFIT model, at any redshift $z > 0$ the power spectrum of simulation *G512g* only follows the HALOFIT model up to $k_{\text{max}} \simeq 0.2\,h/\text{Mpc}$; however, for $k \gtrsim 0.1\,h/\text{Mpc}$, the simulation G^{512}_{400} matches HALOFIT more closely. The same behaviour is seen at larger k for the G^{512}_{400} and G^{512}_{100} boxes. Therefore, we combine the power spectra and bispectra from the simulations in order to use each simulation in the range of scales where its results are the closest to HALOFIT, and we apply a smooth transition between the different boxes. We define a smoothing function $H(k)$ in the range

$k \in [k_s, k_e]$ of the form:

$$H(k) = \frac{1 - \sin\left(\pi \frac{k - k_e/2 - k_s/2}{k_e - k_s}\right)}{2}. \tag{6.29}$$

As we have three realisations for each of the simulations, we match each realisation $i = 1, 2, 3$ from each simulations with the same i realisation in the other simulations, thus obtaining three combined realisations of the power spectra and bispectra over the full k range we consider. We have checked that modifying the smoothing function has only a small impact on the overall results.

6.3.2 Power spectrum

We estimate the power spectrum of the simulations in each k-bin by averaging the squared absolute value of the matter overdensity $|\delta_{\mathbf{q}}|^2$ over all modes that fall into the shell with distance k from the origin (*i.e.* over $\mathbf{q}$ with $|\mathbf{q}| - \Delta k/2 \leq k < |\mathbf{q}| + \Delta k/2$, where Δk is the bin width). We compare in Fig. 6.10 the power spectrum measured from the simulations with the models that we consider: linear theory, the non-linear power spectrum from HALOFIT, EFT, MPTBREEZE and RLPT at one loop, the halo model and the combined halo-PT model (based on EFT). The lower panels of Fig. 6.10 show the power spectrum residuals with respect to the HALOFIT model.

Focusing first on the perturbative methods, we note that they increase their range of validity to higher k modes as the redshift is increased, as expected. We confirm that SPT presents excess power in the quasi-linear regime, departing from the simulations by more than 10% at $k \simeq 0.15\,h/\mathrm{Mpc}$ at $z = 0$. The SPT excess power is however reduced at higher redshifts, as expected given that the one-loop corrections have a higher growth rate compared to the tree level. The EFT method can extend the range of validity by subtracting the SPT excess power. However, the scale range over which EFT is accurate strongly depends on which simulations were used to calibrate the counterterm, and over which range of scales and redshifts. In the present case, the c_s^2 counterterm we are using was calibrated by Ref. [260] with the $G512g$ simulation box we are presenting at $z = 0$; therefore, there is no guarantee that this same counterterm will be accurate at higher k over the smaller-box simulations G_{400}^{512}, G_{100}^{512}, and at $z > 0$. Indeed, it is likely that a re-fitting of c_s^2 over the combined range of simulations we are using would improve the EFT model accuracy over an extended range of k and z. The MPTBREEZE and RLPT approaches include an exponential cut-off: this reduces the range in which the model is accurate to 10% to $k < 0.10\,h/\mathrm{Mpc}$ at $z = 0$; nonetheless, these models feature an improved accuracy in the mildly non-linear regime before the cut-off

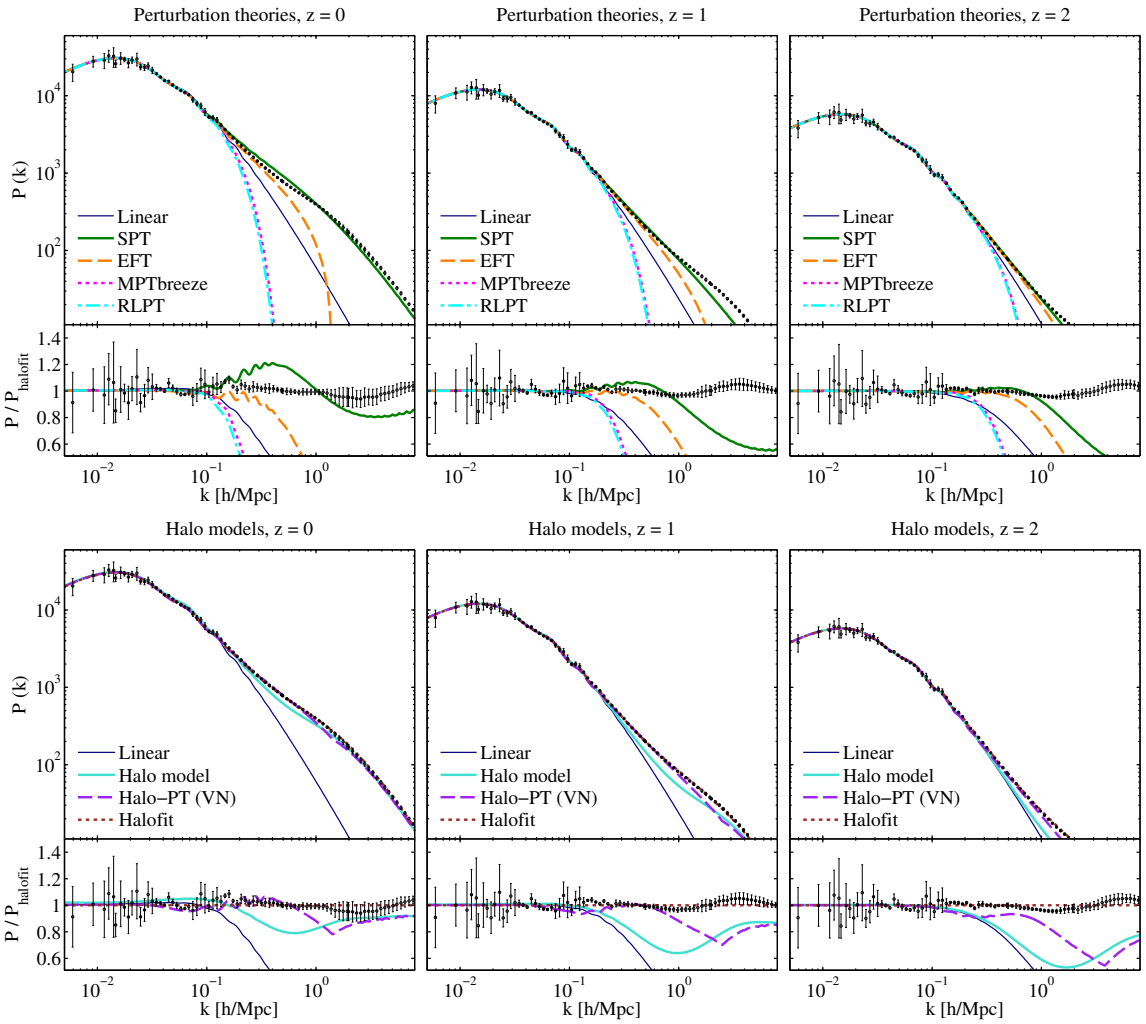

Fig. 6.10 Overview of the matter power spectra predicted by the range of theoretical models we consider, compared with data measured from N-body simulations. The data points are combined from N-body simulations with three different box sizes. The upper and lower rows refer to perturbation theories and halo models respectively. The columns refer to $z = 0$, 1 and 2 from left to right; in each plot, the main upper panel shows the power spectra comparison, while the smaller lower panel shows the residuals with respect to the HALOFIT prediction.

sets in, although the precision of our N-body simulations does not allow detailed quantitative statements at the percent level.

We then consider the halo models: we see that at $z = 0$ this formalism provides a good description of the matter power spectrum on small scales and in the range $k \in [0.01, 0.2]\,h/\mathrm{Mpc}$, after which we find the well-known power deficit in the transition region between the one and two-halo terms. The model performs again better at smaller scales ($k \gtrsim 2\,h/\mathrm{Mpc}$ at $z = 0$),

reaching an accuracy of $\sim 10\%$. On very large scales, the halo model amplitude exceeds the simulations, as the one-halo term does not decay to zero as it physically should. By moving to higher redshifts, we see that at $z = 2$ the halo model provides a worse description of the simulations at intermediate and small scales, as the power deficit in the transition region is exacerbated. This is because the total fraction of dark matter particles that belong to collapsed structures is drastically reduced at this redshift, which undermines the assumptions underlying the halo model approach. On large scales on the other hand, the excess power nearly disappears at high redshift, due to the quick decay of the one-halo term as a function of z.

The combined halo-PT model based on EFT succeeds in removing the excess power seen on large scales at $z = 0$; as we discuss below, this excess will appear even more evidently in the bispectrum. This model is also partly successful in reducing the power deficit on intermediate scales, thanks to the extra power that is added there from the perturbative term. However, due to the negative counterterm, the EFT power spectrum prediction becomes negative on small scales ($k \gtrsim 1\,h/\mathrm{Mpc}$ at $z = 0$). After this point, we base the halo-PT model on the SPT prediction: this is the reason of the cusp we see in the halo-PT model residuals in the non-linear regime.

We finally note the results from the simulations are in good agreement with the non-linear HALOFIT power spectrum, as they are within 10% accuracy over the entire k-range considered at all z.

6.3.3 Modal bispectrum methodology

We next follow the modal decomposition method to reconstruct the dark matter bispectrum, using the method developed by Refs. [244, 245, 297]. In this approach, the full 3D bispectrum $B(k_1,k_2,k_3)$ is expanded on an orthonormal basis defined on the same tetrapyd domain $Q_n(k_1,k_2,k_3)$, with $n = 0,...,n_{\max}$. In this way, the full bispectrum information is encoded in the expansion coefficients β_n^Q, and the bispectrum estimator $\hat{B}$ can be written as

$$\frac{\hat{B}(k_1,k_2,k_3)\,\sqrt{k_1k_2k_3}}{\sqrt{P(k_1)P(k_2)P(k_3)}} = \sum_{n=0}^{n_{\max}-1} \beta_n^Q\, Q_n(k_1,k_2,k_3)\,. \tag{6.30}$$

We note that the left-hand-side is the signal-to-noise weighted bispectrum $B_i^{\mathrm{SN}}(k_1,k_2,k_3)$ defined in Eq. (6.2). The accuracy of this estimator is regulated by the dimension of the expansion basis, $n_{\max}$; for the smooth bispectra that are typical of the LSS, Ref. [242] demonstrated that the choice $n_{\max} \sim 100$ suffices to achieve a convergence of the total

bispectrum signal-to-noise, *i.e.* considering higher $n_{\max}$ has negligible effect on the matter bispectrum. This highlights the benefits of the modal method: once the basis Q_n is chosen, the entire three-dimensional bispectrum information can be simply compressed in a set of ~ 100 numbers.

Ref. [245] tested several different choices of the basis Q_n, demonstrating that the modal method successfully reconstructs the bispectrum in all cases. The most suitable choice for Q_n is however built from a set of tetrahedral polynomials $q_p(x)$, which are analogues of the Legendre polynomials on the unit interval. In more detail, the basis Q_n can be written as

$$\begin{aligned} Q_n(x,y,z) =& \frac{1}{6}\left[q_r(x)\,q_s(y)\,q_t(z) + q_r(x)\,q_t(y)\,q_s(z) + q_s(x)\,q_r(y)\,q_t(z)\right. \\ &\left. + q_s(x)\,q_t(y)\,q_r(z) + q_t(x)\,q_r(y)\,q_s(z) + q_t(x)\,q_s(y)\,q_r(z)\right], \end{aligned} \tag{6.31}$$

where $n = r+s+t$ and the order of the permutations is taken as in Ref. [245]. The polynomials q_p are obtained using the following procedure. By defining an integral of a function $f(k_1,k_2,k_3)$ with weighting $w(k_1,k_2,k_3)$ over the tetrapyd domain defined by the triangle conditions on the wavevectors: $k_1+k_2 \geq k_3$, $k_2+k_3 \geq k_1$ and $k_3+k_1 \geq k_2$ with $\mathscr{I}[f]$, we note (Ref. [245]) that it can be expressed in terms of an integral on a cubic domain by a suitable change of coordinates

$$\begin{aligned} \mathscr{I}[f] = K^3 \left[\int_0^{\frac{1}{2}} dy \int_y^{1-y} dx \int_{x-y}^{x+y} dz FW + \int_0^{\frac{1}{2}} dx \int_x^{1-x} dy \int_{y-x}^{x+y} dz FW \right. \\ \left. + \int_{\frac{1}{2}}^1 dx \int_{1-x}^{x} dy \int_{x-y}^1 dz FW + \int_{\frac{1}{2}}^1 dy \int_{1-y}^{y} dx \int_{y-x}^1 dz FW \right] \end{aligned} \tag{6.32}$$

where $K = k_{\max}$, $F(x,y,z) = f(Kx,Ky,Kz)$ and $W(x,y,z) = w(Kx,Ky,Kz)$. By considering a function $f(x,y,z) \equiv f(x)$, *i.e.* independent of y and z with $K=1$ and performing the y and z integrals in Eq. (6.32), the following weighting function is obtained:

$$W(x) = \frac{1}{2}x(4-3x)\,. \tag{6.33}$$

Then the tetrahedral polynomials of order n can be generated by taking the determinant

$$q_n(x) = \frac{1}{\mathscr{N}_n} \begin{vmatrix} w_0 & w_1 & \cdots & w_n \\ w_1 & w_2 & \cdots & w_{n+1} \\ \vdots & \vdots & \ddots & \vdots \\ w_{n-1} & w_n & \cdots & w_{2n-1} \\ 1 & x & \cdots & x^n \end{vmatrix}, \tag{6.34}$$

where

$$w_n = \mathscr{I}[x^n] = \frac{n+6}{2(n+3)(n+2)}, \tag{6.35}$$

and the normalisation $\mathscr{N}_n$ is chosen so that the polynomials $q_n(x)$ are orthonormal with respect to the product, with the weight specified in Eq. (6.33):

$$\langle q_n, q_m \rangle = \int_0^1 q_n(x)\, q_m(x)\, \frac{1}{2} x(4-3x)\, dx = \delta_{nm}. \tag{6.36}$$

To see that Eq. (6.34) indeed generates orthogonal polynomials, we note that the function produces polynomials of degree n trivially and we only have to show the orthogonality property. We consider the product $\langle q_n, x^k \rangle$ for $k \leq n$ and we expand the determinant by the last row, calculate the products $\langle \cdots \rangle$ and then we regroup everything again as a determinant to get

$$\langle q_n, x^k \rangle = \frac{1}{\mathscr{N}_n} \begin{vmatrix} w_0 & w_1 & \cdots & w_n \\ w_1 & w_2 & \cdots & w_{n+1} \\ \vdots & \vdots & \ddots & \vdots \\ w_{n-1} & w_n & \cdots & w_{2n-1} \\ w_k & w_{k+1} & \cdots & w_{k+n} \end{vmatrix}. \tag{6.37}$$

For $k < n$ this determinant is trivially 0, as two rows would be identical, and hence the result follows. Therefore, $\langle q_n, q_k \rangle = 0$ for $k < n$ and the full result is obtained by induction.

6.3.4 Bispectrum reconstruction from simulations

A modal reconstruction for the matter bispectrum $B_i^{\rm SN}(k_1, k_2, k_3)$ (Eq. 6.30) was obtained using the mode functions (Eq. 6.34) for the full array of simulations described in Subchapter 6.3.1. This decomposition and its validation were described in detail in Ref. [242]: a relatively small number of modes were sufficient to recover the full bispectrum at the required resolutions, that is, using 120 modes for the *G512g* simulations and 50 modes for the other two simulations. We focus attention here on the low-redshift regime $z \leq 3$ where the bispec-

trum is accessible to current and future galaxy surveys and where non-linearities become important. To obtain the full bispectrum across the widest range of scales we combined and averaged all the simulation bispectra, interpolating in overlapping regions using the same prescription as that described for the power spectrum. Error bars for bispectrum correlators were estimated by determining variances from the different simulations.

In Fig. 6.11 we plot the full three-dimensional matter bispectrum we have obtained across the tetrapyd domain for $0.02\,h/\text{Mpc} \leq k \leq 2\,h/\text{Mpc}$ and at four different redshifts $z = \{0, 1, 2, 3\}$. The colour scheme is scaled using the growth factor $D(z)$ such that the tree-level bispectrum would appear constant in the perturbative regime. These plots range from quasi-linear to highly nonlinear regions and several qualitative observations about the nature and evolution of the matter bispectrum are immediately apparent.

At the higher redshifts $z = 2, 3$ shown in Fig. 6.11(a,b), a flattened signal is dominant up to $K \equiv \sum_i k_i \lesssim 4, 3.5\,h/\text{Mpc}$ respectively (*i.e.* the tetrahedron region). This is consistent with the flattened tree-level shape (Eq. 6.14) which is shown in Fig. 6.4(a) at $z = 2$, but at much lower amplitude on a more sensitive scale. This means the flattened signal extrapolates with growing amplitude well beyond the perturbative regime at these redshifts (e.g. from Table 5.1 $K \lesssim 0.6\,h/\text{Mpc}$ at $z = 2$). We focus further on the perturbative regime with $K \lesssim 1\,h/\text{Mpc}$ in Subchapter 6.5.1. For larger K, the bispectrum is dominated by a nearly uniform signal associated with halo formation (*i.e.* the top pyramidal region with $K \gtrsim 4\,h/\text{Mpc}$). Also in Fig. 6.11(a,b), we note that a significant squeezed signal is visible for $1\,h/\text{Mpc} \lesssim K \lesssim 4\,h/\text{Mpc}$ (on the left and bottom tetrapyd edges), which can be compared with Fig. 6.9.

At the lower redshifts $z = 0, 1$ in Fig. 6.11(c,d), the strong halo signal grows to become completely dominant for $K \gtrsim 1\,h/\text{Mpc}$ (saturating the colour scheme with $B^{SN}_{\text{max}} \approx 350$). At $z = 0$, this 'constant' halo signal is so large the other contributions seem to be absent (compare with Fig. 6.8). However, this apparent suppression of flattened and squeezed signals at $z = 0$ is only relative, due to the signal-to-noise weighting (Eq. 6.2) with the nonlinear power spectrum $P_{\text{NL}}(k)$. This deeply nonlinear nature of perturbations today is reflected in the greater difficulty of matching phenomenological models to simulations at low redshift.

6.4 Towards a three-shape bispectrum benchmark model

In this subchapter we analyse the measured bispectrum to identify the shape degrees of freedom required for its accurate construction. We study the growth rates of each of these contributions, highlighting differences with the standard halo model particularly for the

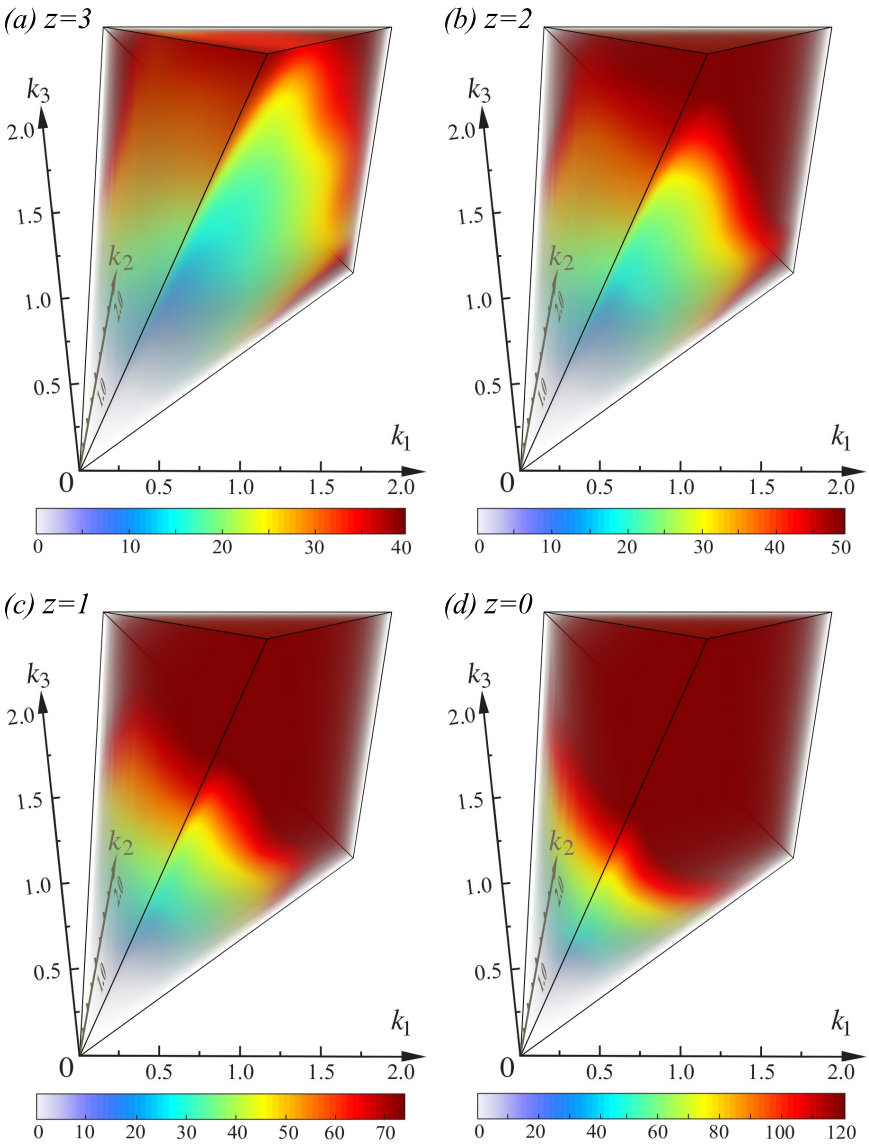

Fig. 6.11 Evolution of the SN-weighted 3D bispectrum from N-body simulations into the nonlinear regime with $k_i \leq 2\,h/\mathrm{Mpc}$ at redshifts (a) $z = 3$, (b) $z = 2$, (c) $z = 1$, and (d) $z = 0$. The bispectrum colour scheme is scaled with the growth factor $D(z)$ and the tetrahedral geometry of the bispectrum domain is illustrated in Fig. 6.2. Note the presence of both a strong flattened and squeezed signal shape at redshifts $z = 2, 3$ (front left face of tetrapyd and lower edge respectively in panels a, b). At lower redshift this is overtaken by a strong uniform or one-halo signal throughout the interior region for $k \gtrsim 1\,h/\mathrm{Mpc}$ (front right face in panel d). The colour scale is fixed at $z = 3$ in (a) to encompass all values up to the maximum. It is then scaled with the growth rate expected for the tree-level signal to aid physical interpretation and reveal non-linear growth rates. This means at small scales in (d) at $z = 0$ the colour scale is saturated, which is useful to highlight features at intermediate scales.

squeezed shape. We use these results to guide the development of simple phenomenological bispectrum models: the two-halo boost model and the three-shape benchmark model.

6.4.1 Simulation bispectrum shapes

We first analyse the shapes of the bispectra measured from N-body simulations, in analogy with the investigation of the perturbative and halo model shapes we presented in Figs. 6.5, 6.6 above. We calculate the sliced or binned shape correlators $\mathscr{S}^S(K)$ between the N-body matter bispectrum and the tree-level (Eq. 6.14), squeezed (Eq. 6.12), and constant (Eq. 6.11) shapes to determine whether, in combination, these three canonical shapes are sufficient to describe the actual bispectrum. The panels of Fig. 6.12 show a consistent behaviour across the range of redshifts considered. We know that, on large scales, perturbations approach linearity and therefore the tree-level bispectrum is expected to be a good approximation to the N-body data. The plots show that this is indeed the case, as on these scales ($K \lesssim 0.5\,h/\mathrm{Mpc}$ at $z = 0$) there is a high correlation between the simulated bispectrum and the tree-level shape. The scales up to which the bispectrum is completely dominated by the tree-level shape move significantly to larger values of K as the redshift increases, as expected. On small scales, Fig. 6.12 shows that deep into the non-linear regime ($K \gtrsim 3\,h/\mathrm{Mpc}$ at $z = 0$) the constant shape dominates, which closely corresponds to the one-halo model discussed in Subchapter 6.5 (and as shown previously in Ref. [242]). On intermediate scales, there are several competing contributions of comparable magnitude in the transition between constant and flattened regimes. Nevertheless, Fig. 6.12 reveals that at all redshifts there is a range of wavenumbers where the squeezed shape exhibits the highest correlation, which is a new result. These quantitative shape correlation results confirm the qualitative picture developed from the evolution of the 3D bispectrum reconstructions shown in Fig. 6.11.

These observations can be interpreted using the halo model formalism for which the basic underlying physical assumptions appear to be corroborated qualitatively. On large scales, the three-halo term is dominant because in this regime the particle triplets over which the bispectrum is estimated should typically be in different halos, thus reflecting the large-scale quasi-linear bispectrum predicted by perturbation theory. As shown in Subchapter 6.2.2, at small K the tree-level shape is the most important contribution to the observed bispectrum. On small scales, the three particles are typically in the same nonlinear virialised halo, and hence the one-halo component dominates; this has a constant shape, which we confirm to be the leading observed bispectrum shape in the high-K limit. The two-halo term contributes over intermediate lengthscales, where two particles are in one halo and the third particle is elsewhere; this corresponds to the squeezed shape, which indeed we find to be dominating the

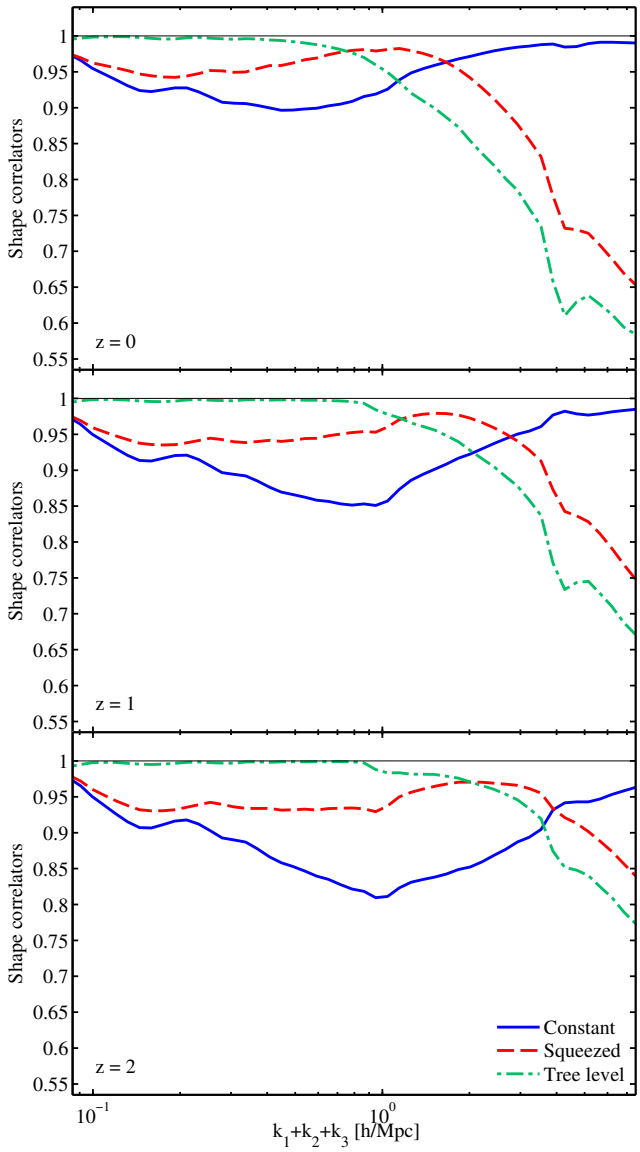

Fig. 6.12 Sliced shape correlations of the measured N-body bispectrum with the three canonical shapes: constant (Eq. 6.11), squeezed (Eq. 6.12) and tree-level (Eq. 6.14) shown at redshifts $z = \{0,1,2\}$ (upper to lower panels). The sliced or binned shape correlator on a given $K = k_1 + k_2 + k_3$ slice is defined in Eq. (6.17).

bispectrum on intermediate scales (though with a larger contribution for $z > 0$ than expected in the standard halo model).

As a further illustration, we show in Fig. 6.13 the equilateral bispectrum ($k_1 = k_2 = k_3$) of the halo model at $z = 0$ and $z = 2$ compared with the measured equilateral N-body bispectrum. Here we can see more clearly the three terms contributing to the halo model and how the

two-halo term provides the most significant contribution at intermediate scales at $z = 0$. However, a deficit emerges relative to N-body simulations at $z = 2$ where the predicted two-halo term no longer dominates over the one- and three-halo terms.

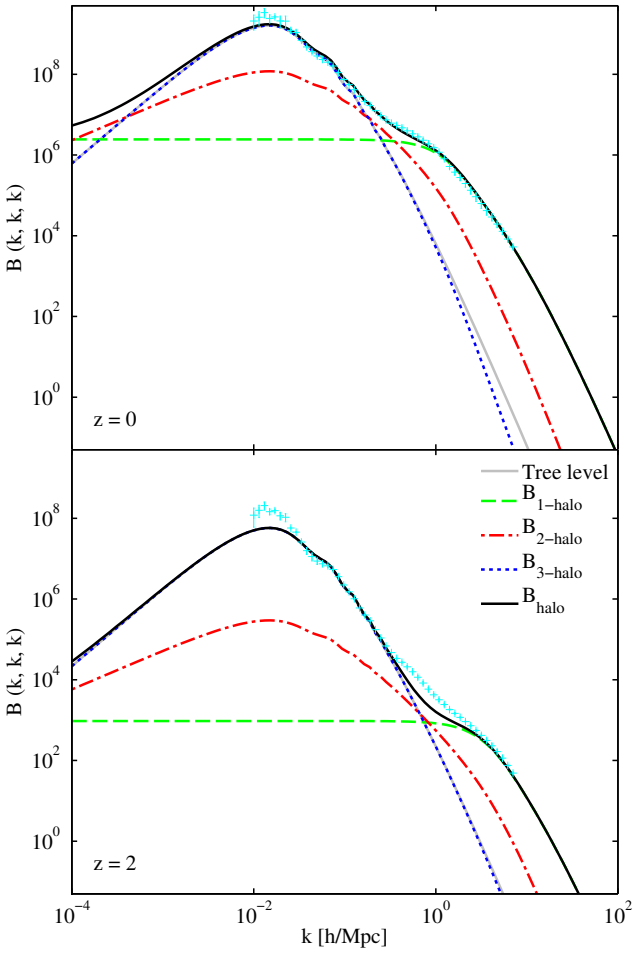

Fig. 6.13 Equilateral configuration of the halo model bispectrum at $z = 0$ (top panel) and $z = 2$ (bottom panel), showing the contributions of the three components of the halo model, contrasted with the measurements from N-body simulations (cyan points). Note the emerging deficit on intermediate scales at $z = 2$.

6.4.2 Two-halo boost model

Based on the observation that the halo model has a deficit at intermediate scales, which is found for bispectrum slices in different configurations and becomes more severe as the redshift increases, we have explored simple phenomenological ways of improving the model.

The two-halo term of the halo model has its highest and most important contribution where the deficit is worst.

As a first simple method to improve the agreement between the model and the simulations, we increase the contribution of the two-halo term at higher redshifts in order to compensate for the deficit. We find that a 'boosted' two-halo term can provide a much better fit to numerical simulations for redshifts $z > 0$ by multiplying the existing two-halo term by the heuristic factor $D(z)^{-1.7}$. We determine this 'best-fit' factor by computing the total correlator $\mathscr{T}$ of Eq. (6.6) between the model and the simulations separately at each redshift, and then obtaining the scaling law by maximising the correlator $\mathscr{T}$. We show in Fig. 6.14 that the function $D(z)^{-1.7}$ describes well the numerical values found over the relevant redshift range.

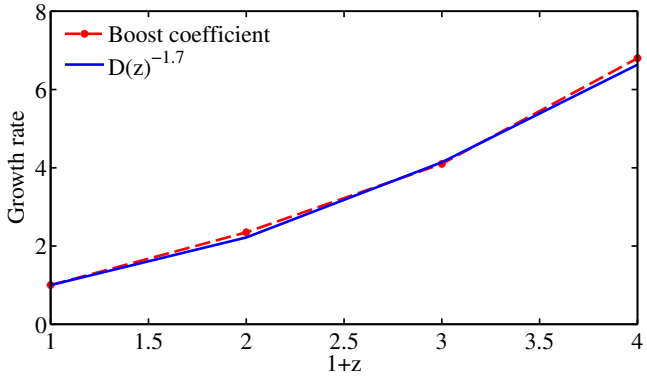

Fig. 6.14 Best-fit boost coefficient to simulations for the two-halo term compared to $D(z)^{-1.7}$.

This simple method solves the power deficit in the intermediate regime but we discussed previously how the halo model already has an excess of power as $k \to 0$, driven by the combination of one- and two-halo terms (for $z > 0$). Therefore, there is a quantitative problem with simply boosting the two-halo term because it increases the excess on very large scales. In Subchapter 6.5.2, we will make direct comparisons with the standard halo and other models.

6.4.3 Two-shape time-shift model

In Ref. [242] using tree-level and constant bispectrum shapes it was already recognised that simple phenomenological models of the bispectrum could be constructed; this was motivated by explaining the different growth rates of primordial non-Gaussian shapes in terms of an initial time offset. This time-shift model relies on the fact that in the non-linear regime the matter bispectrum can be approximated by the constant bispectrum using the following

ansatz (consistent with Eq. 6.9):

$$B_{\text{const}}(k_1,k_2,k_3) = c_1 D(z)^{n_h} K^{\nu}\,, \tag{6.38}$$

with two free parameters, an amplitude c_1 and a growth rate n_h determined from simulations, plus a scale-dependence $\nu \approx -1.7$ for equilateral configurations in the one-halo model [234, 284]. This two-shape model was further improved by replacing the tree-level bispectrum (Eq. 6.14) with the non-linear tree-level bispectrum (Eq. 6.15), *i.e.* the tree-level bispectrum calculated with the non-linear power spectrum from simulations:

$$B_{T\text{-shift}}(k_1,k_2,k_3) = c_1 D(z)^{n_h} K^{\nu} + S^{\text{treeNL}}(k_1,k_2,k_3)\,. \tag{6.39}$$

While this model produced a reasonable description of the matter bispectrum in terms of the shape correlation $\mathscr{S}$ (see Ref. [242]), our more detailed analysis here with the binned shape correlator $\mathscr{S}^S$ has revealed the possibility of further improvement on intermediate scales by extending the model with the additional squeezed shape of Eq. (6.12).

6.4.4 Three-shape bispectrum model

Based on the three shapes we identified in the halo model in Subchapter 6.2.2, we propose a more general benchmark model that incorporates the physical behaviour of all these components, but with rescaled growth factors to provide an improved quantitative fit to simulations. As shown in Fig. 6.6, the one-, two- and three-halo terms have a high shape correlation with the constant, squeezed and tree-level shapes respectively on slices of constant $K \equiv k_1 + k_2 + k_3$. Since these shapes also describe the measured matter bispectrum (see Fig. 6.12), we can construct it as a scale-dependent sum of three templates:

$$\begin{aligned} B_{3\text{-shape}}(k_1,k_2,k_3) &= \sum_{i=1}^{3} f_i(K)\, S^i(k_1,k_2,k_3) \\ &= f_{1h}(K) S^{\text{const}}(k_1,k_2,k_3) + f_{2h}(K) S^{\text{squeez}}(k_1,k_2,k_3) + f_{3h}(K) S^{\text{treeNL}}(k_1,k_2,k_3), \end{aligned} \tag{6.40}$$

where the non-linear tree-level, squeezed, and constant shapes $S^{\text{treeNL}}, S^{\text{squeez}}, S^{\text{const}}$ are defined in Eqs. (6.11), (6.12) and (6.15) respectively, and the amplitudes f_{1h}, f_{2h}, f_{3h} were discussed in Subchapter 6.2.2 in the context of the halo model.[1]

[1] An even simpler three-shape model can be obtained substituting the linear tree level (Eq. 6.14) for the flattened three-halo shape; it provides a satisfactory fit to the simulations. In this simple scenario, the fitting

We know that the one-halo term provides an adequate description of the matter bispectrum on small scales, so we fix the amplitude f_{1h} to the simple functional fit of Eq. (6.20) for the one-halo model presented in Subchapter 6.2.2. On the largest scales, where the three-halo term is dominant, we know that the tree-level shape (Eq. 6.28) provides an excellent fit to simulations. However, on intermediates scales, while the shape correlation remains good beyond the strictly perturbative regime (see Fig. 6.12), its amplitude is insufficient, as can be seen by comparing Fig. 6.4 with Fig. 6.11). For this reason, we have chosen the nonlinear tree-level form (Eq. 6.15) instead because of its higher amplitude and the fact that it is a better approximation to one-loop perturbative expansions. Nevertheless, it is well known that introducing the nonlinear power spectra into halo models generically causes excess power at low redshifts $z \approx 0$, so we need a prescription for cutting off the flattened shape in nonlinear regions (see, for example, the discussion about the combined halo-PT model in Subchapter 5.3.2 or the discussion of halo exclusion in Ref. [298]). In order to keep this three-halo suppression as simple as possible we take an exponential form:

$$f_{3h} = \exp(-K/E)\,, \tag{6.41}$$

where we fit E to simulations at several redshifts to obtain an appropriate amplitude and growth rate; in principle, it should be linked to the nonlinear scale $k_{\rm NL}$ satisfying

$$k_{NL}^3 P_{\rm lin}(k_{NL}, z) = 2\pi^2\,. \tag{6.42}$$

Finally, for the squeezed shape scaling f_{2h} we do not use the two-halo model amplitude, but instead the prescription of Eq. (6.25) with the two free parameters C and D obtained from simulations (see discussion in Subchapter 6.2.2). By matching f_{2h} to the excess in the measured bispectrum at redshifts $z = \{0,1,2,3\}$, together with the cutoff scale in f_{3h}, we obtain the following approximate fit for the coefficients C, D and E:

$$\begin{aligned} C &= 140\,D(z)^{-5/4} \\ D &= 1.9\,h\,{\rm Mpc}^{-1}\,D(z)^{-3/2} \\ E &= 7.5\,k_{\rm NL}(z)\,. \end{aligned} \tag{6.43}$$

functions f_{1h} (Eq. 6.20) and $f_{3h} = 1$ are given by the standard halo model, while for the two-halo term we allow an improved fit and growth scaling (Eq. 6.25) with coefficients $C = 240\,D(z)^{-1}$ and $D = 2.35\,h\,{\rm Mpc}^{-1}\,D(z)^{-1}$. However, the three-shape model of Eq. (6.40) above provides an improved fit in the flattened limit in the quasi-nonlinear regime.

We emphasise that this is different from the previous two-halo fits of Eqs. (6.26-6.27), because these were obtained by fitting to the two-halo model predictions, which underestimate power for $z > 0$. This is illustrated starkly at $z = 2$ in Fig. 6.15, where we compare the standard two-halo model prediction with the squeezed shape of Eq. (6.25) with best fit simulation parameters of Eq. (6.43). We also note that for redshifts $z > 1$, the lengthscale E moves rapidly to large $K \gg 1\,h/\mathrm{Mpc}$, so the exponential suppression f_{3h} term (Eq. 6.41) acts primarily to reduce power in the $z = 0$ bispectrum and is less relevant elsewhere.

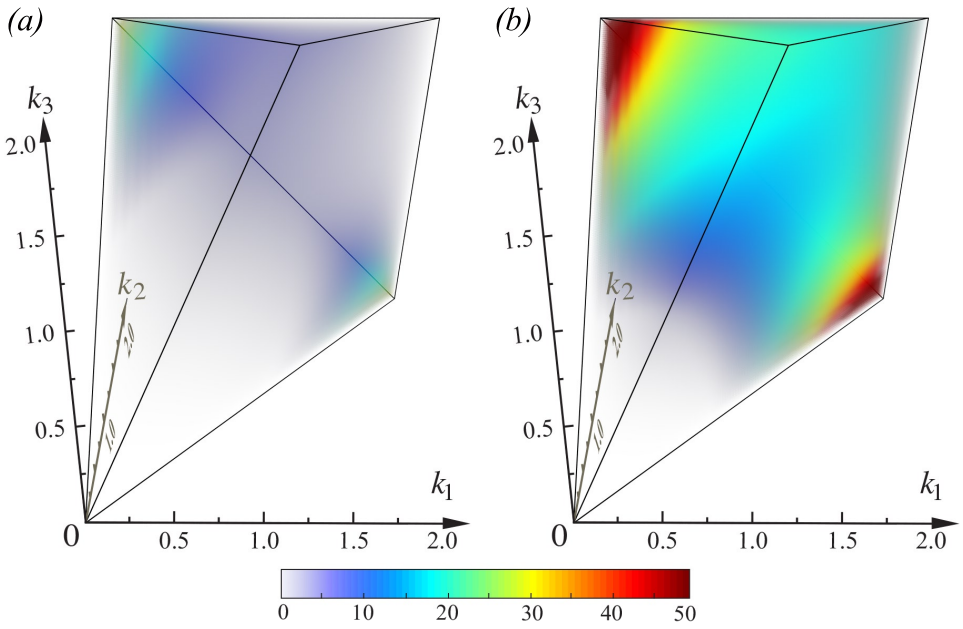

Fig. 6.15 The SN-weighted two-halo bispectrum (Eq. 5.178) (left panel) at $z = 2$ compared to the best-fit two-halo squeezed shape ansatz (Eq. 6.23); this allows the 'three-shape' benchmark model to accurately match the simulation data shown in Fig. 6.11. The two-halo model clearly exhibits a large deficit and does not describe squeezed contributions adequately at higher redshift.

In Fig. 6.16 we plot the value of the binned amplitude $|B|^S(K)$ for the three-shape model of Eq. (6.40), which we compare directly to the measured bispectrum from simulations; we also show the binned shape $\mathscr{S}^S$ and amplitude $\mathscr{A}^S$ correlators between model and N-body bispectrum. The plots show a good fit using the three-shape model across all scales $k > 0.1\,h/\mathrm{Mpc}$ and all redshifts. The shape correlations in this range are approximately 99% or higher and the amplitude correlator is within 10% of the measured bispectrum (consistent given present simulation uncertainties). These correlation results are in line with expectations for a good fit for an $n_{\mathrm{max}} = 50$ eigenfunction decomposition (Eq. 6.30) (see

validation discussions in Ref. [242]). We note that given the high shape correlations, we could introduce additional degrees of freedom in f_{1h}, f_{3h} to improve this quantitative fit further, but our purpose first is to demonstrate the efficacy of this simple approach.

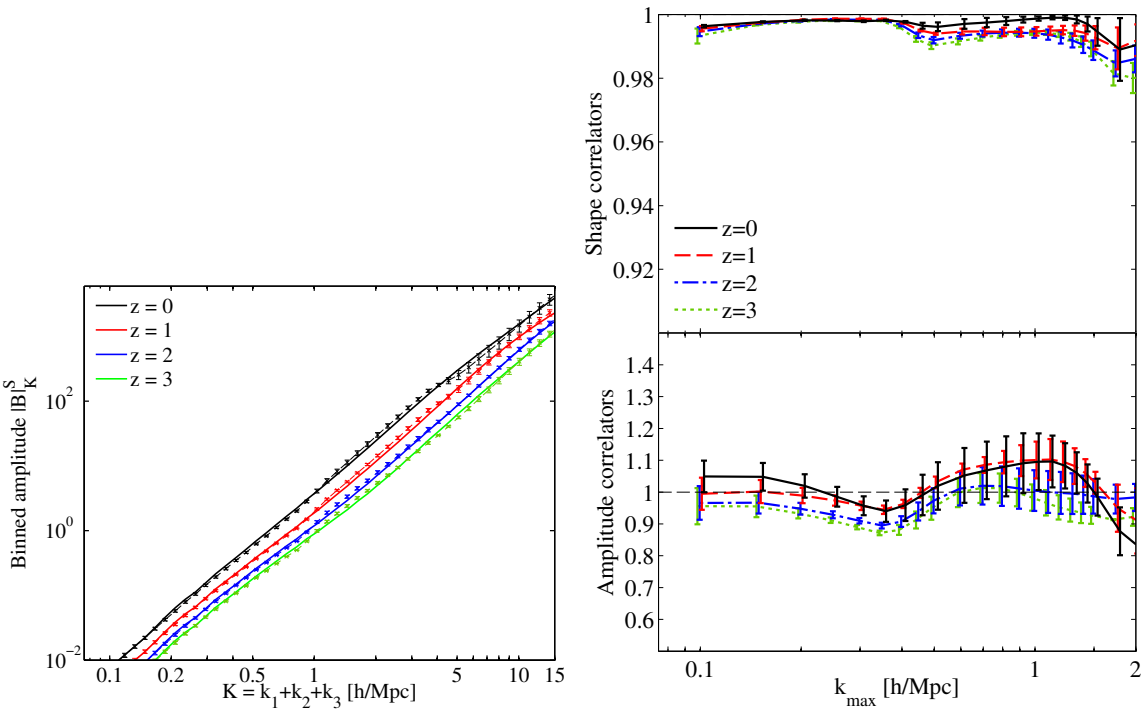

Fig. 6.16 Comparison between the measured N-body matter bispectrum and the three-shape model. The left panel shows the binned amplitude $|B|^S(K)$ from the simulations (points and dashed lines) and from the fitted three-shape model (solid lines) at redshifts $z = \{0,1,2,3\}$. The top and bottom right panels show a relative comparison between the simulations and the benchmark model, using the binned shape and amplitude correlators, $\mathscr{S}^S$ and $\mathscr{A}^S$. These results demonstrate that the three-shape model exhibits a high shape correlation on all scales and describes the simulated data well.

Employing this new three-shape model as a benchmark has several advantages over using the simulated bispectra directly, though we will use both in subsequent discussions. First, it smooths out any systematic discontinuities appearing where the simulations are joined together. Secondly, it allows direct comparisons with theoretical models without performing eigenfunction decompositions on the latter, so residual offsets do not have to be subtracted. And finally the model is simple, capturing the most important features of the halo model without requiring computationally costly re-evaluations at all wavenumber combinations (k_1, k_2, k_3), and thus it can be seen as an initial step towards a full HALOFIT-style phenomenological model of the matter bispectrum.

6.4.5 Directions for further improvement

The three-shape benchmark model achieves a high degree of correlation with the full bispectrum from N-body simulations, however undoubtedly further improvements of this model can be achieved in future, not least by deriving some key results from first principles, such as the modified two-halo growth rates. In principle, showing that the matter bispectrum is well approximated by the separable form of Eq. (6.40) should considerably simplify mathematical modelling.

One improvement that can be incorporated into the model is to replace the nonlinear tree-level shape (Eq. 6.15) with specific one- and two-loop perturbative expansions. However, while this approach could extend the tree-level shape further into the non-linear regime, it requires prescriptions for suppressing the two- and one-halo terms more strongly to avoid over-prediction. This is similar in spirit to the suppression of the perturbative bispectrum contribution in the halo-PT model by Ref. [234]; but it is clear that an exponential cut-off where the perturbative expansion breaks down is likely too aggressive, since Fig. 6.12 shows that the tree-level shape is present up to relatively high $k \sim 1\,h/\mathrm{Mpc}$.

Clearly further improvement of the three-shape model can be achieved through more extensive comparisons with higher-resolution N-body simulations, over a finer grid of scales and redshifts. The quality of fits obtained in the squeezed and flattened limits are constrained in accuracy by the restricted ansatzes chosen, allowing only three redshift-dependent parameters. The likely outcome is a finer tuning of a larger number of phenomenological free parameters, again in the spirit of the HALOFIT method, with extensive surveys required to uncover dependencies on cosmological parameters.

A final point of interest is the question whether the three-shape model we introduced satisfies well-known constraints in the squeezed limit. For example, Ref. [299] derived a consistency relation between the integrated squeezed-limit bispectrum and a response function derived from the power spectrum. In the case of our three-shape model (Eq. 6.40), the tree-level shape term satisfies the consistency relation automatically, as was demonstrated by Ref. [299] for tree-level SPT. We know that the squeezed- and constant-shape terms of the benchmark model are similar to two- and one-halo terms of the standard halo model; furthermore, as we show in Subchapter 6.5 below, our model performs well compared with the N-body simulations in the squeezed limit over the configurations we have tested, so that it is unlikely that there is any large inconsistency. However, a more quantitative test of the consistency relation would require a full numerical evaluation of the integrated bispectrum, which we leave for future investigation.

6.5 Bispectrum model comparison with simulations

We next use the N-body simulations to compare the accuracy of the different theoretical bispectrum models described in the previous subchapters, both perturbative and non-perturbative. We present this model comparison in two ways: we first directly compare the simulated and theoretical bispectra over a range of representative triangular configurations (equilateral, squeezed, and flattened), and we then use the full three-dimensional amplitude and shape correlators presented in Subchapter 6.1.2.

At high redshift, all models are expected to perform well over an extended range of scales, as the fluctuations are nearly linear, the power spectrum is linear and the bispectrum can be described by the tree-level expression. At lower redshifts, non-linearities become more important and significant differences appear between the models. In the comparisons, we concentrate on redshifts $z = \{0, 1, 2\}$, as these span the observable redshift range of most current and future observations from galaxy surveys. We investigate the perturbative methods and the halo models separately, because the perturbative methods decay quickly in the non-linear regime and therefore their predictions for high k are of no interest; we present the comparison of PT models on scales $k \leq 0.4\,h$/Mpc only. On the other hand, the phenomenological models, which are either based on or at least inspired by halo models, are expected to perform well even in the fully non-linear regime; in this case we extend the model comparison up to the smallest scales accessible to the present simulations, *i.e.* $k \leq 7.8\,h/\mathrm{Mpc}$.

6.5.1 Testing alternative perturbative approaches

We first qualitatively compare perturbative bispectrum predictions with the matter bispectrum measured from simulations. In Fig. 6.17 we plot most of these predictions at redshift $z = 2$ in three dimensions for wavenumbers $0.02\,h/\mathrm{Mpc} < k < 0.6\,h/\mathrm{Mpc}$, together with the actual N-body bispectrum (upper left). We choose $z = 2$ so that the perturbative models decay at higher k, and more of the signal is visible, but the overall behaviour is comparable at lower z.

The N-body bispectrum shows a dominant flattened signal over the whole domain, which grows in amplitude as k increases. Qualitatively, this measured signal matches well the one-loop SPT and EFT models, as well as the nonlinear tree-level bispectrum, in regions well beyond the strictly perturbative regime. However, the tree-level and MPTBREEZE predictions are appreciably lower for large $k \approx 1\,h/\mathrm{Mpc}$ (with the latter exponentially suppressed for large k by prescription).

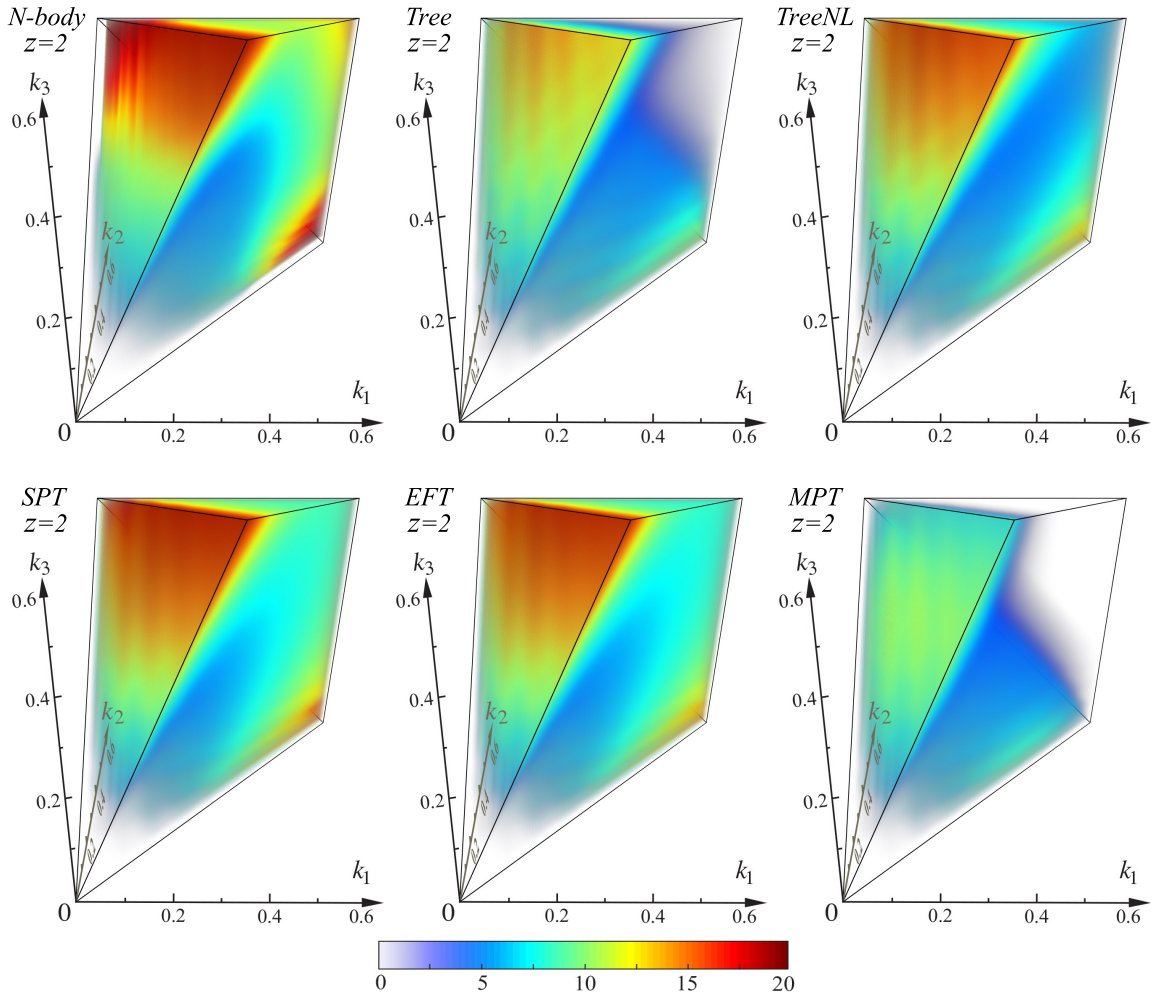

Fig. 6.17 Comparison at redshift $z = 2$ of the SN-weighted bispectrum for perturbative models with the simulation data (top left): the perturbative models are respectively tree-level bispectrum (top centre), non-linear tree-level (top right), standard one-loop perturbation theory SPT (bottom left), one-loop effective field theory EFT (bottom centre) and renormalised perturbation theory MPT (bottom right); RLPT is not plotted as it appears very similar to MPT. Note that all perturbation theories have signal concentrated at flattened triangles (front left face), and so are highly correlated with the tree-level bispectrum shape of Eq. (6.14), when using the binned shape correlator (Eq. 6.17). The N-body bispectrum also exhibits a squeezed signal for $k \gtrsim 0.4h/\mathrm{Mpc}$. We have chosen $z = 2$ so that the PT models decay at higher k and there is more signal to display, but the general behaviour is similar at lower z.

We confirm these observations for three specific limiting cases in Fig. 6.18 with a comparison of PT bispectra amplitudes with measured values: from top to bottom we show the equilateral, squeezed, and flattened triangle configurations. In addition to the bispectrum amplitudes, in each case we also plot residuals with respect to the tree-level

model. Figure 6.18 demonstrates that all models converge to the tree level for $k \lesssim 0.1\,h/\mathrm{Mpc}$ at $z = 0$ in agreement with simulations; the range of validity of the tree-level theory increases for higher redshift and for flatter shapes. For the phenomenological models, we note that both the simple non-linear tree-level model and the nine-parameter tree-level fit both increase the range over which there is agreement with simulations. For $z \geq 1$ these two cases are nearly indistinguishable and both show a similar deficit in power for larger k. In principle the nine-parameter model does provide a better match to the $z = 0$ bispectrum, however, it also exhibits large oscillations which originate through the slope parameter n for a power spectrum with BAO features, as noted and circumvented in Ref. [267]. While it is possible to remove these unwanted oscillations of n with a spline smoothing, we do not apply this extra processing step here for simplicity.

For the one-loop perturbative models plotted in Fig. 6.18, all approaches agree in the strictly perturbative regime at $z = 0$. However, beyond this regime for larger k, SPT generally overestimates the bispectrum, while the RLPT and RPT MPTBREEZE models underestimate it. The EFT approach lies in between the SPT and RLPT curves, and typically extends the range of agreement with simulations. This trend is also apparent at higher redshift with the exception of the squeezed limit where even SPT falls below the measured bispectrum in the quasilinear regime.

Given these interesting observations, we have undertaken a comprehensive quantitative comparative analysis using the integrated amplitude correlator $\mathscr{A}$ (Eq. 6.4) and the shape correlator $\mathscr{S}$ (Eq. 6.3), the results of which are plotted in Fig. 6.19. This corresponds to a signal-to-noise weighted integration over all triangular configurations up to a given resolution k_{max}, rather than the specific limiting configurations Fig. 6.18. Here, we directly compare the theoretical predictions B^j_{theory} to the three-shape benchmark model $B_{\text{3-shape}}$ given in Eq. (6.40) with parameters given in Eq. (6.43), which provides an excellent fit and a smoother representation of the actual bispectrum from simulations (see Subchapter 6.4.4).

We estimate the uncertainties on the correlators as follows. From each simulation realisation i, we obtain the amplitude and shape correlators $\mathscr{A}(B^i_{\mathrm{sim}}, B_{\text{3-shape}})$, $\mathscr{S}(B^i_{\mathrm{sim}}, B_{\text{3-shape}})$ as a function of k_{max}. For each value of k_{max}, we can thus derive mean and standard deviation of the correlators: $\mu_{\mathscr{A}}$, $\sigma_{\mathscr{A}}$, and similarly for the shape. As we are comparing all theoretical models with the benchmark three-shape model, the total uncertainty σ_{tot} on the correlators between each model j and the benchmark, $\mathscr{A}(B^j_{\mathrm{theory}}, B_{\text{3-shape}})$, will be larger than the variance $\sigma_{\mathscr{A}}$ obtained from the scatter of $\mathscr{A}(B^i_{\mathrm{sim}}, B_{\text{3-shape}})$; this is because of the small k-dependent discrepancy that exists between the simulations and the smooth benchmark model. The grey shaded areas in Fig. 6.19 represent two different estimates of σ_{tot}, as follows.

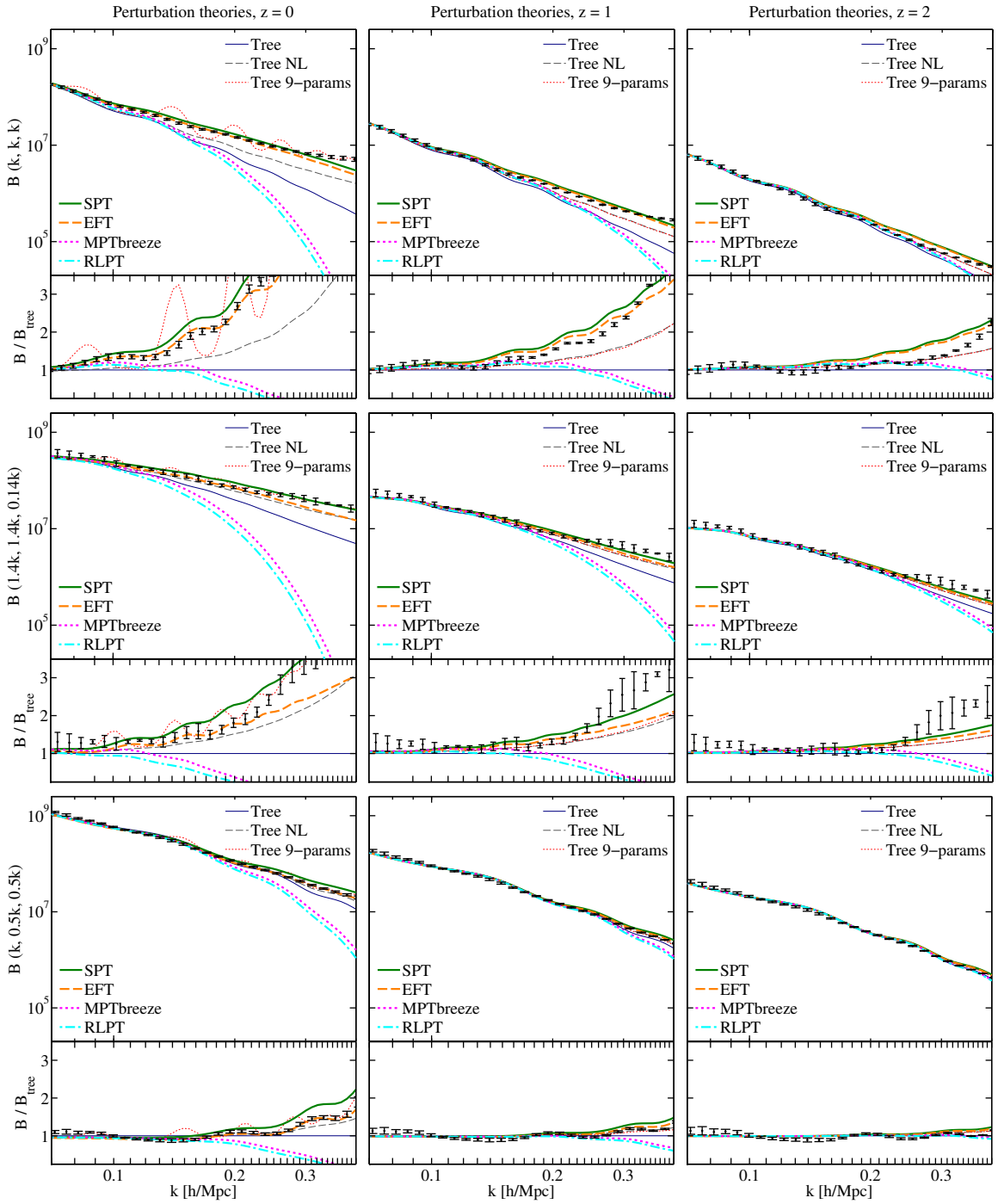

Fig. 6.18 Comparison of perturbation theory models of the matter bispectrum with N-body simulations, at redshifts 0, 1, 2 (left to right), for the equilateral, squeezed, and flattened configurations (top to bottom). The lower panels show the residuals with respect to the tree-level model.

The light grey area represents a conservative error estimate obtained by adding the error bars of the simulation to the deviation from one of the mean of the correlator, *i.e.* assuming $\sigma_{\text{tot}} = |\mu_{\mathscr{A}} - 1| + \sigma_{\mathscr{A}}$, while the darker grey area represents the part of the benchmark model outside the $1\sigma_{\mathscr{A}}$ error bars, *i.e.* assuming

$$\sigma_{\text{tot}} = \begin{cases} 0 & \text{if } 1 \in [\mu_{\mathscr{A}} - \sigma_{\mathscr{A}}, \mu_{\mathscr{A}} + \sigma_{\mathscr{A}}] \\ \mu_{\mathscr{A}} - \sigma_{\mathscr{A}} - 1 & \text{if } \mu_{\mathscr{A}} - \sigma_{\mathscr{A}} > 1 \\ 1 - \mu_{\mathscr{A}} - \sigma_{\mathscr{A}} & \text{if } \mu_{\mathscr{A}} + \sigma_{\mathscr{A}} < 1\,. \end{cases} \tag{6.44}$$

The same reasoning applies to the shape correlators $\mathscr{S}$, with the difference that $\mu_{\mathscr{S}} \leq 1$.

From Fig. 6.19, we note that there are always high shape correlations well beyond the perturbative regime. For example, at $z = 0$ all theories have a shape correlation greater than 99% up to $k < 0.2\,h/\text{Mpc}$, even when there are variations of $\mathscr{O}(20\%)$ in the amplitude correlator. These remarkably high shape correlations imply that bispectrum estimators that measure the projection of the full bispectrum on these theoretical shapes (like in Ref. [243]) should yield a high proportion of the total bispectrum signal-to-noise. Since the shape correlator is not as discerning a tool for distinguishing between different perturbative models, we focus most attention on amplitude deviations.

We also employ the total correlator $\mathscr{T}$, which combines the information of amplitude and shape, in order to directly estimate the range of validity of each model as a function of redshift. In Table 6.1 we give the maximum wavenumber k^*_{max} at which the total correlator between each model and the benchmark model deviates from unity by more than a fixed threshold of 10% (and 5%). While we show results at the three redshifts considered, $z = \{0, 1, 2\}$, an important caveat is that the comparison at $z = 0$ is more approximate, due to the less than perfect match between the simulations and the benchmark model; we therefore do not report the 5% results at $z = 0$, and choose to focus primarily on the results at $z = \{1, 2\}$ in the following discussion. A striking feature of Table 6.1 is the wide range of wavenumbers for which there is good correspondence between theoretical predictions and the measured bispectrum, well beyond expectations for the limits of the perturbative regime estimated in Table 5.1. This shows that even where these theories are no longer expected to be accurate, they can nevertheless be successfully extrapolated into the nonlinear regime for phenomenological modelling.

The tree-level (Eq. 6.14) and the non-linear tree-level (Eq. 6.15) models are the simplest approximations to the matter bispectrum, and their range of validity can be verified from Fig. 6.19: at $z = 1$ we find $k^*_{\text{max}} = 0.22\,h/\text{Mpc}$ for the tree level and $k^*_{\text{max}} = 0.30\,h/\text{Mpc}$ for

Table 6.1 Wavenumber $k^*_{\rm max}$ where the total correlator $\mathscr{T}$ (Eq. 6.6) between the perturbative theory and the benchmark model deviates by more than 10% (5%) from unity. In the case of $z = 0$, we only report the 10% results, as the accuracy of the benchmark model is lower.

Perturbation theories			
Threshold 10% (5%)	$k^*_{\rm max}\,[h/{\rm Mpc}]$		
Theory	$z=0$	$z=1$	$z=2$
Tree-level	0.13	0.22 (0.17)	0.27 (0.20)
NL tree-level	0.17	0.30 (0.22)	0.42 (0.31)
SPT	0.11	0.37 (0.14)	0.66 (0.49)
EFT	0.29	0.45 (0.36)	0.60 (0.50)
MPTBREEZE	0.16	0.24 (0.21)	0.32 (0.28)
RLPT	0.15	0.22 (0.19)	0.30 (0.26)

the non-linear tree level (at 10%). The non-linear bispectrum improves faster than the linear one at higher redshifts: the tree-level increases by roughly $0.05\,h/{\rm Mpc}$ at each redshift, while the non-linear tree-level increases by $> 0.1\,h/{\rm Mpc}$.

The one-loop SPT bispectrum adds four extra terms to the tree-level shape. Two of them give positive contributions and the other two negative contributions. As seen in Fig. 6.19, at low redshift the additional SPT contributions tend to overshoot the measured bispectrum, apparently lowering the value of $k^*_{\rm max}$ up to which predictions are accurate (see Table 6.1). However, at $z = 2$ the overshoot remains within bounds, extending the fit as far as $k < 0.66\,h/{\rm Mpc}$ in the case of the 10% threshold (almost accidentally at this specific redshift, possibly because of additional squeezed contributions in the measured bispectrum). In general, SPT predicts an excess of power on quasi-linear scales, before finally decaying in the fully non-linear regime. This overshoot phenomenon appears because the loop integrals involved require integrating momenta over an infinite range, a regime in which the basic assumption $\delta \ll 1$ is no longer valid. Despite this problem, the shape correlation is excellent up to $k \sim 0.3\,h/{\rm Mpc}$, improving significantly over the tree-level result. We also note that evidence for the amplitude overshoot is not very strong from our simulations because they have rather large uncertainty on $\mathscr{A}$, especially at $z = 0$.

The one-loop EFT bispectrum includes one counterterm, which increases the accuracy of the model due to the one free parameter that is introduced and fitted at the level of the power spectrum. In Fig. 6.19 we observe that this method provides substantially improved agreement with the simulations, albeit at the cost of an extra parameter, which was calibrated on the power spectrum of N-body simulations, assuming a specific cosmological model. This counterterm effectively removes excess power provided by SPT in the quasi-linear

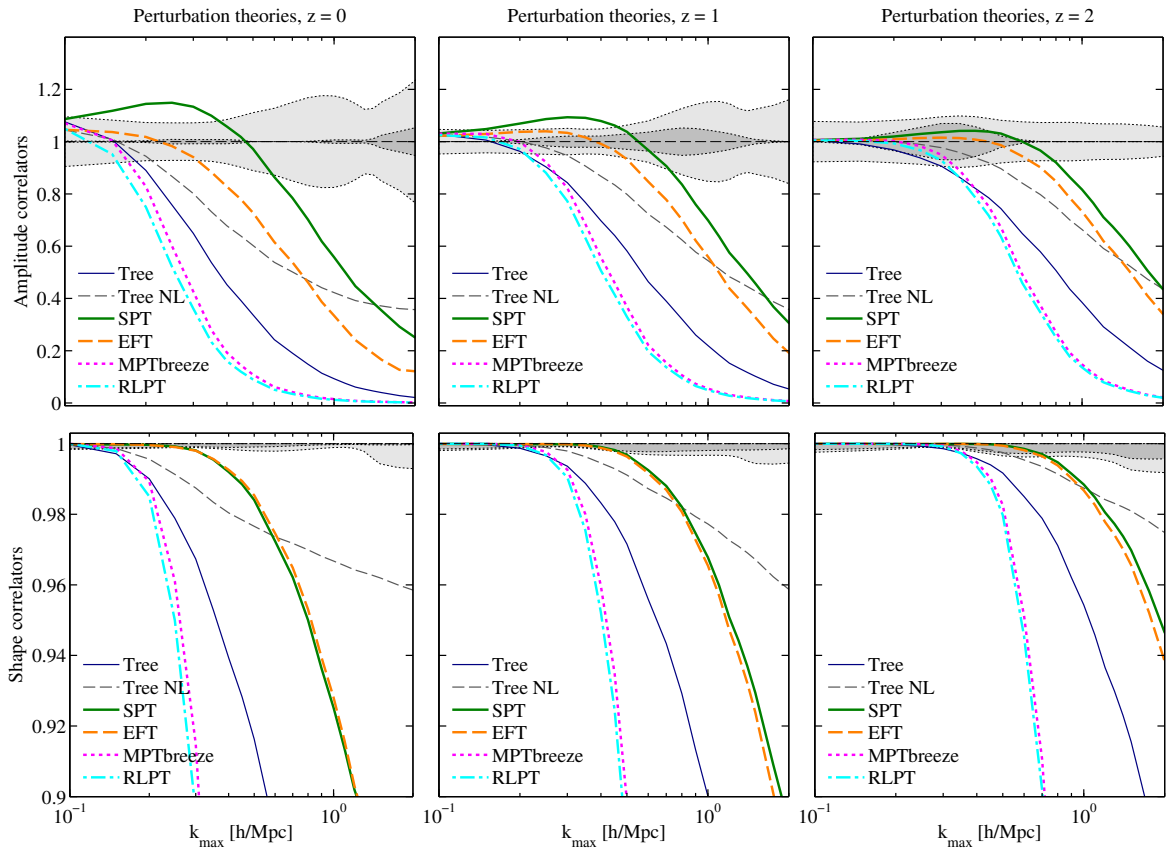

Fig. 6.19 The amplitude $\mathscr{A}$ (top row) and shape $\mathscr{S}$ (bottom row) correlators at redshifts 0, 1, 2 for the perturbative methods, obtained by comparing with the benchmark model. The shaded areas represent error estimates between the benchmark model and the simulations and are explained in the main body of the text.

regime and the results that we obtain from the three-dimensional comparison are consistent with the improved agreement found in Ref. [260]. The EFT method appears to work well up to $k^*_{\rm max} = 0.45\,h/{\rm Mpc}$ at $z = 1$ and $k^*_{\rm max} = 0.60\,h/{\rm Mpc}$ at $z = 2$. However, we must proceed cautiously before using such projections because the detailed correspondence in the equilateral and squeezed limits shown in Fig. 6.18 is not as encouraging. (We also observe additional correlated squeezed signals emerging on these scales in the measured bispectrum which require more sophisticated joint fitting.) At higher redshift, the contribution of the counterterm becomes less significant, because the growth rate of the term is $\propto D^{7.1}(z)$ compared to $\propto D^6(z)$ from the one-loop SPT terms. Although one can in principle add another three additional counterterms for the one-loop EFT bispectrum, we have found that the improvement in the accuracy is modest relative to the cost of introducing these further free parameters.

The RPT approach (MPTBREEZE formalism) at one loop solves the SPT excess by cutting off terms appropriately with an exponential function, as can be seen in Fig. 6.19. Compared to SPT, all terms are positive to any number of loops, and so this is a convergent expansion. With accuracy increasing with number of loops, the amplitude on all scales should always approach the measured bispectrum from below. We see in Table 6.1 that the RPT method appears to be accurate to 10% at $k < 0.24\,h/\mathrm{Mpc}$ at $z = 1$, improving to $k < 0.32\,h/\mathrm{Mpc}$ at $z = 2$. The main improvement of MPTBREEZE compared with the other methods arises on large scales, before the exponential damping begins. The disadvantage of this suppression is that it precludes any extrapolations into the nonlinear regime.

The RLPT results we have obtained are similar to RPT, although the validity range is marginally smaller due to the increased power suppression; in this case we find $k^*_{\mathrm{max}} = 0.22\,h/\mathrm{Mpc}$ at $z = 1$, and $k^*_{\mathrm{max}} = 0.30\,h/\mathrm{Mpc}$ at $z = 2$.

We conclude that all one-loop perturbative methods match simulations at present precision within the expected perturbative regime. In terms of phenomenological extrapolation into the nonlinear regime, the EFT method goes furthest (once the counter-term coefficient has been appropriately fitted). Both RLPT and RPT undershoot the measured bispectrum in this regime by construction, while SPT generically overshoots. On the other hand, the nonlinear tree-level bispectrum Eq. (6.15) provides a useful projection to larger k which has the advantage of being much simpler to calculate.

6.5.2 Testing phenomenological halo models

By analogy with the discussion of the PT methods above, we first make qualitative comparisons of the phenomenological halo models with the measured bispectrum. In Fig. 6.20, we plot these bispectra in three dimensions at two redshifts $z = 0, 2$. While the standard halo model provides a reasonable fit at $z = 0$, it reveals a large deficit on intermediate scales $k \sim 1\,h/\mathrm{Mpc}$. This is corrected in the three-shape model by using the nonlinear tree-level bispectrum and adopting a different growth rate for the squeezed signal at higher redshift. In Fig. 6.21 we offer a more detailed picture in the limiting equilateral, squeezed and flattened configurations, also showing residuals relative to the standard halo model.

From Fig. 6.20, we can see that for all configurations the standard halo model provides a good match to the N-body data on both linear and fully non-linear scales, while a more significant mismatch appears in the transition regime at redshifts $z > 0$. The problem may be due in part to questionable assumptions in the halo model about all the matter in the Universe being in collapsed halos; it is an issue acknowledged in the literature both for the power spectrum and the bispectrum [233, 234, 298, 300]. We confirm that this mismatch becomes

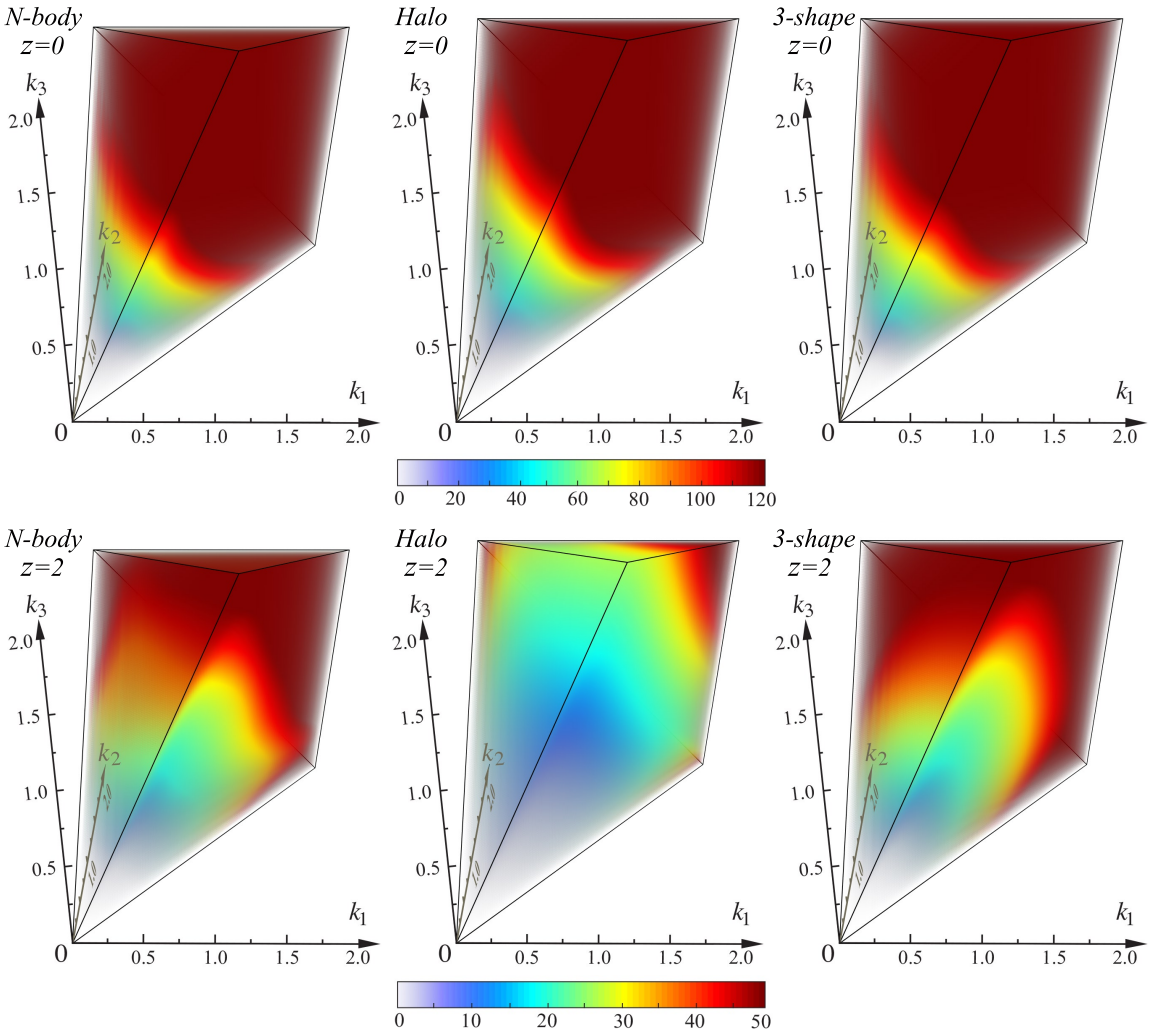

Fig. 6.20 Comparison between N-body simulation bispectrum (left panels) with the standard halo bispectrum model Eqs. (5.177-5.179) (centre panels) and the 'three-shape' benchmark model Eq. (6.40) (right panels) shown at two redshifts $z = 0, 2$. The standard halo model is effectively normalised to fit the measured bispectrum at $z = 0$, which is also achieved well by the phenomenological 'three-shape' model (upper panels). However, at higher redshift $z = 2$ the halo model exhibits the wrong growth rates for the flattened three-halo and squeezed two-halo configurations, yielding a substantial deficit (lower panel centre); the measured bispectrum behaviour can be accommodated in the three-shape benchmark model (lower panel right).

more severe at higher redshift: for example, at $z = 2$ there is up to a factor of three mismatch on these intermediate scales.

The other phenomenological models we consider attempt to improve the behaviour in the transition region in different ways, and with varying degrees of success; they are

also plotted in Fig. 6.21. The combined halo-PT model provides some improvement at $z = 0$ for flattened configurations, but it fails to significantly improve the situation at higher redshifts and especially in the squeezed limit. The phenomenological two-halo boost and three-shape benchmark models improve the N-body results over a broader range of redshifts and configurations, largely by increasing the relative amplitude of the two-halo term at $z > 0$. The three-shape benchmark, in particular, achieves a satisfactory fit in all limits and at all redshifts using only the restricted ansatz (Eq. 6.40) by also increasing power in the flattened limit with the non-linear tree-level bispectrum.

We now turn to a full three-dimensional analysis with the amplitude ($\mathscr{A}$) and shape ($\mathscr{S}$) correlators plotted in Fig. 6.22 for redshifts $z = 0, 1, 2$; as in the previous subchapter, we again compare to the three-shape benchmark model with best-fit parameters of Eq. (6.43). We also determine where the accuracy of different phenomenological models and fits break down in Table 6.2.

It is apparent from Fig. 6.22 that the standard halo model offers an insightful description of the matter bispectrum in the non-linear regime at redshift $z = 0$; the shape correlation is above 99% everywhere investigated and the amplitude deviates less than 15% from the measured simulation bispectrum over the range $0.4\,h/\text{Mpc} < k < 8\,h/\text{Mpc}$. Nevertheless, we observe some excess power on large scales, e.g. at $k_{\text{max}} \sim 0.1\,h/\text{Mpc}$, which is a well-known problem of the standard halo model, due to the one-halo term approaching a constant and the two-halo term not vanishing as $k \to 0$. The large-scale excess is less important as the redshift is increased. However, we see in Fig. 6.22 that there is a new problem on intermediate scales where an amplitude deficit emerges, which increases significantly as a function of redshift: in the transition regime, the amplitude correlator decreases from 0.9 at $z = 0$ to 0.65 at $z = 1$, and 0.45 at $z = 2$. As discussed in previous subchapters, this is primarily due to an underprediction of the two-halo component (squeezed shape) in this k-range. Moreover, the lowest point in the transition regime shifts to higher k at higher redshift, from $k \approx 0.5\,h/\text{Mpc}$ at $z = 0$ to $k \approx 1.5\,h/\text{Mpc}$ at $z = 2$ (see Fig. 6.7 for an illustration of this in the equilateral configuration). In the strongly non-linear regime, after the two-halo component has decayed and the one-halo term becomes dominant, the halo model again approaches the simulations. As we discussed above in Subchapter 6.3, a possible way of solving this problem is by boosting the two-halo component, which peaks exactly in the regime of interest; this leads to the two-halo boost model also shown in Fig. 6.22, which entails a minimal cost of introducing additional power on large scales.

The power excess produced on linear scales by the standard halo model is corrected in the combined halo-PT model of Subchapter 5.3.2. As this model can use any perturbative

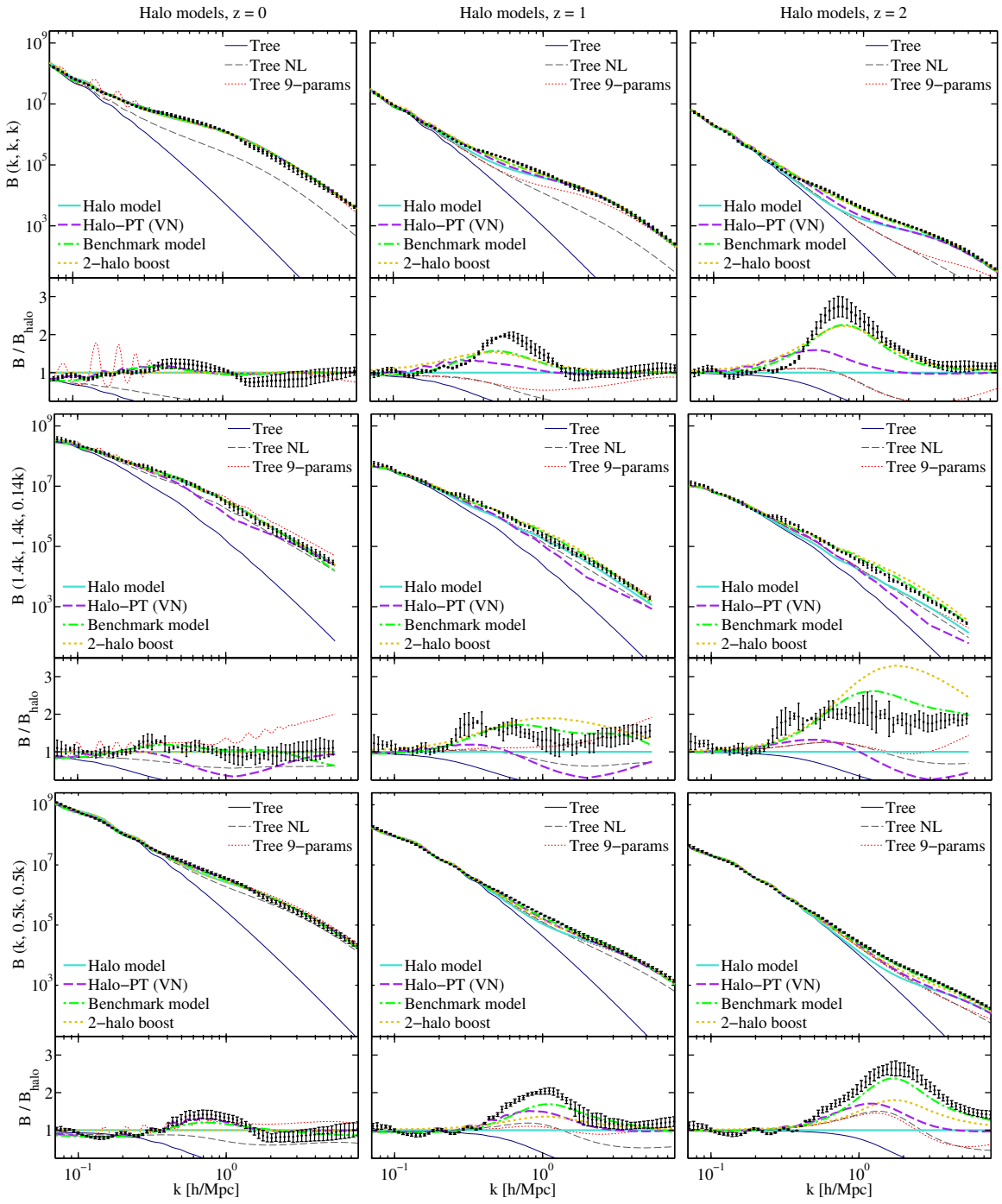

Fig. 6.21 Comparison of phenomenological non-linear models of the matter bispectrum with N-body simulations, at redshifts 0, 1, 2 (left to right), for the equilateral, squeezed, and flattened configurations (top to bottom). The lower panels show the substantial residuals with respect to the standard halo model for $z > 0$, demonstrating that the simple three-shape benchmark model provides a good fit to the N-body matter bispectrum for all three limits and redshifts.

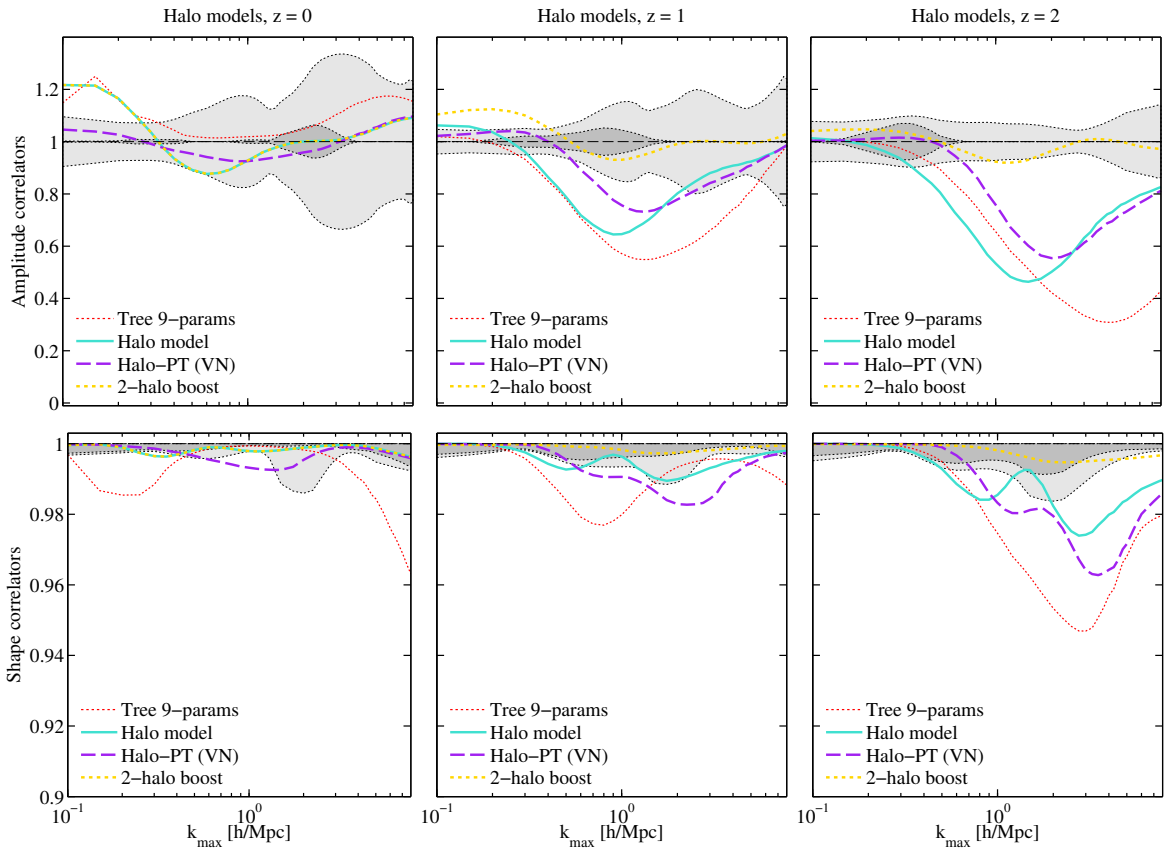

Fig. 6.22 The amplitude $\mathscr{A}$ (top row) and shape $\mathscr{S}$ (bottom row) correlators at redshifts 0, 1, 2 for the phenomenological halo models, obtained by comparing with the three-shape benchmark model. The shaded areas represent error estimates between the three-shape benchmark model and the simulations and are explained in Subchapter 6.5.1.

theory on linear scales, we choose to use EFT, because we found it in the previous subchapter to offer the most extended range of validity. In this prescription, the two- and three-halo terms of the halo model are switched on as the perturbation theory is decaying. Hence, at $z = 0$, this model provides the best fit across all scales considered; in the strongly non-linear regime, the model converges towards the standard halo model result, because on small scales the improved two-halo and the improved one-halo terms are the same as their standard counterparts. Nonetheless, for $z > 0$, the combined halo-PT model has the same problem as the standard halo model, as there is a deficit in the transition regime, though marginally weaker. In this model, the improved one- and especially the two-halo terms are heavily suppressed on large and intermediate scales. This is not visible in Fig. 6.22 because most of the signal comes from EFT on these scales, making it more challenging to solve the deficit by a simple boost of the improved two-halo term.

Table 6.2 Wavenumber $k^*_{\rm max}$ where the amplitude deviation for phenomenological halo models is greater than 20% when compared to the three-shape benchmark model matched to simulations. (The small k excess problem of the standard halo model is ignored.) At $z = 0$ all models agree within 20% over the entire range of scales.

Phenomenological halo models			
Threshold 20%	$k^*_{\rm max}\,[h/{\rm Mpc}]$		
Theory	$z=0$	$z=1$	$z=2$
Standard halo model	>8	0.47	0.51
Combined halo-PT model	>8	0.48	0.68
9-parameter fit	>8	0.82	0.90

The nine-parameter fit, which is based on the simple tree-level model, fitted to $k \leq 0.4\,h/{\rm Mpc}$ and for $z \leq 1.5$ is fairly accurate when extrapolated across the full domain at $z = 0$. (In principle, improvements could be obtained by re-fitting the parameters to higher redshifts and further into the non-linear regime, though the model does not naturally include the squeezed and constant shapes required.) Spurious peaks appearing at $z = 0$ are produced by the BAO features of the power spectrum, as discussed previously. However, at $z = 1,2$ this model becomes increasingly inaccurate at large k with its amplitude decreasing in a similar fashion to the non-linear tree level bispectrum. Nevertheless, the nine-parameter model produces an accurate result up to $k_{\rm max} \sim 0.8\,h/{\rm Mpc}$ for all the redshifts considered.

As for perturbation theories, in Table 6.2 we present the maximum value of the wavenumber $k^*_{\rm max}$ for which the phenomenological halo models show good agreement, that is, by considering the point where the amplitude correlator deviates by more than 20% from unity. The numerical results of the table confirm the general trends discussed above. In contrast to the PT case, here the agreement between models and simulated data becomes worse at higher redshift, as the basic assumptions underlying the halo model become less valid. At higher redshifts, a secondary range of validity exists at high k after the transition region, which is visible from Fig. 6.22 but not reported in the table.

Among the alternative phenomenological models we tested, we conclude that the combined halo-PT model based on EFT is the most accurate, offering a physically well-motivated attempt to solve problems of the standard halo model. Nevertheless, like the standard halo model, it also does not exhibit appropriate growth rates for the two-halo contribution at high redshift and, further, the prescription for transitioning between EFT and the other halo contributions deserves closer scrutiny. From a phenomenological point of view there is

a straightforward means to improve the theory by boosting the two-halo term at higher redshifts, as in the three-shape benchmark model.

6.6 Conclusions

The bispectrum of large-scale structure has so far been a relatively neglected observable, due to the high cost of measuring it with most current sub-optimal estimators, and the relative complexity of its modelling and interpretation. This is however bound to change in the current age of precision cosmology and ever-larger galaxy surveys, as the combination of two- and three-point statistics can improve the constraining power of the upcoming data, by breaking the existing degeneracies between cosmological and astrophysical parameters. The ultimate goal of large-scale structure bispectrum measurements is its potential to constrain models of the early Universe via their non-Gaussian contribution to the primordial density perturbations, thus complementing and improving existing CMB constraints [171, 182].

Achieving these ambitious objectives will require efforts on multiple fronts. A first issue shared with power spectrum analysis is the endeavour to improve the theoretical modelling as far as possible into the non-linear regime; other outstanding points include making the bispectrum estimation faster and more efficient, and developing a comprehensive method for comparing bispectrum predictions with observations.

In this work we have made progress on all these fronts. Firstly, we studied how accurately different theoretical models for the matter bispectrum work on different scales, by comparing them with N-body simulations and introducing a new simplified phenomenological model based on three canonical bispectrum shapes. Secondly, we have used for our study the efficient modal bispectrum estimator by Ref. [242], which allowed us to reconstruct the full three-dimensional bispectrum information based on ~ 100 modes only. Thirdly, we have introduced the amplitude, shape, and total correlators as instruments to estimate the overall goodness of match between a bispectrum model and measurements across its full three-dimensional domain, thus greatly simplifying the process of model comparison and parameter estimation.

The different bispectrum models we considered can be divided into two categories: methods based on perturbation techniques, and phenomenological models based on or inspired by the halo model. The perturbative methods assume a small departure from linear scales, when the density fluctuations are small, and therefore have limited range of validity. Multiple approaches exist for increasing the scales of validity of perturbative theories, such as effective field theories, and resummed perturbation theories. We have confirmed that such

one-loop recipes manage to accurately model non-linearities up to $k_{\rm max} \simeq 0.15\,h/{\rm Mpc}$ at $z = 0$ for the matter bispectrum and further at higher redshift ($k_{\rm max} \simeq 0.4\,h/{\rm Mpc}$ at $z = 2$). This is already beyond the expectations for the strictly perturbative regime, but some methods appear to be amenable for even more ambitious extrapolations into the nonlinear regime, with effective field theory predictions apparently showing good agreement to $k \simeq 0.3\,h/{\rm Mpc}$ at $z = 0$, though at the cost of introducing free extra parameters calibrated to simulations. The much simpler nonlinear tree-level bispectrum also offered useful nonlinear projections out to $k_{\rm max} \simeq 0.17\,h/{\rm Mpc}$ at $z = 0$.

In addition, we have derived for the first time the expressions of the two-loop MPTBREEZE bispectrum in an infrared-safe manner, demonstrating that it is analytically and numerically tractable, even if computationally challenging. We have shown the improvement in the wavenumber range over the one-loop calculation for three triangle shape configurations.

From a different perspective, the halo models rely on models of matter collapse in order to describe non-linearities from a phenomenological point of view. In that sense, they are valid much further beyond the scales that can be modelled by perturbation theories, and can match simulations reasonably well in the strongly non-linear regime at $z = 0$. The combined halo-PT model [234] represents a compromise between the two approaches. It relies on a perturbative method on large scales, chosen here to be the EFT, where the halo model is not accurate, while relying on the halo model on non-linear scales. For these reasons, we found that the halo-PT model gives the most accurate predictions on all scales at $z = 0$. Nevertheless, at higher redshifts, a significant deficit appears at intermediate scales for all halo models.

We have found that a simple way to solve this halo deficit problem is to increase the contribution of the squeezed or two-halo shape at $z > 0$, which we have found dominates in the transition regime. Driven by the observations from N-body simulations, we have generalised this idea, thus developing a simple phenomenological 'three-shape' model that fits the simulations well over the full range of scales and redshifts considered. This benchmark model is based on the fundamental shapes of the halo model — tree-level, squeezed and constant shapes, corresponding to the three-, two- and one-halo terms respectively. This model can be seen as a first step towards the development of an accurate phenomenological model calibrated on N-body simulations, translating the idea behind the HALOFIT method to the bispectrum domain. This will be observationally relevant for weak gravitational lensing which is sensitive to the matter bispectrum.

Solving this two-halo deficit problem motivates our new benchmark model but it uncovers a more serious misconception in the standard halo approach built as it is on a hierarchical

picture of structure formation. The basic premise that nonlinear halos form first and then to use these to classify and calculate non-Gaussian structures is not appropriate. This is clear already from the tree-level bispectrum, which is present at high redshifts $z > 30$ long before any halos form; fundamentally it is associated with the initial stage of gravitational collapse in the first dimension which causes 'pancake-like' structures to form. The three-halo term accommodates this *a posteriori* by noting that the large-scale tree-level signal will be imprinted on the halo distribution. In the same manner, there will be a squeezed signal from the formation of filamentary structures (due to the onset of collapse in the second dimension), which again precedes halos on any given lengthscale. At present the two-halo model is flawed by assuming a hierarchical origin for this squeezed bispectrum contribution, and so it does not capture the appropriate growth rate at higher redshift. Our investigations here present quantitative bispectrum data in the relevant intermediate regime, which shows clear pathways ahead for improving the halo model (see also Ref. [218]), as well as mathematical simplifications due to the approximate separability of the underlying bispectrum.

Future developments of this work will on the one hand lead to a more comprehensive and accurate phenomenological model of the matter bispectrum, fitted on higher-resolution simulations, which will provide a bispectrum counterpart to the HALOFIT method. On the other hand, we will extend the modelling and the comparison to the case of biased tracers, *i.e.* dark matter halos and galaxies, to bridge the gap between modelling and observations by galaxy surveys. Finally, we plan to include the effects of primordial non-Gaussianity of different types to determine how it is amplified through gravitational collapse and how it can be optimally identified.

CHAPTER 7

CONCLUSIONS

In this thesis we have studied two major topic in cosmology: the effects of topological defects on the CMB and the matter bispectrum of large-scale structure. In this Chapter, we will summarise the most important results obtained.

7.1 Effects of topological defects on CMB

The production of topological defects (cosmic strings, domain walls, monopoles, textures) is predicted by most cosmological models involving symmetry breaking in the early Universe. Of the topological defects, the most popular have been cosmic strings because they were considered to be possible seeds for the large-scale structure in the Universe, until it was shown that the power spectrum they produce does not match the one observed by high-precision cosmological probes, such as COBE, WMAP and *Planck*. In the meantime, fluctuations generated from inflation have provided a better match to current observations. Even so, their presence is not ruled out by current observations, and they have become more popular again because such defects are predicted in string theories of inflation and, in particular, they can be produced at the end of brane inflation. Although they have not been detected so far, their observable effects offer the hope that they may be discovered in the near future. They have also been used to explain CMB anomalies, such as the 'cold spot' [67]. Moreover, the recent detection of gravitational waves from black hole mergers represents an encouraging sign of possible observations of gravitational waves from the decay of cosmic string loops in the future [69].

In order to analyse the cosmological predictions of strings, we have used three high resolution simulations describing the evolution of cosmic string networks, covering the period from recombination until the late-time cosmological constant epoch, to determine their CMB

power spectrum. Constraints on the cosmic string density parameter of $G\mu/c^2 < 1.29 \times 10^{-7}$ were obtained using *Planck* data using a Markov chain-Monte Carlo method.

Contrary to cosmic strings, domain walls are severely constrained by observations up to an energy of $\eta < 1$ MeV (the Zel'dovich bound) and are therefore unlikely to play a major cosmological role except perhaps for large-angle CMB anomalies. Nevertheless, finding a precise constraint on the energy scale of formation of these defects was long overdue. We have run three field theory walls simulations based on the Press-Ryden-Spergel algorithm in the radiation, matter and cosmological constant eras and we have adapted the formalism that we have developed for cosmic strings to the case of domain walls, finding a constraint of $\eta < 0.93$ MeV, which is surprisingly close to the Zel'dovich bound of 1 MeV. [1]

7.2 Matter bispectrum of large-scale structure

The late-time matter distribution in the Universe contains a wealth of information that has not yet been fully exploited. Compared to the CMB, which only contains information from last scattering and is thus two-dimensional in nature, the LSS encodes data from different times as well and therefore the number of available modes is significantly increased over the CMB. The perturbation information extracted corresponding to galaxy clustering is related to the matter fluctuations through biasing. Current data extracted from LSS is still consistent with the hypothesis that the primordial fluctuations are Gaussian, but a possible detection of primordial non-Gaussianity by galaxy surveys would open new windows on inflation and would provide important information on the early Universe. This requires the study of the three-point correlation function, or bispectrum of density fluctuations.

To be able to distinguish between different cosmological scenarios, it is useful to understand the advantages and limitations of models in the literature. In this thesis, we have made a comprehensive review of perturbative models in the literature: Eulerian standard perturbation theory at one loop which extends the linear power spectrum and tree-level bispectrum, the effective field theory at one loop, the renormalised perturbation theory where we have also derived for the first time the two-loop bispectrum, the resummed Lagrangian perturbation theory and a simple phenomenological model based on the tree-level bispectrum. In addition we have looked with a critical eye at the halo model and on a combination of the halo model and perturbation theory.

[1] At the time Zel'dovich made this serendipitously accurate walls estimate, cosmology was far from being a precision science. He was often quoted as saying "What's a factor of two in cosmology!". Times have changed.

We have compared the models described above with results from N-body simulations for the bispectum for $k \leq 7.8h/\text{Mpc}$ and $z < 3$, showing the scales and redshifts where they are valid. Thus, for perturbation theories, we have shown that standard perturbation theory predicts excess power on mildly nonlinear scales, while the other theories only decay after a certain scale. At redshift $z = 0$, the effective field theory of LSS is within 10% of the N-body simulation bispectrum up to $k = 0.29h/\text{Mpc}$, while all the other theories considered can only reach $k = (0.11 - 0.17)h/\text{Mpc}$ (though they are parameter-free). For halo models, we have identified a significant missing squeezed component on intermediate scales, where the two-halo term is the most important, which worsens as the redshift is increased.

We have developed a model based on the shapes of the components of the halo model: constant for the 1-halo term, squeezed for the 2-halo term and flattened for the 3-halo term, that provides a very good fit to the numerical simulations after suitable parameter calibration. Moreover, we have shown that all the perturbative theories at one loop have a similar shape to the tree-level bispectrum, *i.e.* flattened. This points towards a simple 'HALOFIT'-style treatment of the bispectrum for future quantitative modelling and measurement, which is also being developed for modelling the growth of primordial non-Gaussianity.

Our work presented here using the dark matter distribution has a direct application for investigating the bispectrum of weak gravitational lensing and it can be developed further to study halos and galaxy distributions. If properly harnessed with sophisticated modelling and efficient estimators, it will expand the constraining power of upcoming surveys by breaking the degeneracies between cosmological parameters and galaxy bias. There is the strong prospect of improving upon the CMB constraints on primordial non-Gaussianity with significant discovery potential. Future galaxy surveys, such as LSST, *Euclid*, DESI and *WFIRST* will provide an unprecedented amount of new data and the study of non-Gaussianity will open new windows on the Universe.

REFERENCES

[1] A. Lazanu, E. P. S. Shellard, and M. Landriau, *CMB power spectrum of Nambu-Goto cosmic strings*, *Phys. Rev. D* **91** (Apr., 2015) 083519, [arXiv:1410.4860], [doi:10.1103/PhysRevD.91.083519].

[2] A. Lazanu and P. Shellard, *Constraints on the Nambu-Goto cosmic string contribution to the CMB power spectrum in light of new temperature and polarisation data*, *J. Cosmol. Astropart. Phys.* **2** (Feb., 2015) 024, [arXiv:1410.5046], [doi:10.1088/1475-7516/2015/02/024].

[3] A. Lazanu, C. J. A. P. Martins, and E. P. S. Shellard, *Contribution of domain wall networks to the CMB power spectrum*, *Physics Letters B* **747** (July, 2015) 426–432, [arXiv:1505.03673], [doi:10.1016/j.physletb.2015.06.034].

[4] A. Lazanu, T. Giannantonio, M. Schmittfull, and E. P. S. Shellard, *Matter bispectrum of large-scale structure: Three-dimensional comparison between theoretical models and numerical simulations*, *Phys. Rev. D* **93** (Apr., 2016) 083517, [arXiv:1510.04075], [doi:10.1103/PhysRevD.93.083517].

[5] A. Lazanu, T. Giannantonio, M. Schmittfull, and E. P. S. Shellard, *Characterising the matter bispectrum of large-scale structure: halo models, perturbation theory and a three-shape model*, *ArXiv e-prints* (Nov., 2015) [arXiv:1511.02022].

[6] Planck Collaboration, R. Adam, P. A. R. Ade, N. Aghanim, Y. Akrami, M. I. R. Alves, M. Arnaud, F. Arroja, J. Aumont, C. Baccigalupi, and et al., *Planck 2015 results. I. Overview of products and scientific results*, *ArXiv e-prints* (Feb., 2015) [arXiv:1502.01582].

[7] Planck Collaboration, *Planck 2015 results. XIII. Cosmological parameters*, *ArXiv e-prints* (Feb., 2015) [arXiv:1502.01589].

[8] M. Hindmarsh, *Signals of Inflationary Models with Cosmic Strings*, *Progress of Theoretical Physics Supplement* **190** (2011) 197–228, [arXiv:1106.0391], [doi:10.1143/PTPS.190.197].

[9] Planck Collaboration, P. A. R. Ade, N. Aghanim, C. Armitage-Caplan, M. Arnaud, M. Ashdown, F. Atrio-Barandela, J. Aumont, C. Baccigalupi, A. J. Banday, and et al., *Planck 2013 results. XXV. Searches for cosmic strings and other topological defects*, *Astron. Astrophys.* **571** (Nov., 2014) A25, [arXiv:1303.5085], [doi:10.1051/0004-6361/201321621].

[10] D. Lyth and A. Liddle, *The Promordial Density Perturbation: Cosmology, Inflation and the Origin of Structure*. Cambridge University Press, 2009.

[11] G. Lemaître, *The Beginning of the World from the Point of View of Quantum Theory.*, *Nature* **127** (May, 1931) 706, [doi:10.1038/127706b0].

[12] G. Gamow, *Expanding Universe and the Origin of Elements*, *Physical Review* **70** (Oct., 1946) 572–573, [doi:10.1103/PhysRev.70.572.2].

[13] V. Mukhanov, *Physical Foundations of Cosmology*. Cambridge University Press, 2005.

[14] S. Weinberg, *Cosmology*. Oxford University Press, 2008.

[15] G. F. Smoot, C. L. Bennett, A. Kogut, E. L. Wright, *et al.*, *Structure in the COBE differential microwave radiometer first-year maps*, *Astrophys. J. Lett.* **396** (Sept., 1992) L1–L5, [doi:10.1086/186504].

[16] D. N. Spergel, L. Verde, H. V. Peiris, E. Komatsu, *et al.*, *First-Year Wilkinson Microwave Anisotropy Probe (WMAP) Observations: Determination of Cosmological Parameters*, *Astrophys. J. Supp.* **148** (Sept., 2003) 175–194, [astro-ph/0302209], [doi:10.1086/377226].

[17] Planck Collaboration, P. A. R. Ade, N. Aghanim, M. I. R. Alves, C. Armitage-Caplan, M. Arnaud, M. Ashdown, F. Atrio-Barandela, J. Aumont, H. Aussel, and et al., *Planck 2013 results. I. Overview of products and scientific results*, *Astron. Astrophys.* **571** (Nov., 2014) A1, [arXiv:1303.5062], [doi:10.1051/0004-6361/201321529].

[18] Planck Collaboration, P. A. R. Ade, N. Aghanim, C. Armitage-Caplan, M. Arnaud, M. Ashdown, F. Atrio-Barandela, J. Aumont, C. Baccigalupi, A. J. Banday, and et al., *Planck 2013 results. XVI. Cosmological parameters*, *Astron. Astrophys.* **571** (Nov., 2014) A16, [arXiv:1303.5076], [doi:10.1051/0004-6361/201321591].

[19] W. L. Freedman, B. F. Madore, *et al.*, *Final Results from the Hubble Space Telescope Key Project to Measure the Hubble Constant*, *Astrophys. J.* **553** (May, 2001) 47–72, [astro-ph/0012376], [doi:10.1086/320638].

[20] **Supernova Cosmology Project** Collaboration, S. Perlmutter *et al.*, *Measurements of Omega and Lambda from 42 high redshift supernovae*, *Astrophys. J.* **517** (1999) 565–586, [arXiv:astro-ph/9812133], [doi:10.1086/307221].

[21] A. G. Riess, A. V. Filippenko, *et al.*, *Observational Evidence from Supernovae for an Accelerating Universe and a Cosmological Constant*, *Astron. J.* **116** (Sept., 1998) 1009–1038, [astro-ph/9805201], [doi:10.1086/300499].

[22] A. Liddle, *An Introduction to Modern Cosmology*. John Wiley and Sons, 2003.

[23] P. Coles and F. Lucchin, *Cosmology. The origin and evolution of cosmic structure*. John Wiley & Sons, 1995.

[24] A. Friedmann, *Über die Krümmung des Raumes*, *Z. Phys.* **10** (1922) 377–386.

[25] G. Lemaître, *L'univers en expansion*, *Ann. Soc. Sci. Brux.* **53** (1933) 51.

[26] W. de Sitter, *On Einstein's theory of gravitation and its astronomical consequences. Second paper*, *Mon. Not. R. Astron. Soc.* **77** (Dec., 1916) 155–184, [doi:10.1093/mnras/77.2.155].

[27] V. M. Slipher, *Spectrographic Observations of Nebulae*, *Pop. Astron.* **23** (January, 1915) 21 – 24.

[28] K. Lundmark, *The determination of the curvature of space-time in de Sitter's world*, *Mon. Not. R. Astron. Soc.* **84** (June, 1924) 747–770, [doi:10.1093/mnras/84.9.747].

[29] E. Hubble and M. L. Humason, *The Velocity-Distance Relation among Extra-Galactic Nebulae*, *Astrophys. J.* **74** (July, 1931) 43, [doi:10.1086/143323].

[30] U. Seljak and M. Zaldarriaga, *A Line-of-Sight Integration Approach to Cosmic Microwave Background Anisotropies*, *Astrophys. J.* **469** (Oct., 1996) 437, [astro-ph/9603033], [doi:10.1086/177793].

[31] A. Lewis, A. Challinor, and A. Lasenby, *Efficient Computation of Cosmic Microwave Background Anisotropies in Closed Friedmann-Robertson-Walker Models*, *Astrophys. J.* **538** (Aug., 2000) 473–476, [astro-ph/9911177], [doi:10.1086/309179].

[32] A. Lewis, *CAMB code - http://camb.info*, 2013.

[33] J. M. Bardeen, *Gauge-invariant cosmological perturbations*, *Phys. Rev. D* **22** (Oct, 1980) 1882–1905, [doi:10.1103/PhysRevD.22.1882].

[34] A. A. Penzias and R. W. Wilson, *A Measurement of Excess Antenna Temperature at 4080 Mc/s.*, *Astrophys. J.* **142** (July, 1965) 419–421, [doi:10.1086/148307].

[35] R. H. Dicke, P. J. E. Peebles, P. G. Roll, and D. T. Wilkinson, *Cosmic Black-Body Radiation.*, *Astrophys. J.* **142** (July, 1965) 414–419, [doi:10.1086/148306].

[36] S. Dodelson, *Modern Cosmology*. Academic Press, 2003.

[37] A. Challinor, *Anisotropies in the Cosmic Microwave Background*, *ArXiv Astrophysics e-prints* (Mar., 2004) [astro-ph/0403344].

[38] Y. B. Zel'Dovich, I. Y. Kobzarev, and L. B. Okun', *Cosmological consequences of a spontaneous breakdown of a discrete symmetry*, *Soviet Journal of Experimental and Theoretical Physics* **40** (July, 1975) 1.

[39] T. H. R. Skyrme, *A Nonlinear field theory*, *Proc. Roy. Soc. Lond.* **A260** (1961) 127–138, [doi:10.1098/rspa.1961.0018].

[40] A. Vilenkin and E. P. S. Shellard, *Cosmic Strings and Other Topological Defects*. Cambridge University Press, 1994.

[41] D. Kirzhnits and A. Linde, *Macroscopic consequences of the Weinberg model*, *Phys. Lett. B* **42** (1972), no. 4 471 – 474, [doi:10.1016/0370-2693(72)90109-8].

[42] E. J. Weinberg, *Multivortex solutions of the ginzburg-landau equations*, *Phys. Rev. D* **19** (May, 1979) 3008–3012, [doi:10.1103/PhysRevD.19.3008].

[43] I. B. Zeldovich, *Cosmological fluctuations produced near a singularity*, *Mon. Not. R. Astron. Soc.* **192** (Sept., 1980) 663–667.

[44] A. Vilenkin, *Cosmological density fluctuations produced by vacuum strings*, *Phys. Rev. Lett.* **46** (Apr, 1981) 1169–1172, [doi:10.1103/PhysRevLett.46.1169].

[45] E. J. Copeland, R. C. Myers, and J. Polchinski, *Cosmic superstrings II*, *Comptes Rendus Physique* **5** (Nov., 2004) 1021–1029, [doi:10.1016/j.crhy.2004.10.008].

[46] J. Goldstone, *Field Theories with Superconductor Solutions*, *Nuovo Cim.* **19** (1961) 154–164, [doi:10.1007/BF02812722].

[47] T. Vachaspati, *Kinks and domain walls: An introduction to classical and quantum solitons*. Cambridge University Press, 2010.

[48] W. H. Press, B. S. Ryden, and D. N. Spergel, *Dynamical evolution of domain walls in an expanding universe*, *Astrophys. J.* **347** (Dec., 1989) 590–604, [doi:10.1086/168151].

[49] T. W. B. Kibble, *Phase transitions and topological defects in the early Universe.*, *Australian Journal of Physics* **50** (1997) 697–722, [doi:10.1071/P96076].

[50] A. Vilenkin, *Cosmic strings and domain walls*, *Phys. Rep.* **121** (1985) 263–315, [doi:10.1016/0370-1573(85)90033-X].

[51] A. D. Linde and D. H. Lyth, *Axionic domain wall production during inflation*, *Physics Letters B* **246** (Aug., 1990) 353–358, [doi:10.1016/0370-2693(90)90613-B].

[52] M. F. Parry and A. T. Sornborger, *Domain wall production during inflationary reheating*, *Phys. Rev. D* **60** (Nov., 1999) 103504, [hep-ph/9805211], [doi:10.1103/PhysRevD.60.103504].

[53] T. W. B. Kibble, *Topology of cosmic domains and strings*, *Journal of Physics A: Mathematical and General* **9** (1976), no. 8 1387.

[54] T. Vachaspati, L. Pogosian, and D. Steer, *Cosmic strings*, *Scholarpedia* **10** (2015) 31682, [doi:10.4249/scholarpedia.31682].

[55] R. H. Brandenberger, *Cosmic strings and the large-scale structure of the universe*, *Physica Scripta Volume T* **36** (1991) 114–126, [doi:10.1088/0031-8949/1991/T36/013].

[56] C. R. Contaldi, *Cosmic strings in the age of Boomerang*, *ArXiv Astrophysics e-prints* (May, 2000) [astro-ph/0005115].

[57] S. Sarangi and S.-H. H. Tye, *Cosmic string production towards the end of brane inflation*, *Physics Letters B* **536** (June, 2002) 185–192, [hep-th/0204074], [doi:10.1016/S0370-2693(02)01824-5].

[58] M. Majumdar and A.-C. Davis, *Cosmological creation of D-branes and anti-D-branes*, *Journal of High Energy Physics* **3** (Mar., 2002) 056, [hep-th/0202148], [doi:10.1088/1126-6708/2002/03/056].

[59] R. Battye and A. Moss, *Updated constraints on the cosmic string tension*, *Phys. Rev. D* **82** (July, 2010) 023521, [arXiv:1005.0479], [doi:10.1103/PhysRevD.82.023521].

[60] J. Polchinski, *Cosmic Superstrings Revisited*, *Int. J. Mod Phys A* **20** (2005) 3413–3415, [hep-th/0410082], [doi:10.1142/S0217751X05026686].

[61] N. Arkani-Hamed, S. Dimopoulos, and G. Dvali, *The hierarchy problem and new dimensions at a millimeter*, *Physics Letters B* **429** (June, 1998) 263–272, [hep-ph/9803315], [doi:10.1016/S0370-2693(98)00466-3].

[62] L. Randall and R. Sundrum, *An Alternative to Compactification*, *Phys. Rev. Lett.* **83** (Dec., 1999) 4690–4693, [hep-th/9906064], [doi:10.1103/PhysRevLett.83.4690].

[63] R. Jeannerot, J. Rocher, and M. Sakellariadou, *How generic is cosmic string formation in supersymmetric grand unified theories*, *Phys. Rev. D* **68** (Nov., 2003) 103514, [hep-ph/0308134], [doi:10.1103/PhysRevD.68.103514].

[64] J. Lizarraga, J. Urrestilla, D. Daverio, M. Hindmarsh, M. Kunz, and A. R. Liddle, *Can Topological Defects Mimic the BICEP2 B-Mode Signal?*, *Phys. Rev. Lett.* **112** (May, 2014) 171301, [arXiv:1403.4924], [doi:10.1103/PhysRevLett.112.171301].

[65] A. Moss and L. Pogosian, *Did BICEP2 See Vector Modes? First B-Mode Constraints on Cosmic Defects*, *Phys. Rev. Lett.* **112** (May, 2014) 171302, [arXiv:1403.6105], [doi:10.1103/PhysRevLett.112.171302].

[66] *Detection of B-mode polarization at degree angular scales by BICEP2*, *Phys. Rev. Lett.* **112** (June, 2014) 241101, [arXiv:1403.3985], [doi:10.1103/PhysRevLett.112.241101].

[67] C. Ringeval, D. Yamauchi, J. Yokoyama, and F. R. Bouchet, *Large scale CMB anomalies from thawing cosmic strings*, *J. Cosmol. Astropart. Phys.* **2** (Feb., 2016) 033, [arXiv:1510.01916], [doi:10.1088/1475-7516/2016/02/033].

[68] M. G. Jackson, N. T. Jones, and J. Polchinski, *Collisions of cosmic F- and D-strings*, *Journal of High Energy Physics* **10** (Oct., 2005) 013, [hep-th/0405229], [doi:10.1088/1126-6708/2005/10/013].

[69] **Virgo, LIGO Scientific** Collaboration, B. P. Abbott *et al.*, *Observation of Gravitational Waves from a Binary Black Hole Merger*, *Phys. Rev. Lett.* **116** (2016), no. 6 061102, [arXiv:1602.03837], [doi:10.1103/PhysRevLett.116.061102].

[70] M. B. Hindmarsh and T. W. B. Kibble, *Cosmic strings*, *Reports on Progress in Physics* **58** (May, 1995) 477–562, [hep-ph/9411342], [doi:10.1088/0034-4885/58/5/001].

[71] N. Kaiser and A. Stebbins, *Microwave anisotropy due to cosmic strings*, *Nature* **310** (Aug., 1984) 391–393, [doi:10.1038/310391a0].

[72] J. R. Gott III, *Gravitational lensing effects of vacuum strings: Exact solutions*, *Astrophys.J.* **288** (1985) 422–427, [doi:10.1086/162808].

[73] P. A. M. Dirac, *Quantised Singularities in the Electromagnetic Field*, *Proceedings of the Royal Society of London Series A* **133** (Sept., 1931) 60–72, [doi:10.1098/rspa.1931.0130].

[74] G. 't Hooft, *Magnetic Monopoles in Unified Gauge Theories*, *Nucl. Phys.* **B79** (1974) 276–284, [doi:10.1016/0550-3213(74)90486-6].

[75] A. M. Polyakov, *Particle spectrum in quantum field theory*, *Soviet Journal of Experimental and Theoretical Physics Letters* **20** (Sept., 1974) 194.

[76] P. Peter and J.-P. Uzan, *Primordial Cosmology*. Oxford University Press, 2009.

[77] M. Cruz, N. Turok, P. Vielva, E. Martínez-González, and M. Hobson, *A Cosmic Microwave Background Feature Consistent with a Cosmic Texture*, *Science* **318** (Dec., 2007) 1612, [arXiv:0710.5737], [doi:10.1126/science.1148694].

[78] S. M. Feeney, M. C. Johnson, D. J. Mortlock, and H. V. Peiris, *Robust Constraint on Cosmic Textures from the Cosmic Microwave Background*, *Phys. Rev. Lett.* **108** (June, 2012) 241301, [arXiv:1203.1928], [doi:10.1103/PhysRevLett.108.241301].

[79] N. Turok, *Global texture as the origin of cosmic structure*, *Phys. Rev. Lett.* **63** (Dec., 1989) 2625–2628, [doi:10.1103/PhysRevLett.63.2625].

[80] L. Pogosian and T. Vachaspati, *Cosmic microwave background anisotropy from wiggly strings*, *Phys. Rev. D* **60** (Oct., 1999) 083504, [astro-ph/9903361], [doi:10.1103/PhysRevD.60.083504].

[81] N. Bevis, M. Hindmarsh, M. Kunz, and J. Urrestilla, *CMB power spectrum contribution from cosmic strings using field-evolution simulations of the Abelian Higgs model*, *Phys. Rev. D* **75** (Mar., 2007) 065015, [astro-ph/0605018], [doi:10.1103/PhysRevD.75.065015].

[82] A. A. Fraisse, C. Ringeval, D. N. Spergel, and F. R. Bouchet, *Small-angle CMB temperature anisotropies induced by cosmic strings*, *Phys. Rev. D* **78** (Aug., 2008) 043535, [arXiv:0708.1162], [doi:10.1103/PhysRevD.78.043535].

[83] C. Ringeval and F. R. Bouchet, *All sky CMB map from cosmic strings integrated Sachs-Wolfe effect*, *Phys. Rev. D* **86** (July, 2012) 023513, [arXiv:1204.5041], [doi:10.1103/PhysRevD.86.023513].

[84] D. M. Regan and E. P. S. Shellard, *Cosmic string power spectrum, bispectrum, and trispectrum*, *Phys. Rev. D* **82** (Sept., 2010) 063527, [arXiv:0911.2491], [doi:10.1103/PhysRevD.82.063527].

[85] S. A. Sanidas, R. A. Battye, and B. W. Stappers, *Constraints on cosmic string tension imposed by the limit on the stochastic gravitational wave background from the European Pulsar Timing Array*, *Phys. Rev. D* **85** (June, 2012) 122003, [arXiv:1201.2419], [doi:10.1103/PhysRevD.85.122003].

[86] J. J. Blanco-Pillado, K. D. Olum, and B. Shlaer, *Number of cosmic string loops*, *Phys. Rev. D* **89** (Jan., 2014) 023512, [arXiv:1309.6637], [doi:10.1103/PhysRevD.89.023512].

[87] A. A. Abrikosov, *Theoretical Prediction of Vortices in Type-II Superconductors*, *Soviet Physics JETP* **53** (1957) 1174–1182.

[88] H. B. Nielsen and P. Olesen, *Vortex-line models for dual strings*, Nuclear Physics B **61** (1973), no. 0 45–61, [doi:10.1016/0550-3213(73)90350-7].

[89] K. Maeda and N. Turok, *Finite-width corrections to the Nambu action for the Nielsen-Olesen string*, Physics Letters B **202** (1988), no. 3 376–380, [doi:10.1016/0370-2693(88)90488-1].

[90] T. Vachaspati and A. Vilenkin, *Formation and evolution of cosmic strings*, *Phys. Rev. D* **30** (Nov, 1984) 2036–2045, [doi:10.1103/PhysRevD.30.2036].

[91] D. P. Bennett and F. R. Bouchet, *High-resolution simulations of cosmic-string evolution. i. Network evolution*, *Phys. Rev. D* **41** (Apr, 1990) 2408–2433, [doi:10.1103/PhysRevD.41.2408].

[92] C. J. A. P. Martins and E. P. S. Shellard, *Scale-invariant string evolution with friction*, *Phys. Rev. D* **53** (Jan., 1996) R575–R579, [hep-ph/9507335], [doi:10.1103/PhysRevD.53.R575].

[93] C. J. A. P. Martins and E. P. S. Shellard, *Quantitative string evolution*, *Phys. Rev. D* **54** (Aug., 1996) 2535–2556, [hep-ph/9602271], [doi:10.1103/PhysRevD.54.2535].

[94] C. J. A. P. Martins and E. P. S. Shellard, *Extending the velocity-dependent one-scale string evolution model*, *Phys. Rev. D* **65** (Feb., 2002) 043514, [hep-ph/0003298], [doi:10.1103/PhysRevD.65.043514].

[95] A. Albrecht, R. A. Battye, and J. Robinson, *Detailed study of defect models for cosmic structure formation*, *Phys. Rev. D* **59** (Jan., 1999) 023508, [astro-ph/9711121], [doi:10.1103/PhysRevD.59.023508].

[96] R. A. Battye, J. Robinson, and A. Albrecht, *Structure Formation by Cosmic Strings with a Cosmological Constant*, *Phys. Rev. Lett.* **80** (June, 1998) 4847–4850, [astro-ph/9711336], [doi:10.1103/PhysRevLett.80.4847].

[97] A. Avgoustidis, E. J. Copeland, A. Moss, and D. Skliros, *Fast analytic computation of cosmic string power spectra*, *Phys. Rev. D* **86** (Dec., 2012) 123513, [arXiv:1209.2461], [doi:10.1103/PhysRevD.86.123513].

[98] B. Carter, *Integrable equation of state for noisy cosmic string*, *Phys. Rev. D* **41** (June, 1990) 3869–3872, [doi:10.1103/PhysRevD.41.3869].

[99] L. Pogosian, *CMBACT code - http://www.sfu.ca/~levon/cmbact.html*, 2009-2014.

[100] B. Allen and E. P. S. Shellard, *Cosmic-string evolution - A numerical simulation*, *Phys. Rev. Lett.* **64** (Jan., 1990) 119–122, [doi:10.1103/PhysRevLett.64.119].

[101] C. J. A. P. Martins and E. P. S. Shellard, *Fractal properties and small-scale structure of cosmic string networks*, *Phys. Rev. D* **73** (Feb., 2006) 043515, [astro-ph/0511792], [doi:10.1103/PhysRevD.73.043515].

[102] M. Landriau and E. P. S. Shellard, *Cosmic string induced CMB maps*, *Phys. Rev. D* **83** (Feb., 2011) 043516, [arXiv:1004.2885], [doi:10.1103/PhysRevD.83.043516].

[103] B. Allen, R. R. Caldwell, E. P. S. Shellard, A. Stebbins, and S. Veeraraghavan, *Large Angular Scale Anisotropy in Cosmic Microwave Background Induced by Cosmic Strings*, *Phys. Rev. Lett.* **77** (Oct., 1996) 3061–3065, [astro-ph/9609038], [doi:10.1103/PhysRevLett.77.3061].

[104] J.-H. P. Wu, P. P. Avelino, E. P. S. Shellard, and B. Allen, *Cosmic Strings, Loops, and Linear Growth of Matter Perturbations*, International Journal of Modern Physics D **11** (2002) 61–102, [astro-ph/9812156], [doi:10.1142/S0218271802001299].

[105] V. Vanchurin, K. D. Olum, and A. Vilenkin, *Scaling of cosmic string loops*, *Phys. Rev. D* **74** (Sept., 2006) 063527, [gr-qc/0511159], [doi:10.1103/PhysRevD.74.063527].

[106] K. D. Olum and V. Vanchurin, *Cosmic string loops in the expanding universe*, *Phys. Rev. D* **75** (Mar., 2007) 063521, [astro-ph/0610419], [doi:10.1103/PhysRevD.75.063521].

[107] M. Landriau and E. P. Shellard, *Fluctuations in the cosmic microwave background induced by cosmic strings: Methods and formalism*, *Phys. Rev. D* **67** (May, 2003) 103512, [astro-ph/0208540], [doi:10.1103/PhysRevD.67.103512].

[108] N. Turok, *Causality and the Doppler peaks*, *Phys. Rev. D* **54** (Sept., 1996) R3686–R3689, [astro-ph/9604172], [doi:10.1103/PhysRevD.54.R3686].

[109] U.-L. Pen, D. N. Spergel, and N. Turok, *Cosmic structure formation and microwave anisotropies from global field ordering*, *Phys. Rev. D* **49** (Jan., 1994) 692–729, [doi:10.1103/PhysRevD.49.692].

[110] R. Durrer, M. Kunz, and A. Melchiorri, *Cosmic structure formation with topological defects*, *Phys. Rep.* **364** (June, 2002) 1–81, [astro-ph/0110348], [doi:10.1016/S0370-1573(02)00014-5].

[111] C. Contaldi, M. Hindmarsh, and J. Magueijo, *Power Spectra of the Cosmic Microwave Background and Density Fluctuations Seeded by Local Cosmic Strings*, *Phys. Rev. Lett.* **82** (Jan., 1999) 679–682, [astro-ph/9808201], [doi:10.1103/PhysRevLett.82.679].

[112] U.-L. Pen, U. Seljak, and N. Turok, *Power spectra in global defect theories of cosmic structure formation*, *Phys. Rev. Lett.* **79** (Sept., 1997) 1611, [astro-ph/9704165], [doi:10.1103/PhysRevLett.79.1611].

[113] N. Bevis, M. Hindmarsh, M. Kunz, and J. Urrestilla, *CMB power spectra from cosmic strings: Predictions for the Planck satellite and beyond*, *Phys. Rev. D* **82** (Sept., 2010) 065004, [arXiv:1005.2663], [doi:10.1103/PhysRevD.82.065004].

[114] A. Lewis, *COSMOMC code - http://cosmologist.info/cosmomc*, 2013.

[115] A. Lewis and S. Bridle, *Cosmological parameters from CMB and other data: A Monte Carlo approach*, *Phys. Rev. D* **66** (Nov., 2002) 103511, [astro-ph/0205436], [doi:10.1103/PhysRevD.66.103511].

[116] M. Wyman, L. Pogosian, and I. Wasserman, *Bounds on cosmic strings from WMAP and SDSS*, *Phys. Rev. D* **72** (July, 2005) 023513, [astro-ph/0503364], [doi:10.1103/PhysRevD.72.023513].

[117] M. Landriau and E. P. Shellard, *Large angle cosmic microwave background fluctuations from cosmic strings with a cosmological constant*, *Phys. Rev. D* **69** (Jan., 2004) 023003, [astro-ph/0302166], [doi:10.1103/PhysRevD.69.023003].

[118] N. Bevis, M. Hindmarsh, and M. Kunz, *WMAP constraints on inflationary models with global defects*, *Phys. Rev. D* **70** (Aug., 2004) 043508, [astro-ph/0403029], [doi:10.1103/PhysRevD.70.043508].

[119] R. A. Battye, B. Garbrecht, and A. Moss, *Constraints on supersymmetric hybrid inflation models*, *J. Cosmol. Astropart. Phys.* **9** (Sept., 2006) 007, [astro-ph/0607339], [doi:10.1088/1475-7516/2006/09/007].

[120] J. Urrestilla, N. Bevis, M. Hindmarsh, and M. Kunz, *Cosmic string parameter constraints and model analysis using small scale Cosmic Microwave Background data*, *J. Cosmol. Astropart. Phys.* **12** (Dec., 2011) 021, [arXiv:1108.2730], [doi:10.1088/1475-7516/2011/12/021].

[121] B. Freivogel, M. Kleban, M. Rodriguez Martinez, and L. Susskind, *Observational Consequences of a Landscape: Epilogue*, *ArXiv e-prints* (Apr., 2014) [arXiv:1404.2274].

[122] J. L. Rosner, *Three sterile neutrinos in E_6*, *Phys. Rev. D* **90** (Aug., 2014) 035005, [arXiv:1404.5198], [doi:10.1103/PhysRevD.90.035005].

[123] J. Lizarraga, J. Urrestilla, D. Daverio, M. Hindmarsh, M. Kunz, and A. R. Liddle, *Constraining topological defects with temperature and polarization anisotropies*, *Phys. Rev. D* **90** (Nov., 2014) 103504, [arXiv:1408.4126], [doi:10.1103/PhysRevD.90.103504].

[124] N. Bevis, M. Hindmarsh, M. Kunz, and J. Urrestilla, *CMB polarization power spectra contributions from a network of cosmic strings*, *Phys. Rev. D* **76** (Aug., 2007) 043005, [arXiv:0704.3800], [doi:10.1103/PhysRevD.76.043005].

[125] M. Sakellariadou, *How well do we understand the thermal history of the Universe? Implications of the recent BICEP2 data*, *Phys. Rev.* **D90** (2014), no. 8 087301, [arXiv:1403.6688], [doi:10.1103/PhysRevD.90.087301].

[126] BICEP2/Keck and Planck Collaborations, P. A. R. Ade, N. Aghanim, Z. Ahmed, R. W. Aikin, K. D. Alexander, M. Arnaud, J. Aumont, C. Baccigalupi, A. J. Banday, and et al., *Joint Analysis of BICEP2/Keck Array and Planck Data*, *Phys. Rev. Lett.* **114** (Mar., 2015) 101301, [arXiv:1502.00612], [doi:10.1103/PhysRevLett.114.101301].

[127] J. Lesgourgues and S. Pastor, *Neutrino mass from Cosmology*, *Adv. High Energy Phys.* **2012** (2012) 608515, [arXiv:1212.6154], [doi:10.1155/2012/608515].

[128] J. Lizarraga, I. Sendra, and J. Urrestilla, *Correlations between cosmic strings and extra relativistic species*, *Phys. Rev. D* **86** (Dec., 2012) 123014, [arXiv:1207.6266], [doi:10.1103/PhysRevD.86.123014].

[129] M. Hindmarsh, C. Ringeval, and T. Suyama, *CMB temperature bispectrum induced by cosmic strings*, *Phys. Rev. D* **80** (Oct., 2009) 083501, [arXiv:0908.0432], [doi:10.1103/PhysRevD.80.083501].

[130] M. Hindmarsh, C. Ringeval, and T. Suyama, *CMB temperature trispectrum of cosmic strings*, *Phys. Rev. D* **81** (Mar., 2010) 063505, [arXiv:0911.1241], [doi:10.1103/PhysRevD.81.063505].

[131] R. Khatri and B. D. Wandelt, *Cosmic (Super)String Constraints from 21cm Radiation*, *Phys. Rev. Lett.* **100** (Mar., 2008) 091302, [arXiv:0801.4406], [doi:10.1103/PhysRevLett.100.091302].

[132] F. A. Jenet, G. B. Hobbs, W. van Straten, R. N. Manchester, *et al.*, *Upper Bounds on the Low-Frequency Stochastic Gravitational Wave Background from Pulsar Timing Observations: Current Limits and Future Prospects*, *Astrophys. J.* **653** (Dec., 2006) 1571–1576, [astro-ph/0609013], [doi:10.1086/508702].

[133] K. J. Mack, D. H. Wesley, and L. J. King, *Observing cosmic string loops with gravitational lensing surveys*, *Phys. Rev. D* **76** (Dec., 2007) 123515, [astro-ph/0702648], [doi:10.1103/PhysRevD.76.123515].

[134] L. Sousa and P. P. Avelino, *Evolution of domain wall networks: The Press-Ryden-Spergel algorithm*, *Phys. Rev. D* **81** (Apr., 2010) 087305, [arXiv:1101.3350], [doi:10.1103/PhysRevD.81.087305].

[135] A. M. M. Leite and C. J. A. P. Martins, *Scaling properties of domain wall networks*, *Phys. Rev. D* **84** (Nov., 2011) 103523, [arXiv:1110.3486], [doi:10.1103/PhysRevD.84.103523].

[136] J. C. Oliveira, C. J. Martins, and P. P. Avelino, *Cosmological evolution of domain wall networks*, *Phys. Rev. D* **71** (Apr., 2005) 083509, [hep-ph/0410356], [doi:10.1103/PhysRevD.71.083509].

[137] A. M. M. Leite, C. J. A. P. Martins, and E. P. S. Shellard, *Accurate calibration of the velocity-dependent one-scale model for domain walls*, *Physics Letters B* **718** (Jan., 2013) 740–744, [arXiv:1206.6043], [doi:10.1016/j.physletb.2012.11.070].

[138] A. H. Guth, *Inflationary universe: A possible solution to the horizon and flatness problems*, *Phys. Rev. D* **23** (Jan., 1981) 347–356, [doi:10.1103/PhysRevD.23.347].

[139] V. F. Mukhanov and G. V. Chibisov, *Quantum fluctuations and a nonsingular universe*, *Soviet Journal of Experimental and Theoretical Physics Letters* **33** (May, 1981) 532.

[140] S. W. Hawking, *The development of irregularities in a single bubble inflationary universe*, *Physics Letters B* **115** (Sept., 1982) 295–297, [doi:10.1016/0370-2693(82)90373-2].

[141] S. Kachru, R. Kallosh, A. Linde, J. Maldacena, L. McAllister, and S. P. Trivedi, *Towards inflation in string theory*, *J. Cosmol. Astropart. Phys.* **10** (Oct., 2003) 013, [hep-th/0308055], [doi:10.1088/1475-7516/2003/10/013].

[142] N. Turok, *A critical review of inflation*, *Classical and Quantum Gravity* **19** (July, 2002) 3449–3467, [doi:10.1088/0264-9381/19/13/305].

[143] D. Baumann and L. McAllister, *Inflation and String Theory*. Cambridge University Press, 2015.

[144] J. Martin, C. Ringeval, and V. Vennin, *Encyclopædia Inflationaris*, *Physics of the Dark Universe* **5** (Dec., 2014) 75–235, [arXiv:1303.3787], [doi:10.1016/j.dark.2014.01.003].

[145] Planck Collaboration, P. A. R. Ade, N. Aghanim, M. Arnaud, F. Arroja, M. Ashdown, J. Aumont, C. Baccigalupi, M. Ballardini, A. J. Banday, and et al., *Planck 2015 results. XX. Constraints on inflation*, *ArXiv e-prints* (Feb., 2015) [arXiv:1502.02114].

[146] X. Chen, *Primordial Non-Gaussianities from Inflation Models*, *Advances in Astronomy* **2010** (2010) 72, [arXiv:1002.1416], [doi:10.1155/2010/638979].

[147] Planck Collaboration, P. A. R. Ade, N. Aghanim, M. Arnaud, F. Arroja, M. Ashdown, J. Aumont, C. Baccigalupi, M. Ballardini, A. J. Banday, and et al., *Planck 2015 results. XVII. Constraints on primordial non-Gaussianity*, *ArXiv e-prints* (Feb., 2015) [arXiv:1502.01592].

[148] J. J. M. Carrasco, M. P. Hertzberg, and L. Senatore, *The effective field theory of cosmological large scale structures*, *Journal of High Energy Physics* **9** (Sept., 2012) 82, [arXiv:1206.2926], [doi:10.1007/JHEP09(2012)082].

[149] M. Alvarez *et al.*, *Testing Inflation with Large Scale Structure: Connecting Hopes with Reality*, *ArXiv e-prints* (Dec., 2014) [arXiv:1412.4671].

[150] D. G. York *et al.*, *The Sloan Digital Sky Survey: Technical Summary*, *Astron. J.* **120** (Sept., 2000) 1579–1587, [astro-ph/0006396], [doi:10.1086/301513].

[151] D. J. Eisenstein *et al.*, *SDSS-III: Massive Spectroscopic Surveys of the Distant Universe, the Milky Way, and Extra-Solar Planetary Systems*, *Astron. J.* **142** (Sept., 2011) 72, [arXiv:1101.1529], [doi:10.1088/0004-6256/142/3/72].

[152] K. S. Dawson, D. J. Schlegel, *et al.*, *The baryon oscillation spectroscopic survey of SDSS-iii*, *Astron. J.* **145** (Jan., 2013) 10, [arXiv:1208.0022], [doi:10.1088/0004-6256/145/1/10].

[153] The Dark Energy Survey Collaboration, *The Dark Energy Survey*, *ArXiv Astrophysics e-prints* (Oct., 2005) [astro-ph/0510346].

[154] **DES** Collaboration, H. T. Diehl *et al.*, *The Dark Energy Survey and Operations: Year 1*, *Proc. SPIE Int. Soc. Opt. Eng.* **9149** (2014) 91490V, [doi:10.1117/12.2056982].

[155] Z. Ivezic, J. A. Tyson, B. Abel, *et al.*, *LSST: from science drivers to reference design and anticipated data products*, *ArXiv e-prints* (May, 2008) [arXiv:0805.2366].

[156] R. Laureijs, J. Amiaux, S. Arduini, *et al.*, *Euclid Definition Study Report*, *ArXiv e-prints* (Oct., 2011) [arXiv:1110.3193].

[157] B. Flaugher and C. Bebek, *The Dark Energy Spectroscopic Instrument (DESI)*, in *Society of Photo-Optical Instrumentation Engineers (SPIE) Conference Series*, vol. 9147 of *Society of Photo-Optical Instrumentation Engineers (SPIE) Conference Series*, July, 2014.

[158] D. Spergel, N. Gehrels, C. Baltay, *et al.*, *Wide-Field InfrarRed Survey Telescope-Astrophysics Focused Telescope Assets WFIRST-AFTA 2015 Report*, *ArXiv e-prints* (Mar., 2015) [arXiv:1503.03757].

[159] O. Doré *et al.*, *Cosmology with the SPHEREX All-Sky Spectral Survey*, *ArXiv e-prints* (Dec., 2014) [arXiv:1412.4872].

[160] N. Dalal, O. Doré, D. Huterer, and A. Shirokov, *Imprints of primordial non-Gaussianities on large-scale structure: Scale-dependent bias and abundance of virialized objects*, *Phys. Rev. D* **77** (June, 2008) 123514, [arXiv:0710.4560], [doi:10.1103/PhysRevD.77.123514].

[161] S. Matarrese and L. Verde, *The Effect of Primordial Non-Gaussianity on Halo Bias*, *Astrophys. J. Lett.* **677** (Apr., 2008) L77–L80, [arXiv:0801.4826], [doi:10.1086/587840].

[162] A. Slosar, C. Hirata, U. Seljak, S. Ho, and N. Padmanabhan, *Constraints on local primordial non-Gaussianity from large scale structure*, *J. Cosmol. Astropart. Phys.* **8** (Aug., 2008) 31, [arXiv:0805.3580], [doi:10.1088/1475-7516/2008/08/031].

[163] J.-Q. Xia, A. Bonaldi, C. Baccigalupi, G. De Zotti, S. Matarrese, L. Verde, and M. Viel, *Constraining primordial non-Gaussianity with high-redshift probes*, *J. Cosmol. Astropart. Phys.* **8** (Aug., 2010) 13, [arXiv:1007.1969], [doi:10.1088/1475-7516/2010/08/013].

[164] A. Mana, T. Giannantonio, J. Weller, B. Hoyle, G. Hütsi, and B. Sartoris, *Combining clustering and abundances of galaxy clusters to test cosmology and primordial non-Gaussianity*, *Mon. Not. R. Astron. Soc.* **434** (Sept., 2013) 684–695, [arXiv:1303.0287], [doi:10.1093/mnras/stt1062].

[165] A. J. Ross *et al.*, *The clustering of galaxies in the SDSS-III DR9 Baryon Oscillation Spectroscopic Survey: constraints on primordial non-Gaussianity*, *Mon. Not. R. Astron. Soc.* **428** (Jan., 2013) 1116–1127, [arXiv:1208.1491], [doi:10.1093/mnras/sts094].

[166] T. Giannantonio, A. J. Ross, W. J. Percival, R. Crittenden, D. Bacher, M. Kilbinger, R. Nichol, and J. Weller, *Improved primordial non-Gaussianity constraints from measurements of galaxy clustering and the integrated Sachs-Wolfe effect*, *Phys. Rev. D* **89** (Jan., 2014) 023511, [arXiv:1303.1349], [doi:10.1103/PhysRevD.89.023511].

[167] T. Giannantonio and W. J. Percival, *Using correlations between cosmic microwave background lensing and large-scale structure to measure primordial non-Gaussianity*, *Mon. Not. R. Astron. Soc.* **441** (June, 2014) L16–L20, [arXiv:1312.5154], [doi:10.1093/mnrasl/slu036].

[168] L. Verde, L. Wang, A. F. Heavens, and M. Kamionkowski, *Large-scale structure, the cosmic microwave background and primordial non-Gaussianity*, *Mon. Not. R. Astron. Soc.* **313** (Mar., 2000) 141–147, [astro-ph/9906301], [doi:10.1046/j.1365-8711.2000.03191.x].

[169] R. Scoccimarro, E. Sefusatti, and M. Zaldarriaga, *Probing primordial non-Gaussianity with large-scale structure*, *Phys. Rev. D* **69** (May, 2004) 103513, [astro-ph/0312286], [doi:10.1103/PhysRevD.69.103513].

[170] N. Bartolo, S. Matarrese, and A. Riotto, *Signatures of primordial non-Gaussianity in the large-scale structure of the universe*, *J. Cosmol. Astropart. Phys.* **10** (Oct., 2005) 10, [astro-ph/0501614], [doi:10.1088/1475-7516/2005/10/010].

[171] D. Jeong and E. Komatsu, *Primordial Non-Gaussianity, Scale-dependent Bias, and the Bispectrum of Galaxies*, *Astrophys. J.* **703** (Oct., 2009) 1230–1248, [arXiv:0904.0497], [doi:10.1088/0004-637X/703/2/1230].

[172] T. Nishimichi, A. Taruya, K. Koyama, and C. Sabiu, *Scale dependence of halo bispectrum from non-Gaussian initial conditions in cosmological N-body simulations*, *J. Cosmol. Astropart. Phys.* **7** (July, 2010) 2, [arXiv:0911.4768], [doi:10.1088/1475-7516/2010/07/002].

[173] M. Liguori, E. Sefusatti, J. R. Fergusson, and E. P. S. Shellard, *Primordial Non-Gaussianity and Bispectrum Measurements in the Cosmic Microwave Background and Large-Scale Structure*, *Advances in Astronomy* **2010** (2010) 73, [arXiv:1001.4707], [doi:10.1155/2010/980523].

[174] T. Baldauf, U. Seljak, and L. Senatore, *Primordial non-Gaussianity in the bispectrum of the halo density field*, *J. Cosmol. Astropart. Phys.* **4** (Apr., 2011) 6, [arXiv:1011.1513], [doi:10.1088/1475-7516/2011/04/006].

[175] J. N. Fry, *Gravity, bias, and the galaxy three-point correlation function*, *Phys. Rev. Lett.* **73** (July, 1994) 215–219, [doi:10.1103/PhysRevLett.73.215].

[176] E. Sefusatti, M. Crocce, S. Pueblas, and R. Scoccimarro, *Cosmology and the bispectrum*, *Phys. Rev. D* **74** (July, 2006) 023522, [astro-ph/0604505], [doi:10.1103/PhysRevD.74.023522].

[177] S. Matarrese, L. Verde, and A. F. Heavens, *Large-scale bias in the Universe: bispectrum method*, *Mon. Not. R. Astron. Soc.* **290** (Oct., 1997) 651–662, [astro-ph/9706059], [doi:10.1093/mnras/290.4.651].

[178] R. Scoccimarro, S. Colombi, J. N. Fry, J. A. Frieman, E. Hivon, and A. Melott, *Nonlinear Evolution of the Bispectrum of Cosmological Perturbations*, *Astrophys. J.* **496** (Mar., 1998) 586–604, [astro-ph/9704075], [doi:10.1086/305399].

[179] A. Shirata, Y. Suto, C. Hikage, T. Shiromizu, and N. Yoshida, *Galaxy clustering constraints on deviations from Newtonian gravity at cosmological scales. II. Perturbative and numerical analyses of power spectrum and bispectrum*, *Phys. Rev. D* **76** (Aug., 2007) 044026, [arXiv:0705.1311], [doi:10.1103/PhysRevD.76.044026].

[180] L. Verde, A. F. Heavens, S. Matarrese, and L. Moscardini, *Large-scale bias in the Universe - II. Redshift-space bispectrum*, *Mon. Not. R. Astron. Soc.* **300** (Nov., 1998) 747–756, [astro-ph/9806028], [doi:10.1046/j.1365-8711.1998.01937.x].

[181] R. Scoccimarro, H. M. P. Couchman, and J. A. Frieman, *The Bispectrum as a Signature of Gravitational Instability in Redshift Space*, *Astrophys. J.* **517** (June, 1999) 531–540, [astro-ph/9808305], [doi:10.1086/307220].

[182] E. Sefusatti and E. Komatsu, *Bispectrum of galaxies from high-redshift galaxy surveys: Primordial non-Gaussianity and nonlinear galaxy bias*, *Phys. Rev. D* **76** (Oct., 2007) 083004, [arXiv:0705.0343], [doi:10.1103/PhysRevD.76.083004].

[183] H. Guo and Y. P. Jing, *Determine the Galaxy Bias Factors on Large Scales Using the Bispectrum Method*, *Astrophys. J.* **702** (Sept., 2009) 425–432, [arXiv:0907.0282], [doi:10.1088/0004-637X/702/1/425].

[184] J. E. Pollack, R. E. Smith, and C. Porciani, *Modelling large-scale halo bias using the bispectrum*, *Mon. Not. R. Astron. Soc.* **420** (Mar., 2012) 3469–3489, [arXiv:1109.3458], [doi:10.1111/j.1365-2966.2011.20279.x].

[185] S. Saito, T. Baldauf, Z. Vlah, U. Seljak, T. Okumura, and P. McDonald, *Understanding higher-order nonlocal halo bias at large scales by combining the power spectrum with the bispectrum*, *Phys. Rev. D* **90** (Dec., 2014) 123522, [arXiv:1405.1447], [doi:10.1103/PhysRevD.90.123522].

[186] J. N. Fry, *The Galaxy correlation hierarchy in perturbation theory*, *Astrophys. J.* **279** (Apr., 1984) 499–510, [doi:10.1086/161913].

[187] M. H. Goroff, B. Grinstein, S.-J. Rey, and M. B. Wise, *Coupling of modes of cosmological mass density fluctuations*, *Astrophys. J.* **311** (Dec., 1986) 6–14, [doi:10.1086/164749].

[188] B. Jain and E. Bertschinger, *Second-order power spectrum and nonlinear evolution at high redshift*, *Astrophys. J.* **431** (Aug., 1994) 495–505, [astro-ph/9311070], [doi:10.1086/174502].

[189] F. Bernardeau, S. Colombi, E. Gaztañaga, and R. Scoccimarro, *Large-scale structure of the Universe and cosmological perturbation theory*, *Phys. Rep.* **367** (Sept., 2002) 1–248, [astro-ph/0112551], [doi:10.1016/S0370-1573(02)00135-7].

[190] T. Buchert, *A class of solutions in Newtonian cosmology and the pancake theory*, *Astron. Astrophys.* **223** (Oct., 1989) 9–24.

[191] F. Moutarde, J.-M. Alimi, F. R. Bouchet, R. Pellat, and A. Ramani, *Precollapse scale invariance in gravitational instability*, *Astrophys. J.* **382** (Dec., 1991) 377–381, [doi:10.1086/170728].

[192] T. Buchert, *Lagrangian theory of gravitational instability of Friedman-Lemaitre cosmologies and the 'Zel'dovich approximation'*, *Mon. Not. R. Astron. Soc.* **254** (Feb., 1992) 729–737, [doi:10.1093/mnras/254.4.729].

[193] T. Buchert, *Lagrangian Theory of Gravitational Instability of Friedman-Lemaitre Cosmologies - a Generic Third-Order Model for Nonlinear Clustering*, *Mon. Not. R. Astron. Soc.* **267** (Apr., 1994) 811, [astro-ph/9309055].

[194] F. R. Bouchet, S. Colombi, E. Hivon, and R. Juszkiewicz, *Perturbative Lagrangian approach to gravitational instability.*, *Astron. Astrophys.* **296** (Apr., 1995) 575, [astro-ph/9406013].

[195] J. Ehlers and T. Buchert, *Newtonian Cosmology in Lagrangian Formulation: Foundations and Perturbation Theory*, *General Relativity and Gravitation* **29** (June, 1997) 733–764, [astro-ph/9609036], [doi:10.1023/A:1018885922682].

[196] T. Tatekawa, *Lagrangian perturbation theory in Newtonian cosmology*, *Recent Res. Devel. Phys.* **2** (2005) 1–26, [arXiv:astro-ph/0412025].

[197] M. White, *The Zel'dovich approximation*, *Mon. Not. R. Astron. Soc.* **439** (Apr., 2014) 3630–3640, [arXiv:1401.5466], [doi:10.1093/mnras/stu209].

[198] J. Carlson, M. White, and N. Padmanabhan, *Critical look at cosmological perturbation theory techniques*, *Phys. Rev. D* **80** (Aug., 2009) 043531, [arXiv:0905.0479], [doi:10.1103/PhysRevD.80.043531].

[199] P. Valageas, *Accuracy of analytical models of the large-scale matter distribution*, *Phys. Rev. D* **88** (Oct., 2013) 083524, [arXiv:1308.6755], [doi:10.1103/PhysRevD.88.083524].

[200] S. Tassev, *Lagrangian or Eulerian; real or Fourier? Not all approaches to large-scale structure are created equal*, *J. Cosmol. Astropart. Phys.* **6** (June, 2014) 8, [arXiv:1311.4884], [doi:10.1088/1475-7516/2014/06/008].

[201] Z. Vlah, U. Seljak, and T. Baldauf, *Lagrangian perturbation theory at one loop order: Successes, failures, and improvements*, *Phys. Rev. D* **91** (Jan., 2015) 023508, [arXiv:1410.1617], [doi:10.1103/PhysRevD.91.023508].

[202] R. Scoccimarro, *A new angle on gravitational clustering*, *Annals of the New York Academy of Sciences* **927** (2001), no. 1 13–23, [astro-ph/0008277], [doi:10.1111/j.1749-6632.2001.tb05618.x].

[203] M. Crocce and R. Scoccimarro, *Renormalized cosmological perturbation theory*, *Phys. Rev. D* **73** (Mar., 2006) 063519, [astro-ph/0509418], [doi:10.1103/PhysRevD.73.063519].

[204] M. Crocce and R. Scoccimarro, *Memory of initial conditions in gravitational clustering*, *Phys. Rev. D* **73** (Mar., 2006) 063520, [astro-ph/0509419], [doi:10.1103/PhysRevD.73.063520].

[205] M. Crocce and R. Scoccimarro, *Nonlinear evolution of baryon acoustic oscillations*, *Phys. Rev. D* **77** (Jan., 2008) 023533, [arXiv:0704.2783], [doi:10.1103/PhysRevD.77.023533].

[206] F. Bernardeau, M. Crocce, and R. Scoccimarro, *Multipoint propagators in cosmological gravitational instability*, *Phys. Rev. D* **78** (Nov., 2008) 103521, [arXiv:0806.2334], [doi:10.1103/PhysRevD.78.103521].

[207] F. Bernardeau, M. Crocce, and R. Scoccimarro, *Constructing regularized cosmic propagators*, *Phys. Rev. D* **85** (June, 2012) 123519, [arXiv:1112.3895], [doi:10.1103/PhysRevD.85.123519].

[208] M. Crocce, R. Scoccimarro, and F. Bernardeau, *MPTBREEZE: a fast renormalized perturbative scheme*, *Mon. Not. R. Astron. Soc.* **427** (Dec., 2012) 2537–2551, [arXiv:1207.1465], [doi:10.1111/j.1365-2966.2012.22127.x].

[209] P. Valageas, *Large-N expansions applied to gravitational clustering*, *Astron. Astrophys.* **465** (Apr., 2007) 725–747, [astro-ph/0611849], [doi:10.1051/0004-6361:20066832].

[210] A. Taruya and T. Hiramatsu, *A Closure Theory for Nonlinear Evolution of Cosmological Power Spectra*, *Astrophys. J.* **674** (Feb., 2008) 617–635, [arXiv:0708.1367], [doi:10.1086/526515].

[211] P. McDonald, *Dark matter clustering: A simple renormalization group approach*, *Phys. Rev. D* **75** (Feb., 2007) 043514, [astro-ph/0606028], [doi:10.1103/PhysRevD.75.043514].

[212] S. Matarrese and M. Pietroni, *Resumming cosmic perturbations*, *J. Cosmol. Astropart. Phys.* **6** (June, 2007) 26, [astro-ph/0703563], [doi:10.1088/1475-7516/2007/06/026].

[213] T. Matsubara, *Resumming cosmological perturbations via the Lagrangian picture: One-loop results in real space and in redshift space*, *Phys. Rev. D* **77** (Mar., 2008) 063530, [arXiv:0711.2521], [doi:10.1103/PhysRevD.77.063530].

[214] T. Okamura, A. Taruya, and T. Matsubara, *Next-to-leading resummation of cosmological perturbations via the Lagrangian picture: 2-loop correction in real and redshift spaces*, *J. Cosmol. Astropart. Phys.* **8** (Aug., 2011) 12, [arXiv:1105.1491], [doi:10.1088/1475-7516/2011/08/012].

[215] J. Carlson, B. Reid, and M. White, *Convolution Lagrangian perturbation theory for biased tracers*, *Mon. Not. R. Astron. Soc.* **429** (Feb., 2013) 1674–1685, [arXiv:1209.0780], [doi:10.1093/mnras/sts457].

[216] C. Rampf and T. Buchert, *Lagrangian perturbations and the matter bispectrum I: fourth-order model for non-linear clustering*, *J. Cosmol. Astropart. Phys.* **6** (June, 2012) 21, [arXiv:1203.4260], [doi:10.1088/1475-7516/2012/06/021].

[217] C. Rampf and Y. Y. Y. Wong, *Lagrangian perturbations and the matter bispectrum II: the resummed one-loop correction to the matter bispectrum*, *J. Cosmol. Astropart. Phys.* **6** (June, 2012) 18, [arXiv:1203.4261], [doi:10.1088/1475-7516/2012/06/018].

[218] P. Valageas, T. Nishimichi, and A. Taruya, *Matter power spectrum from a Lagrangian-space regularization of perturbation theory*, *Phys. Rev. D* **87** (Apr., 2013) 083522, [arXiv:1302.4533], [doi:10.1103/PhysRevD.87.083522].

[219] T. Matsubara, *Integrated perturbation theory and one-loop power spectra of biased tracers*, *Phys. Rev. D* **90** (Aug., 2014) 043537, [arXiv:1304.4226], [doi:10.1103/PhysRevD.90.043537].

[220] N. S. Sugiyama, *Using Lagrangian Perturbation Theory for Precision Cosmology*, *Astrophys. J.* **788** (June, 2014) 63, [arXiv:1311.0725], [doi:10.1088/0004-637X/788/1/63].

[221] D. Baumann, A. Nicolis, L. Senatore, and M. Zaldarriaga, *Cosmological non-linearities as an effective fluid*, *J. Cosmol. Astropart. Phys.* **7** (July, 2012) 051, [arXiv:1004.2488], [doi:10.1088/1475-7516/2012/07/051].

[222] M. P. Hertzberg, *Effective field theory of dark matter and structure formation: Semianalytical results*, *Phys. Rev. D* **89** (Feb., 2014) 043521, [arXiv:1208.0839], [doi:10.1103/PhysRevD.89.043521].

[223] J. J. M. Carrasco, S. Foreman, D. Green, and L. Senatore, *The 2-loop matter power spectrum and the IR-safe integrand*, *J. Cosmol. Astropart. Phys.* **7** (July, 2014) 56, [arXiv:1304.4946], [doi:10.1088/1475-7516/2014/07/056].

[224] J. J. M. Carrasco, S. Foreman, D. Green, and L. Senatore, *The Effective Field Theory of Large Scale Structures at two loops*, *J. Cosmol. Astropart. Phys.* **7** (July, 2014) 57, [arXiv:1310.0464], [doi:10.1088/1475-7516/2014/07/057].

[225] E. Pajer and M. Zaldarriaga, *On the renormalization of the effective field theory of large scale structures*, *J. Cosmol. Astropart. Phys.* **8** (Aug., 2013) 37, [arXiv:1301.7182], [doi:10.1088/1475-7516/2013/08/037].

[226] S. M. Carroll, S. Leichenauer, and J. Pollack, *Consistent effective theory of long-wavelength cosmological perturbations*, *Phys. Rev. D* **90** (July, 2014) 023518, [arXiv:1310.2920], [doi:10.1103/PhysRevD.90.023518].

[227] R. A. Porto, L. Senatore, and M. Zaldarriaga, *The Lagrangian-space Effective Field Theory of large scale structures*, *J. Cosmol. Astropart. Phys.* **5** (May, 2014) 22, [arXiv:1311.2168], [doi:10.1088/1475-7516/2014/05/022].

[228] L. Senatore and M. Zaldarriaga, *The IR-resummed Effective Field Theory of Large Scale Structures*, *J. Cosmol. Astropart. Phys.* **2** (Feb., 2015) 13, [arXiv:1404.5954], [doi:10.1088/1475-7516/2015/02/013].

[229] U. Seljak, *Analytic model for galaxy and dark matter clustering*, *Mon. Not. R. Astron. Soc.* **318** (Oct., 2000) 203–213, [astro-ph/0001493], [doi:10.1046/j.1365-8711.2000.03715.x].

[230] C.-P. Ma and J. N. Fry, *Deriving the Nonlinear Cosmological Power Spectrum and Bispectrum from Analytic Dark Matter Halo Profiles and Mass Functions*, *Astrophys. J.* **543** (Nov., 2000) 503–513, [astro-ph/0003343], [doi:10.1086/317146].

[231] J. A. Peacock and R. E. Smith, *Halo occupation numbers and galaxy bias*, *Mon. Not. R. Astron. Soc.* **318** (Nov., 2000) 1144–1156, [astro-ph/0005010], [doi:10.1046/j.1365-8711.2000.03779.x].

[232] A. Cooray and R. Sheth, *Halo models of large scale structure*, *Phys. Rep.* **372** (Dec., 2002) 1–129, [astro-ph/0206508], [doi:10.1016/S0370-1573(02)00276-4].

[233] P. Valageas and T. Nishimichi, *Combining perturbation theories with halo models*, *Astron. Astrophys.* **527** (Mar., 2011) A87, [arXiv:1009.0597], [doi:10.1051/0004-6361/201015685].

[234] P. Valageas and T. Nishimichi, *Combining perturbation theories with halo models for the matter bispectrum*, *Astron. Astrophys.* **532** (Aug., 2011) A4, [arXiv:1102.0641], [doi:10.1051/0004-6361/201116638].

[235] I. Mohammed and U. Seljak, *Analytic model for the matter power spectrum, its covariance matrix and baryonic effects*, *Mon. Not. R. Astron. Soc.* **445** (Dec., 2014) 3382–3400, [arXiv:1407.0060], [doi:10.1093/mnras/stu1972].

[236] U. Seljak and Z. Vlah, *Halo Zel'dovich model and perturbation theory: Dark matter power spectrum and correlation function*, *Phys. Rev. D* **91** (June, 2015) 123516, [arXiv:1501.07512], [doi:10.1103/PhysRevD.91.123516].

[237] R. E. Smith, J. A. Peacock, A. Jenkins, S. D. M. White, C. S. Frenk, F. R. Pearce, P. A. Thomas, G. Efstathiou, and H. M. P. Couchman, *Stable clustering, the halo model and non-linear cosmological power spectra*, *Mon. Not. R. Astron. Soc.* **341** (June, 2003) 1311–1332, [astro-ph/0207664], [doi:10.1046/j.1365-8711.2003.06503.x].

[238] R. Takahashi, M. Sato, T. Nishimichi, A. Taruya, and M. Oguri, *Revising the Halofit Model for the Nonlinear Matter Power Spectrum*, *Astrophys. J.* **761** (Dec., 2012) 152, [arXiv:1208.2701], [doi:10.1088/0004-637X/761/2/152].

[239] K. Heitmann, M. White, C. Wagner, S. Habib, and D. Higdon, *The Coyote Universe. I. Precision Determination of the Nonlinear Matter Power Spectrum*, *Astrophys. J.* **715** (May, 2010) 104–121, [arXiv:0812.1052], [doi:10.1088/0004-637X/715/1/104].

[240] E. Sefusatti, M. Crocce, and V. Desjacques, *The matter bispectrum in N-body simulations with non-Gaussian initial conditions*, *Mon. Not. R. Astron. Soc.* **406** (Aug., 2010) 1014–1028, [arXiv:1003.0007], [doi:10.1111/j.1365-2966.2010.16723.x].

[241] E. Sefusatti, M. Crocce, and V. Desjacques, *The halo bispectrum in N-body simulations with non-Gaussian initial conditions*, *Mon. Not. R. Astron. Soc.* **425** (Oct., 2012) 2903–2930, [arXiv:1111.6966], [doi:10.1111/j.1365-2966.2012.21271.x].

[242] M. M. Schmittfull, D. M. Regan, and E. P. S. Shellard, *Fast estimation of gravitational and primordial bispectra in large scale structures*, *Phys. Rev. D* **88** (Sept., 2013) 063512, [arXiv:1207.5678], [doi:10.1103/PhysRevD.88.063512].

[243] M. Schmittfull, T. Baldauf, and U. Seljak, *Near optimal bispectrum estimators for large-scale structure*, *Phys. Rev. D* **91** (Feb., 2015) 043530, [arXiv:1411.6595], [doi:10.1103/PhysRevD.91.043530].

[244] J. R. Fergusson, D. M. Regan, and E. P. S. Shellard, *Rapid separable analysis of higher order correlators in large-scale structure*, *Phys. Rev. D* **86** (Sept., 2012) 063511, [arXiv:1008.1730], [doi:10.1103/PhysRevD.86.063511].

[245] J. R. Fergusson, M. Liguori, and E. P. S. Shellard, *General CMB and primordial bispectrum estimation: Mode expansion, map making, and measures of F_{NL}*, *Phys. Rev. D* **82** (July, 2010) 023502, [arXiv:0912.5516], [doi:10.1103/PhysRevD.82.023502].

[246] Y. P. Jing and G. Börner, *The Three-Point Correlation Function of Galaxies Determined from the Las Campanas Redshift Survey*, *Astrophys. J.* **503** (Aug., 1998) 37–47, [astro-ph/9802011], [doi:10.1086/305997].

[247] H. A. Feldman, J. A. Frieman, J. N. Fry, and R. Scoccimarro, *Constraints on Galaxy Bias, Matter Density, and Primordial Non-Gaussianity from the PSCz Galaxy Redshift Survey*, *Phys. Rev. Lett.* **86** (Feb., 2001) 1434, [astro-ph/0010205], [doi:10.1103/PhysRevLett.86.1434].

[248] R. Scoccimarro, H. A. Feldman, J. N. Fry, and J. A. Frieman, *The Bispectrum of IRAS Redshift Catalogs*, *Astrophys. J.* **546** (Jan., 2001) 652–664, [astro-ph/0004087], [doi:10.1086/318284].

[249] L. Verde *et al.*, *The 2dF Galaxy Redshift Survey: the bias of galaxies and the density of the Universe*, *Mon. Not. R. Astron. Soc.* **335** (Sept., 2002) 432–440, [astro-ph/0112161], [doi:10.1046/j.1365-8711.2002.05620.x].

[250] Y. P. Jing and G. Börner, *The Three-Point Correlation Function of Galaxies Determined from the Two-Degree Field Galaxy Redshift Survey*, *Astrophys. J.* **607** (May, 2004) 140–163, [astro-ph/0311585], [doi:10.1086/383343].

[251] Y. Wang, X. Yang, H. J. Mo, F. C. van den Bosch, and Y. Chu, *The three-point correlation function of galaxies: comparing halo occupation models with observations*, *Mon. Not. R. Astron. Soc.* **353** (Sept., 2004) 287–300, [astro-ph/0404143], [doi:10.1111/j.1365-2966.2004.08141.x].

[252] F. Marín, *The Large-scale Three-point Correlation Function of Sloan Digital Sky Survey Luminous Red Galaxies*, *Astrophys. J.* **737** (Aug., 2011) 97, [arXiv:1011.4530], [doi:10.1088/0004-637X/737/2/97].

[253] F. A. Marín *et al.*, *The WiggleZ Dark Energy Survey: constraining galaxy bias and cosmic growth with three-point correlation functions*, *Mon. Not. R. Astron. Soc.* **432** (July, 2013) 2654–2668, [arXiv:1303.6644], [doi:10.1093/mnras/stt520].

[254] H. Gil-Marín, J. Noreña, L. Verde, W. J. Percival, C. Wagner, M. Manera, and D. P. Schneider, *The power spectrum and bispectrum of SDSS DR11 BOSS galaxies - I. Bias and gravity*, *Mon. Not. R. Astron. Soc.* **451** (July, 2015) 5058–5099, [arXiv:1407.5668], [doi:10.1093/mnras/stv961].

[255] H. Gil-Marín, L. Verde, J. Noreña, A. J. Cuesta, L. Samushia, W. J. Percival, C. Wagner, M. Manera, and D. P. Schneider, *The power spectrum and bispectrum of SDSS DR11 BOSS galaxies - II. Cosmological interpretation*,

Mon. Not. R. Astron. Soc. **452** (Sept., 2015) 1914–1921, [arXiv:1408.0027], [doi:10.1093/mnras/stv1359].

[256] L. D. Landau and E. M. Lifshitz, *Fluid Mechanics: Volume 6*. Butterworth-Heinemann, 1987.

[257] R. Scoccimarro, S. Colombi, J. N. Fry, J. A. Frieman, E. Hivon, and A. Melott, *Nonlinear Evolution of the Bispectrum of Cosmological Perturbations*, *Astrophys. J.* **496** (Mar., 1998) 586–604, [astro-ph/9704075], [doi:10.1086/305399].

[258] M. Peloso and M. Pietroni, *Galilean invariance and the consistency relation for the nonlinear squeezed bispectrum of large scale structure*, *J. Cosmol. Astropart. Phys.* **5** (May, 2013) 031, [arXiv:1302.0223], [doi:10.1088/1475-7516/2013/05/031].

[259] A. Kehagias and A. Riotto, *Symmetries and consistency relations in the large scale structure of the universe*, *Nuclear Physics B* **873** (Aug., 2013) 514–529, [arXiv:1302.0130], [doi:10.1016/j.nuclphysb.2013.05.009].

[260] R. E. Angulo, S. Foreman, M. Schmittfull, and L. Senatore, *The One-Loop Matter Bispectrum in the Effective Field Theory of Large Scale Structures*, *J. Cosmol. Astropart. Phys.* **1510** (2015), no. 10 039, [arXiv:1406.4143], [doi:10.1088/1475-7516/2015/10/039].

[261] T. Hahn, *CUBA - a library for multidimensional numerical integration*, *Computer Physics Communications* **168** (June, 2005) 78–95, [hep-ph/0404043], [doi:10.1016/j.cpc.2005.01.010].

[262] A. Taruya, F. Bernardeau, T. Nishimichi, and S. Codis, *Direct and fast calculation of regularized cosmological power spectrum at two-loop order*, *Phys. Rev. D* **86** (Nov., 2012) 103528, [arXiv:1208.1191], [doi:10.1103/PhysRevD.86.103528].

[263] T. Baldauf, L. Mercolli, M. Mirbabayi, and E. Pajer, *The bispectrum in the Effective Field Theory of Large Scale Structure*, *J. Cosmol. Astropart. Phys.* **5** (May, 2015) 7, [arXiv:1406.4135], [doi:10.1088/1475-7516/2015/05/007].

[264] A. N. Taylor and A. J. S. Hamilton, *Non-linear cosmological power spectra in real and redshift space*, *Mon. Not. R. Astron. Soc.* **282** (Oct., 1996) 767–778, [astro-ph/9604020], [doi:10.1093/mnras/282.3.767].

[265] K. B. Fisher and A. Nusser, *The non-linear redshift-space power spectrum: Omega from redshift surveys*, *Mon. Not. R. Astron. Soc.* **279** (Mar., 1996) L1–L5, [astro-ph/9510049], [doi:10.1093/mnras/279.1.1L].

[266] R. Scoccimarro and H. M. P. Couchman, *A fitting formula for the non-linear evolution of the bispectrum*, *Mon. Not. R. Astron. Soc.* **325** (Aug., 2001) 1312–1316, [astro-ph/0009427], [doi:10.1046/j.1365-8711.2001.04281.x].

[267] H. Gil-Marín, C. Wagner, F. Fragkoudi, R. Jimenez, and L. Verde, *An improved fitting formula for the dark matter bispectrum*, *J. Cosmol. Astropart. Phys.* **2** (Feb., 2012) 047, [arXiv:1111.4477], [doi:10.1088/1475-7516/2012/02/047].

[268] J. Neyman and E. L. Scott, *A Theory of the Spatial Distribution of Galaxies.*, *Astrophys. J.* **116** (July, 1952) 144, [doi:10.1086/145599].

[269] S. D. M. White and M. J. Rees, *Core condensation in heavy halos - A two-stage theory for galaxy formation and clustering*, *Mon. Not. R. Astron. Soc.* **183** (May, 1978) 341–358, [doi:10.1093/mnras/183.3.341].

[270] J. E. Gunn and J. R. Gott, III, *On the Infall of Matter Into Clusters of Galaxies and Some Effects on Their Evolution*, *Astrophys. J.* **176** (Aug., 1972) 1, [doi:10.1086/151605].

[271] W. H. Press and P. Schechter, *Formation of Galaxies and Clusters of Galaxies by Self-Similar Gravitational Condensation*, *Astrophys. J.* **187** (Feb., 1974) 425–438, [doi:10.1086/152650].

[272] R. K. Sheth and G. Tormen, *Large-scale bias and the peak background split*, *Mon. Not. R. Astron. Soc.* **308** (Sept., 1999) 119–126, [astro-ph/9901122], [doi:10.1046/j.1365-8711.1999.02692.x].

[273] J. Tinker, A. V. Kravtsov, A. Klypin, K. Abazajian, M. Warren, G. Yepes, S. Gottlöber, and D. E. Holz, *Toward a Halo Mass Function for Precision Cosmology: The Limits of Universality*, *Astrophys. J.* **688** (Dec., 2008) 709–728, [arXiv:0803.2706], [doi:10.1086/591439].

[274] J. L. Tinker, B. E. Robertson, A. V. Kravtsov, A. Klypin, M. S. Warren, G. Yepes, and S. Gottlöber, *The Large-scale Bias of Dark Matter Halos: Numerical Calibration and Model Tests*, *Astrophys. J.* **724** (Dec., 2010) 878–886, [arXiv:1001.3162], [doi:10.1088/0004-637X/724/2/878].

[275] J. F. Navarro, C. S. Frenk, and S. D. M. White, *The Structure of Cold Dark Matter Halos*, *Astrophys. J.* **462** (May, 1996) 563, [astro-ph/9508025], [doi:10.1086/177173].

[276] A. A. Klypin, S. Trujillo-Gomez, and J. Primack, *Dark Matter Halos in the Standard Cosmological Model: Results from the Bolshoi Simulation*, *Astrophys. J.* **740** (Oct., 2011) 102, [arXiv:1002.3660], [doi:10.1088/0004-637X/740/2/102].

[277] T. Giannantonio, C. Porciani, J. Carron, A. Amara, and A. Pillepich, *Constraining primordial non-Gaussianity with future galaxy surveys*, *Mon. Not. R. Astron. Soc.* **422** (June, 2012) 2854–2877, [arXiv:1109.0958], [doi:10.1111/j.1365-2966.2012.20604.x].

[278] E. Massara, F. Villaescusa-Navarro, and M. Viel, *The halo model in a massive neutrino cosmology*, *J. Cosmol. Astropart. Phys.* **12** (Dec., 2014) 053, [arXiv:1410.6813], [doi:10.1088/1475-7516/2014/12/053].

[279] G. L. Bryan and M. L. Norman, *Statistical Properties of X-Ray Clusters: Analytic and Numerical Comparisons*, *Astrophys. J.* **495** (Mar., 1998) 80–99, [astro-ph/9710107], [doi:10.1086/305262].

[280] G. Kauffmann, J. M. Colberg, A. Diaferio, and S. D. M. White, *Clustering of galaxies in a hierarchical universe - I. Methods and results at z=0*, *Mon. Not. R. Astron. Soc.* **303** (Feb., 1999) 188–206, [astro-ph/9805283], [doi:10.1046/j.1365-8711.1999.02202.x].

[281] R. Scoccimarro, R. K. Sheth, L. Hui, and B. Jain, *How Many Galaxies Fit in a Halo? Constraints on Galaxy Formation Efficiency from Spatial Clustering*, *Astrophys. J.* **546** (Jan., 2001) 20–34, [astro-ph/0006319], [doi:10.1086/318261].

[282] H. J. Mo, Y. P. Jing, and S. D. M. White, *High-order correlations of peaks and haloes: a step towards understanding galaxy biasing*, *Mon. Not. R. Astron. Soc.* **284** (Jan., 1997) 189–201, [astro-ph/9603039], [doi:10.1093/mnras/284.1.189].

[283] A. Refregier and R. Teyssier, *Numerical and analytical predictions for the large-scale Sunyaev-Zel'dovich effect*, *Phys. Rev. D* **66** (Aug., 2002) 043002, [astro-ph/0012086], [doi:10.1103/PhysRevD.66.043002].

[284] D. G. Figueroa, E. Sefusatti, A. Riotto, and F. Vernizzi, *The effect of local non-Gaussianity on the matter bispectrum at small scales*, *J. Cosmol. Astropart. Phys.* **8** (Aug., 2012) 036, [arXiv:1205.2015], [doi:10.1088/1475-7516/2012/08/036].

[285] R. E. Smith, R. K. Sheth, and R. Scoccimarro, *Analytic model for the bispectrum of galaxies in redshift space*, *Phys. Rev. D* **78** (July, 2008) 023523, [arXiv:0712.0017], [doi:10.1103/PhysRevD.78.023523].

[286] R. E. Smith, R. Scoccimarro, and R. K. Sheth, *Scale dependence of halo and galaxy bias: Effects in real space*, *Phys. Rev. D* **75** (Mar., 2007) 063512, [astro-ph/0609547], [doi:10.1103/PhysRevD.75.063512].

[287] C. Giocoli, F. Marulli, M. Baldi, L. Moscardini, and R. B. Metcalf, *Characterizing dark interactions with the halo mass accretion history and structural properties*, *Mon. Not. R. Astron. Soc.* **434** (Oct., 2013) 2982–2998, [arXiv:1301.3151], [doi:10.1093/mnras/stt1218].

[288] P. Schneider and M. Bartelmann, *The power spectrum of density fluctuations in the Zel'dovich approximation*, *Mon. Not. R. Astron. Soc.* **273** (mar, 1995) 475–483.

[289] D. Babich, P. Creminelli, and M. Zaldarriaga, *The shape of non-Gaussianities*, *J. Cosmol. Astropart. Phys.* **8** (Aug., 2004) 009, [astro-ph/0405356], [doi:10.1088/1475-7516/2004/08/009].

[290] T. Baldauf, U. Seljak, V. Desjacques, and P. McDonald, *Evidence for Quadratic Tidal Tensor Bias from the Halo Bispectrum*, *Phys. Rev.* **D86** (2012) 083540, [arXiv:1201.4827], [doi:10.1103/PhysRevD.86.083540].

[291] J. R. Fergusson and E. P. S. Shellard, *Shape of primordial non-Gaussianity and the CMB bispectrum*, *Phys. Rev. D* **80** (Aug., 2009) 043510, [arXiv:0812.3413], [doi:10.1103/PhysRevD.80.043510].

[292] P. Creminelli, A. Nicolis, L. Senatore, M. Tegmark, and M. Zaldarriaga, *Limits on non-Gaussianities from WMAP data*, *J. Cosmol. Astropart. Phys.* **5** (May, 2006) 004, [astro-ph/0509029], [doi:10.1088/1475-7516/2006/05/004].

[293] P. D. Meerburg, J. P. van der Schaar, and P. S. Corasaniti, *Signatures of initial state modifications on bispectrum statistics*, *J. Cosmol. Astropart. Phys.* **5** (May, 2009) 018, [arXiv:0901.4044], [doi:10.1088/1475-7516/2009/05/018].

[294] V. Springel, N. Yoshida, and S. D. White, *GADGET: a code for collisionless and gasdynamical cosmological simulations*, *New Astronomy* **6** (2001), no. 2 79 – 117, [astro-ph/0003162], [doi:10.1016/S1384-1076(01)00042-2].

[295] V. Springel, *The cosmological simulation code GADGET-2*, *Mon. Not. R. Astron. Soc.* **364** (2005), no. 4 1105–1134, [astro-ph/0505010], [doi:10.1111/j.1365-2966.2005.09655.x].

[296] E. Komatsu *et al.*, *Seven-year Wilkinson Microwave Anisotropy Probe (WMAP) Observations: Cosmological Interpretation*, *Astrophys. J. Supp.* **192** (Feb., 2011) 18, [arXiv:1001.4538], [doi:10.1088/0067-0049/192/2/18].

[297] D. M. Regan, M. M. Schmittfull, E. P. S. Shellard, and J. R. Fergusson, *Universal non-gaussian initial conditions for n-body simulations*, *Phys. Rev. D* **86** (Dec, 2012) 123524, [arXiv:1108.3813], [doi:10.1103/PhysRevD.86.123524].

[298] R. E. Smith, V. Desjacques, and L. Marian, *Nonlinear clustering in models with primordial non-gaussianity: The halo model approach*, *Phys. Rev. D* **83** (Feb, 2011) 043526, [arXiv:1009.5085], [doi:10.1103/PhysRevD.83.043526].

[299] C.-T. Chiang, C. Wagner, F. Schmidt, and E. Komatsu, *Position-dependent power spectrum of the large-scale structure: a novel method to measure the squeezed-limit bispectrum*, *J. Cosmol. Astropart. Phys.* **5** (May, 2014) 48, [arXiv:1403.3411], [doi:10.1088/1475-7516/2014/05/048].

[300] A. Mead, J. Peacock, C. Heymans, S. Joudaki, and A. Heavens, *An accurate halo model for fitting non-linear cosmological power spectra and baryonic feedback models*, *Mon. Not. Roy. Astron. Soc.* **454** (2015), no. 2 1958–1975, [arXiv:1505.07833], [doi:10.1093/mnras/stv2036].